Technische Universität München
Physik-Department
Institut für Theoretische Physik T39
Univ.-Prof. Dr. W. Weise

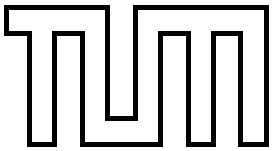

Chiral Dynamics and the Nuclear Many-Body Problem

Dipl.-Phys. Univ. Stefan Fritsch

Vollständiger Abdruck der von der Fakultät für Physik der Technischen Universität München zur Erlangung des akademischen Grades eines

Doktors der Naturwissenschaften (Dr. rer. nat.)

genehmigten Dissertation.

Vorsitzender: Univ.-Prof. Dr. Stephan Paul

Prüfer der Dissertation:

1. Univ.-Prof. Dr. Wolfram Weise
2. Univ.-Prof. Dr. Peter Ring

Die Dissertation wurde am 4.11.2004 bei der Technischen Universität München eingereicht und durch die Fakultät für Physik am 30.11.2004 angenommen.

Summary

The goal of this work is to draw a connection from the nuclear many-body problem to the fundamental theory of the strong interaction, quantum chromodynamics. Chiral perturbation theory, which is based on the symmetries and symmetry breaking patterns of low-energy QCD, is used to treat the relevant pion-nucleon dynamics in a systematic expansion in small scales. In a second step, the $\Delta(1232)$-isobar is included as explicit degree of freedom since the delta-nucleon mass splitting is of a size comparable to the other relevant small scales, the Fermi momentum and the pion mass. Using this systematic framework, the equations of state of isospin-symmetric nuclear matter and of pure neutron matter, the asymmetry energy, and the in-medium single particle potential are calculated. The scheme is then extended to non-zero temperatures and the liquid-gas phase transition of nuclear matter is reproduced. In addition, the energy density functional relevant for inhomogeneous systems is computed.

Zusammenfassung

Das Ziel dieser Arbeit ist es, einen Zusammenhang zwischen dem Vielteilchenproblem der Kernphysik und der fundamentalen Theorie der starken Wechselwirkung, der Quantenchromodynamik, herzustellen. Die chirale Störungstheorie, welche auf den Symmetrien und der Symmetriebrechungsstruktur der Niederenergie-QCD basiert, wird verwendet um die Pion-Nukleon-Dynamik in einer systematischen Entwicklung in kleinen Skalen zu behandeln. In einem zweiten Schritt wird das $\Delta(1232)$-Isobar als expliziter Freiheitsgrad eingeführt, da die Delta-Nukleon-Massendifferenz eine zu den anderen relevanten kleinen Skalen, dem Fermiimpuls und der Pionmasse, vergleichbare Größe hat. Mit diesem systematischen Entwicklungsschema werden die Zustandsgleichungen von Isospin-symmetrischer Kernmaterie und von Neutronenmaterie, sowie die Asymmetrieenergie und das Einteilchenpotential in Materie berechnet. Das Schema wird dann auf nicht verschwindende Temperaturen erweitert, wobei der Flüssigkeits-Gas-Phasenübergang von Kernmaterie reproduziert wird. Außerdem wird das Energiedichtefunktional berechnet, welches für inhomogene Systeme von Bedeutung ist.

Contents

Chapter 1

Introduction

One of the central problems in nuclear physics is the description of nuclear matter and finite nuclei in terms of a microscopic theory. In this context, microscopic theory usually means that one uses a model of the free nucleon-nucleon (NN) interaction, which is tuned to reproduce the available NN-scattering phase-shifts and deuteron properties. Such nucleon-nucleon interactions usually have a phenomenological repulsive short-range core which implies that nuclear matter is a strongly correlated quantum liquid. A description starting from these NN-interactions requires advanced many-body methods such as (relativistic) Brueckner-Hartree-Fock [1] or quantum Monte Carlo techniques [2–4].

In general, an accurate reproduction of nuclear matter properties demands either a relativistic treatment or the inclusion of a three-body force in addition to the phenomenological NN-interaction. The present status is that nuclei with up to $A = 10$ nucleons [3] have been calculated using Green's function Monte Carlo methods. Systems containing only neutrons (or homogeneous neutron matter) have been calculated both with Green's function Monte Carlo [4] and auxiliary field diffusion Monte Carlo techniques [5].

Apart from such ab-initio approaches there are less basic frameworks using effective interactions. Examples are shell model calculations which perform exact diagonalizations of the Hamiltonian matrix in finite but large model spaces [6]. Self-consistent mean field models are also widely used [7]. The effective interactions introduced in such models are adjusted exclusively for the respective model. The Gogny force and the many variants of the Skyrme force [8] are examples for nonrelativistic variants of such effective interactions. On the other hand, relativistic mean field models [9–12] often use interactions formulated in terms of the exchange of scalar and vector bosons.[1] An important advantage of such relativistic approaches is that they explain the strong nuclear spin-orbit force in a natural way by the interplay of strong scalar and vector fields.

While the methods mentioned so far are successful in describing the properties of nuclear matter and finite nuclei they are all lacking one important aspect: there is no direct connection to quantum chromodynamics, the underlying theory of the strong interaction which is ultimately responsible for the nuclear forces.

This issue has been addressed recently by a novel approach to the nuclear matter problem [13–15]. This approach, which is also the subject of this thesis, is based on effective field theory (in particular chiral perturbation theory) which exploits the separation of

[1] The bosons appearing in such approaches (σ, ω, ρ, ...) are effective fields named according to their spin and isospin quantum numbers and are not to be confused with existing physical mesons.

scales present in QCD. In the particle spectrum, this separation is visible in the mass gap between the pion mass and other typical hadronic mass scales, such as the nucleon mass. This allows one to reformulate the low-energy sector of QCD in terms of pions and nucleons, the degrees of freedom active at those energies. Details of the short-distance NN-interaction are not resolved at low-energies and can therefore be subsumed in a few effective NN-contact interactions. This leads to a separation of long- and short-distance dynamics and an ordering scheme in powers of small momenta [16, 17].

The importance of the pion is also demonstrated by a simple consideration of scales. The relevant scale in nuclear matter at nuclear saturation density $\rho_0 \simeq 0.16\,\mathrm{fm}^{-3}$ is the Fermi momentum $k_{\mathrm{f},0} \simeq 262\,\mathrm{MeV}$, about twice the pion mass m_π. Therefore, pions must be included as explicit degrees of freedom in the description of the nuclear many-body dynamics. A similar consideration also suggests the inclusion of the $\Delta(1232)$-isobar. The delta-nucleon mass splitting $\Delta = 293\,\mathrm{MeV}$ is comparable in magnitude with the Fermi momentum $k_{\mathrm{f},0}$ at equilibrium. Propagation effects of virtual $\Delta(1232)$-isobars can therefore be resolved at the densities of interest. The importance of the $\Delta(1232)$-degrees of freedom has also been pointed out in refs. [3, 18].

The separation of scales present in the nuclear many-body problem becomes also apparent when considering the model dependence of the phenomenological NN-interactions. While the long-range part of all realistic phenomenological potentials is given by one pion exchange, they employ quite different treatments of the intermediate- and short-range dynamics. However, since the details of the short-range dynamics are not resolved at low energies, the different potentials can all be combined into a single model-independent low momentum interaction $V_{\mathrm{low}\,k}$ [19].

The effective field theory approach has also been used to calculate the free NN-interaction. Thus, it is possible to establish a connection between nuclear physics and low-energy QCD by using this interaction in many-body calculations instead of a phenomenological NN-potential. The work on the NN-interaction has now reached fourth order in chiral perturbation theory [20] and has resulted in a potential of a precision comparable to the best phenomenological potentials available.

Nevertheless, in this thesis we follow the more direct approach from [13–15] and calculate nuclear matter properties from in-medium chiral perturbation theory directly without first calculating a high-precision NN-potential.

This thesis is structured as follows:

Chapter 2 starts with an overview of some properties of nuclei and nuclear matter. We then outline elements of QCD and its symmetries which lead to chiral perturbation theory. The last section provides details about chiral perturbation theory at finite density.

In chapter 3, we first describe the calculational framework introduced in refs. [14, 15], which deals with homogeneous nuclear matter at zero temperature. We then present results for the equations of state of isospin symmetric nuclear matter and pure neutron matter, the asymmetry energy, and the single particle potential. In this first step, using in-medium chiral perturbation theory with pions and nucleons as the only "active" degrees of freedom, the description of nuclear saturation is already very good, whereas the strong momentum dependence of the single particle potential hints at remaining problems we will encounter later at finite temperatures. We also discuss the relative importance of the various pieces of chiral pion exchange and consider the density dependence of the chiral condensate.

In chapter 4, we extend our framework to finite temperatures. The pressure isotherms for symmetric nuclear matter show the characteristic behavior of a liquid-gas phase transition of the van der Waals type. However, the critical temperature is somewhat higher than the one usually assumed for the liquid-gas phase transition in nuclear matter. This is a reflection of the too strong slope of the single particle potential near the Fermi surface.

Chapter 5 is devoted to inhomogeneous systems. We calculate the energy density functional for weakly inhomogeneous nuclear matter based on the density-matrix expansion method. Problems with the spin-orbit strength and the behavior of the energy density functional at very low densities cause the calculation of the ^{40}Ca ground state properties to give unsatisfactory results. Possible reasons for these shortcomings are considered. In the last section we give a brief summary of an alternative ansatz to finite nuclei taking into account both chiral pion dynamics and strong scalar and vector mean fields constrained by in-medium QCD sum rules [21, 22]. This method has the advantage of giving a correct description of the nuclear spin-orbit force.

In chapter 6, we investigate what influence the detailed treatment of the short-range NN-contact terms has on our results. A comparison with a Dirac-Brueckner calculation lets us conclude that the short-range NN-terms must not be iterated further since they already represent the complete short-range T-matrix information. This prescription is the main difference between our framework and the work of Lutz et al. [13].

We then extend our framework to include the $\Delta(1232)$-isobar as an explicit degree of freedom in chapter 7. We investigate the influences on the various (semi-)empirical properties discussed in the previous chapters. Most importantly, there is a considerable improvement of the single particle properties and, as a consequence, the finite temperature behavior. The equation of state of neutron matter and the density dependence of the asymmetry energy are also improved.

The thesis finishes with conclusions and an outlook in chapter 8.

Chapter 2

Basics of nuclear matter and low-energy QCD

2.1 Nuclei and nuclear matter

Atomic nuclei are aggregates of nucleons (protons and neutrons) that interact through nuclear and Coulomb forces. Nucleons in turn consist of quarks and gluons whose behavior is described by quantum chromodynamics. In nuclei and at low energies in general, these constituents are tightly bound and confined in the nucleons and need not be explicitly considered when describing the low-energy properties of nuclei. However their strong interaction is responsible for the nuclear interaction in a similar way as the electromagnetic interaction is responsible for the effective van der Waals forces between atoms. It is therefore interesting and important to establish a theoretical connection between nuclear physics and QCD.

In stable nuclei, the attractive part of the nuclear force overcompensates the repulsive Coulomb-force leading to a bound state in equilibrium. The charge distribution of the protons in a nucleus can be probed with electron scattering. For not too small nuclei with a nucleon number $A \gtrsim 15$, the radius scales with the mass number as

$$R \approx r_0 A^{1/3}$$

with $r_0 \approx 1.12\,\mathrm{fm}$ [23]. This behavior implies an approximately constant density of the nuclear core. It is a consequence of the saturation properties of nuclear matter.

For first orientation, we summarize bulk properties of nuclei and nuclear matter which have been discussed already very early in the history of nuclear physics, but can still serve as a basis for further discussion.

Liquid drop model and semi-empirical mass formula

The bulk of nuclear matter in the interior of heavy nuclei behaves like a Fermi liquid. An ancient, very simple but useful model is the so-called liquid drop model. In this model, a nucleus is considered to be a drop of incompressible nuclear liquid. The usefulness of the model becomes apparent when the energy of the drop is calculated. For a nucleus with N neutrons and Z protons, the result can be written in the form of the Bethe-Weizsäcker

formula

$$E_{\mathrm{nucl}} = ZM_{\mathrm{p}} + NM_{\mathrm{n}} - a_1 A + a_2 A^{2/3} + a_3 \frac{Z(Z-1)}{A^{1/3}} + a_4 \frac{(Z-N)^2}{A} + \frac{a_{\mathrm{P}}}{A^{1/2}}\,, \qquad (2.1)$$

with $M_{\mathrm{p,n}}$ being the proton/neutron mass. The coefficients $a_1, \ldots, a_4$ and a_{P} are fitted to the empirical masses of nuclei. A recent fit [24] yields $a_1 = 15.4\,\mathrm{MeV}$, $a_2 = 16.9\,\mathrm{MeV}$, $a_3 = 0.695\,\mathrm{MeV}$, $a_4 = 22.4\,\mathrm{MeV}$ and $a_{\mathrm{P}} = 11.2\,\mathrm{MeV}$ (odd N/odd Z), $0\,\mathrm{MeV}$ (odd A), $-11.2\,\mathrm{MeV}$ (even N/even Z).

The binding energy $E_{\mathrm{nucl}} - ZM_{\mathrm{p}} - NM_{\mathrm{n}}$ is predominantly determined by the volume term $-a_1 A$ which grows linearly with the number of nucleons A. If all nucleons in the nucleus were interacting pairwise with all other nucleons, one would expect an approximately quadratic behavior, proportional to the number of pairs $A(A-1)/2$. An analogous behavior, modified by the characteristic $1/r$ dependence, is found for the Coulomb force $a_3 Z(Z-1)/A^{1/3}$ of the protons. On the other hand, the linear growth of the volume energy with A means that the NN-interaction has a finite range and a repulsive component. Thus, the nucleons only interact with a small number of other nucleons that is independent of the size of the nucleus. The binding energy per nucleon remains approximately constant even with growing A. This and the constant density in the interior of heavy nuclei lead to the idea to study the saturation properties of a system of infinite nuclear matter at constant density and equal numbers of protons and neutrons. In this system, there are no surface effects and the electromagnetic interaction is ignored. Later in this section we will briefly describe the properties of nuclear matter. The explanation of those properties in terms of a theory exhibiting the connection to QCD is one of the main topics of this thesis.

The surface term $a_2 A^{2/3}$ in eq. (2.1) takes into account the effects caused by the finite size of the nucleus. Furthermore, the asymmetry energy proportional to $(Z-N)^2/A$ accounts for the fact that nuclei are preferably stable in states with equal numbers of protons and neutrons (apart from effects of the Coulomb interaction). The same is true for nuclei with even proton and neutron numbers, leading to the pairing energy a_{P}.

Fermi gas

The starting point for discussions of the nucleus as a system of Fermions (nucleons) is the Fermi gas. It emphasizes the essential role of the Pauli principle but ignores all interactions between nucleons at this stage.

Since no two fermions can be in states with the same quantum numbers, the nucleons, confined in a finite volume, move with a characteristic momentum distribution. At temperature $T = 0$, all states with a momentum p below the Fermi momentum k_{f} are occupied, i. e. the distribution is proportional to a step function $\theta(k_{\mathrm{f}} - p)$. With this information, one can connect the density and the Fermi momentum: For an unpolarized isospin symmetric ($N = Z$) system the particle number density is

$$\rho(k_{\mathrm{f}}) = \underset{\text{spin}}{2} \cdot \underset{\text{isospin}}{2} \cdot \int_0^{k_{\mathrm{f}}} \frac{4\pi p^2 \mathrm{d}p}{(2\pi)^3} = \frac{2k_{\mathrm{f}}^3}{3\pi^2}\,. \qquad (2.2)$$

The (relativistic) energy density is $\mathscr{E}(k_\mathrm{f}) = \big(M_\mathrm{N} + \bar{E}_\mathrm{kin}(k_\mathrm{f})\big)\rho(k_\mathrm{f})$ with the kinetic energy per particle, $\bar{E}_\mathrm{kin}(k_\mathrm{f}) = E_\mathrm{kin}/A$, and the nucleon mass $M_\mathrm{N} = 939\,\mathrm{MeV}$. The kinetic energy density has the nonrelativistic expansion:

$$\bar{E}_\mathrm{kin}(k_\mathrm{f})\rho(k_\mathrm{f}) = 4\int_0^{k_\mathrm{f}} \frac{\mathrm{d}^3p}{(2\pi)^3}\left(\sqrt{\mathbf{p}^2 + M_\mathrm{N}^2} - M_\mathrm{N}\right) = \rho(k_\mathrm{f})\left(\frac{3k_\mathrm{f}^2}{10M_\mathrm{N}} + \frac{3k_\mathrm{f}^4}{56M_\mathrm{N}^3} + \ldots\right). \tag{2.3}$$

The Fermi gas model also allows to calculate how the energy changes when neutron and proton numbers are not equal. One finds that the Pauli principle alone is responsible for approximately half of the empirically determined asymmetry energy a_4 in eq. (2.1) (see ref. [23]).

The most precise determination of the nuclear Fermi momentum for isospin-symmetric systems comes from extrapolation of quasi-elastic electron-nucleus scattering data, analyzed using the Fermi gas model. The result is [25]

$$k_{\mathrm{f},0} = (262 \pm 4)\,\mathrm{MeV}\,, \tag{2.4}$$

corresponding to a density $\rho_0 = (0.158 \pm 0.008)\,\mathrm{fm}^{-3}$.

The equation of state of nuclear matter

The part of the equation of state of infinite symmetric nuclear matter that is accessible to experiments is the vicinity of the saturation point. It is defined by the equilibrium Fermi momentum and the energy per particle. The empirical value for the latter is

$$\bar{E}_0 = (-16 \pm 1)\,\mathrm{MeV}\,, \tag{2.5}$$

quoted in ref. [1], and $k_{\mathrm{f},0}$ is given in eq. (2.4). From the fact that $\bar{E}(k_\mathrm{f})$ must have a minimum at the saturation point, it is possible to derive a simple but surprisingly realistic parametrization in powers of the Fermi momentum:

$$\bar{E}(k_\mathrm{f}) = \frac{3k_\mathrm{f}^2}{10M_\mathrm{N}} - \alpha\frac{k_\mathrm{f}^3}{M_\mathrm{N}^2} + \beta\frac{k_\mathrm{f}^4}{M_\mathrm{N}^3}\,. \tag{2.6}$$

The first term is the kinetic energy contribution of a free Fermi gas. The powers of M_N in the other terms have been chosen such that α and β are dimensionless. The interesting feature of this parametrization is that once α and β are adjusted to the nuclear matter saturation point (2.4,2.5), the empirical nuclear matter compressibility [26]

$$K = k_{\mathrm{f},0}^2\,\frac{\partial^2\bar{E}(k_\mathrm{f})}{\partial k_\mathrm{f}^2}\bigg|_{k_\mathrm{f}=k_{\mathrm{f},0}} = (220 \pm 50)\,\mathrm{MeV} \tag{2.7}$$

comes out correctly. Adjusting the parameters α and β to the saturation point results in $\alpha = 5.29$ and $\beta = 12.29$, which leads to a *predicted* value $K = 236\,\mathrm{MeV}$ for the compressibility.

In fig. 2.1 we compare the density dependence of $\bar{E}(k_\mathrm{f})$, given by eq. (2.6) (full line) with the equation of state resulting from the many-body calculation of ref. [27] (dashed

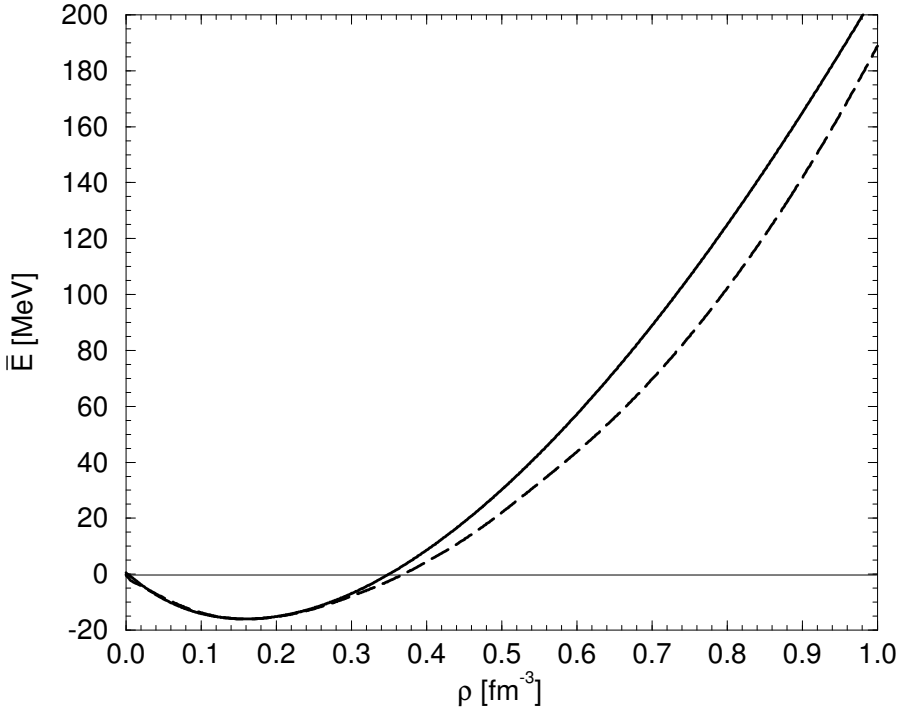

Figure 2.1: Energy per particle of isospin symmetric nuclear matter as a function of baryon density. The full line is the parametrization of eq. (2.6) with $\alpha = 5.29$ and $\beta = 12.29$. The dashed line stems from the many-body calculation of ref. [27].

line). Of course, the low density part of the curves with negative slope is not stable. Nuclear matter at those densities would not be a uniform Fermi gas of nucleons but rather a gas of tightly bound clusters. Therefore, the equation of state should not go to zero energy for $\rho \to 0$ but rather approach the per-particle binding energy of deuterons (or even larger clusters).

Returning to fig. 2.1, one observes that the relative deviation of both curves does not exceed 10% even at very high densities, $\rho \simeq 1.0\,\mathrm{fm}^{-3}$. Keeping in mind that eq. (2.6) provides a realistic parametrization of the nuclear matter equation of state will be very useful in order to understand the saturation mechanism underlying the chiral two-pion exchange. In the chiral limit ($m_\pi = 0$) and truncating to order $\mathcal{O}(k_\mathrm{f}^4)$, the equation of state resulting from one- and two-pion exchange will be precisely of the form of eq. (2.6).

Approaches to nuclear structure

Before we outline the chiral perturbation theory approach to the nuclear many-body problem and its connection to low-energy QCD, we briefly mention other successful

methods for nuclear structure calculations.

The free nucleon-nucleon interaction known from scattering experiments is attractive at long and medium distances and strongly repulsive at short distances. This strongly repulsive core makes calculations of nuclei and nuclear matter difficult, since a perturbative expansion using the strength of the interaction is not possible. Many models avoid these difficulties by starting from an effective in-medium interaction that has no connection to free-space scattering data.

The shell model, for example, uses a simple oscillator mean-field and performs an exact diagonalization of the Hamiltonian matrix in a band of nucleon states around the Fermi surface. The residual interaction used in this valence space is usually fitted phenomenologically. However, there are also calculations starting from the bare NN-interaction ("no-core" shell model). For a recent review, see ref. [6].

Self-consistent mean-field models are also widely used. Such models determine the nuclear mean-field in a self-consistent way by varying an energy density functional and thus minimizing the ground state energy of the nucleus. Nonrelativistic self-consistent mean-field models usually use the density dependent Hartree-Fock method (equivalent to Kohn-Sham theory in electronic systems) with variants of the Skyrme force or the Gogny force (see appendix A and ref. [7]).

Relativistic mean-field models, on the other hand, usually use relativistic Hartree approximation with finite range potentials which are parametrized in terms of one-boson exchange [9–12]. At first glance, the need for relativity is not obvious since the momenta of interest in nuclei are considerably smaller than the (free) nucleon mass. However, this argument is weakened by the reduced effective nucleon mass in a nuclear medium. Furthermore, it turns out that the distinction of scalar and vector fields specific to a relativistic treatment is quite important, in particular for the explanation of the strong nuclear spin-orbit force (see also chapter 5 and section 7.4).

There are also various methods which start from the bare free-space NN-interaction. To solve the problem of the strong repulsive core, nonrelativistic Brueckner theory performs a self-consistent resummation of ladder diagrams up to infinite order. The Brueckner G-matrix obtained by this procedure serves as an effective in-medium two-body interaction. A systematic expansion can then be achieved using a hole-line or Brueckner-Bethe-Goldstone expansion. A diagram with n hole-lines in this expansion accounts for n-body correlations. One- and two-body correlations dominate because the average distance $d_{\mathrm{NN}} \simeq 1.8\,\mathrm{fm}$ between nucleons in the bulk of nuclei is much larger than the radius of the repulsive core of the NN-interaction. A review of this method can be found in ref. [28].

While nonrelativistic Brueckner theory describes the nuclear saturation mechanism qualitatively, it fails on a quantitative level. The saturation points obtained with different NN-interactions do not meet the empirical region but lie on a so-called Coester-line in the $\bar{E}$–ρ plane. This deficiency is fixed by using a relativistic treatment which leads to Dirac-Brueckner theory. For a recent review, see ref. [12].

Other ab-initio approaches starting from a phenomenological free-space NN-interaction are the quantum Monte Carlo techniques. They determine an approximation to the energy and wave functions of the ground state by employing variational methods with correlated trial wave functions. The Green's function Monte Carlo technique then projects

out the exact ground state by propagation in Euclidean space [2,18]. Common to all calculations of this type is however the need for an additional phenomenological three-body force that cannot be determined from NN-scattering [3].

2.2 Elements of QCD

Quantum chromodynamics (QCD) in its "fundamental" form is written in terms of quarks and gluons as basic degrees of freedom. This form is not suitable for the description of nuclear matter since at low energies, quarks and gluons are confined and do not appear as explicit degrees of freedom. Symmetries and symmetry breaking patterns of low-energy QCD are the basis for chiral perturbation theory. We briefly outline some properties of QCD in the following.

2.2.1 The QCD-Lagrangian

QCD is a SU(3) gauge field theory that describes point-like, massive spin–$\frac{1}{2}$ fermions interacting with massless spin–1 gauge bosons, which in turn interact nonlinearly with each other. The Lagrangian is given by

$$\mathscr{L} = \bar{\psi}(iD_\mu\gamma^\mu - \tilde{m})\psi - \frac{1}{2}\,\mathrm{Tr}\;G_{\mu\nu}G^{\mu\nu}\,, \tag{2.8}$$

with the gluonic field strength tensor

$$G_{\mu\nu} = \partial_\mu A^a_\nu t_a - \partial_\nu A^a_\mu t_a + g f_{abc} A^a_\mu A^b_\nu t_c\,,$$

the covariant derivative

$$D_\mu = \partial_\mu - ig A^a_\mu t_a\,,$$

and the generators $t_a = \lambda_a/2$ $(a = 1,\ldots,8)$ of SU(3). The fields ψ describe the six species of quarks which are usually classified into two groups according to their mass: the light quarks with $m_\mathrm{u} \simeq 4\,\mathrm{MeV}$, $m_\mathrm{d} \simeq 8\,\mathrm{MeV}$, $m_\mathrm{s} \simeq (100\ldots150)\,\mathrm{MeV}$ and the heavy quarks with $m_\mathrm{c} \simeq 1.3\,\mathrm{GeV}$, $m_\mathrm{b} \simeq 4.2\,\mathrm{GeV}$, $m_\mathrm{t} \simeq 174\,\mathrm{GeV}$ (at a renormalization scale of approx. 1 GeV). The heavy quarks are irrelevant for the physics of nuclear matter and the s–quark will also be neglected in the main part of this thesis. Therefore, we will restrict ourselves to the two lightest quarks, u and d, in the following. In this case, ψ and the quark mass matrix $\tilde{m}$ are of the form:

$$\psi(x) = \begin{pmatrix} u(x) \\ d(x) \end{pmatrix}, \qquad \tilde{m} = \begin{pmatrix} m_\mathrm{u} & 0 \\ 0 & m_\mathrm{d} \end{pmatrix}. \tag{2.9}$$

Here, $u(x)$ and $d(x)$ are triplets in color space. For example,

$$u(x) = \begin{pmatrix} u_\mathrm{R}(x) \\ u_\mathrm{G}(x) \\ u_\mathrm{B}(x) \end{pmatrix}.$$

An important property of QCD is that the coupling strength $\alpha_\mathrm{s} = g^2/4\pi$ depends on the momentum scale Q. At high energies, α_s is small leading to the so-called asymptotic freedom. In this regime, it is possible to apply perturbation theory in α_s. However, for $Q \lesssim 1\,\mathrm{GeV}$ α_s rises strongly and the elementary colored quarks and gluons are no longer visible as degrees of freedom. Instead, they are replaced by color neutral bound states, the hadrons. This property of QCD is called confinement. At those energies, one needs tools and methods different from those used in perturbative QCD, e. g. lattice QCD or effective field theories such as chiral perturbation theory.

2.2.2 Symmetries

Besides the local SU(3) gauge symmetry, the QCD Lagrangian also possesses a global U(1) symmetry, i. e. the Lagrangian is invariant under global phase transformations $\psi \to e^{\mathrm{i}\theta}\psi$. By applying Noether's theorem, this symmetry yields the conservation of baryon number,

$$B = \frac{1}{3}\int \mathrm{d}^3x \psi^\dagger\psi\,.$$

More symmetries exist in the limit of massless quarks. This limiting case is important as the u- and d-quark masses, those relevant for nuclear systems, are small compared to typical hadronic mass scales like the nucleon mass M_N.

Let us decompose the u and d–quark fields into parts with left or right handed chirality:

$$\begin{pmatrix} u \\ d \end{pmatrix}_L = \frac{1-\gamma_5}{2}\begin{pmatrix} u \\ d \end{pmatrix}, \qquad \begin{pmatrix} u \\ d \end{pmatrix}_R = \frac{1+\gamma_5}{2}\begin{pmatrix} u \\ d \end{pmatrix},$$
$$\psi = \begin{pmatrix} u \\ d \end{pmatrix} = \begin{pmatrix} u \\ d \end{pmatrix}_L + \begin{pmatrix} u \\ d \end{pmatrix}_R.$$

In the Lagrangian ($\not{D} \equiv \gamma_\mu D^\mu$)

$$\mathscr{L} = \bar\psi(\mathrm{i}\not{D} - \tilde m)\psi = \bar\psi_L \mathrm{i}\not{D}\psi_L + \bar\psi_R \mathrm{i}\not{D}\psi_R - \bar\psi_R\tilde m\psi_L - \bar\psi_L\tilde m\psi_R\,, \tag{2.10}$$

only the mass terms mix the left and right handed contributions of the quark fields. For $\tilde m = 0$, $\mathscr{L}$ is therefore invariant under separate SU(2) transformations in flavor space,

$$\begin{pmatrix} u \\ d \end{pmatrix}_L \to U_L \begin{pmatrix} u \\ d \end{pmatrix}_L, \qquad \begin{pmatrix} u \\ d \end{pmatrix}_R \to U_R \begin{pmatrix} u \\ d \end{pmatrix}_R. \tag{2.11}$$

Noether's theorem yields the conserved currents corresponding to these symmetries:

$$j_L^{\mu a} = \bar\psi_L\gamma^\mu\frac{\tau^a}{2}\psi_L \quad \text{and} \quad j_R^{\mu a} = \bar\psi_R\gamma^\mu\frac{\tau^a}{2}\psi_R\,.$$

Addition or subtraction gives the often useful isospin or axial vector currents, respectively:

$$j_V^{\mu a} = \bar\psi\gamma^\mu\frac{\tau^a}{2}\psi\,, \qquad j_A^{\mu a} = \bar\psi\gamma^\mu\gamma_5\frac{\tau^a}{2}\psi\,.$$

From the particle spectrum observed in nature, one deduces that the "axial $\mathrm{SU}(2)_A$ symmetry" related to the axial current $j_A^{\mu a}$ is spontaneously broken: For an intact $\mathrm{SU}(2)_L \times \mathrm{SU}(2)_R$ symmetry, the particles should exist in parity doublets. However, such doublets are not observed. For example the lightest pseudoscalar ($J^P = 0^-$) mesons have much smaller masses than the lightest scalar ($J^P = 0^+$) mesons.

According to Goldstone's theorem, in a quantum field theory every spontaneously broken continuous global symmetry leads to massless particles with the same quantum numbers as the generators of the broken symmetry. In our case the Goldstone bosons belonging to $\mathrm{SU}(2)_A$ are the three pions. However, chiral symmetry is not an exact symmetry of QCD but is explicitly broken by the small but finite quark masses. As a consequence the pion mass is finite (but small compared to other typical hadronic masses like the nucleon mass).

The same arguments are valid when one also considers the s quark. However, its larger mass leads to a stronger $\mathrm{SU}(3)_L \times \mathrm{SU}(3)_R$ symmetry breaking resulting in larger masses of the other mesons of the pseudoscalar SU(3)–octet (kaons, η–meson).

2.2.3 Chiral condensate

Spontaneous symmetry breaking is linked to a scalar operator whose nonvanishing expectation value plays the role of the order parameter of the symmetry breaking. In our case, this is the so-called chiral condensate or (scalar) quark condensate:

$$\langle 0|\bar{\psi}\psi|0\rangle = \langle 0|\bar{\psi}_L\psi_R + \bar{\psi}_R\psi_L|0\rangle = -\operatorname{Tr}\lim_{y\to x_+}\langle 0|\mathcal{T}\psi(x)\bar{\psi}(y)|0\rangle\,. \tag{2.12}$$

Here, $\mathcal{T}$ is the time ordering operator. The chiral condensate is connected to the pion decay constant in the chiral limit ($m_{\mathrm{u,d}} = 0$), f_0, and the quark and pion masses by the Gell-Mann–Oakes–Renner relation (GOR):

$$m_\pi^2 = -\frac{1}{2f_0^2}(m_\mathrm{u} + m_\mathrm{d})\langle \bar{u}u + \bar{d}d\rangle + \mathcal{O}(m_{\mathrm{u,d}}^2)\,.$$

We note that the square of the pion mass is proportional to the sum of u- and d-quark masses and also indicates the amount of the explicit chiral symmetry breaking. It vanishes in the chiral limit. Small corrections to f_0 yield the physical pion decay constant $f_\pi = 92.4\,\mathrm{MeV} = f_0 + \mathcal{O}(m_{\mathrm{u,d}})$. Thus, the GOR relation can also be written as

$$m_\pi^2 = -\frac{1}{2f_\pi^2}(m_\mathrm{u} + m_\mathrm{d})\langle \bar{u}u + \bar{d}d\rangle + \mathcal{O}(m_{\mathrm{u,d}}^2)\,. \tag{2.13}$$

Taking $m_\mathrm{u} + m_\mathrm{d} \simeq 12\,\mathrm{MeV}$ leads to a vacuum expectation value of the condensate of $\langle\bar{q}q\rangle := \langle\bar{u}u\rangle = \langle\bar{d}d\rangle \simeq -(239\,\mathrm{MeV})^3 \simeq -1.8\,\mathrm{fm}^{-3}$.

It is also possible to express the condensate in terms of the energy density $\mathscr{E}_\phi = \langle\phi|\mathscr{H}_\mathrm{QCD}|\phi\rangle$. Let the QCD Hamiltonian $\mathscr{H}_\mathrm{QCD}$ be decomposed into the quark mass-term and the part from massless QCD,

$$\mathscr{H}_\mathrm{QCD} = \mathscr{H}_\mathrm{QCD}^{(0)} + m_\mathrm{u}\,\bar{u}u + m_\mathrm{d}\,\bar{d}d \approx \mathscr{H}_\mathrm{QCD}^{(0)} + \bar{m}(\bar{u}u + \bar{d}d)\,,$$

where $\bar{m} = (m_\mathrm{u}+m_\mathrm{d})/2$ is the average quark mass. The Hellmann–Feynman theorem [29] gives for a state ϕ

$$\frac{\partial \mathscr{E}_\phi}{\partial \bar{m}} = \left\langle \phi \middle| \frac{\partial \mathscr{H}_\mathrm{QCD}}{\partial \bar{m}} \middle| \phi \right\rangle = \langle \phi | \bar{u}u + \bar{d}d | \phi \rangle \,. \tag{2.14}$$

For the vacuum $|\phi\rangle = |0\rangle$, using the GOR relation (2.13) leads to

$$\bar{m}\frac{\partial \mathscr{E}_0}{\partial \bar{m}} = \bar{m}\langle \bar{u}u + \bar{d}d \rangle_0 = -m_\pi^2 f_\pi^2 \,. \tag{2.15}$$

For a state $|\rho\rangle$ with finite baryon density and energy density $\mathscr{E}(\rho)$, one gets (after inserting eq. (2.15) into eq. (2.14))

$$\langle \bar{u}u + \bar{d}d \rangle_\rho = \langle \bar{u}u + \bar{d}d \rangle_0 + \frac{\partial}{\partial \bar{m}}(\mathscr{E}(\rho) - \mathscr{E}_0) \,.$$

The GOR relation can then be used to convert the derivative with respect to the quark mass to one with respect to the pion mass:

$$\frac{\langle \bar{q}q \rangle_\rho}{\langle \bar{q}q \rangle_0} = 1 - \frac{\bar{m}}{m_\pi^2 f_\pi^2}\frac{\partial}{\partial \bar{m}}(\mathscr{E}(\rho) - \mathscr{E}_0) = 1 - \frac{1}{2m_\pi f_\pi^2}\frac{\partial}{\partial m_\pi}(\mathscr{E}(\rho) - \mathscr{E}_0) \,. \tag{2.16}$$

This relation will allow us to study the behavior of the chiral condensate as a function of the density.

It is interesting to note that one can draw a connection from the chiral condensate and the vector condensate $\langle q^\dagger q \rangle$ (which is directly related to the nucleon density) to the large scalar and vector self-energies of relativistic nuclear phenomenology. QCD sum rules suggest [30] that the change of the QCD condensates with the nucleon density gives rise to large scalar and vector self-energies of approximately equal size but opposite sign. Such large background fields agree qualitatively with the findings of relativistic mean field models [9].

2.3 Chiral perturbation theory

2.3.1 Mesonic sector

At low energies, the effective degrees of freedom of QCD are no longer quarks and gluons but hadrons. A description of low energy QCD is nevertheless possible by reformulating the theory in terms of the new active degrees of freedom. This implies replacing the QCD Lagrangian with an effective Lagrangian $\mathscr{L}_\mathrm{eff}$ with the same symmetry and symmetry breaking properties. $\mathscr{L}_\mathrm{eff}$ can then be expanded with respect to some small external momentum over some characteristic scale of the theory:

$$\mathscr{L}_\mathrm{eff} = \mathscr{L}_2 + \mathscr{L}_4 + \ldots \,. \tag{2.17}$$

For this expansion, momenta and derivatives are equivalent. Therefore, $\mathscr{L}_n$ contains exactly n derivatives or momenta. Only even n are possible since the Lagrangian has to

be a Lorentz scalar. The expansion converges if the momenta are much smaller than a characteristic scale. In the case of chiral perturbation theory, this scale is $\Lambda_\chi = 4\pi f_\pi = 1161\,\mathrm{MeV}$. In actual calculations of physical amplitudes, nearby resonances can limit the convergence radius to smaller scales.

The active degrees of freedom at low energies are the pseudo-scalar Goldstone bosons that are, in the two-flavour case, the pions.

For the formulation of $\mathscr{L}_\mathrm{eff}$ it is useful to collect the pseudo-scalar fields π_a $(a = 1, 2, 3)$ in a unitary matrix U that transforms linearly under chiral rotations $\psi_R \to R\psi_R$ and $\psi_L \to L\psi_L$:

$$U \to L\,U R^\dagger \quad \text{with} \quad U = \exp\left(\mathrm{i}\boldsymbol{\tau}\cdot\boldsymbol{\pi}/f_0\right). \tag{2.18}$$

It is easy to see, that

$$\mathrm{Tr}(\partial^\mu U\,\partial_\mu U^\dagger) \quad \to \quad \mathrm{Tr}(L\,\partial^\mu U R^\dagger R\,\partial_\mu U^\dagger L^\dagger) = \mathrm{Tr}(\partial^\mu U\,\partial_\mu U^\dagger)$$

is invariant under chiral transformations. This term is part of $\mathscr{L}_2$. A completely symmetric Lagrangian would lead to massless Goldstone bosons, whereas the physical pions are massive. This is fixed by adding a symmetry breaking term:

$$\mathscr{L}_2 = \frac{f_0^2}{4}\,\mathrm{Tr}(\partial^\mu U\,\partial_\mu U^\dagger) + \frac{m_\pi^2}{4} f_0^2\,\mathrm{Tr}(U + U^\dagger)\,. \tag{2.19}$$

This Lagrangian contains already all possible terms up to second order. Expansion to leading order with respect to powers of $\boldsymbol{\pi}$ yields the pion Lagrangian plus a constant vacuum contribution:

$$\mathscr{L}_2 = \frac{1}{2}\partial_\mu\boldsymbol{\pi}\cdot\partial^\mu\boldsymbol{\pi} - \frac{1}{2}m_\pi^2\boldsymbol{\pi}\cdot\boldsymbol{\pi} + m_\pi^2 f_0^2 + \mathcal{O}(\boldsymbol{\pi}^4)\,. \tag{2.20}$$

The GOR relation (2.13) converts the vacuum contribution $m_\pi^2 f_0^2$ to the expectation value of the mass term of the original QCD Lagrangian, $-(m_\mathrm{u}\langle\bar{u}u\rangle + m_\mathrm{d}\langle\bar{d}d\rangle)$. This means that $\mathscr{L}_\mathrm{eff}$ breaks chiral symmetry in the same way as QCD does.

2.3.2 Adding baryons

Of course, before applying our effective theory to nuclear matter, we have to include baryons. The derivation of the lowest order Lagrangian can be found e. g. in ref. [17]. Expansion to second order in the pion fields yields:

$$\mathscr{L}_{\pi\mathrm{N}} = \bar{N}\big(\mathrm{i}\partial\!\!\!/ - M_\mathrm{N}\big)N - \frac{g_\mathrm{A}}{2f_\pi}\bar{N}\gamma^\mu\gamma_5\boldsymbol{\tau}N\cdot\partial_\mu\boldsymbol{\pi} - \frac{1}{4f_\pi^2}\bar{N}\gamma^\mu\boldsymbol{\tau}N\cdot\boldsymbol{\pi}\times\partial_\mu\boldsymbol{\pi} + \frac{\sigma_{\pi\mathrm{N}}}{2f_\pi^2}\bar{N}N\boldsymbol{\pi}^2\,. \tag{2.21}$$

Since the theory described by this Lagrangian gives rise to ultraviolet divergences it requires renormalization and regularization. The resulting counter terms, not shown in eq. (2.21), subsume short-range dynamics not resolved at low energies. We will return to this issue in the next chapter.

Now we want to expand the theory resulting from eq. (2.21) in powers of momenta. However, this leads to problems since the nucleon mass M_N introduces another dimensionful quantity besides f_π that does not vanish in the chiral limit and is not small compared to the characteristic scale $\Lambda_\chi \simeq 1\,\mathrm{GeV}$ of the theory. In fact, M_N (taken in the chiral limit) reflects just that scale. Therefore, loop corrections can be formally of order $\mathcal{O}(1)$ making a consistent expansion impossible.

Nevertheless, by eliminating the nucleon mass from the Lagrangian it is possible to construct a consistent expansion scheme. In this case, only momenta relative to the rest mass M_N appear and these can be small compared to Λ_χ. This amounts to taking the nonrelativistic limit of the full theory and expanding in powers of the inverse nucleon mass. All in all, this leads to an expansion in small momenta q, where the higher powers are suppressed either by Λ_χ or by M_N. Here, the pion mass is also considered to be a small quantity. A complete derivation of the procedure can be found in ref. [17].

In the nonrelativistic limit, it is also possible to include the $\Delta(1232)$-resonance without the large $\Delta(1232)$–mass appearing explicitly in the expansion. Only the delta-nucleon mass difference $\Delta = 293\,\mathrm{MeV}$ contributes. It can be treated as a small quantity, i. e. of order $\mathcal{O}(q)$.

2.3.3 Finite density

Finally, we must spend some thought on calculations in a system of finite density. We will limit ourselves to temperature $T = 0$ in this section. The extension to non-zero temperatures will be done in chapter 4. In a medium, the occupation of all nucleon states up to some Fermi momentum k_f has to be taken into account. Instead of the empty vacuum $|0\rangle$, one has a new ground state $|\phi_0\rangle$ with a filled Fermi sea. The creation and annihilation operators $a^{s\dagger}_{\mathbf{p}}$ and $a^{s}_{\mathbf{p}}$ for nucleons exchange their meaning below the Fermi momentum and annihilate and create holes respectively. Which of the two operators annihilates the ground state now depends on the momentum:

$$\begin{aligned} a^{s}_{\mathbf{p}}|\phi_0\rangle &= 0 \quad \text{for} \quad k_\mathrm{f} < |\mathbf{p}|\,, \\ a^{s\dagger}_{\mathbf{p}}|\phi_0\rangle &= 0 \quad \text{for} \quad 0 \le |\mathbf{p}| < k_\mathrm{f}\,. \end{aligned} \tag{2.22}$$

The Feynman propagator in coordinate space changes to:

$$S^0_F(x-y) = \langle 0|\mathcal{T}\psi(x)\bar{\psi}(y)|0\rangle \qquad \rightarrow \qquad S_F(x-y) = \langle \phi_0|\mathcal{T}\psi(x)\bar{\psi}(y)|\phi_0\rangle\,,$$

with $|\phi_0\rangle$ being the ground state of the filled Fermi sea. In momentum space, this change leads to a changing sign of the infinitesimal imaginary part characterizing the pole of the propagator:

$$S_F(p) = \frac{\mathrm{i}(\not{p} + M_\mathrm{N})}{p^2 - M_\mathrm{N}^2 + \mathrm{i}\epsilon\,\mathrm{sgn}(|\mathbf{p}| - k_\mathrm{f})}\,.$$

There is a very useful *additive* decomposition of this in-medium nucleon propagator,

$$S_F(p) = (\not{p} + M_\mathrm{N})\left[\frac{\mathrm{i}}{p^2 - M_\mathrm{N}^2 + \mathrm{i}\epsilon} - 2\pi\,\delta(p^2 - M^2)\,\theta(k_\mathrm{f} - |\mathbf{p}|)\,\theta(p_0)\right]. \tag{2.23}$$

The first term in the square brackets is the vacuum nucleon propagator. The second term takes into account all effects caused by the non-zero density and is therefore called medium insertion. Ordering the contributions according to the number of medium insertions will simplify our calculations significantly.

Chapter 3

Chiral approach to nuclear matter

3.1 Chiral expansion

In [14, 15] we have used chiral perturbation theory for a systematic expansion of the equation of state of nuclear matter. Its key element is a separation of long- and short-distance dynamics and an ordering scheme in powers of small momenta. In a medium, the relevant quantity for this expansion is the Fermi momentum k_f, which defines the nucleon density at temperature $T = 0$ via the relation

$$\rho(k_\mathrm{f}) = \underset{\text{spin}}{2} \cdot \underset{\text{isospin}}{2} \cdot \int_0^{k_\mathrm{f}} \frac{\mathrm{d}^3 p}{(2\pi)^3} = \frac{2k_\mathrm{f}^3}{3\pi^2}\,. \tag{3.1}$$

At nuclear matter saturation density $\rho_0 \simeq 0.16\,\mathrm{fm}^{-3}$ the Fermi momentum $k_{\mathrm{f},0}$ and the pion mass m_π are comparable scales ($k_{\mathrm{f},0} \simeq 2m_\pi$), and therefore pions must be included as explicit degrees of freedom in the description of the nuclear many-body dynamics. In the expansion of the energy per particle $\bar{E}(k_\mathrm{f}) = \mathscr{E}(k_\mathrm{f})/\rho(k_\mathrm{f}) - M_\mathrm{N}$, the coefficients are nontrivial functions of the ratio k_f/m_π which must not be expanded further:

$$\bar{E}(k_\mathrm{f}) = \sum_n k_\mathrm{f}^n F_n\big(\tfrac{k_\mathrm{f}}{m_\pi}\big)\,. \tag{3.2}$$

The contributions to $\bar{E}$ are obtained by calculating closed vacuum diagrams which are connected to the ground state energy density. Of course, instead of the free nucleon propagator, the in-medium propagator (2.23) is used. A demonstration of the procedure can be found in appendix A of ref. [15].

Naive chiral power counting (which is basically a counting in terms of mass dimension) suggests that closed vacuum diagrams with L loops (which represent the ground state energy density in diagrammatic language) give rise to a contribution to the energy per particle of the form $\bar{E}(k_\mathrm{f}) = k_\mathrm{f}^{2L-1}\mathcal{F}_L(k_\mathrm{f}/m_\pi)$. The number $2L - 1 = L \cdot 4 + 2(L-1) \cdot 1 + 2(L-1) \cdot (-1) + (L-1) \cdot (-2) - 3$ is simply counting the mass dimensions of loop integrations, vertex factors, fermion propagators, and pion propagators appearing in the respective diagram. However, the two-nucleon system is known to provide exceptions to the naive counting rules by the so-called iterated one-pion exchange. In that case the relevant energy denominator is a difference of nucleon kinetic energies causing the large scale factor M_N (the nucleon mass) to appear in the numerator of the Feynman

amplitude. There are indeed certain closed three-loop diagrams (see the second and third diagrams in fig. 3.1) which contribute to the energy per particle already at fourth order in small momenta [13]. By the same argument one expects that the four-loop Fock diagram which includes the twice-iterated one-pion exchange (proportional to M_{N}^2) will contribute already at order $\mathcal{O}(k_{\mathrm{f}}^5)$.[1] Luckily, the analogous four-loop Hartree diagram vanishes when taking the spin- or Dirac-trace. Because of the enormous complexity of four-loop diagrams we restrict ourselves (as in [14]) to all contributions up-to-and-including order $\mathcal{O}(k_{\mathrm{f}}^5)$ as they are given by closed three-loop diagrams incorporating pions and nucleons. These contributions are the kinetic energy, the one-pion exchange Fock diagram (the corresponding Hartree diagram is zero), the iterated one-pion exchange Hartree and Fock diagrams, and the irreducible two-pion exchange Fock diagrams (the corresponding Hartree diagrams contribute only at $\mathcal{O}(k_{\mathrm{f}}^6)$).

Not included are diagrams involving virtual $\Delta(1232)$-excitations in intermediate states. Some effects of these diagrams are included in the low-energy coupling constants $c_1, \ldots, c_4$ of the next-to-leading-order chiral pion nucleon Lagrangian [17]. Diagrams with these effective couplings would contribute only at $\mathcal{O}(k_{\mathrm{f}}^6)$ and higher in our counting scheme. Of course, including virtual Δ-excitations via low-energy constants implicitly assumes that the characteristic scale arising from the calculation of such diagrams, the Delta nucleon mass difference $\Delta \simeq 293\,\mathrm{MeV}$, is large compared to the momenta appearing in our problem. Obviously, this is not the case. Rather, the Fermi momentum k_{f} at nuclear matter density is comparable to the mass splitting Δ, and therefore it makes more sense to treat the Delta isobar as explicit degree of freedom. We will include these diagrams with explicit Delta excitations later in chapter 7. Formally, with the mass splitting Δ treated as small quantity, they contribute at order $\mathcal{O}(k_{\mathrm{f}}^5)$. However, it turns out that basic properties of the equation of state for isospin-symmetric nuclear matter can already be quite well reproduced by πN-dynamics alone [13–15]. Therefore, we will first investigate what other properties of nuclear matter are mainly determined by πN-dynamics and will, in the first step, omit the diagrams involving virtual Δ-excitations as was done in [14, 31, 32].

For the calculation of the vacuum diagrams, the additive decomposition (2.23) of the in-medium nucleon propagator into a vacuum part and a medium part is very convenient. If one organizes the diagrammatic calculation according to the number of medium insertions, diagrams with no medium insertion lead to an unobservable shift of the vacuum energy. Diagrams with exactly one medium insertion just renormalize the nucleon mass to its measured value M_{N}. Thus the interesting nontrivial many-body effects from interactions start with diagrams having two or more medium insertions.

The pion-nucleon interaction vertices relevant in this work are the pseudovector πNN-vertex and the Tomozawa-Weinberg ππNN-contact vertex of the form,

$$\frac{g_{\mathrm{A}}}{2f_\pi} \not{q}_a \gamma_5 \tau_a \quad \text{and} \quad \frac{1}{4f_\pi^2} (\not{q}_b - \not{q}_a) \epsilon_{abc} \tau_c \,.$$

Here, the pion four-momenta $q_{a,b}$ are out-going and $f_\pi = 92.4\,\mathrm{MeV}$ denotes the pion

[1] Note that due to the form of the expansion eq. (3.2), the expression $\mathcal{O}(k_{\mathrm{f}}^n)$ is synonymous to "n-th order in small momenta", where the quantities k_{f}, m_π (and Δ) are considered to be small.

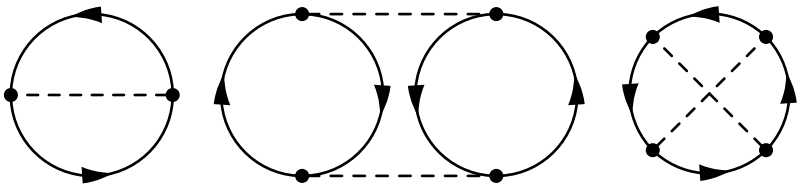

Figure 3.1: One-pion exchange Fock diagram and iterated one-pion exchange Hartree and Fock diagrams.

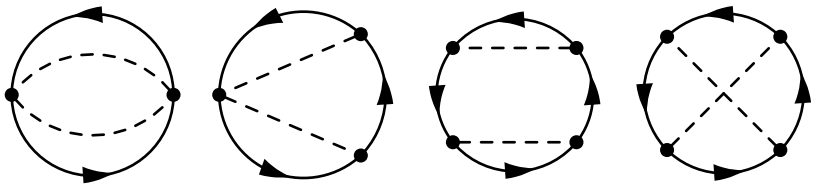

Figure 3.2: Irreducible two-pion exchange Fock diagrams.

decay constant. For the nucleon axial vector coupling constant g_A we choose the value $g_\mathrm{A} = 1.3$. Via the Goldberger-Treiman relation this corresponds to a πNN-coupling constant of $g_{\pi\mathrm{N}} = g_\mathrm{A} M_\mathrm{N}/f_\pi = 13.2$ which agrees with present empirical determinations of $g_{\pi\mathrm{N}}$ from πN-dispersion relation analysis [33].

In addition to the important pion dynamics, there is also unknown short-distance dynamics relevant in nuclear matter. However this short-distance dynamics works at momenta $p \gg k_\mathrm{f}$ much higher than the Fermi momentum and is thus not resolved in detail. Instead it can be accounted for by the introduction of nucleon-nucleon contact interactions. Equivalently it is also possible to introduce a high momentum cut-off Λ which is then tuned to adjust the strength of the contact interaction. The latter approach has been taken in the first part of this work.

3.2 Saturation properties

The energy per particle of symmetric nuclear matter has been calculated up to $\mathcal{O}(k_\mathrm{f}^5)$ and up to three loops in refs. [14, 15]. There, we have taken into account the contributions from the kinetic energy (contributing at $\mathcal{O}(k_\mathrm{f}^2)$), from chiral one-pion exchange ($\mathcal{O}(k_\mathrm{f}^3)$), from iterated one-pion exchange ($\mathcal{O}(k_\mathrm{f}^4)$), and from irreducible two-pion exchange ($\mathcal{O}(k_\mathrm{f}^5)$). The corresponding closed-loop diagrams are shown in figs. 3.1 and 3.2. Note that there is one Fock diagram that has both a reducible part contributing to the iterated 1π exchange and an irreducible part. The analytical results are summarized in appendix B.2.1. The few divergent parts from iterated one-pion exchange and irreducible two-pion exchange have been regularized with a three-momentum cut-off Λ. The cut-off dependent contributions are attractive and grow (apart from a small correction from irred. 2π exchange) linearly with the nucleon density $\rho \propto k_\mathrm{f}^3$ and are thus indistinguishable from the contributions of a NN-contact interaction.

3.2.1 Chiral limit

To illustrate the saturation mechanism, we briefly go to the chiral limit, $m_\pi = 0$, and truncate the expansion at $\mathcal{O}(k_\mathrm{f}^4)$. In that case the complete expression for the energy per particle $\bar{E}(k_\mathrm{f})$ turns into the form of the parameterization eq. (2.6), with the coefficients α and β given by

$$\alpha = 10\Big(\frac{g_{\pi\mathrm{N}}}{4\pi}\Big)^4 \frac{\Lambda}{M_\mathrm{N}} - \Big(\frac{g_{\pi\mathrm{N}}}{4\pi}\Big)^2 \qquad \text{and} \tag{3.3}$$

$$\beta = \frac{3}{70}\Big(\frac{g_{\pi\mathrm{N}}}{4\pi}\Big)^4 (4\pi^2 + 237 - 24\ln 2) - \frac{3}{56} = 13.55\,. \tag{3.4}$$

Note that the parameter-free expression for β gives a number quite close to $\beta = 12.29$ as extracted from the empirical saturation point. Furthermore, by adjusting the cut-off scale to $\Lambda = (0.5 \ldots 0.6) M_\mathrm{N}$ (which in fact lies in the physically reasonable range), α will take on its required value. Therefore, as long as the effects due to the finite pion mass and the higher order terms do not change this picture completely, realistic nuclear binding is guaranteed by chiral pion-nucleon dynamics, together with fine-tuning of the single scale Λ representing the short-distance NN-dynamics.

We also note that there is no physical scale in the problem that would suggest the small binding energy at the saturation point. Rather, the value $\bar{E}_0 = -16\,\mathrm{MeV}$ is due to a cancellation of individually much larger terms. This feature is common to most microscopic calculations of nuclear matter.

3.2.2 Finite pion mass

Now we set $m_\pi = 135\,\mathrm{MeV}$ (the neutral pion mass) and adjust the cut-off Λ to fix the (negative) binding energy at the value $\bar{E}_0 = -15.3\,\mathrm{MeV}$ obtained in ref. [34] from extensive fits to nuclide masses. The resulting equation of state is shown in fig. 3.3 including all calculated terms up to order $\mathcal{O}(k_\mathrm{f}^4)$ (dotted line) and $\mathcal{O}(k_\mathrm{f}^5)$ (full line). In the $\mathcal{O}(k_\mathrm{f}^5)$ case with a cut-off scale of $\Lambda = 646.3\,\mathrm{MeV}$, the energy per particle $\bar{E}(\rho)$ has a minimum with the value $\bar{E}_0$ at a density $\rho_0 = 0.178\,\mathrm{fm}^{-3}$ corresponding to a Fermi momentum of $k_{\mathrm{f},0} = 272.7\,\mathrm{MeV}$. This value is slightly larger than the currently accepted empirical value of $k_{\mathrm{f},0} = (262 \pm 4)\,\mathrm{MeV}$ [25]. The nuclear compressibility K related to the curvature of the saturation curve at its minimum comes out as $K = 255\,\mathrm{MeV}$, in very good agreement with the nowadays accepted empirical value $K = (220 \pm 50)\,\mathrm{MeV}$ [26].

If one truncates the expansion at order $\mathcal{O}(k_\mathrm{f}^4)$ and readjusts the cut-off to $\Lambda = 611.4\,\mathrm{MeV}$ to yield the same binding energy $\bar{E}_0$, the equation of state remains nearly unchanged (dotted line in fig. 3.3). The saturation density changes only slightly to $\rho_0 = 0.173\,\mathrm{fm}^{-3}$ corresponding to $k_{\mathrm{f},0} = 270\,\mathrm{MeV}$.

At the saturation point, the decomposition of the binding energy into contributions from the chiral powers $\mathcal{O}(k_\mathrm{f}^\nu)$, $(\nu = 2, 3, 4, 5)$ is given by $\bar{E}_0 = (23.8 - 154.5 + 124.6 - 9.1) = -15.3\,\mathrm{MeV}$. As in the chiral limit, there is a cancellation of large $\mathcal{O}(k_\mathrm{f}^3)$ and $\mathcal{O}(k_\mathrm{f}^4)$ terms. However, the $\mathcal{O}(k_\mathrm{f}^5)$ term is clearly less important. Therefore we conclude that the saturation mechanism is primarily generated by Pauli blocking acting on iterated

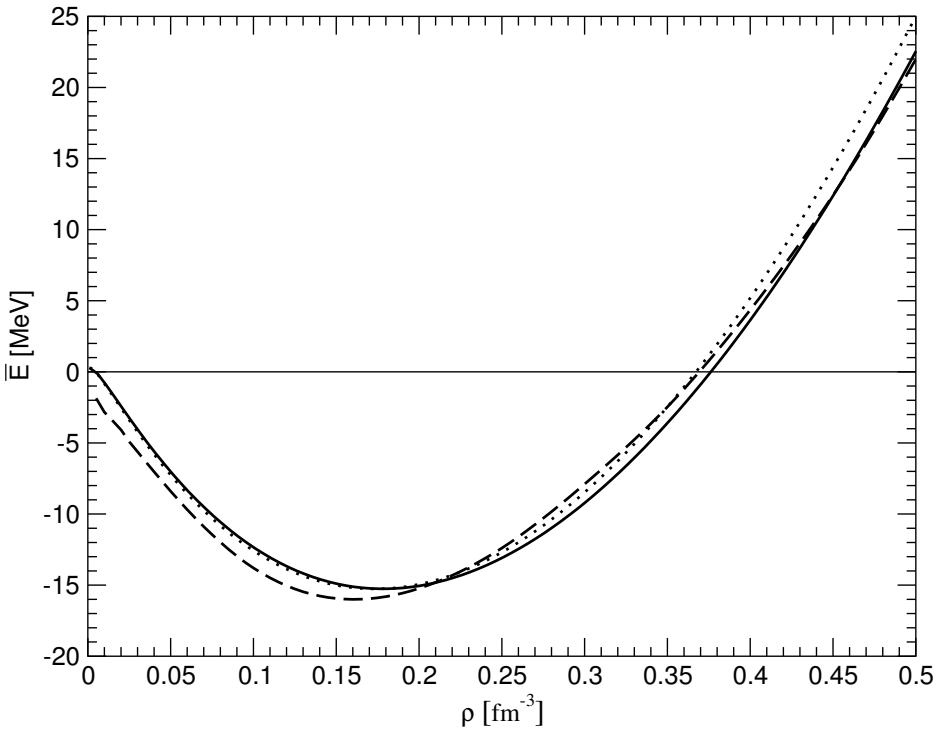

Figure 3.3: Energy per particle of symmetric nuclear matter as determined by chiral one- and two-pion exchange up to order $\mathcal{O}(k_{\rm f}^5)$ with $\Lambda = 646.3\,\mathrm{MeV}$ (full line) and up to order $\mathcal{O}(k_{\rm f}^4)$ with $\Lambda = 611.4\,\mathrm{MeV}$ (dotted line). The dashed line shows the result of ref. [27].

one-pion exchange. Specifically, in the chiral limit, strong attraction proportional to $k_{\rm f}^3$ is produced by its cut-off dependent pieces and stabilizing repulsion proportional to $k_{\rm f}^4$ is largely due to Pauli blocking effects from the diagrams with three medium insertions [15].

Judging by the fact that nuclear saturation is described well already by a chiral expansion to $\mathcal{O}(k_{\rm f}^4)$, it seems that higher order terms are not very important for the equation of state of symmetric nuclear matter. However we will see that they play an important role for more detailed observables like the single particle potential.

Finally, we point out that the saturation mechanism of our scheme is quite different from the one observed in relativistic mean field models [9]. There, saturation is achieved by the balance of the large scalar and vector mean fields S and V of opposite sign which are absent at this stage in our nonrelativistic calculation. Our framework, on the other hand, shows that pionic fluctuations alone can explain saturation. Therefore, we argue that the difference of the absolute values of the scalar and vector mean fields, and therefore their influence on the nuclear equation of state, is quite small. However, the difference $S - V$, which contributes prominently to the nuclear spin-orbit force, is large due to the different signs of S and V. The fact that the spin-orbit force is not correctly reproduced in our nonrelativistic approach (see sections 5.1 and 7.4) then leads to the idea of treating pionic fluctuations on top of strong scalar and vector background fields of approximately equal size [21, 22]. We will come back to this idea briefly in section 5.2.

3.3 A toy model

The fact that a second order tensor force gives a large contribution to the energy in nuclei and nuclear matter has been known for a long time (see e. g. ref. [35]). Actually, the tensor character of the pion exchange potential is crucial for realistic nuclear binding as can be illustrated by considering a toy model with an isovector–spin-spin potential of range λ and strength C:

$$V_{(\mathrm{toy})}(r) = \boldsymbol{\sigma}_1 \cdot \boldsymbol{\sigma}_2 \; \boldsymbol{\tau}_1 \cdot \boldsymbol{\tau}_2 \, C \frac{e^{-\lambda r}}{4\pi r} \,. \tag{3.5}$$

This potential corresponds to the (Born) T-matrix

$$\mathcal{T}_{\mathrm{NN}}^{(\mathrm{toy})} = \frac{C}{\lambda^2 + \mathbf{q}^{\,2}} \, \boldsymbol{\sigma}_1 \cdot \boldsymbol{\sigma}_2 \, \boldsymbol{\tau}_1 \cdot \boldsymbol{\tau}_2 \,, \tag{3.6}$$

which is, except for the spin structure, very similar to the well known pion exchange amplitude,

$$\begin{aligned} \mathcal{T}_{\mathrm{NN}}^{(\pi)} &= \frac{g_{\mathrm{A}}^2}{4 f_\pi^2} \, \frac{(\boldsymbol{\sigma}_1 \cdot \mathbf{q})(\boldsymbol{\sigma}_2 \cdot \mathbf{q})}{m_\pi^2 + \mathbf{q}^{\,2}} \; \boldsymbol{\tau}_1 \cdot \boldsymbol{\tau}_2 \\ &= \frac{g_{\mathrm{A}}^2}{12 f_\pi^2} \left(\frac{S_{12}(\mathbf{q}) - m_\pi^2 (\boldsymbol{\sigma}_1 \cdot \boldsymbol{\sigma}_2)}{m_\pi^2 + \mathbf{q}^2} + \boldsymbol{\sigma}_1 \cdot \boldsymbol{\sigma}_2 \right) \boldsymbol{\tau}_1 \cdot \boldsymbol{\tau}_2 \,, \end{aligned} \tag{3.7}$$

with the tensor operator $S_{12}(\mathbf{q}) = 3(\boldsymbol{\sigma}_1 \cdot \mathbf{q})(\boldsymbol{\sigma}_2 \cdot \mathbf{q}) - (\boldsymbol{\sigma}_1 \cdot \boldsymbol{\sigma}_2)\mathbf{q}^2$. For the first order diagram, the contribution to the energy per particle is (with $u = k_{\mathrm{f}}/\lambda$):

$$\bar{E}^{(1)}(k_{\mathrm{f}}) = \frac{9C\lambda}{4\pi^2} \left[\frac{1}{8u} - \frac{3u}{4} + \arctan 2u - \left(\frac{3}{8u} + \frac{1}{32u^3} \right) \ln\left(1 + 4u^2\right) \right] . \tag{3.8}$$

With values of the range and strength parameters of

$$\lambda_\pi = m_\pi \qquad C_\pi = \frac{g_{\mathrm{A}}^2 m_\pi^2}{12 f_\pi^2} = 0.3 \,, \tag{3.9}$$

one recovers exactly the corresponding 1π-exchange result (the first line in eq. (B.12)) except for a missing term $\propto k_{\mathrm{f}}^3$. The second order contributions to the energy per particle can be found in appendix B.5.

After combining all contributions and adding the kinetic energy, one finds that, for the pion-like parameter set (3.9), the toy interaction (3.5,3.6) gives only weak contributions and does not yield enough repulsion at higher densities to stabilize nuclear matter. For high densities, all contributions of the interaction to the energy per particle rise in fact slower than the kinetic energy (which is $\propto \rho^{2/3}$). Therefore one can not achieve saturation in the way of eq. (2.6), even after adding an appropriate contact force (which here cannot be parametrized as a momentum cut-off, since all contributions from the toy force are finite).

In principle, it is possible to produce a saturation minimum by adjusting the strength C of the interaction. A value of $C = 1.2$ results in the correct saturation density of $\rho_0 = 0.16\,\mathrm{fm}^{-3}$ but completely unrealistic binding energy $\bar{E}_0 \approx -5\,\mathrm{MeV}$ and compression modulus $K \approx 28\,\mathrm{MeV}$. The binding energy could be fixed by adding a repulsive contact interaction contributing to $\bar{E}$ with a strength of $0.52 k_\mathrm{f}^3/M_\mathrm{N}^2$ and readjusting the toy interaction strength to $C = 1.81$. However, this would still leave the compressibility at an unrealistic value of $K = 86\,\mathrm{MeV}$.

These two cases of "saturation" show us that the structure of an attractive k_f^3 term balanced by a repulsive k_f^4 term as in eq. (2.6) is indeed essential to get all three quantities $\bar{E}_0$, ρ_0, and K in the right regime. Structures of the type attractive k_f^2 term versus repulsive k_f^3 term are simply not realistic.

Furthermore one can conclude that the pion exchange tensor-force is required to get the necessary amount of repulsion at higher densities to stabilize nuclear matter.

On the other hand, individually large terms in the equation of state of nuclear matter balance each other to generate the much smaller binding energy of about 16 MeV. Therefore, even the smaller contributions to the energy per particle are comparable to $\bar{E}_0$ and thus are also important for the correct saturation behavior (except when they can be accounted for by readjusting the cut-off Λ). Consequently, a calculation omitting less important terms, such as the Fock diagrams or the spin-spin part of the pion exchange T-matrix (3.7), does not yield realistic values for all three empirical quantities $\bar{E}_0$, ρ_0, and K at the same time (even if the short-range NN interaction is readjusted). All in all we conclude that the second order tensor force alone does not provide realistic saturation properties.

Therefore, it is far from trivial that all the contributions of chiral pion exchange produce the right balance of density dependent attraction and repulsion for realistic saturation properties already at order $\mathcal{O}(k_\mathrm{f}^4)$ and furthermore that the saturation behavior is not spoiled when going to order $\mathcal{O}(k_\mathrm{f}^5)$.

3.4 Single particle potential

As we have seen in section 3.2, the bulk properties of nuclear matter can be well described by chiral pion-nucleon dynamics treated up to three loop order. In a next step, consider quantities which characterize in more detail the behavior of a single nucleon moving in the dense nuclear matter environment. In ref. [31], we calculated the momentum and density dependent (complex-valued) single particle potential of nucleons in isospin-symmetric nuclear matter using the same framework.

Let us consider the structure of the energy density according to an ordering by the number of medium insertions. It consists of a sum of convolution integrals of the form,

$$\mathscr{E}[d] = \int \mathrm{d}^3p_1 \mathcal{K}_1 d(\mathbf{p}_1) + \int \mathrm{d}^3p_1 \mathrm{d}^3p_2 \mathcal{K}_2 d(\mathbf{p}_1) d(\mathbf{p}_2) + \int \mathrm{d}^3p_1 \mathrm{d}^3p_2 \mathrm{d}^3p_3 \mathcal{K}_3 d(\mathbf{p}_1) d(\mathbf{p}_2) d(\mathbf{p}_3) + \int \mathrm{d}^3p_1 \mathrm{d}^3p_2 \mathrm{d}^3p_3 \mathrm{d}^3p_4 \mathcal{K}_4 d(\mathbf{p}_1) d(\mathbf{p}_2) d(\mathbf{p}_3) d(\mathbf{p}_4)\,. \quad (3.10)$$

The one-body kernel $\mathcal{K}_1 = 4T_{\rm kin}(|\mathbf{p}_1|)$ is four times the relativistically improved kinetic energy (see eq. (3.12)). $\mathcal{K}_{2,3}$ are two- and three-body kernels related to contributions of closed diagrams with two and three medium insertions. In three-loop approximation the four-body kernel $\mathcal{K}_4$ is proportional to $\delta^3(\mathbf{p}_1+\mathbf{p}_2+\mathbf{p}_3+\mathbf{p}_4)$ and purely imaginary. The quantity $d(\mathbf{p}_j)$ denotes the density of states in momentum space. Inserting the density of states of a filled Fermi sea, $d(\mathbf{p}_j) = (2\pi)^{-3}\,\theta(k_{\rm f}-|\mathbf{p}_j|)$, into eq. (3.10) yields the energy density of nuclear matter, $\rho\bar{E}(k_{\rm f})$, with the nucleon density $\rho = 2k_{\rm f}^3/3\pi^2$. The single particle potential can now be directly constructed from the energy density functional (3.10) by adding a test nucleon of fixed momentum $\mathbf{p}$ to the filled Fermi sea. This situation is described by the density of states $d(\mathbf{p}_j) = (2\pi)^{-3}\,\theta(k_{\rm f}-|\mathbf{p}_j|) + \eta\,\delta^3(\mathbf{p}-\mathbf{p}_j)$ with the infinitesimal parameter η to be interpreted as $(\pm)$ the inverse (infinite) volume. The plus sign applies for a particle ($|\mathbf{p}\,| > k_{\rm f}$) and the minus sign for a hole ($|\mathbf{p}\,| < k_{\rm f}$). Inserting this density of states into eq. (3.10) leads to

$$\mathscr{E} = \rho\,\bar{E}(k_{\rm f}) + 4\eta\left\{T_{\rm kin}(p) + U(p,k_{\rm f}) + i\,W(p,k_{\rm f})\right\}, \tag{3.11}$$

with

$$T_{\rm kin}(p) = \frac{p^2}{2M_{\rm N}} - \frac{p^4}{8M_{\rm N}^3}\,, \tag{3.12}$$

the relativistically improved kinetic energy. The factor 4 in eq. (3.11) simply counts the spin and isospin multiplicity of a nucleon. The real and imaginary parts of the single particle potential have, according to eq. (3.10), a decomposition into two-, three- and four-body contributions,

$$U(p,k_{\rm f}) = U_2(p,k_{\rm f}) + U_3(p,k_{\rm f})\,, \qquad W(p,k_{\rm f}) = W_2(p,k_{\rm f}) + W_3(p,k_{\rm f}) + W_4(p,k_{\rm f})\,, \tag{3.13}$$

where the index on each term refers to the corresponding kernel $\mathcal{K}_\nu$ in eq. (3.10).

In isospin asymmetric nuclear matter, the deviation from equal numbers of neutrons and protons leads to different single-particle potentials for protons and neutrons [36]. For a relative neutron excess of $\delta = (N-Z)/(N+Z)$, the total single particle potential is given by

$$U(p,k_{\rm f}) + iW(p,k_{\rm f}) - [U_I(p,k_{\rm f}) + iW_I(p,k_{\rm f})]\tau_3\delta + \mathcal{O}(\delta^2)\,, \tag{3.14}$$

with $U_I(p,k_{\rm f}) + iW_I(p,k_{\rm f})$ the (complex) isovector single-particle potential and $\tau_3 \to \pm 1$ for a proton or a neutron. The isovector single-particle potential in this framework has been evaluated by N. Kaiser [36].

3.4.1 Real part

In this section we present results for the real part of the single particle potential $U(p,k_{\rm f})$ as given by chiral one- and two-pion exchange with only nucleons in intermediate states. The closed vacuum diagrams related to one-pion exchange (Fock-diagram) and iterated one-pion exchange (Hartree- and Fock-diagrams) are shown in fig. 3.1. Each nucleon propagator (2.23) consists of a vacuum part and a medium insertion. Self energy diagrams are obtained from these closed graphs by opening one nucleon line with a medium

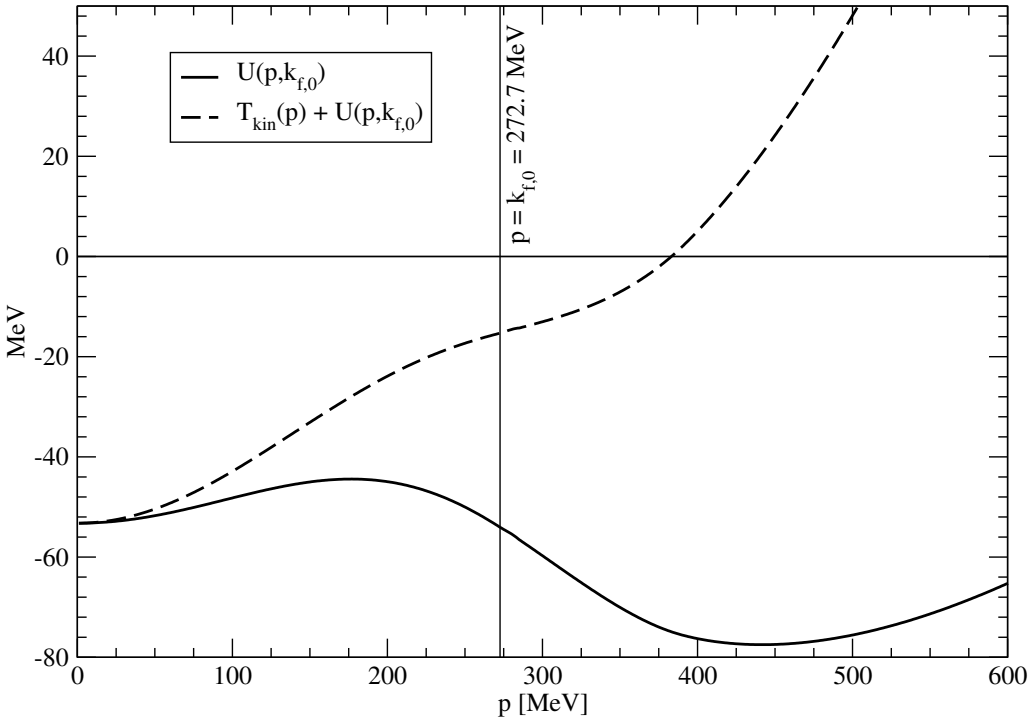

Figure 3.4: The real part of the single-particle potential $U(p, k_{\mathrm{f},0})$ versus the nucleon momentum p at nuclear saturation density, $k_{\mathrm{f},0} = 272.7\,\mathrm{MeV}$.

insertion. In order to keep their number small and in order to avoid repetitions we associate the contributions to the (real) nuclear mean field $U(p, k_\mathrm{f})$ with the closed vacuum diagram before the opening of a nucleon line. The explicit results from ref. [31] for a nucleon momentum p below the Fermi surface are given in appendix B.6.1. In addition to that, the corresponding results for the extension to $p > k_\mathrm{f}$ are given in appendix B.6.2. In general this extension is not just an analytical continuation of the potential from below the Fermi surface.

The momentum dependence of the real part $U(p, k_{\mathrm{f},0})$ of the single particle potential evaluated up to order $\mathcal{O}(k_\mathrm{f}^5)$ at nuclear saturation density $k_{\mathrm{f},0} = 272.7\,\mathrm{MeV}$ is shown in fig. 3.4. For a nucleon at rest, we find $U(0, k_{\mathrm{f},0}) = -53.2\,\mathrm{MeV}$. For comparison, the calculation of ref. [37] based on the phenomenological Paris NN-potential finds a potential depth of $U(0, k_{\mathrm{f},0}) \simeq -64\,\mathrm{MeV}$. In the relativistic Dirac-Brueckner approach of ref. [38] using the Bonn-A NN-potential a somewhat deeper real single particle potential with $U(0, k_{\mathrm{f},0}) \simeq -80\,\mathrm{MeV}$ has been found. Also, the empirical optical-model potential $U_0 \approx -52\,\mathrm{MeV}$ deduced by extrapolations from elastic nucleon-nucleon scattering data is of comparable magnitude [39].

The dashed line in fig. 3.4 represents the total single particle energy, $T_{\mathrm{kin}}(p) + U(p, k_{\mathrm{f},0})$, i.e. the sum of single nucleon kinetic and potential energy. As required by the Hugenholtz-van Hove theorem [40],

$$T_{\mathrm{kin}}(k_\mathrm{f}) + U(k_\mathrm{f}, k_\mathrm{f}) = \bar{E}(k_\mathrm{f}) + \frac{k_\mathrm{f}}{3}\frac{\partial \bar{E}(k_\mathrm{f})}{\partial k_\mathrm{f}}\,, \tag{3.15}$$

the dashed line ends at the Fermi surface, $p = k_{\mathrm{f},0} = 272.7\,\mathrm{MeV}$, with the value $\bar{E}(k_{\mathrm{f},0}) = -15.26\,\mathrm{MeV}$. The total single particle energy $T_{\mathrm{kin}}(p) + U(p, k_{\mathrm{f},0})$ rises monotonically with the nucleon momentum p, as it should. Note however that there is no a priori guarantee for such a behavior in a perturbative calculation. As a matter of fact, an earlier chiral expansion scheme by Lutz et. al [13] treating the short-range dynamics differently fails to meet this criterion [41].

While the value of $U(0, k_{\mathrm{f},0})$ lies in the right region and the value of $U(k_{\mathrm{f},0}, k_{\mathrm{f},0})$ is fixed by the Hugenholtz–van-Hove theorem, the momentum dependence of $U(p, k_{\mathrm{f},0})$ between those two points is stronger than other calculations indicate [37, 38]. Also, the dropping of $U(p, k_{\mathrm{f},0})$ above the Fermi surface is not seen in other calculations. Such a strong momentum dependence is only possible since the small pion mass is present as a dynamical scale in our calculation. The mass scales appearing in commonly used boson exchange potentials are much larger.

The momentum dependence of $U(p, k_{f0})$ translates into a variable effective nucleon mass $M_{\mathrm{N}}^{\star}(p)$ by the relation,

$$\frac{1}{M_{\mathrm{N}}^{\star}(p)} = \frac{1}{p}\frac{\partial}{\partial p}\big[T_{\mathrm{kin}}(p) + U(p, k_{\mathrm{f},0})\big]\,. \tag{3.16}$$

The strong momentum dependence in our result leads to a considerable negative slope of $U(p, k_{\mathrm{f},0})$ at $p = k_{\mathrm{f},0}$ resulting in a too large effective nucleon mass $M_{\mathrm{N}}^{\star}(k_{\mathrm{f},0}) \simeq 3.5 M_{\mathrm{N}}$ at the Fermi surface. Since the single-particle properties around the Fermi surface are decisive for the spectrum of thermal excitations and therefore crucially influence the low-temperature behavior of nuclear matter, the strong momentum dependence seen in fig. 3.4 poses a problem for the finite temperature behavior (see chapter 4). A significant improvement of the momentum dependence of $U(p, k_{\mathrm{f},0})$ is possible by explicitly including diagrams involving virtual Δ-excitations (see chapter 7).

3.4.2 Imaginary part

In this section, we discuss the imaginary part $W(p, k_{\mathrm{f}})$ of the single particle potential. Below the Fermi surface, one-hole states can be prepared by removing a nucleon with restricted momentum $0 \leq p \leq k_{\mathrm{f}}$ from the Fermi sea. Their total energy is $-T_{\mathrm{kin}}(p) - U(p, k_{\mathrm{f}}) - i\,W(p, k_{\mathrm{f}})$, according to eq. (3.11). The (positive) imaginary single particle potential $W(p, k_{\mathrm{f}})$ accounts for the finite life time of such a hole state via $\tau_{\mathrm{hole}}^{-1} = 2W(p, k_{\mathrm{f}})$. By on-shell NN-scattering processes the energy of a deeply bound hole-state gets redistributed among two-hole-one-particle states, with the two holes closer to the Fermi surface and a nucleon particle-state in the continuum (i.e. above the Fermi surface). On the other hand, a nucleon above the Fermi surface $p > k_{\mathrm{f}}$ can scatter into one hole-state and two continuum particle-states closer to the Fermi surface. The life time of such a nucleon-particle state is given by $\tau_{\mathrm{part.}}^{-1} = -2W(p, k_{\mathrm{f}})$. In both cases, energy and momentum conservation as well as Pauli blocking limit the available phase space. According to Luttinger's theorem [42], $W(p, k_{\mathrm{f}})$ vanishes quadratically $\sim (k_{\mathrm{f}} - p)^2$ for $p \to k_{\mathrm{f}}$ and its curvature is equal in magnitude but of opposite sign above and below the Fermi surface (in the close vicinity of the Fermi surface).

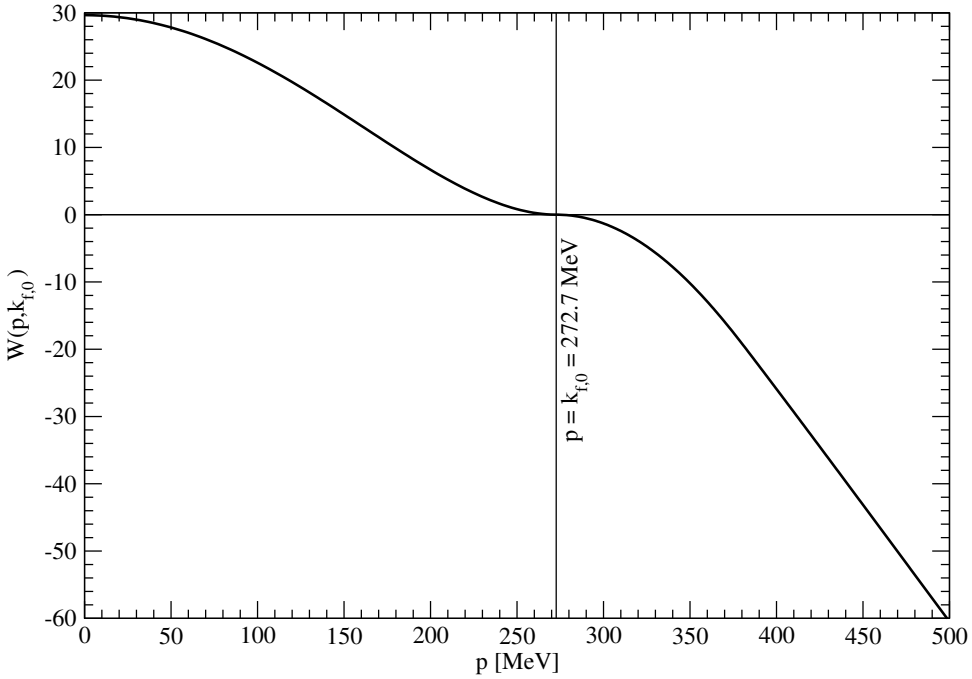

Figure 3.5: The imaginary part of the single-particle potential $W(p, k_{\mathrm{f},0})$ versus the nucleon momentum p at nuclear saturation density, $k_{\mathrm{f},0} = 272.7\,\mathrm{MeV}$.

Within the present three-loop chiral perturbation theory calculation of nuclear matter the contributions to the imaginary single particle potential $W(p, k_f)$ arise entirely from iterated one-pion exchange. The analytical results from ref. [31] for $p < k_\mathrm{f}$ are summarized in appendix B.6.3. The results for $p > k_\mathrm{f}$, which are not simply analytical continuations from below the Fermi surface, are given in eqs. (B.109,B.110) in appendix B.6.4. As before, we associate the contributions to $W(p, k_f)$ with the closed vacuum diagram (see fig. 3.1) before the opening of a nucleon line. The results are completely parameter-free (to the order we are working here).

It is also interesting to consider the imaginary single-particle potential $W(p, k_\mathrm{f})$ in the chiral limit $m_\pi = 0$. One finds the following closed form expressions:

$$W(p,k_\mathrm{f})|_{m_\pi=0} = \frac{9\pi g_\mathrm{A}^4 M_\mathrm{N}}{4(4\pi f_\pi)^4}\,(k_\mathrm{f}^2 - p^2)^2\,, \qquad p < k_\mathrm{f}\,, \tag{3.17}$$

$$W(p,k_\mathrm{f})|_{m_\pi=0} = \frac{3\pi g_\mathrm{A}^4 M_\mathrm{N}}{(4\pi f_\pi)^4}\left\{\frac{7k_\mathrm{f}^5}{5p} - k_\mathrm{f}^3 p - \frac{2}{5p}(2k_\mathrm{f}^2 - p^2)^{5/2}\,\theta\Big(\sqrt{2}k_\mathrm{f} - p\Big)\right\}, \quad p > k_\mathrm{f}\,, \tag{3.18}$$

to which the iterated 1π-exchange Hartree and Fock diagrams have contributed in the ratio $4 : -1$. The analytical results (3.17,3.18) agree with Galitskii's calculation [43] of a contact interaction to second order. In the chiral limit $m_\pi = 0$ the spin-averaged πNN-interaction vertices get canceled by the pion propagators and thus one is effectively dealing with a zero-range NN-contact interaction. The agreement with Galitskii's

result [43] serves as an important check on the technically involved calculation behind eqs. (B.109,B.110).

The resulting curve for $W(p, k_{\mathrm{f},0})$ is shown in fig. 3.5. The half-width for a hole-state of a nucleon at the bottom of the Fermi sea is $W(0, k_{\mathrm{f},0}) = 29.7\,\mathrm{MeV}$. This value lies in between the values $W(0, k_{\mathrm{f},0}) \simeq 20\,\mathrm{MeV}$ and $W(0, k_{\mathrm{f},0}) \simeq 40\,\mathrm{MeV}$ obtained in the self-consistent Brueckner calculation of ref. [37] and the calculation employing the Gogny D1 effective interaction ref. [44], respectively. Taking these two calculations as reasonable benchmark, we conclude that our result is probably realistic. As a consequence of the decreasing phase-space for redistributing the hole-state energy, the curve in fig. 3.5 drops with momentum p and $W(p, k_{\mathrm{f},0})$ and reaches zero at the Fermi surface $p = k_{\mathrm{f},0}$. The curve in fig. 3.5 clearly shows this vanishing to be of quadratic order, $\sim (p - k_{\mathrm{f}})^2$, and thus fulfills Luttinger's theorem [42].

When crossing the Fermi surface the curvature of the imaginary single-particle potential $W(p, k_{\mathrm{f}})$ changes sign. We have checked numerically that the absolute value of the curvature has the same limit when approaching k_{f} from both sides. Above the Fermi surface, a rapid fall to negative values sets in. In fact the width $\Gamma_{\mathrm{sp}} = -2W(p, k_{\mathrm{f}})$ represents the spreading of a single-particle state above the Fermi surface into two-particle-one-hole states with growing phase space as $p - k_{\mathrm{f}}$ increases.

The rapid growth of Γ_{sp} at large momenta $p > 400\,\mathrm{MeV}$ is not shared by the results of refs. [37, 44]. Presumably this shows the limited range of validity of the present chiral perturbation theory calculation.

3.5 Asymmetry energy

The saturation properties of isospin symmetric nuclear matter can be well reproduced in our framework with just one single adjustable cut-off scale Λ. The minimal way to extend this scheme to isospin asymmetric matter is to use the same cut-off for all isospin channels. In order to test the isospin dependence of such an approach, we have investigated the asymmetry energy [14]. In isospin asymmetric matter the Fermi seas of protons and neutrons are not equally filled. With the help of the projection operators $(1 \pm \tau_3)/2$, such an isospin-asymmetric situation is realized by the simple substitution,

$$\theta(k_{\mathrm{f}} - |\mathbf{p}|) \quad \to \quad \frac{1+\tau_3}{2}\theta(k_{\mathrm{p}} - |\mathbf{p}|) + \frac{1-\tau_3}{2}\theta(k_{\mathrm{n}} - |\mathbf{p}|) \tag{3.19}$$

in the in-medium nucleon propagator eq. (2.23). Here k_{p} and k_{n} denote the (different) Fermi momenta of protons and neutrons. Choosing $k_{\mathrm{p,n}} = k_{\mathrm{f}}(1 \mp \delta)^{1/3}$ (with δ a small parameter) the nucleon density $\rho = \rho_{\mathrm{p}} + \rho_{\mathrm{n}} = (k_{\mathrm{p}}^3 + k_{\mathrm{n}}^3)/3\pi^2 = 2k_{\mathrm{f}}^3/3\pi^2$ stays constant. The expansion of the energy per particle of isospin asymmetric nuclear matter,

$$\bar{E}_{\mathrm{as}}(k_{\mathrm{p}}, k_{\mathrm{n}}) = \bar{E}(k_{\mathrm{f}}) + \delta^2 \bar{A}(k_{\mathrm{f}}) + \dots\,,$$

around the symmetry line ($k_{\mathrm{p}} = k_{\mathrm{n}}$ or $\delta = 0$) defines the asymmetry energy per nucleon, $\bar{A}(k_{\mathrm{f}})$. Note that the parameter δ is equal to $(\rho_{\mathrm{n}} - \rho_{\mathrm{p}})/(\rho_{\mathrm{n}} + \rho_{\mathrm{p}})$ or $(N - Z)/(N + Z)$. The explicit expressions for $\bar{A}(k_{\mathrm{f}})$ as given by chiral pion exchange can be found in eqs. (B.48) to (B.55) in the appendix.

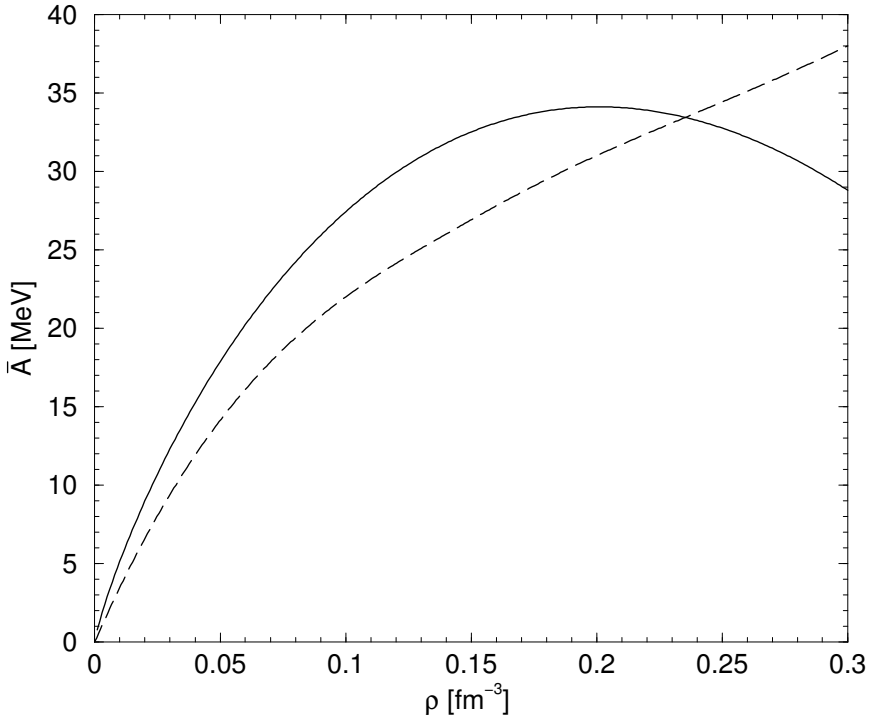

Figure 3.6: The asymmetry energy $\bar{A}(\rho)$ versus the nucleon density ρ. The cut-off parameter is $\Lambda = 646.3\,\mathrm{MeV}$. The dashed line shows the result of ref. [45]

In fig. 3.6, we show the density dependence of $\bar{A}(k_\mathrm{f})$ as determined by πN-dynamics up to $\mathcal{O}(k_\mathrm{f}^5)$ and up to three loop order. At the saturation point $k_{\mathrm{f},0} = 272.7\,\mathrm{MeV}$, we find the asymmetry energy to be $\bar{A}_0 = \bar{A}(k_{\mathrm{f},0}) = 33.8\,\mathrm{MeV}$ which is in very good agreement with the empirical value of $\bar{A}_0 = 33.2\,\mathrm{MeV}$ obtained in ref. [34] from extensive fits to nuclide masses. The $\mathcal{O}(k_\mathrm{f}^5)$ contributions of irreducible 2π-exchange (see fig. 3.2) which plays only a very minor role in the saturation mechanism of symmetric nuclear matter shifts the asymmetry energy noticeably downwards. If we truncate the series expansion at $\mathcal{O}(k_\mathrm{f}^4)$ we get the value $\bar{A}(k_{\mathrm{f},0} = 270\,\mathrm{MeV}, \Lambda = 611.4\,\mathrm{MeV}) = 38.9\,\mathrm{MeV}$.

However, the downward bending of our asymmetry energy $\bar{A}(k_\mathrm{f})$ at densities $\rho > 0.2\,\mathrm{fm}^{-3}$ is not influenced by irreducible 2π exchange and presumably indicates the limits of validity of the chiral expansion scheme as long as it is restricted to pion-nucleon dynamics only. It is remarkable, however, that the isospin dependent forces generated by chiral πN-dynamics alone are already sufficient to produce a realistic value of the asymmetry energy. The result from ref. [45] (the dashed line in fig. 3.6) gives, as most other calculations of the asymmetry energy, a curve monotonically rising with ρ.

3.6 Pure neutron matter

The extreme of asymmetric nuclear matter is pure neutron matter. While empirical constraints exist only for relatively high densities $\rho \gtrsim 2\rho_0$ and involve large uncertainties

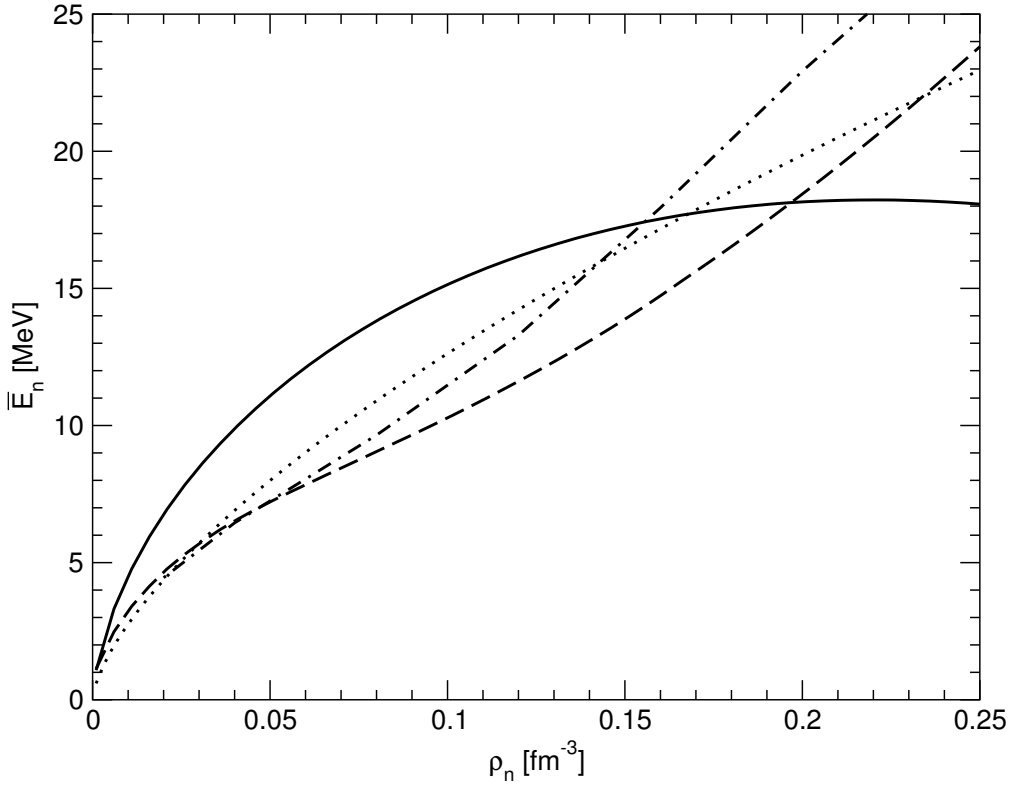

Figure 3.7: The density dependence of the energy per particle of pure neutron matter (solid line). The cut-off parameter is $\Lambda = 646.3\,\mathrm{MeV}$. The dotted line shows $\bar{E}_{\mathrm{n,kin}}/2$. The other lines give the results of ref. [27] (dashed) and ref. [18] (dash-dotted).

[46], all existing realistic calculations agree that pure neutron matter is unbound [4, 5, 18, 27, 38]. Its energy per particle rises monotonically with the neutron density. For very low densities $\rho_\mathrm{n} < 0.05\,\mathrm{fm}^{-3}$, many calculations agree that the equation of state $\bar{E}_\mathrm{n}(\rho_\mathrm{n})$ should behave approximately as half the (neutron) kinetic energy, $\frac{1}{2}\bar{E}_{\mathrm{n,kin}}$ (see also ref. [4]). This behavior is confirmed by the complete resummation of in-medium multi-loop diagrams for a system with an unnaturally large scattering length (such as neutron matter), as demonstrated in ref. [47] in the limit of a large number of space-time dimensions D. For an infinite scattering length a_nn and neglecting $1/D$ corrections, one gets $\bar{E}_\mathrm{n}(k_\mathrm{n}) = \frac{4}{9}\bar{E}_{\mathrm{n,kin}}$. Positive corrections for a finite scattering length shift the result even further towards $\frac{1}{2}\bar{E}_{\mathrm{n,kin}}$.

In order to arrive at the energy per particle $\bar{E}_\mathrm{n}(k_\mathrm{n})$ of neutron matter in our diagrammatic framework it is sufficient to substitute

$$\theta(k_\mathrm{f} - |\mathbf{p}|) \quad \to \quad \frac{1-\tau_3}{2}\,\theta(k_\mathrm{n} - |\mathbf{p}|) \tag{3.20}$$

in the in-medium nucleon propagator eq. (2.23). Here k_n denotes the Fermi momentum of the neutrons which is related to the neutron density by $\rho_\mathrm{n} = k_\mathrm{n}^3/3\pi^2$. As a consequence of the substitution (3.20) only the isospin factors of individual diagrams change and all Fermi spheres have the radius k_n. The explicit expressions for $\bar{E}_\mathrm{n}(k_\mathrm{f})$ as given by chiral

pion exchange can be found in appendix B.4.

The equation of state determined by πN-dynamics up to $\mathcal{O}(k_\mathrm{f}^5)$ is shown as the solid line in fig. 3.7. One sees that neutron matter is indeed unbound. A priori, this is not guaranteed in a perturbative calculation and is thus already a nontrivial result. For comparison, we also show the results of ref. [27] and ref. [18] as the dashed and dash-dotted lines in fig. 3.7. At higher densities $\rho_\mathrm{n} > 0.2\,\mathrm{fm}^{-3}$, our result starts to become unrealistic because of its downward bending. This feature is inherited from the asymmetry energy (see fig. 3.6). At low densities, even if our result shows qualitatively the right behavior, it fails to reproduce these curves on a quantitative level. Most importantly, for very small densities it does not lie as close to $\frac{1}{2}\bar{E}_\mathrm{n,kin}$ as expected.

However, one should not forget that the treatment of the short-range dynamics with just one single momentum cut-off for all isospin channels is too simplistic. In fact, if one uses the same cut-off as for isospin symmetric nuclear matter, our neutron matter equation of state has no free parameters. The situation will be much improved once πNΔ-dynamics is incorporated (see sections 7.5, 7.6).

3.7 Chiral condensate

Our calculation of the nuclear equation of state results in analytic expressions as functions of the pion mass m_π (see eqs. (B.11-B.18)). This allows in principle to determine the density dependence of the chiral condensate which is the order parameter of spontaneous chiral symmetry breaking in QCD.

An expression for this density dependence has been given in eq. (2.16). Written in terms of the energy per particle $\bar{E}$, it is

$$\frac{\langle\bar{q}q\rangle_\rho}{\langle\bar{q}q\rangle_0} = 1 - \frac{\rho}{2m_\pi f_\pi^2}\frac{\mathrm{d}}{\mathrm{d}m_\pi}\Big(M_\mathrm{N} + \bar{E}(k_\mathrm{f})\Big) = 1 - \frac{\rho}{2m_\pi f_\pi^2}\left(\frac{2\sigma_{\pi\mathrm{N}}}{m_\pi} + \frac{\mathrm{d}\bar{E}(k_\mathrm{f})}{\mathrm{d}m_\pi}\right). \tag{3.21}$$

Here, the so-called πN-sigma term $\sigma_{\pi\mathrm{N}}$ is that part of the nucleon mass M_N that is caused by the nonvanishing average quark mass $\bar{m}$. It is

$$\sigma_{\pi\mathrm{N}} = \bar{m}\frac{\partial M_\mathrm{N}}{\partial\bar{m}} = \frac{m_\pi}{2}\frac{\partial M_\mathrm{N}}{\partial m_\pi} \tag{3.22}$$

with the empirical value [48]

$$\sigma_{\pi\mathrm{N}} = (45 \pm 8)\,\mathrm{MeV}\,.$$

As leading term in eq. (3.21), the $\sigma_{\pi\mathrm{N}}$ term causes a linear decrease of the chiral condensate $\langle\bar{q}q\rangle_\rho/\langle\bar{q}q\rangle_0$ with density ρ.[2] At $\rho \simeq 3\rho_0$, this leading term by itself would cause the condensate to vanish and chiral symmetry to be restored. However, there is general

[2] The correct leading term for a Fermi gas of nucleons is given in terms of the scalar density $\rho_\mathrm{s} = \langle\bar{\mathrm{N}}\mathrm{N}\rangle$ (see e. g. [49]):

$$\frac{\langle\bar{q}q\rangle_\rho}{\langle\bar{q}q\rangle_0} = 1 - \frac{\sigma_{\pi\mathrm{N}}}{m_\pi^2 f_\pi^2}\rho_\mathrm{s}\,.$$

This leading term is approximated in our nonrelativistic approach by expanding the difference between the scalar density and the baryon density to order $k_\mathrm{f}^2/M_\mathrm{N}^2$.

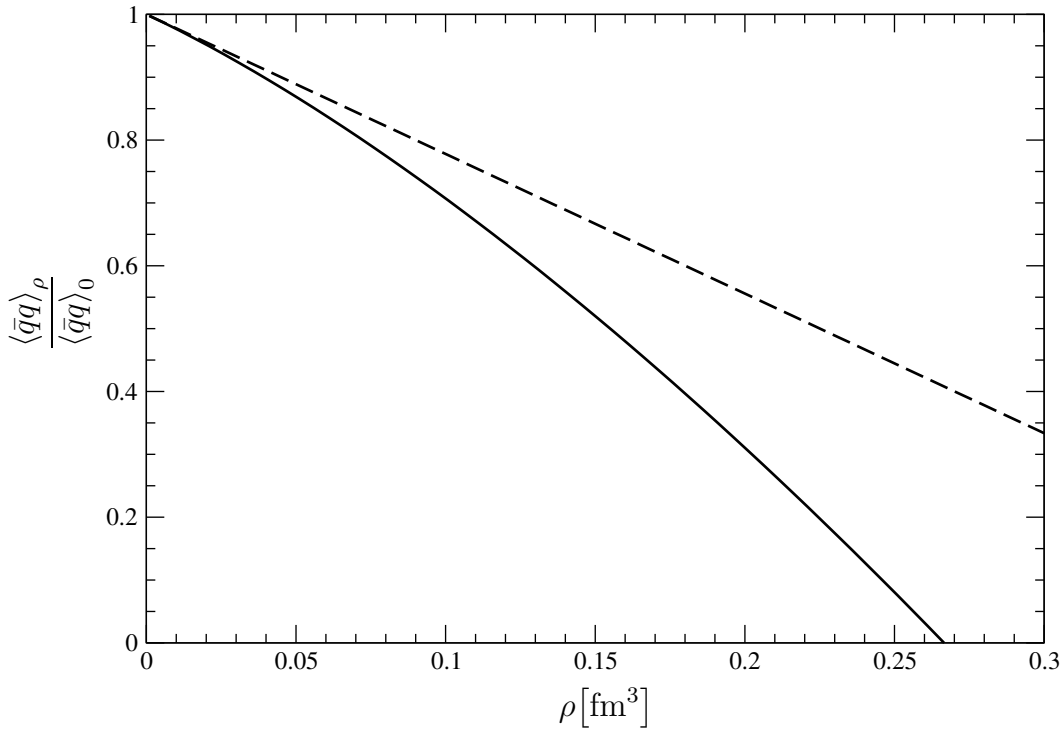

Figure 3.8: Influence of the explicit m_π dependence of 1π- and 2π-exchange on the chiral condensate at density ρ. Not included are any contributions from short-range dynamics. The dashed line shows the leading term from eq. (3.21) which involves $\sigma_{\pi N}$.

agreement that the nonlinear contributions stabilize the order parameter such that chiral restoration is shifted to higher densities (see e. g. ref. [50]).

In addition to the explicit m_π dependence, the energy per particle contains also an implicit dependence on m_π via various physical constants being modified by chiral symmetry breaking: $M_N = M_N(m_\pi)$, $g_A = g_A(m_\pi)$, and $f_\pi = f_\pi(m_\pi)$. While it is possible to get some estimates of the m_π dependencies of $g_A(m_\pi)$ and $f_\pi(m_\pi)$ from chiral logarithms, their exact form is not known. Because of these uncertainties we will restrict ourselves here to the explicit m_π dependencies only. Note that the considerations in ref. [15] showed that the influence of the the implicit m_π dependence arising via $M_N(m_\pi)$ in the long range pion exchange contributions is quite small. Note also that our considerations are necessarily incomplete at this point since the m_π dependence of the momentum cut-off Λ and the effects of short-range correlations are unknown.

The full line in fig. 3.8 shows the influence of the finite parts of chiral one- and two-pion exchange on the chiral condensate as a function of ρ. As one can see, the long range dynamics drive the condensate even faster towards chiral restoration than the leading linear term (the dashed line in fig. 3.8). This behavior is caused mainly by the iterated 1π-exchange Hartree diagram (the middle diagram in fig. 3.1) with two medium

insertions [15]. Its finite part eq. (B.13) gives a large repulsive contribution of 46 MeV to $\bar{E}$ at finite pion mass $m_\pi = 135\,\mathrm{MeV}$ but vanishes in the chiral limit $m_\pi \to 0$. This strong m_π dependence results in a large positive contribution to $\mathrm{d}\bar{E}/\mathrm{d}m_\pi$ in eq. (3.21) pushing the chiral condensate further downwards.

If there were no other contributions affecting the chiral condensate, the behavior shown in fig. 3.8 would cast serious doubt on the expansion scheme described in this chapter: Chiral perturbation theory is based on the spontaneous breaking of chiral symmetry and the occurrence of the corresponding Goldstone bosons. Chiral restoration occurring already at relatively low densities $\rho < 2\rho_0$ in nuclear matter would invalidate the applicability of chiral perturbation theory in nuclear matter.

On the other hand, there is general agreement that many body effects at finite density work *against* chiral restoration. This behavior is shown by several other calculations, e. g. with Brueckner or Dirac-Brueckner approach [50]. There, short-range correlations give the crucial contribution to stabilize the chiral condensate. If our scheme is extended to include diagrams involving virtual $\Delta(1232)$-excitations, there are additional contributions working against chiral restoration and there are also indications that the short-range contributions work in the same direction as well (see section 7.7).

Chapter 4

Finite temperature

The analysis of data from low-energy heavy-ion collisions in the regime of nuclear fragmentation has lead to the picture that heated nuclear matter undergoes a phase transition from a liquid-like state to a vaporized gas state [26, 51]. This liquid-gas phase transition of isospin symmetric nuclear matter is in fact very similar to that of the familiar van der Waals gas. The experimental determination of the critical point of this phase transition from heavy-ion collisions is made difficult by the facts that phase transitions in finite systems are not as well defined as in infinite systems and that an estimation of the temperature is difficult for nonstationary systems with finite life-times. However, there is some agreement that for nuclear matter the critical temperature is $T_c \simeq (16 - 18)\,\mathrm{MeV}$ and the critical density is $\rho_c = (0.06 - 0.07)\,\mathrm{fm}^{-3}$ [26]. Recently, Natzowitz et al. inferred the value $T_c = (16.8 \pm 0.9)$ from experimental observations of limiting temperatures in heavy ion collisions [52].

Clearly, the dynamical description of this phase transition is an important topic in any microscopic calculation of nuclear matter. In the $\sigma\omega$ mean-field model of Serot and Walecka [9] nucleons are described as Dirac quasi-particles moving in self-consistently generated scalar and vector mean fields. In such approaches a critical temperature of $T_c \simeq 19\,\mathrm{MeV}$ is typically found [53]. Furthermore, the sophisticated many-body calculations of the Urbana group using the V14 effective NN-interaction (plus an adjustable three-nucleon interaction) predict a critical temperature of $T_c \simeq 18\,\mathrm{MeV}$ [27]. For earlier work on this topic using effective Skyrme forces, see ref. [54].

In the previous section, we have seen that many properties of nuclear matter can be well described by chiral πN-dynamics treated (perturbatively) up to three loop order. Of course it is now interesting to also consider finite temperatures T in order to check whether the first-order liquid-gas phase transition of nuclear matter is correctly reproduced by this particular dynamics [32].

4.1 Calculational framework

For the relatively low temperatures $T \leq 30\,\mathrm{MeV}$ which are of interest in this context one can safely neglect effects from thermal pions or thermally excited nucleon-antinucleon pairs. As a consequence, nucleons can be treated nonrelativistically and the new parameter, the temperature T, enters only through the nucleons' thermal occupation probabilities given by a Fermi-Dirac distribution.

In the framework described in chapter 3, the diagrammatic calculation of the energy density at $T = 0$ (as a function of the particle density ρ) has been organized in the number of medium insertions. A thermodynamically consistent extension of such an ordering scheme to finite temperatures is to relate it directly to the free energy density $\rho\,\bar{F}(\rho,T)$, since its natural thermodynamical variables are the particle density ρ and the temperature T. In that case the free energy density of isospin symmetric nuclear matter consists of a sum of convolution integrals of the form,

$$\begin{aligned}\rho\,\bar{F}(\rho,T) &= 4\int_0^\infty \mathrm{d}p_1\, p_1\,\mathcal{K}_1\, d(p_1) + \int_0^\infty \mathrm{d}p_1 \int_0^\infty \mathrm{d}p_2\,\mathcal{K}_2\, d(p_1)d(p_2) \\ &\quad + \int_0^\infty \mathrm{d}p_1 \int_0^\infty \mathrm{d}p_2 \int_0^\infty \mathrm{d}p_3\,\mathcal{K}_3\, d(p_1)d(p_2)d(p_3) + \rho\,\bar{\mathcal{A}}(\rho,T)\,, \qquad (4.1)\end{aligned}$$

with the kernels $\mathcal{K}_j$ corresponding to the contributions with j medium-insertions and the anomalous contribution $\bar{\mathcal{A}}(\rho,T)$ to be specified.[1] The quantity

$$d(p_j) = \frac{p_j}{2\pi^2}\left[1+\exp\frac{p_j^2-2M_\mathrm{N}\tilde{\mu}}{2M_\mathrm{N}T}\right]^{-1}, \qquad (4.2)$$

denotes the density of nucleon states in momentum space. It is the product of the temperature dependent Fermi-Dirac distribution and a kinematical prefactor $p_j/2\pi^2$ which has been included in $d(p_j)$ for convenience.[2] $M_\mathrm{N} = 939\,\mathrm{MeV}$ stands for the (free) nucleon mass. The particle density ρ is calculated from the density of states in momentum space as

$$\rho = 4\int_0^\infty \mathrm{d}p_1\, p_1\, d(p_1) = -\sqrt{2}\left(\frac{M_\mathrm{N}T}{\pi}\right)^{3/2}\mathrm{Li}_{3/2}\big(-e^{\tilde{\mu}/T}\big)\,, \qquad (4.3)$$

and this relationship determines the dependence of the effective one-body "chemical potential" $\tilde{\mu}(\rho,T)$ on the thermodynamical variables ρ and T. The "true" chemical potential is different and given by the formula $\mu = \bar{F} + \rho\;\partial\bar{F}/\partial\rho$. Concerning eqs. (4.1,4.2,4.3) we are following here (partially) the approximation scheme of ref. [55]. Our approach is (by construction) thermodynamically consistent, since all thermodynamic quantities are derived (via standard relations) from the free energy density $\rho\,\bar{F}(\rho,T)$. The infinite series $\mathrm{Li}_\nu(x) = \sum_{k=1}^\infty k^{-\nu}x^k$ defines the polylogarithmic function of index ν for $|x|<1$. The factor 4 in eqs. (4.1,4.3) counts the spin-isospin multiplicity of a nucleon.

[1] Let us briefly motivate our approach. The standard procedure in field theory is to calculate the grand canonical partition function Z or equivalently the thermodynamic potential $\Omega(\mu,T) = -(T/V)\ln Z$ as a function of its natural variables, the (nonrelativistic) chemical potential μ and the temperature T. In the case of nuclear matter at $T=0$ the functional relationship $\Omega(\mu,0)$ is however double-valued for $\mu \le 0$. Since perturbation theory usually gives single-valued thermodynamic functions it is more appropriate to calculate first the (single-valued) energy density $\rho\,\bar{E}(k_\mathrm{f})$ of nuclear matter as a function of the particle density ρ, as done in chapter 3. Then eq. (4.1) defines a thermodynamically consistent extension to finite temperatures T, with the correct $T=0$ limit. This calculational scheme can also be understood such that in the Legendre-transformation from $\Omega(\mu,T)$ to the free energy density, $\rho\,\bar{F}(\rho,T) = \Omega(\mu,T) - \mu\,\partial\Omega/\partial\mu$, the derivative term is taken into account only for the noninteracting (free nucleon gas) part and the (static) one-pion exchange contribution, but not for the higher order contributions coming from chiral 2π-exchange.

[2] Note that this is not the same notation as in section 3.4.

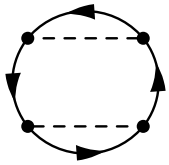

Figure 4.1: Anomalous Fock diagram contributing at finite temperature.

The one-body kernel $\mathcal{K}_1$ in eq. (4.1) represents the contribution of the noninteracting nucleon gas to the free energy density and reads

$$\mathcal{K}_1 = \tilde{\mu} - \frac{p_1^2}{3M_\mathrm{N}} - \frac{p_1^4}{8M_\mathrm{N}^3}\,. \tag{4.4}$$

While the first two terms are standard [55], the correction term, $-p_1^4/8M_\mathrm{N}^3$, has been constructed according to the following criteria: First, it ensures the correct $T = 0$ limit for the energy per particle $\bar{E}(k_\mathrm{f})$ up to order k_f^4, in which $\tilde{\mu}(\rho, 0) = k_\mathrm{f}^2/2M_\mathrm{N}$ and $\rho = 2k_\mathrm{f}^3/3\pi^2$. Secondly, the so-constructed kernel $\mathcal{K}_1$ combined with the nonrelativistic Fermi-Dirac distribution (see eq. (4.2)) gives a very accurate approximation of the free energy density of a fully relativistic free nucleon gas [53] for the densities and temperatures of interest here.

The (non-anomalous) contributions to the free energy density $\rho\,\bar{F}(\rho, T)$ arising from pion exchange interactions are encoded in the kernels $\mathcal{K}_{2,3}$ in eq. (4.1). The closed vacuum diagrams related to one-pion exchange (Fock diagram) and iterated one-pion exchange (Hartree and Fock diagrams) are shown in fig. 3.1. In addition to that, the diagrams of irreducible 2π-exchange are shown in fig. 3.2. The explicit expressions for $\mathcal{K}_{2,3}$ are given in eqs. (B.29) to (B.36) in appendix B.2.2.

4.2 Anomalous contribution

Next, we come to the so-called anomalous contribution $\bar{\mathcal{A}}(\rho, T)$ in eq. (4.1). This is a special feature at finite temperatures [56–58] with no counterpart in the calculation of the ground state energy density $\rho\,\bar{E}(k_\mathrm{f})$ at $T = 0$. The Fock diagram in fig. 4.1 involves an integral over $\theta(k_\mathrm{f} - p)\,\theta(p - k_\mathrm{f})$ and thus vanishes for $T = 0$. At $T > 0$, on the other hand, the thermal occupation probabilities yield a non-zero value that does not vanish even when taking the $T \to 0$ limit. However, in a Fermion system in the absence of symmetry breaking, this contribution is canceled by the perturbative shift of the chemical potential

$$\tilde{\mu} \to \tilde{\mu} - \Omega'_{1\pi}(\rho, T)/\Omega''_0(\rho, T)\,, \tag{4.5}$$

as shown by Kohn, Luttinger, and Ward [56]. Their theorem holds of course in our case since the Fermi surface and the pion-induced interactions are invariant under spatial rotations.

The diagram in fig. 4.1 gives the following contribution to the free energy per particle

of isospin symmetric nuclear matter:

$$\begin{aligned}\bar{\mathcal{A}}(\rho,T) &= -\frac{[\Omega'_{1\pi}(\rho,T)]^2}{2\rho\,\Omega''_0(\rho,T)} \\ &\quad +\frac{9g_{\rm A}^4}{8f_\pi^4 T\rho}\int_0^\infty {\rm d}p_1\int_0^\infty {\rm d}p_2\int_0^\infty {\rm d}p_3\; d(p_1)d(p_2)[2\pi^2 d(p_2)-p_2]d(p_3) \\ &\quad \times\left[p_1-\frac{m_\pi^2}{4p_2}\ln\frac{m_\pi^2+(p_1+p_2)^2}{m_\pi^2+(p_1-p_2)^2}\right]\left[p_3-\frac{m_\pi^2}{4p_2}\ln\frac{m_\pi^2+(p_3+p_2)^2}{m_\pi^2+(p_3-p_2)^2}\right], \quad (4.6)\end{aligned}$$

with the $\tilde{\mu}$-derivative of the thermodynamical potential due to static 1π-exchange,

$$\Omega'_{1\pi}(\rho,T)=\frac{3g_{\rm A}^2M_{\rm N}}{2f_\pi^2}\int_0^\infty {\rm d}p_1\int_0^\infty {\rm d}p_2\; d(p_1)\frac{d(p_2)}{p_2}\left[\frac{(p_1+p_2)^3}{m_\pi^2+(p_1+p_2)^2}+\frac{(p_1-p_2)^3}{m_\pi^2+(p_1-p_2)^2}\right], \quad (4.7)$$

and the second $\tilde{\mu}$-derivative of the free nucleon gas part,

$$\Omega''_0(\rho,T)=-4M_{\rm N}\int_0^\infty {\rm d}p_1\;\frac{d(p_1)}{p_1}=\sqrt{2T}\left(\frac{M_{\rm N}}{\pi}\right)^{3/2}{\rm Li}_{1/2}(-e^{\tilde{\mu}/T})\,. \quad (4.8)$$

The first term in eq. (4.6) originates from taking into account the (static) 1π-exchange contribution in the Legendre transformation from the thermodynamical potential to the free energy density and from the perturbative shift of the chemical potential, eq. (4.5) (for details on that procedure, see ref. [56]). We have explicitly checked the Kohn-Luttinger-Ward theorem, i. e. that the anomalous contribution $\bar{\mathcal{A}}(\rho,T)$ vanishes identically at $T=0$ for all densities ρ. For $T>0$, we find the anomalous contribution always negative, $\bar{\mathcal{A}}(\rho,T)<0$, as it should be [56]. Furthermore, it is interesting to observe that the temperature and density dependent anomalous contribution $\bar{\mathcal{A}}(\rho,T)$ vanishes identically in the chiral limit $m_\pi=0$.

The calculation in ref. [59] shows (using the same toy interaction as in section 3.3), that for temperatures near the Fermi temperature $T_{\rm f}=k_{\rm f}^2/2M_{\rm N}$ the anomalous contribution can be of considerable size. Note also that the anomalous contribution $\bar{\mathcal{A}}(\rho,T)$ is (formally) of the same order in small momenta as the contributions to $\bar{F}(\rho,T)$ coming from iterated 1π-exchange. It should therefore not be neglected in a consistent and complete calculation. However, our calculations show that the contribution of $\bar{\mathcal{A}}(\rho,T)$ to the free energy is quite small compared to the other contributions from pion exchange.

4.3 Results

Via general thermodynamical relations [53] one can derive from the free energy per particle $\bar{F}(\rho,T)$ the pressure $P(\rho,T)$ and the entropy per particle $\bar{S}(\rho,T)$:

$$P(\rho,T)=\rho^2\,\frac{\partial\bar{F}(\rho,T)}{\partial\rho}\,,\qquad \bar{S}(\rho,T)=-\frac{\partial\bar{F}(\rho,T)}{\partial T}\,. \quad (4.9)$$

We are now in the position to present numerical results for isospin symmetric nuclear matter at finite temperatures. We use the same value of the cut-off scale $\Lambda=646.3\,{\rm MeV}$

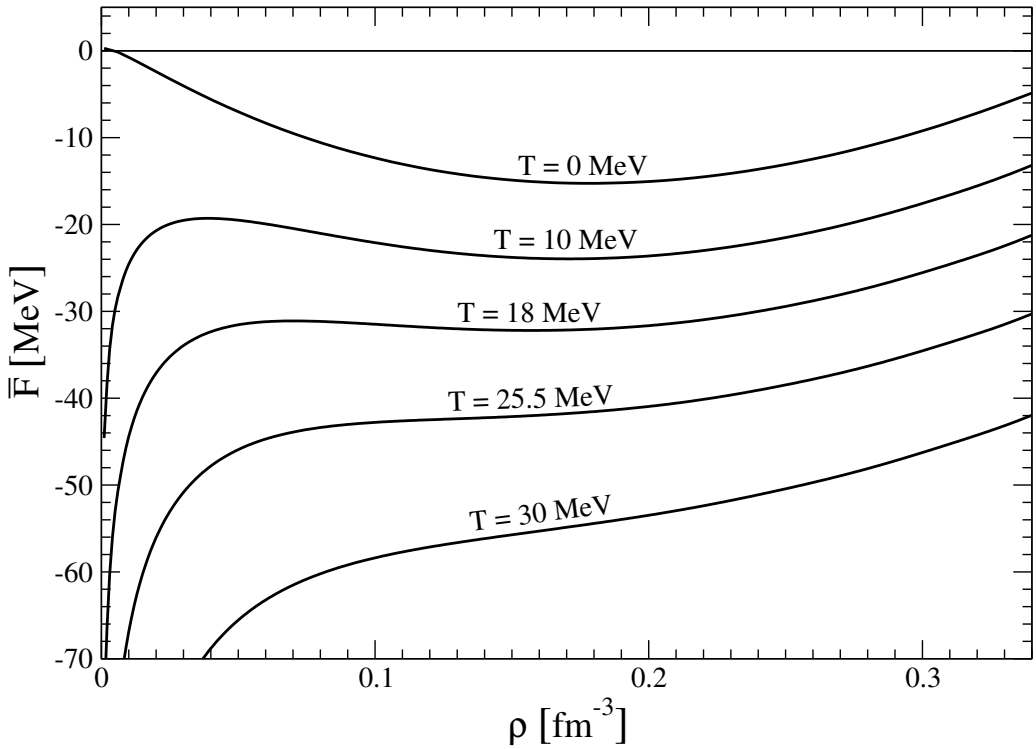

Figure 4.2: The free energy per particle of isospin symmetric nuclear matter $\bar{F}(\rho, T)$ versus the nucleon density ρ. Each curve is labeled with its corresponding constant temperature T.

as in chapter 3. Figure 4.2 shows the free energy per particle $\bar{F}(\rho, T)$ as a function of the nucleon density ρ for various temperatures $T = 0, 10, 18, 25.5, 30\,\mathrm{MeV}$. The uppermost line is the nuclear matter saturation curve at $T = 0$. The singular behavior of the free energy per particle $\bar{F}(\rho, T)$ for $\rho \to 0$ at $T > 0$ is a generic feature (see e.g. the figures and tables corresponding to the results of the Urbana group in ref. [27]). The internal energy per particle $\bar{F}(\rho, T) + T\,\bar{S}(\rho, T)$, on the other hand, approaches approximately the value $3T/2$ for $\rho \to 0$.

Figure 4.3 shows the calculated pressure isotherms $P(\rho, T)$ of isospin symmetric nuclear matter. As it should be these curves display a first-order liquid-gas phase transition similar to that of the van der Waals gas. The coexistence region between the liquid and the gas phase (determined by the Maxwell construction [53]) terminates at the critical temperature T_c. From there on the pressure isotherms $P(\rho, T)$ grow monotonically with the particle density ρ. At this stage, with only pions and nucleons as explicit degrees of freedom, we find a critical temperature of $T_c = 25.5\,\mathrm{MeV}$ and a critical density of $\rho_c = 0.09\ \mathrm{fm}^{-3} \simeq 0.5\rho_0$ (with $\rho_0 = 0.178\ \mathrm{fm}^{-3}$, the predicted nuclear matter saturation density). Together with the critical pressure $P(\rho_c, T_c) = 0.69\,\mathrm{MeV\,fm}^{-3}$ this prediction of the critical point still deviates considerably from most other calculations. The too high value of the critical temperature, $T_c = 25.5\,\mathrm{MeV}$, finds its explanation in the strong momentum dependence of the underlying single-particle potential $U(p, k_{\mathrm{f},0})$ near the

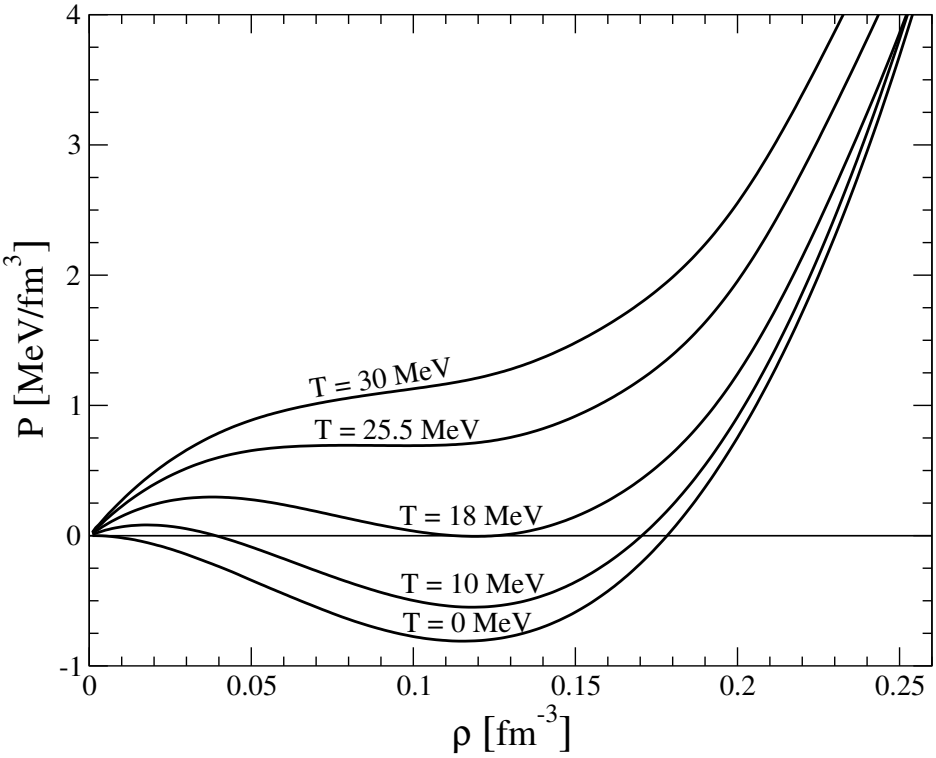

Figure 4.3: Pressure isotherms $P(\rho, T)$ of isospin symmetric nuclear matter. The coexistence region of the liquid and gas phase ends at the critical point $\rho_c \simeq 0.09$ fm^{-3} and $T_c \simeq 25.5\,\mathrm{MeV}$.

Fermi surface $p = k_{\mathrm{f},0}$ (see fig. 3.4). The nominal value of the effective nucleon mass at the Fermi surface is $M_{\mathrm{N}}^{\star}(k_{\mathrm{f},0}) \simeq 3.5 M_{\mathrm{N}}$. The latter quantity determines, via the density of states at the Fermi surface, the low-temperature behavior of a Fermi liquid. In the present calculation the density of thermally excitable quasi-particles is too low, so that nuclear matter has to be heated up to relatively high temperatures until it evaporates completely. As we will see in section 7.2, this particular problem of the large effective nucleon mass $M_{\mathrm{N}}^{\star}(k_{\mathrm{f},0})$ can be cured by including diagrams involving virtual Δ-excitations. Note that despite its large isospin factor 18 the anomalous contribution $\bar{\mathcal{A}}(\rho, T)$ does practically not influence the behavior of nuclear matter at low temperatures $T < 30\,\mathrm{MeV}$.

As a final remark, we consider the chiral limit $m_\pi = 0$. With a reduced cut-off scale of $\Lambda = 555.8\,\mathrm{MeV}$ (and fixed $g_{\mathrm{A}}, f_\pi, M_{\mathrm{N}}$) the same maximum binding energy per particle ($15.26\,\mathrm{MeV}$) is obtained at a saturation density of $\rho_0 = 0.145\,\mathrm{fm}^{-3}$. Interestingly, the critical temperature $T_c \simeq 27\,\mathrm{MeV}$ remains nearly unchanged when taking the chiral limit. This confirms the expectation that the critical temperature T_c is primarily determined by the binding energy per particle $-\bar{E}(k_{\mathrm{f},0})$ and the effective nucleon mass $M_{\mathrm{N}}^{\star}(k_{\mathrm{f},0})$ at the Fermi surface.

Chapter 5

Inhomogeneous Systems

Given the fact that many properties of infinite homogeneous nuclear matter can be well described by chiral πN-dynamics in the framework described in the previous chapters it is natural to extend this scheme to inhomogeneous many-nucleon systems. We do this by using the density-matrix expansion of Negele and Vautherin [60] to calculate the relevant energy density functional. In order to motivate this approach, we now have a brief look at the Skyrme force [8].

The Skyrme force is a phenomenological zero-range effective interaction that is very popular for nuclear structure calculations because of its analytical simplicity and its ability to reproduce nuclear properties over the whole periodic table. While the corresponding energy density functional is derived using the density-matrix expansion, there is no microscopic interpretation of the parameters of this interaction. Rather, these parameters are tuned for the exclusive use in the restricted wave function space of the self-consistent Hartree-Fock approximation. A brief outline of the Skyrme-Hartree-Fock method is given in appendix A.

Many different Skyrme parameterizations have been tailored to account for different observables such as single-particle spectra [61], giant monopole resonances [62] or fission barriers of heavy nuclei [63]. Recently, a new Skyrme force which also reproduces the equation of state of pure neutron matter up to neutron star densities, $\rho_{\rm n} \simeq 1.5\,{\rm fm}^{-3}$, has been proposed in ref. [64] for the study of nuclei far from stability.

In the following, we will use the density-matrix expansion to obtain the form of the medium insertion eq. (2.23) relevant in an inhomogeneous nuclear medium. This will allow us to calculate the energy density functional from chiral one pion and iterated one pion exchange, leading to novel density dependence compared to the Skyrme force's energy density functional. In section 5.1.4 we take this additional density dependence into account when calculating the ground state properties of ^{40}Ca. In this chapter, we will restrict ourselves to the isospin symmetric case of equal proton and neutron number $N = Z$.

The procedure described above has its limitations which we shall discuss in detail. We will also briefly outline in section 5.2 an alternative (relativistic) approach to finite nuclei by Finelli et al. [21,22] that turns out to have some advantages over the (nonrelativistic) energy density functional method.

5.1 Energy density functional from chiral pion-nucleon dynamics

5.1.1 Density-matrix expansion and energy density functional

The starting point for the construction of a nuclear energy density functional is the density-matrix as given by the sum over the occupied energy eigenfunctions ϕ_i of this (nonrelativistic) many-fermion system. According to Negele and Vautherin [60] the bilocal density-matrix can be expanded in relative and center-of-mass coordinates, $\mathbf{a}$ and $\mathbf{r}$, as follows:

$$\sum_{i\in\mathrm{occ}} \phi_i(\mathbf{r}-\mathbf{a}/2)\phi_i^\dagger(\mathbf{r}+\mathbf{a}/2) = \frac{3\rho}{ak_\mathrm{f}}\, j_1(ak_\mathrm{f}) - \frac{35}{2ak_\mathrm{f}^3}\, j_3(ak_\mathrm{f})\left[\tau - \frac{3}{5}\rho k_\mathrm{f}^2 - \frac{1}{4}\boldsymbol{\nabla}^2\rho\right] + \frac{i}{2}\, j_0(ak_\mathrm{f})\, \boldsymbol{\sigma}\cdot(\mathbf{a}\times\mathbf{J}) + \dots\,, \quad (5.1)$$

where the functions $j_l(ak_\mathrm{f})$ are ordinary spherical Bessel functions. The other quantities appearing on the right hand side of eq. (5.1) are the local nucleon density,

$$\rho(\mathbf{r}) = \frac{2k_\mathrm{f}^3(\mathbf{r})}{3\pi^2} = \sum_{i\in\mathrm{occ}} \phi_i^\dagger(\mathbf{r})\phi_i(\mathbf{r})\,, \quad (5.2)$$

written here in terms of the local Fermi momentum $k_\mathrm{f}(\mathbf{r})$, the local kinetic energy density,

$$\tau(\mathbf{r}) = \sum_{i\in\mathrm{occ}} \boldsymbol{\nabla}\phi_i^\dagger(\mathbf{r})\cdot\boldsymbol{\nabla}\phi_i(\mathbf{r})\,, \quad (5.3)$$

and the local spin-orbit density,

$$\mathbf{J}(\mathbf{r}) = \sum_{i\in\mathrm{occ}} \phi_i^\dagger(\mathbf{r})\mathrm{i}\,\boldsymbol{\sigma}\times\boldsymbol{\nabla}\phi_i(\mathbf{r})\,. \quad (5.4)$$

For notational simplicity we have dropped the argument $\mathbf{r}$ in eq. (5.1) and will continue doing so in the following. It is important to note that a pairwise filling of time-reversed orbitals i has been assumed in eq. (5.1). If the many-body ground state is not time-reversal invariant (as it is the case for odd nuclei and for rotating nuclei) various additional time-reversal-odd fields come into play [7]. The Fourier transform of the density-matrix eq. (5.1) with respect to both coordinates $\mathbf{a}$ and $\mathbf{r}$ defines the medium insertion for the inhomogeneous many-nucleon system characterized by the time-reversal-even fields $\rho(\mathbf{r})$, $\tau(\mathbf{r})$, and $\mathbf{J}(\mathbf{r})$:

$$\Gamma(\mathbf{p},\mathbf{q}) = \int \mathrm{d}^3r\, e^{-i\mathbf{q}\cdot\mathbf{r}} \left\{\theta(k_\mathrm{f}-|\mathbf{p}|)\left[1+\frac{35\pi^2}{8k_\mathrm{f}^7}(5\mathbf{p}^2-3k_\mathrm{f}^2)\left(\tau-\frac{3}{5}\rho k_\mathrm{f}^2-\frac{1}{4}\boldsymbol{\nabla}^2\rho\right)\right] + \frac{\pi^2}{4k_\mathrm{f}^4}\Big[\delta(k_\mathrm{f}-|\mathbf{p}|) - k_\mathrm{f}\,\delta'(k_\mathrm{f}-|\mathbf{p}|)\Big]\,\boldsymbol{\sigma}\cdot(\mathbf{p}\times\mathbf{J})\right\}. \quad (5.5)$$

The double line in fig. 5.1 symbolizes this medium insertion together with the assignment of the out- and in-going nucleon momenta $\mathbf{p}\pm\mathbf{q}/2$. The momentum transfer $\mathbf{q}$ is provided by the Fourier components of the inhomogeneous (matter) distributions: $\rho(\mathbf{r})$, $\tau(\mathbf{r})$, and $\mathbf{J}(\mathbf{r})$. As a check one verifies that the Fourier transform $(1/2\pi^3)\int \mathrm{d}^3p\, e^{-i\mathbf{p}\cdot\mathbf{a}}$ of the (partly very singular) expression in the curly brackets in eq. (5.5) gives exactly the right hand side of the density-matrix expansion in eq. (5.1). For homogeneous nuclear matter (where $\tau = 3\rho k_\mathrm{f}^2/5$ and $\boldsymbol{\nabla}\rho = \mathbf{J} = \mathbf{0}$), only the step-function $\theta(k_\mathrm{f} - |\mathbf{p}|)$ known from eq. (2.23) remains from the medium insertion (5.5) as the density of nucleon states in momentum space.

Up to second order in spatial gradients (i. e. deviations from homogeneity) the energy density functional relevant for $N = Z$ even-even nuclei reads [65]:

$$\mathcal{E}[\rho,\tau,\mathbf{J}] = \rho\,\bar{E}(k_\mathrm{f}) + \left[\tau - \frac{3}{5}\rho k_\mathrm{f}^2\right]\left[\frac{1}{2M_\mathrm{N}} - \frac{5k_\mathrm{f}^2}{56M_\mathrm{N}^3} + F_\tau(k_\mathrm{f})\right] + (\boldsymbol{\nabla}\rho)^2\,F_\nabla(k_\mathrm{f}) + \boldsymbol{\nabla}\rho\cdot\mathbf{J}\,F_\mathrm{so}(k_\mathrm{f}) + \mathbf{J}^2\,F_J(k_\mathrm{f})\,. \quad (5.6)$$

Here, $\bar{E}(k_\mathrm{f})$ is the energy per particle of isospin symmetric nuclear matter evaluated at the local Fermi momentum $k_\mathrm{f}(\mathbf{r})$. The (small) relativistic correction term $-5k_\mathrm{f}^2/56M_\mathrm{N}^3$ has been included in eq. (5.6) for the following reason: When multiplied with $-3\rho k_\mathrm{f}^2/5$, it cancels together with the foregoing term $1/2M_\mathrm{N}$ the relativistically improved kinetic energy in $\bar{E}(k_\mathrm{f})$ (see eq. (2.3)). The functions $F_\tau(k_\mathrm{f})$, $F_\nabla(k_\mathrm{f})$, $F_\mathrm{so}(k_\mathrm{f})$ and $F_J(k_\mathrm{f})$ arising from NN-interactions encode new dynamical information specific for inhomogeneous many-nucleon systems. In Skyrme parameterizations (see eq. (A.21)), $F_\tau(k_\mathrm{f})$ depends linearly on the (local) density $\rho = 2k_\mathrm{f}^3/3\pi^2$ whereas $F_{\nabla,so,J}(k_\mathrm{f})$ are just constants (by construction). Note that $F_\mathrm{so}(k_\mathrm{f})$ gives the strength of the nuclear spin-orbit coupling while $F_\nabla(k_\mathrm{f})$ is responsible for the formation of the nuclear surface. Variation of the energy density functional $\mathcal{E}[\rho,\tau,\mathbf{J}]$ with respect to single-particle wave functions under the condition that these are normalized to unity leads to self-consistent density dependent Kohn-Sham equations [65].

Returning to the medium insertion in eq. (5.5), one sees that the strength function $F_\tau(k_\mathrm{f})$ emerges via a perturbation relative to the density of states $\theta(k_\mathrm{f} - |\mathbf{p}|)$. As shown in section 3.4, the single-particle potential in nuclear matter can actually be constructed in the same way by introducing a delta-function-like perturbation. Consequently, the strength function $F_\tau(k_\mathrm{f})$ can be directly expressed in terms of the real part $U(p,k_\mathrm{f})$ of the momentum and density dependent single-particle potential as:

$$F_\tau(k_\mathrm{f}) = \frac{35}{4k_\mathrm{f}^7}\int_0^{k_\mathrm{f}} \mathrm{d}p\, p^2(5p^2 - 3k_\mathrm{f}^2)\,U(p,k_\mathrm{f})\,. \quad (5.7)$$

In eq. (5.5) the term $\tau - 3\rho k_\mathrm{f}^2/5$ is accompanied by $-\boldsymbol{\nabla}^2\rho/4$. Performing a partial integration of the energy $\int \mathrm{d}^3r\,\mathcal{E}$ one sees immediately that part of the strength function $F_\nabla(k_\mathrm{f})$ is given by the ρ-derivative of $F_\tau(k_\mathrm{f})/4$. These considerations lead to the following decomposition:

$$F_\nabla(k_\mathrm{f}) = \frac{\pi^2}{8k_\mathrm{f}^2}\,\frac{\partial F_\tau(k_\mathrm{f})}{\partial k_\mathrm{f}} + F_d(k_\mathrm{f})\,, \quad (5.8)$$

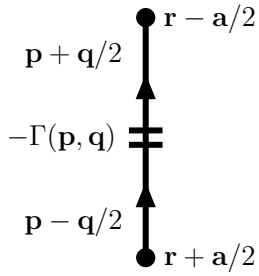

Figure 5.1: The double line symbolizes the medium insertion defined by eq. (5.5).

where $F_d(k_\mathrm{f})$ comprises all those contributions for which the $(\boldsymbol{\nabla}\rho)^2$-factor originates directly from the interactions. An example for this mechanism is described in appendix B.7.2.

As a check on the present formalism (summarized in eq. (5.5)) we rederived the Skyrme energy density functional eq. (A.21) from the matrix elements of the underlying two-body potential eq. (A.15) in a purely diagrammatic framework.

In ref. [66] we have used this formalism to compute the nuclear energy density functional eq. (5.6) from one-pion and iterated one-pion exchange diagrams. The contributing graphs are shown in fig. 3.1. The analytical formulas for the four strength functions $F_\tau(k_\mathrm{f})$, $F_d(k_\mathrm{f})$, $F_\mathrm{so}(k_\mathrm{f})$ and $F_J(k_\mathrm{f})$ are repeated in appendix B.7. We give for each diagram only the final result omitting all technical details related to extensive algebraic manipulations and solving elementary integrals. Some "master integrals" used for the calculation are listed in appendix B.7.4.

The analytical results given in appendix B.7 do not involve any adjustable parameter (since all loop integrals are ultraviolet-convergent). Only well-known physical quantities like the nucleon axial-vector coupling constant $g_\mathrm{A} = 1.3$, the nucleon mass $M_\mathrm{N} = 939\,\mathrm{MeV}$, the pion decay constant $f_\pi = 92.4\,\mathrm{MeV}$, and the (neutral) pion mass $m_\pi = 135\,\mathrm{MeV}$ enter.

Let us end this section with general power counting considerations for the nuclear energy density functional $\mathcal{E}[\rho,\tau,\mathbf{J}]$. Counting the Fermi momentum k_f, the pion mass m_π and a spatial gradient $\boldsymbol{\nabla}$ collectively as small scales one deduces from eqs. (5.2-5.4) that the nucleon density $\rho(\mathbf{r})$, the kinetic energy density $\tau(\mathbf{r})$ and the spin-orbit density $\mathbf{J}(\mathbf{r})$ are quantities of third, fifth and fourth order in small momenta, respectively. With these counting rules the contributions from 1π-exchange to the nuclear energy density functional $\mathcal{E}[\rho,\tau,\mathbf{J}]$ are of sixth order in small momenta while all contributions from iterated 1π-exchange are of seventh order. For consistency, the saturation curve $\bar{E}(k_\mathrm{f})$ appearing in eq. (5.6) must of course be truncated at $\mathcal{O}(k_\mathrm{f}^4)$ (corresponding to the dotted line in fig. 3.3). Concerning NN-interactions induced by pion exchange the nuclear energy density functional presented here is in fact complete up-to-and-including seventh order in small momenta.

5.1.2 Isospin asymmetric case

For an extension to even-even nuclei with $N > Z$ the first obvious step would be to include the density dependent asymmetry energy $\bar{A}(k_\mathrm{f})$ [14,41] (subtracted by its kinetic

energy contribution) in the nuclear energy density functional:

$$\mathcal{E}_{\rm as}[\rho_{\rm p},\rho_{\rm n},\tau_{\rm p},\tau_{\rm n},\mathbf{J}_{\rm p},\mathbf{J}_{\rm n}] \;=\; \mathcal{E}[\rho,\tau,\mathbf{J}]+\mathcal{E}_{\rm Coul}[\rho_{\rm p},\tau_{\rm p},\mathbf{J}_{\rm p}]+\frac{(\rho_{\rm n}-\rho_{\rm p})^2}{\rho} \times\left\{\bar{A}(k_{\rm f})-\frac{k_{\rm f}^2}{6M_{\rm N}}+\frac{k_{\rm f}^4}{12M_{\rm N}^3}-\frac{5\tau k_{\rm f}^2}{56\rho M_{\rm N}^3}\right\}+\ldots\,, \quad (5.9)$$

with $\rho=\rho_p+\rho_n=2k_{\rm f}^3/3\pi^2$, $\tau=\tau_p+\tau_n$ and $\mathbf{J}=\mathbf{J}_p+\mathbf{J}_n$. In an ordering scheme where one counts deviations from homogeneity and deviations from isospin symmetry simultaneously as small, the energy density functional in eq. (5.9) would already be complete. However, such a formal consideration may be too simplistic in view of neutron skins, neutron halos etc. In any case, the density-matrix expansion in eq. (5.1) can be straightforwardly generalized to the isospin asymmetric situation and this way the strength functions of terms like $[\tau_n-\tau_p+k_{\rm f}^2(\rho_p-\rho_n)](\rho_n-\rho_p)$, $(\boldsymbol{\nabla}\rho_n-\boldsymbol{\nabla}\rho_p)^2$, $(\boldsymbol{\nabla}\rho_n-\boldsymbol{\nabla}\rho_p)\cdot(\mathbf{J}_n-\mathbf{J}_p)$ and $(\mathbf{J}_n-\mathbf{J}_p)^2$ in the nuclear energy density functional become also accessible in our diagrammatic framework. The isovector spin-orbit strength functions have been calculated by N. Kaiser [67]. For the Coulomb energy density $\mathcal{E}_{Coul}[\rho_p,\tau_p,\mathbf{J}_p]$ of the protons, see ref. [68].

5.1.3 Results for the strength functions

Returning to the energy density functional $\mathcal{E}[\rho,\tau,\mathbf{J}]$ in eq. (5.6) one observes that the expression in square brackets multiplying the kinetic energy density $\tau(\mathbf{r})$ has the interpretation of a reciprocal density dependent effective nucleon mass:

$$\tilde{M}_{\rm N}^{\star}(\rho)=M_{\rm N}\left[1-\frac{5k_{\rm f}^2}{28M_{\rm N}^2}+2M_{\rm N}\,F_\tau(k_{\rm f})\right]^{-1}. \quad (5.10)$$

We note that this effective nucleon mass $\tilde{M}_{\rm N}^{\star}(\rho)$ is conceptually different from the so-called "Landau" mass which is derived from the slope of the single particle potential $U(p,k_{\rm f})$ at the Fermi surface $p=k_{\rm f}$. Only if the (real) single particle potential has a simple quadratic dependence on the nucleon momentum, $U(p,k_{\rm f})=U_0(k_{\rm f})+U_1(k_{\rm f})\,p^2$, do these two variants of effective nucleon mass agree with each other.

In fig. 5.2 we show the ratio of effective over free nucleon mass, $\tilde{M}_{\rm N}^{\star}(\rho)/M_{\rm N}$, as a function of the nucleon density $\rho=2k_{\rm f}^3/3\pi^2$. One observes a reduced effective nucleon mass $0.89M_{\rm N}<\tilde{M}_{\rm N}^{\star}(\rho)<M_{\rm N}$ for densities $\rho<0.11\,{\rm fm}^{-3}$ and an enhanced effective nucleon mass $\tilde{M}_{\rm N}^{\star}(\rho)>M_{\rm N}$ for higher densities. In the region below the nuclear matter saturation density, $\rho<\rho_0=0.174\,{\rm fm}^{-3}$, relevant for nuclear structure the deviations of the effective nucleon mass $\tilde{M}_{\rm N}^{\star}(\rho)$ from its free space value $M_{\rm N}$ do not exceed $\pm15\%$. Let us give a qualitative explanation for the (unusual) behavior of the curve in fig. 5.2. Consider the iterated 1π-exchange Hartree diagram in fig. 3.1 at sufficiently high densities such that the pion mass m_π can be neglected in comparison with the Fermi momentum $k_{\rm f}$. In this (limiting) case the πN-interaction vertices get canceled by the pion propagators. One is effectively dealing with a zero-range contact interaction in second order which

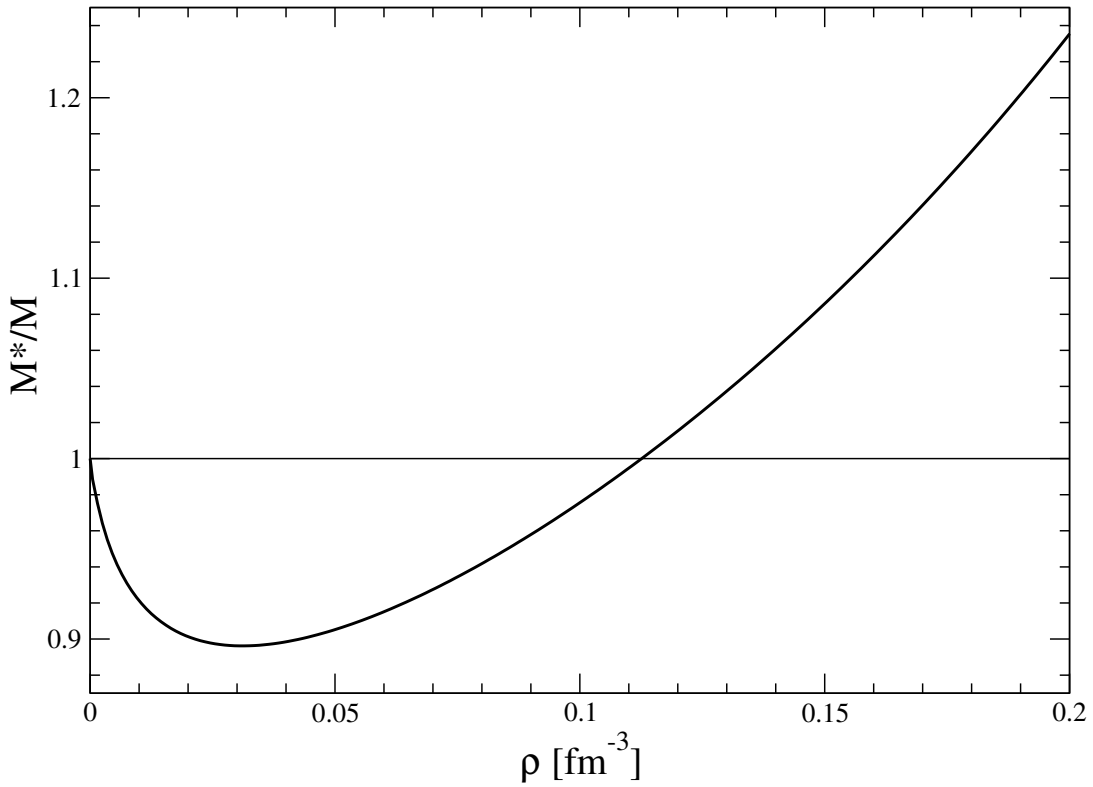

Figure 5.2: The effective nucleon mass $\tilde{M}_{\rm N}^{\star}(\rho)$ divided by the free nucleon mass $M_{\rm N}$ versus the nucleon density ρ.

according to Galitskii's 1958 calculation [43, 58] generates an enhanced in-medium mass. In this sense the curve in fig. 5.2 delineates the two density regimes $k_{\rm f} < \sqrt{3}m_\pi$ and $k_{\rm f} > \sqrt{3}m_\pi$ where the (qualitative) behavior in the latter is ruled by Galitskii's second order result. Interestingly, a recent large scale fit of 1888 nuclide masses by Pearson et al. [69] using a "Hartree-Fock nuclear mass formula" has given an effective nucleon mass of $\tilde{M}_{\rm N}^{\star}(\rho_0) = 1.05 M_{\rm N}$. This value is comparable with our parameter-free result $\tilde{M}_{\rm N}^{\star}(\rho_0) = 1.15 M_{\rm N}$. Most other (nonrelativistic) mean-field calculations [61–64] give however a reduced effective nucleon mass $0.7 M_{\rm N} < \tilde{M}_{\rm N}^{\star}(\rho_0) < M_{\rm N}$. Fit functions for $\tilde{M}_{\rm N}^{\star}(\rho)/M_{\rm N}$ and for the strength functions $F_{\nabla,{\rm so},J}(\rho)$ are given in appendix B.7.5. These can be used for nuclear structure calculations (see section 5.1.4). We recall that at this stage, the framework is still limited to pion-nucleon dynamics. The role of the Δ-isobar as an additional explicit degree of freedom will turn out to be very important in this context (see section 7.4).

Next, we show in fig. 5.3 by the full line the strength function $F_\nabla(k_{\rm f})$ belonging to the $(\boldsymbol{\nabla}\rho)^2$-term in the nuclear energy density functional eq. (5.6) versus the nucleon density ρ. The three horizontal dashed lines represent the constant values $F_\nabla(k_{\rm f}) = [9t_1 - (5 + 4x_2)t_2]/64$ of the Skyrme forces Sly [64], SIII [61] and MSk [69]. In the case of Sly and MSk we have performed averages over the various parameter sets Sly4-7 and MSk1-6. At nuclear matter saturation density $\rho_0 = 0.174\,{\rm fm}^{-3}$ our parameter-free

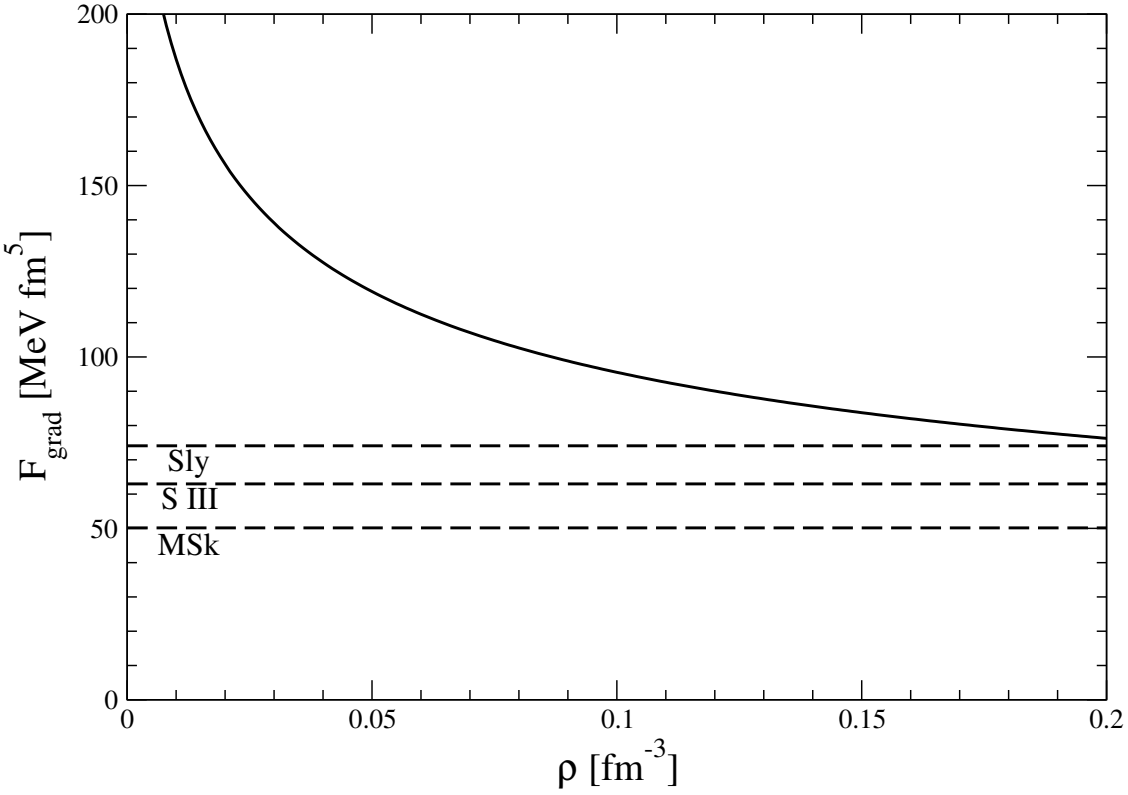

Figure 5.3: The strength function $F_\nabla(k_\mathrm{f})$ related to the $(\boldsymbol{\nabla}\rho)^2$-term in the nuclear energy density functional versus the nucleon density $\rho = 2k_\mathrm{f}^3/3\pi^2$. The three horizontal dashed lines show the constant values $F_\nabla = [9t_1 - (5+4x_2)t_2]/64$ of the Skyrme forces Sly [64], SIII [61] and MSk [69].

prediction $F_\nabla(k_{\mathrm{f},0}) = 80.1\,\mathrm{MeV\,fm}^5$ is comparable to these empirical values. The strong increase of the strength function $F_\nabla(k_\mathrm{f})$ with decreasing density has to do with the presence of a small mass scale, $m_\pi = 135\,\mathrm{MeV}$, and with associated chiral singularities (of the form m_π^{-2} and m_π^{-1}). We will return to this issue again towards the end of this section.

The strength function $F_\nabla(k_\mathrm{f})$ and the equation of state $\bar{E}(k_\mathrm{f})$ are the parts of the energy density functional that mainly determine the nuclear surface energy a_s [70]:

$$a_\mathrm{s} = \left(\frac{36\pi}{\rho_0^2}\right)^{\frac{1}{3}} \int_{-\infty}^{\infty} \mathrm{d}z \left\{\mathcal{E}[\rho(z)] - \bar{E}_0\rho(z)\right\}. \tag{5.11}$$

By inserting for $\rho(z)$ the density profile that minimizes a_s and using the approximation $\tau = 3\rho k_\mathrm{f}^2/5$, one gets

$$a_\mathrm{s} = 2\left(\frac{36\pi}{\rho_0^2}\right)^{\frac{1}{3}} \int_0^{\rho_0} \mathrm{d}\rho \,\sqrt{\rho\, F_\nabla(\rho)\left[\bar{E}(\rho) - \bar{E}_0\right]}\,, \tag{5.12}$$

which evaluates to $a_\mathrm{s} = 25.2\,\mathrm{MeV}$ for our result from chiral pion exchange. This value is about 20% larger than semi-empirical determinations of the surface energy, such as

$a_s = 20.7\,\mathrm{MeV}$ of ref. [71], $a_s = 18.2\,\mathrm{MeV}$ of ref. [70], or $a_s = 18.56\,\mathrm{MeV}$ used in ref. [23] (a_2 in eq. (2.1)). The reason for our high value $a_s = 25.2\,\mathrm{MeV}$ is of course the strong increase of $F_\nabla(k_f)$ at low densities. While for constant $F_\nabla(k_f)$, the integrand in eq. (5.12) peaks around $\rho_0/3$, it gives sizable contributions also for lower densities.

As we will see in sections 5.1.4 and 7.4, the strong rise of $F_\nabla(k_f)$ at low densities also prevents reproducing the correct binding energy in ^{40}Ca. Therefore, this strong increase is probably unrealistic and could hint at limitations of the density-matrix expansion of Negele et al. [60]. Recently, there have been some indications that this expansion might get unreliable at low densities [72] and it is also known that a derivation of the parameters of the expansion from given Brueckner-Hartree-Fock calculations gives only a fair reproduction of nuclear properties but fails at a quantitative level [7]. Therefore one should probably not trust the curve in fig. 5.3 below $\rho = 0.05\,\mathrm{fm}^{-3}$.

The full line in fig. 5.4 shows the result of iterated 1π-exchange for the strength function $F_{so}(k_f)$ related to the spin-orbit coupling term in the nuclear energy density functional. For comparison we have drawn the constant values $F_{so}(k_f) = 3W_0/4$ of the three Skyrme forces Sly [64], SIII [61] and MSk [69] (horizontal dashed lines). One observes that the strength of the nuclear spin-orbit interaction as generated by iterated 1π-exchange at ρ_0 is about half as large as the corresponding empirical value, however, with the wrong (negative) sign.

This "negative" result is dominated by the contribution of the iterated 1π-exchange Hartree diagram with two medium insertions (see eq. (B.116)). For example, one obtains numerically from this diagram at saturation density $\rho_0 = 0.174\,\mathrm{fm}^{-3}$ (where $u = k_{f,0}/m_\pi = 2.0$) the negative contribution $F_{so}^{(H,2)}(k_{f,0}) = -83.7\,\mathrm{MeV\,fm}^5$. The other diagrams with lower spin- and isospin weight factors reduce this number to approximately half its magnitude. The "negative" result for $F_{so}(k_f)$ is to some extent already indicated by the calculation of the momentum and density dependent nuclear spin-orbit strength[1] $U_{ls}(p, k_f)$ in ref. [36]. Going back to the medium insertion in eq. (5.5) one learns that only the values of $U_{ls}(p, k_f)$ near the Fermi surface $p = k_f$ will contribute to $F_{so}(k_f)$. As a matter of fact the curves in fig. 7 of ref. [36] drop from positive to negative values when p runs from zero to $k_{f,0} = 272.7\,\mathrm{MeV}$. Actually, for the contributions to $F_{so}(k_f)$ from diagrams with two medium insertions (see eqs. (B.116,B.119)) the following relationship holds:

$$F_{so}(k_f) = \frac{\pi^2}{4k_f^2}\left[\frac{\partial U_{ls}(p,k_f)}{\partial k_f} + \frac{k_f}{3}\,\frac{\partial^2 U_{ls}(p,k_f)}{\partial p\,\partial k_f}\right]_{p=k_f}, \tag{5.13}$$

to be applied to the expressions $U_{ls}^{(a,e)}(p, k_f)$ in eqs. (9,17) of ref. [36]. Our finding that the (leading order) long-range pion-induced contribution to the spin-orbit coupling $F_{so}(k_f)$ is sizable and of the wrong sign poses a problem for the microscopic understanding of the phenomenological nuclear spin-orbit interaction. There must obviously be mechanisms beyond chiral two-pion exchange that are responsible for the extraordinarily large and "positive" nuclear spin-orbit force. Possible sources are the large scalar and vector back-

[1] This quantity is defined via the spin dependent interaction energy $\Sigma_{spin} = \frac{i}{2}\boldsymbol{\sigma}\cdot(\mathbf{q}\times\mathbf{p})\,U_{ls}(p, k_f)$ of a nucleon scattering off weakly inhomogeneous isospin-symmetric nuclear matter from initial momentum $\mathbf{p} - \mathbf{q}/2$ to final momentum $\mathbf{p} + \mathbf{q}/2$.

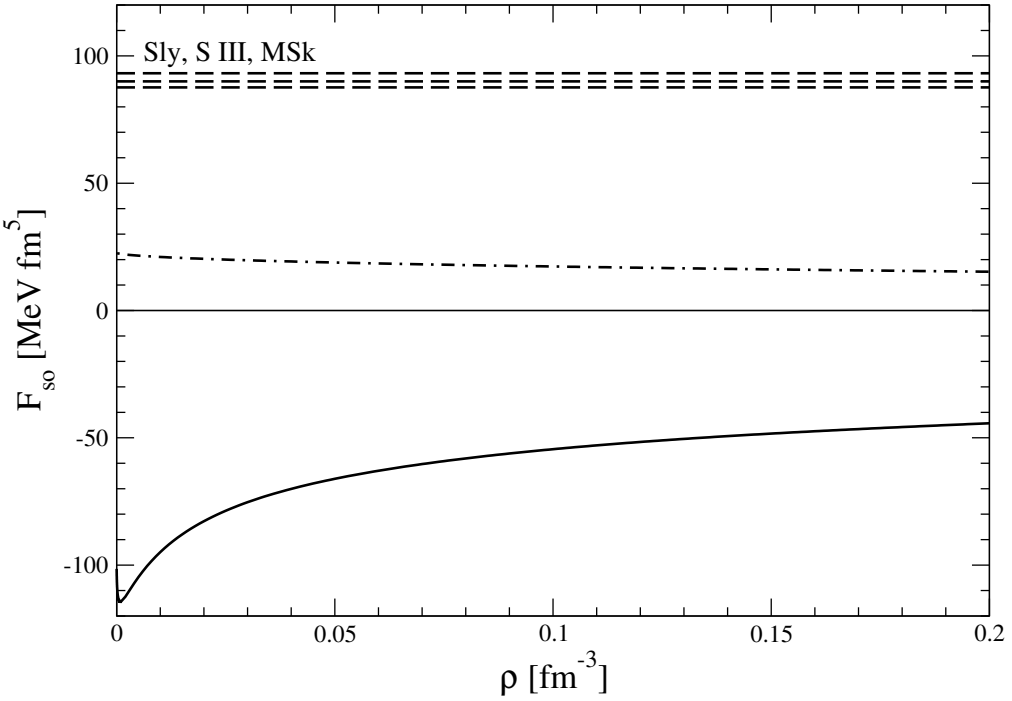

Figure 5.4: The strength function $F_{\rm so}(k_{\rm f})$ related to the spin-orbit coupling term in the nuclear energy density functional versus the nucleon density $\rho = 2k_{\rm f}^3/3\pi^2$. The three horizontal dashed lines show the constant values $F_{\rm so}(k_{\rm f}) = 3W_0/4$ of the Skyrme forces Sly [64], SIII [61] and MSk [69]. The dashed-dotted line shows the contribution from irreducible 2π-exchange written in eq. (5.14) for a cut-off $\Lambda = 0.65\,\mathrm{GeV}$.

ground fields of the QCD ground state in the presence of a nuclear medium (see section 2.2.3) not being included in our nonrelativistic calculation. According to relativistic phenomenology, the difference of these mean fields gives rise to a large spin-orbit force [9]. In contrast, the contributions from iterated 1π-exchange to $F_{\rm so}(k_{\rm f})$ are *not* a relativistic effect; they are proportional to the nucleon mass $M_{\rm N}$.

It is well-known that irreducible two-pion exchange generates (via relativistic $1/M_{\rm N}$-corrections) spin-orbit amplitudes in the T-matrix of elastic nucleon-nucleon scattering [73]. Their effect on the nuclear spin-orbit interaction has been calculated in ref. [74]. Inserting the expression $U_{ls}^{(2\pi)}(p, k_{\rm f})$ in eq. (18) of ref. [74] into the "master formula" eq. (5.13) one derives the following contribution from irreducible 2π-exchange to the spin-orbit strength function:

$$F_{\rm so}(k_{\rm f}) = \frac{g_{\rm A}^2}{\pi M_{\rm N}(4f_\pi)^4}\bigg\{(16+19g_{\rm A}^2)\frac{\Lambda}{2\pi} + \frac{m_\pi^3}{6k_{\rm f}^2}(4-3g_{\rm A}^2)\ln\frac{k_{\rm f}^2+m_\pi^2}{m_\pi^2} - \frac{m_\pi}{3}(8+27g_{\rm A}^2) + \frac{2}{3k_{\rm f}}\Big[3m_\pi^2(g_{\rm A}^2-2) - 4k_{\rm f}^2\Big]\arctan\frac{k_{\rm f}}{m_\pi}\bigg\}. \quad (5.14)$$

Here, Λ is the momentum cut-off which has been used to regularize the linear divergences

of the irreducible 2π-exchange (triangle and box) diagrams. The dashed-dotted line in fig. 5.4 shows the relatively small contribution of irreducible 2π-exchange to the spin-orbit strength $F_{\rm so}(k_{\rm f})$ for a cut-off scale of $\Lambda = 0.65\,\mathrm{GeV}$ (as appropriate for $\mathcal{O}(k_{\rm f}^5)$, see section 3.2). We note that without the zero-range Λ-dependent term in eq. (5.14) the dashed-dotted curve would be shifted downward by $45.7\,\mathrm{MeV\,fm}^5$ to negative values. From the point of view of the expansion in small momenta the contribution to $F_{\rm so}(k_{\rm f})$ in eq. (5.14) is a higher order correction.

In this context we mention also the relativistic $1/M_{\rm N}^2$-correction to $F_{\rm so}(k_{\rm f})$ from the 1π-exchange Fock diagram. Inserting the expression $U_{ls}^{(1\pi)}(p, k_{\rm f})$ in eq. (6) of ref. [36] into the "master formula" eq. (5.13) leads to the simple result: $F_{\rm so}(k_{\rm f}) = g_{\rm A}^2[\ln(1+4u^2) - 4u^2]/(16 M_{\rm N} f_\pi u)^2$, with $u = k_{\rm f}/m_\pi$. As expected, this contribution is negligibly small: $F_{\rm so}(2m_\pi) = -0.86\,\mathrm{MeV\,fm}^5$.

Finally, we show in fig. 5.5 the strength function $F_J(k_{\rm f})$ accompanying the squared spin-orbit density $\mathbf{J}^2$ in the nuclear energy density functional versus the nucleon density $\rho = 2k_{\rm f}^3/3\pi^2$. For comparison we have drawn the constant values $F_J(k_{\rm f}) = [t_1(1-2x_1) - t_2(1+2x_2)]/32$ of the three Skyrme forces MSk [69], SIII [61] and Sly [64] (dashed lines).

One observes that our prediction for $F_J(k_{\rm f})$ is considerably larger. Again, there is a strong rise of the strength function $F_J(k_{\rm f})$ as one goes down to very low nucleon densities $\rho < \rho_0/10$. This time the dominant contribution comes from the iterated 1π-exchange Hartree diagram with three medium insertions (see eq. (B.124)), which gives numerically $F_J^{(\mathrm{H},3)}(2m_\pi) = 52.5\,\mathrm{MeV\,fm}^5$ at saturation density. It should also be noted that the $\mathbf{J}^2$-term in the energy density functional is often neglected in nuclear structure calculations.

The $\mathbf{J}^2$-term in the energy density functional gives rise to an additional spin-orbit single-particle field of the form $2F_J(k_{\rm f})\mathbf{J}$. According to our calculation this additional spin-orbit field is rather large and strongly density dependent. However, it turns out that the effects from the additional spin-orbit field $2F_J(k_{\rm f})\mathbf{J}$ are still too small to compensate the wrong sign of the "normal" one $F_{\rm so}(k_{\rm f})\boldsymbol{\nabla}\rho$ (see section 5.1.4).

The full curves in figs. 5.3 and 5.5 show a strong increase as the density ρ tends to zero. Although not visible, each curve approaches a finite value at $\rho = 0$. One can analytically derive the following low density limits:

$$\lim_{\rho\to 0} \rho^{-1} F_\tau(k_{\rm f}) = \frac{3g_{\rm A}^2}{(4m_\pi f_\pi)^2}\left[1 - \frac{g_{\rm A}^2 M_{\rm N} m_\pi}{128\pi f_\pi^2}\right] = 571.3\,\mathrm{MeV\,fm}^5\,, \tag{5.15}$$

$$F_\nabla(0) = \frac{g_{\rm A}^2}{(8m_\pi f_\pi)^2}\left[3 + \frac{59 g_{\rm A}^2 M_{\rm N} m_\pi}{128\pi f_\pi^2}\right] = 339.2\,\mathrm{MeV\,fm}^5\,, \tag{5.16}$$

$$F_J(0) = \frac{3g_{\rm A}^2}{(4m_\pi f_\pi)^2}\left[1 - \frac{3 g_{\rm A}^2 M_{\rm N} m_\pi}{256\pi f_\pi^2}\right] = 552.2\,\mathrm{MeV\,fm}^5\,, \tag{5.17}$$

$$F_{\rm so}(0) = -\frac{g_{\rm A}^4 M_{\rm N}}{\pi m_\pi (4f_\pi)^4} = -101.4\,\mathrm{MeV\,fm}^5\,, \tag{5.18}$$

to which only the diagrams with two medium insertions contribute. The large numbers in eqs. (5.15-5.18) arise from negative powers of the pion mass m_π (so-called chiral singularities). The most singular m_π^{-2}-terms can be traced back to the 1π-exchange Fock

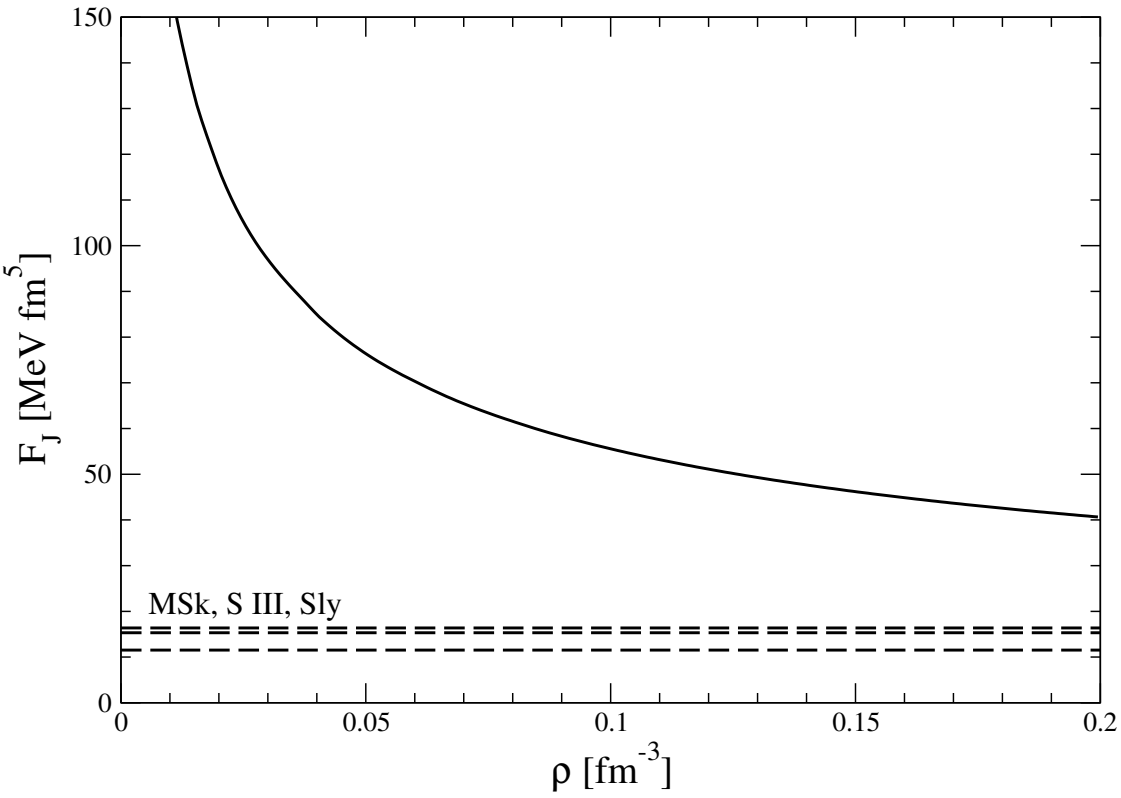

Figure 5.5: The strength function $F_J(k_\mathrm{f})$ accompanying the squared spin-orbit density $\mathbf{J}^2$ in the nuclear energy density functional versus the nucleon density $\rho = 2k_\mathrm{f}^3/3\pi^2$. The three horizontal dashed lines show the constant values $F_J(k_\mathrm{f}) = [t_1(1-2x_1) - t_2(1+2x_2)]/32$ of the Skyrme forces MSk [69], SIII [61] and Sly [64].

diagram. At extremely low densities $k_\mathrm{f} \ll m_\pi/2$ the remnant of the pion-propagator $[m_\pi^2 + (\mathbf{p}_1 - \mathbf{p}_2)^2]^{-1}$ becomes a proportionality factor m_π^{-2}. Moreover, with given fixed powers of f_π^{-1} and M_N in the prefactors of the 1π-exchange and the iterated 1π-exchange diagrams, negative powers of the pion mass m_π are simply necessary in order to get the correct mass dimension of $F_{\nabla,so,J}(0)$ in eqs. (5.16-5.18). The chiral singularities in eqs. (5.15-5.18) are of same physical origin as the diverging values of the isovector magnetic radius and electromagnetic polarizabilities of the nucleon [75] in the chiral limit $m_\pi \to 0$.

In this context it is important to keep in mind that if pionic degrees of freedom are treated explicitly in the nuclear matter problem the low density limit is realized only at extremely low densities, $k_\mathrm{f} \ll m_\pi/2$. On the other hand, the opposite limit where the pion mass m_π can be neglected compared to the Fermi momentum k_f is usually already applicable at the moderate densities relevant for conventional nuclear physics. This is exemplified here by the approximate density dependence $F_{\nabla,so,J}(k_\mathrm{f}) \sim k_\mathrm{f}^{-1}$. Such a $\rho^{-1/3}$-behavior becomes exact in the chiral limit $m_\pi = 0$ as can be deduced by simple mass dimension counting of the dominant iterated 1π-exchange diagrams (the basic argument

is that $M_N/f_\pi^4 k_f$ has the correct unit of $\mathrm{MeV\,fm}^5$).

5.1.4 Finite nuclei

Using the energy density functional with its novel density dependence derived in the previous section, we now proceed to calculate some ground state properties of actual nuclei. For this purpose, we have adapted a publicly available spherical Skyrme-Hartree-Fock Fortran code by P.-G. Reinhard which is both fast and well documented [76].

Skyrme-Hartree-Fock calculations of the nuclear ground state start with the energy density functional,

$$\mathcal{E} = \mathcal{E}_{\mathrm{Skyrme}/\pi\mathrm{N}} + \mathcal{E}_{\mathrm{Coulomb}} + \mathcal{E}_{\mathrm{pair}} - \mathcal{E}_{\mathrm{cm}}\,. \tag{5.19}$$

Of course, in our case the Skyrme energy functional $\mathcal{E}_{\mathrm{Skyrme}}$ from eq. (A.21) will be replaced by the one obtained from chiral pion-nucleon dynamics, eq. (5.6). In addition one has to add the Coulomb energy, $\mathcal{E}_{\mathrm{Coulomb}}$, the contribution of some schematic pairing interaction $\mathcal{E}_{\mathrm{pair}}$, and a correction for the spurious center-of-mass motion of the mean field $\mathcal{E}_{\mathrm{cm}}$.

Since the results for $F_\nabla(k_f)$ and $F_{\mathrm{so}}(k_f)$ shown in figs. 5.3 and 5.4 seem problematic when compared to the values used in Skyrme calculations, we add to each strength functions a constant (C_∇ and C_{so}) representing short-range dynamics of unspecified origin.

We now briefly mention the approximations used in the program. For a detailed description of the methods, see ref. [76]. The Coulomb exchange term is treated in the so-called Slater approximation. In the direct part of the Coulomb interaction, the finite size of the protons is taken into account. A BCS pairing with a constant pairing force is used. The center-of-mass correction is only computed after variation and does not contribute to the Hartree-Fock equations. The difference between proton and neutron mass is neglected. For the solution of the Hartree-Fock equations, an inverse gradient step method is used.

Because of the explicit density dependence in all terms of the density functional eq. (5.6), an optimization for the calculation of the energy used in the program had to be removed. Instead of "half single-particle energies plus half kinetic energy plus rearrangement energy", we calculate the energy directly from the energy functional eq. (5.6).

Here we present only the results for the doubly magic $N = Z$ even-even nucleus ^{40}Ca. The results for ^{16}O are quite similar. From experiment, one knows the total energy per nucleon and the charge radius:

$$^{40}\mathrm{Ca}: \qquad E/A^{\mathrm{exp}} = -8.55\,\mathrm{MeV}\,, \qquad r_{\mathrm{C}}^{\mathrm{exp}} = 3.49\,\mathrm{fm}\,. \tag{5.20}$$

For the pure energy density functional as derived from chiral pion nucleon dynamics (i. e. with $C_\nabla = C_{\mathrm{so}} = 0$), we obtain unrealistic values of $E/A = -4.95\,\mathrm{MeV}$ and $r_{\mathrm{C}} = 3.74\,\mathrm{fm}$. Also, the ordering of the single-particle energy levels is $1s_{1/2}$, $1p_{1/2}$, $1p_{3/2}$, $1d_{3/2}$, $1d_{5/2}$, $2s_{1/2}$, instead of the empirical $1s_{1/2}$, $1p_{3/2}$, $1p_{1/2}$, $1d_{5/2}$, $2s_{1/2}$, $1d_{3/2}$. Of course, considering the wrong sign of the spin-orbit strength function $F_{\mathrm{so}}(k_f)$, this was to be expected. The strength function $F_J(k_f)$ has a much smaller influence on the nucleus

than $F_{\rm so}(k_{\rm f})$. Therefore, even the comparatively large value of $F_J(k_{\rm f})$ does not cancel the effects from the negative $F_{\rm so}(k_{\rm f})$.

Because of the too large surface energy coefficient $a_{\rm s} = 25.2\,\text{MeV}$ obtained in section 5.1.3, the radius of ^{40}Ca is too large. Also, the surface contribution to the total energy is much too large resulting in a too small total binding energy.

The shell ordering can be fixed by adjusting the constant $C_{\rm so}$ which subsumes the effects of all short-range dynamics not explicitly included in our approach. A value of $C_{\rm so} = 134\,\text{MeV fm}^5$, which changes the sign of $F_{\rm so}(k_{\rm f})$, leads to the correct empirical spin-orbit splitting in the 1d orbital of $\sim 6\,\text{MeV}$. Clearly, the nuclear spin-orbit strength cannot be generated by (long-range) pion exchange dynamics. Rather, its successful description by relativistic phenomenology leads to the picture that it is mainly caused by the large scalar and vector mean fields experienced by the nucleus in the QCD vacuum. We will return to this idea in the next section.

In a similar way, the constant C_∇ contains additional short-range contributions to $F_\nabla(k_{\rm f})$. A value of $C_\nabla = -53.2\,\text{MeV fm}^5$ gives the correct Coulomb radius for ^{40}Ca. This also reduces the surface energy of the nucleus, leading to $E/A = -6.71\,\text{MeV}$ and $r_{\rm C} = 3.49\,\text{fm}$. However, this value of the binding energy is still more than 20% from the experimental value.

This result is of course not satisfactory. Unfortunately, the inclusion of diagrams with $\Delta(1232)$-excitations gives only a small improvement (see section 7.4.2). Therefore, the main problem is presumably the strong density dependence of $F_\nabla(k_{\rm f})$. However, one should keep in mind that this density-matrix expansion is an expansion in small density gradients $\boldsymbol{\nabla}\rho$. Thus it is strictly speaking only valid for weakly inhomogeneous nuclear matter. Since $\boldsymbol{\nabla}\rho/\rho$ is not that small at the surface of finite nuclei, one should not be surprised that problems ensue.

5.2 A point coupling model for finite nuclei

As we have seen, the approach to inhomogeneous nuclear matter described in the previous section has problems at low density. Also, the correct spin-orbit strength seems to be a relativistic or short-range effect that is not included in our framework but has to be modeled by adjusting an additional parameter. Therefore it is a logical step to try different approaches to finite nuclei while still taking into account the fact that the pion mass and the Fermi momentum are of comparable magnitudes.

Finelli et al. have done this in refs. [21, 22]. Their relativistic point-coupling model includes chiral pionic fluctuations which, in combination with Pauli blocking effects, are mainly responsible for nuclear binding and saturation as we have described in chapter 3. However, these pionic fluctuations are treated on top of a nuclear ground state characterized by large Lorentz scalar and vector fields of approximately equal magnitude but opposite sign. These fields are connected to QCD by their origin in the leading-order changes of the chiral condensate and of the quark density in the nuclear medium.

A quantitative connection of the mean fields to the quark condensates can be derived from QCD sum rules [30]. Taking into account only the leading linear term of the

density dependence of the chiral condensate (3.21), one gets for the ratio of the nucleon self-energies generated by scalar and vector mean fields:

$$\frac{\Sigma_S^{(0)}}{\Sigma_V^{(0)}} = -\frac{\sigma_{\pi N}}{4(m_u + m_d)} \frac{\rho_s}{\rho} , \tag{5.21}$$

where $\sigma_{\pi N} \simeq 50\,\mathrm{MeV}$ is the pion-nucleon sigma term and the quark masses are taken as $m_u + m_d \simeq 12\,\mathrm{MeV}$ (at a renormalization scale of about 1 GeV). At nuclear saturation density, the scalar and the nucleon densities are approximately equal, $\rho_s \simeq \rho$, and the ratio eq. (5.21) is compatible with -1 (though with an uncertainty of about 20%, as pointed out in ref. [22]).

The model of Finelli et al. takes into account the πN-dynamics by adjusting density dependent coupling constants to the self-energies calculated from chiral pion exchange. After this, the remaining free parameters are the momentum cut-off Λ introduced in chapter 3, two couplings $G_{S,V}^{(0)}$ encoding the background fields $\Sigma_{S,V}^{(0)}$, and an additional small parameter subsuming higher order effects proportional to k_f^6. These free parameters are then fitted to the empirical properties of nuclear matter. Remarkably, the resulting values for the couplings $G_{S,V}^{(0)}$ deviate from relation (5.21) by less than 10%, thus fulfilling the QCD sum rule expectations. For finite nuclei, Finelli et al. include an additional parameter, the strength of an isoscalar-scalar derivative coupling that does not contribute in (translational invariant) infinite nuclear matter. This parameter is then adjusted to the ground state properties of ^{16}O and ^{40}Ca. After this fitting procedure, the model of ref. [22] reproduces the ground state properties of many light and medium-heavy even-even nuclei to an accuracy of less than a few per cent.

Interestingly, even with contributions only from chiral pion exchange, Finelli et al. can already approximately reproduce most ground state properties of nuclei except for the spin-orbit splittings. The spin-orbit partners are however nearly degenerate in this case. This fact again emphasizes that the spin-orbit potential is mainly due to the difference between strong scalar and vector background fields which is large because of the different signs of these fields.

Chapter 6

Dealing with the short range NN-terms

In the previous chapters, we have seen that chiral two-pion exchange restricted to nucleon intermediate states (basically the second-order spin-spin and tensor force plus Pauli blocking effects), together with a single contact term representing short-distance dynamics, is already surprisingly successful in binding and saturating nuclear matter and reproducing the compression modulus. We have also seen that while the prediction for the asymmetry energy at saturation density $\bar{A}(k_{\mathrm{f},0}) = 33.8\,\mathrm{MeV}$ is in good agreement with its empirical value, one finds a downward bending of $\bar{A}(k_{\mathrm{f}})$ at densities $\rho > 0.2\,\mathrm{fm}^{-3}$ (see fig. 3.6). Such a behavior of the asymmetry energy $\bar{A}(k_{\mathrm{f}})$ is presumably not realistic. The energy per particle of pure neutron matter $\bar{E}_{\mathrm{n}}(k_{\mathrm{n}})$ as a function of the neutron density shows a similar downward bending behavior (see fig. 3.7) and at lower neutron densities, there is also some deviation from realistic neutron matter calculations. The mere fact that neutron matter comes out to be unbound with no further adjusted parameter is however nontrivial.

The most serious problem we have found in our approach, up to this point, concerns the single-particle properties, represented by the complex-valued momentum and density dependent nucleon self energy $U(p, k_{\mathrm{f}}) + i\,W(p, k_{\mathrm{f}})$. On the one hand, the resulting potential depth $U(0, k_{\mathrm{f},0}) = -53.2\,\mathrm{MeV}$ is in good agreement with that of the empirical nuclear shell [39] or optical model [77]. However, the momentum dependence of the real single-particle potential $U(p, k_{\mathrm{f},0})$ with its up- and downward bending (see fig. 3.4) turns out to be too strong. As a consequence, the nominal value of the effective nucleon mass at the Fermi surface $p = k_{\mathrm{f},0}$ would be much too high: $M_{\mathrm{N}}^{\star}(k_{\mathrm{f},0}) \simeq 3.5 M_{\mathrm{N}}$. However, the single-particle properties around the Fermi surface are decisive for the spectrum of thermal excitations and therefore they crucially influence the low temperature behavior of isospin-symmetric nuclear matter. The rather high critical temperature $T_c \simeq 25.5\,\mathrm{MeV}$ for the liquid-gas phase transition obtained in chapter 4 is a visible manifestation of this intimate relationship.

Consequently, there is need to improve our approach. As mentioned in section 3.1, one obvious way is the inclusion of diagrams involving virtual $\Delta(1232)$-excitations. We follow this strategy in the next chapter and introduce explicit $\Delta(1232)$-degrees of freedom into our framework. Before proceeding in this direction, we want to briefly investigate the role of short-range NN-terms and their influence on the nuclear matter results.

In the previous chapters, we have used a 3-momentum cut-off Λ to regularize the divergent parts of iterated 1π-exchange and irreducible 2π-exchange. The resulting terms

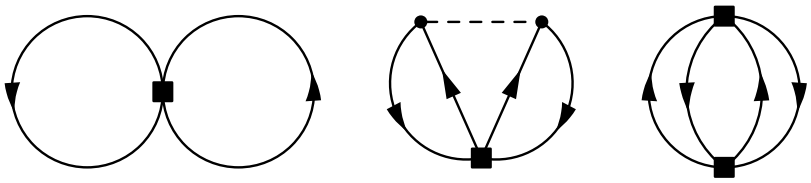

Figure 6.1: Additional in-medium diagrams generated by the NN-contact interaction. The filled square vertex symbolizes this zero-range NN-contact interaction.

proportional to powers of the cut-off Λ are understood to subsume all short-range physics that is not resolved at the relatively low momenta relevant in nuclear matter of moderate densities. In fact, since these terms are proportional to the nucleon density, they are equivalent to the contribution of a momentum independent isoscalar-scalar NN-contact interaction (the first diagram in fig. 6.1).

However, there are several aspects of this approach which should be investigated further. Firstly, by using the same cut-off momentum for pure neutron matter as for isospin symmetric nuclear matter, one assumes that the isospin behavior of all unresolved short-range dynamics is correctly described by the isospin structure of chiral one- and two-pion exchange. This simplifying assumption is not realistic and one should in principle allow for different NN-contact interactions (or equivalently different cut-off momenta) in the different isospin channels. Secondly, the introduction of an explicit NN-contact interaction leads to additional contributions when iterating the contact interaction with pion exchange or with itself (the second and third diagrams in fig. 6.1). When treating the short-range dynamics by means of a cut-off, such terms do not appear. Finally, momentum dependent NN-contact terms contribute already at order $\mathcal{O}(k_{\rm f}^5)$. While, due to the higher order in small momenta, one expects these contributions to be smaller than those from momentum independent contact terms, they should be included in a complete $\mathcal{O}(k_{\rm f}^5)$ calculation. We will take the effects of such contributions into account in chapter 7 and focus now on the other two aspects mentioned.

In ref. [22], Finelli et al. have compared the $k_{\rm f}$-dependence of the self energies $\Sigma_{S,V}(\rho)$ of their point-coupling model, based on the chiral perturbation theory calculation described in chapter 3, with that of the self energies obtained in full Dirac-Brueckner calculations using the realistic Bonn A NN-potential [78]. After slightly readjusting the background field parameters (controlling the "trivial" linear density dependence in the energy per particle) to account for the somewhat higher saturation density $\rho_0 = 0.185\,\mathrm{fm}^{-3}$ of ref. [78], they have found that the difference in the $k_{\rm f}$-dependence is less than 10% over the entire range of densities from $0.5\rho_0$ to $2.5\rho_0$ (see fig. 6.2).

Both the compared approaches treat pion exchange explicitly, including the Pauli blocking effects on iterated one pion exchange which create the nontrivial $k_{\rm f}$-dependence in the self energies (beyond order $k_{\rm f}^3$). On the other hand, the iteration of short-distance interactions to all orders in the Brueckner ladder (involving momenta much larger than $k_{\rm f}$) generates similar self energy pieces (proportional to the density ρ) as a contact interaction described by a single high-momentum cut-off scale Λ. The successful comparison between the perturbative chiral dynamics approach and the nonperturbative Brueckner

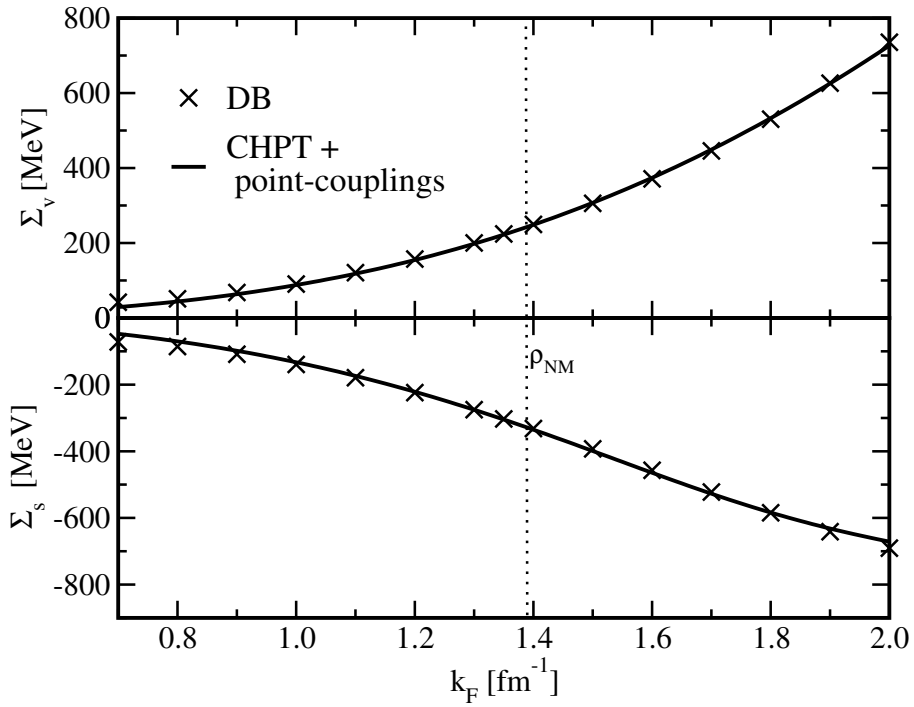

Figure 6.2: Comparison of the $k_{\rm f}$-dependence of the isoscalar vector and scalar self energies resulting from a Dirac-Brueckner G-matrix calculation (crosses: DB [78]), with the self energies generated from in-medium chiral perturbation theory (solid line: CHPT + point-couplings up to 3-loop order in the energy density). This plot is taken from ref. [22].

calculation implies that this contact interaction already represents the full short-range T-matrix information and must *not* be iterated further.

Nevertheless, there have been calculations [13, 41, 79] which iterate the contact interaction or parts of it with itself and with pion exchange. We will briefly look at the results obtained in these approaches. In their $\mathcal{O}(k_{\rm f}^4)$ calculation, Lutz et al. [13] have, in addition to chiral pion exchange, explicitly introduced two zero-range NN-contact interactions (acting in ${}^3S_1$ and ${}^1S_0$ NN-states) proportional to the dimensionless parameters $g_0 + g_{\rm A}^2/4$ and $g_1 + g_{\rm A}^2/4$ (see eq. (4) in ref. [13]). The components proportional to $g_{\rm A}^2/4$ cancel (order by order) the zero-range contribution generated by one-pion exchange. The other components proportional to g_0 and g_1 are understood to subsume all nonperturbative short-range NN-dynamics relevant at densities around nuclear matter saturation density ρ_0. Because of the nonperturbative dynamics contained in the parameters $g_{0,1}$, Lutz et al. do not iterate these parts with themselves. However, the $g_{0,1}$ and $g_A^2/4$ terms are iterated with pion exchange and the $g_{\rm A}^2/4$ parts are also iterated with itself.

While in ref. [13] Lutz et al. obtain an equation of state with realistic saturation and compressibility, we have shown in ref. [41] that the asymmetry energy and the neutron matter equation of state in their approach suffer from the same deficiencies as the ones shown in chapter 3, namely a downward bending at higher densities. The most serious

problem are however the unrealistic single-particle properties obtained in this scheme. The potential depth of $U(0, k_{\rm f,0}) = -20\,\mathrm{MeV}$ is by far too weakly attractive while on the other hand the imaginary single-particle potential $W(0, k_{\rm f,0}) = 51\,\mathrm{MeV}$ is too large. Most importantly, the total single-particle energy $T_{\rm kin}(p)+U(p, k_{\rm f,0})$ does not rise monotonically with the nucleon momentum p, thus implying a negative effective nucleon mass at the Fermi surface $p = k_{\rm f,0}$ (see fig. 3 in ref. [41]). In such an abnormal situation there exist occupied nucleon-states in the Fermi sea with total energy higher than the Fermi energy, indicating an instability of the system. As a matter of fact the overly strong momentum dependence of the nuclear mean-field $U(p, k_{\rm f})$ in the scheme of Lutz et al. (leading to $\partial U/\partial p < -p/M$) originates from those diagrams in which the strong and attractive NN-contact interaction (proportional to $g_0 + g_1 + g_{\rm A}^2/2$) is further iterated. Of course, such unrealistic single-particle properties also ruin the finite temperature behavior. This becomes visible in a much too high critical temperature of the liquid-gas phase transition of $T_c \gtrsim 40\,\mathrm{MeV}$.

We have also studied an extended version of the Lutz approach in ref. [79]. There, pion exchange is complemented by two zero-range NN-contact interactions thus exhausting all possible terms up-to-and-including $\mathcal{O}(k_{\rm f}^4)$. Alternatively, the interacting part of the energy per particle can be understood (within this approximation to order $\mathcal{O}(k_{\rm f}^4)$) as to result from the Hartree and Fock contributions of a nucleon-nucleon T-matrix of the form

$$\mathcal{T}_{NN} = \frac{g_{\rm A}^2}{4f_\pi^2}\left[\frac{\boldsymbol{\sigma}_1\cdot\mathbf{q}\;\boldsymbol{\sigma}_2\cdot\mathbf{q}}{m_\pi^2+\mathbf{q}^2}\,\boldsymbol{\tau}_1\cdot\boldsymbol{\tau}_2 + \frac{\gamma_0+3\gamma_1}{2} + \frac{\gamma_1-\gamma_0}{2}\,\boldsymbol{\tau}_1\cdot\boldsymbol{\tau}_2\right], \tag{6.1}$$

which is evaluated in first and second order perturbation theory (i. e. it is also iterated once with itself). The two coefficients γ_0 and γ_1 parameterize the strength of the contact interaction in NN-states with total isospin $I = 0, 1$. The linearly divergent loop-integrals resulting from this iteration are regularized by a momentum cut-off $\Lambda_{0,1}$ which is allowed to depend on the total isospin $I = 0, 1$ of the two-nucleon system thus resulting in total in four adjustable parameters.

The finding of ref. [79] is that within such a complete fourth order calculation there is no optimal set of the four short-range parameters with which one could reproduce simultaneously and accurately all semi-empirical properties of nuclear matter. The conditions for a good neutron matter equation of state and an improved strength function $F_\nabla(k_{\rm f})$ in the energy density functional (5.6) on the one hand and equally good single-particle properties (and consequently a realistic finite temperature behavior) on the other hand are in fact mutually exclusive in that approach.

The results of refs. [13, 41, 79] show that allowing an isospin dependence of the short-range interaction does not significantly improve the detailed description of nuclear and neutron matter. It seems that the isospin structure dictated by chiral one- and two-pion exchange gives already a surprisingly good description of the isospin dependence of the short-range dynamics. Furthermore, we see that iterating the NN-contact interaction gives no improvement either. Therefore we stick to the conclusion that this iteration should *not* be done, as indicated by the comparison to the Dirac-Brueckner results. The NN-contact interaction already represents the full nonperturbative short-distance dynamics.

Chapter 7

Including virtual $\Delta(1232)$-excitations

As already mentioned, the previously discussed chiral calculations of nuclear matter [13, 14, 79] are still incomplete from the point of view of the driving pion-nucleon dynamics. They include only (S- and) P-wave Born terms but leave out the excitation of the spin-isospin-3/2 $\Delta(1232)$-resonance which is the prominent feature of low-energy πN-scattering. It is also well known that the two-pion exchange between nucleons with excitation of virtual Δ-isobars generates most of the needed isoscalar central NN-attraction. In phenomenological one-boson exchange models this part of the NN-interaction is often simulated by a fictitious "σ"-meson exchange. A parameter-free calculation of the isoscalar central potential $\widetilde{V}_C(r)$ generated by 2π-exchange with single and double Δ-excitation in ref. [80] (see fig. 2 therein) agrees almost perfectly with the phenomenological "σ"-exchange potential at distances $r > 2\,\mathrm{fm}$, but not at shorter distances. The more detailed behavior of the 2π-exchange isoscalar central potential with single virtual Δ-excitation has the form [80]

$$\widetilde{V}_C^{(N\Delta)}(r) = -\frac{3g_{\rm A}^4}{64\pi^2 f_\pi^4 \Delta}\,\frac{e^{-2x}}{r^6}(6+12x+10x^2+4x^3+x^4)\,,$$

reminiscent of the van der Waals potential. Here $x = m_\pi r$ and the prefactor includes the spin-isospin (axial) polarizability of the nucleon [81], $g_{\rm A}^2/f_\pi^2\Delta = 5.2\,\mathrm{fm}^3$, from the virtual $\mathrm{N} \to \Delta(1232) \to \mathrm{N}$ transition. The familiar r^{-6}-dependence of the nonrelativistic van der Waals interaction emerges in the chiral limit, $m_\pi = 0$.

As pointed out earlier, a consideration of mass scales also suggests to include the $\Delta(1232)$-isobar as an explicit degree of freedom in nuclear matter calculations. The delta-nucleon mass splitting of $\Delta = 293\,\mathrm{MeV}$ is comparable to the Fermi momentum $k_{\mathrm{f},0} \simeq 262\,\mathrm{MeV}$ at nuclear matter saturation density. Propagation effects of virtual $\Delta(1232)$-isobars can therefore be resolved at the densities of interest. Based on these scale arguments we adopt a calculational scheme in which we count the Fermi momentum k_{f}, the pion mass m_π and the ΔN-mass splitting Δ simultaneously as "small scales". The nonrelativistic treatment of the nuclear matter many-body problem naturally goes conform with such an expansion in powers of small momenta. Relativistic corrections are relegated to higher orders in this expansion scheme. The leading contributions from 2π-exchange with virtual Δ-excitation to the energy per particle (or the single-particle potential) are generically of fifth power in the small momenta $(k_{\mathrm{f}}, m_\pi, \Delta)$. With respect to the counting in small momenta the effects from irreducible 2π-exchange evaluated in

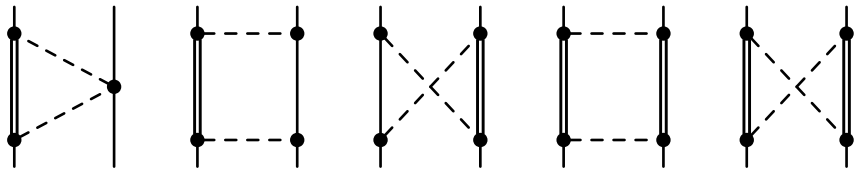

Figure 7.1: One-loop two-pion exchange diagrams with single and double Δ(1232)-isobar excitation. Diagrams for which the role of both nucleons is interchanged are not shown.

chapters 3 and 4 belong to the same order. However, since the πNΔ-coupling constant is about twice as large as the πNN-coupling constant, one can expect that the Δ-driven 2π-exchange effects are the dominant ones. The importance of Δ(1232)-degrees of freedom has also been pointed out in the "ab-initio" calculations of the Illinois group [3, 18].

In this chapter we extend the calculations of chapters 3 to 5 and systematically include all effects from 2π-exchange with virtual Δ-excitation up to three-loop order in the energy density. The contributions to the energy per particle (or the single-particle potential) are again classified as two-body terms and three-body terms. The two-body terms can be directly expressed through the NN-scattering T-matrix (i. e. the NN-potential in momentum space). The three-body terms on the other hand can be interpreted as Pauli blocking effects on the two-body terms imposed by the filled Fermi sea of nucleons. Note that the notion of "three-body term" is taken here in a generalized context, namely in the sense that three nucleons in the Fermi sea participate in interactions.

The NN T-matrix involves pion-loop diagrams which are in general ultra-violet divergent and require regularization (and renormalization). We adopt here a suitably subtracted dispersion-relation representation of the T-matrix where this procedure is accounted for by a few subtraction constants. These constants are understood to encode unresolved short-distance NN-dynamics and include all contributions from both momentum independent and p^2 dependent NN-contact interactions (which are not further iterated with pion exchange or with itself). The associated k_f^3- and k_f^5-terms in the energy per particle are then adjusted to some empirical property of nuclear matter (e.g. the binding energy of 16 MeV). This procedure replaces the cut-off regularization used in chapters 3 to 5 and now also takes into account the effects from p^2-dependent contact terms.

7.1 Equation of state of symmetric nuclear matter

We start the discussion with the equation of state of isospin-symmetric nuclear matter. We first present the contributions to the energy per particle $\bar{E}(k_\mathrm{f})$ as they arise from 2π-exchange with single and double virtual Δ-isobar excitation.

Figure 7.1 shows the relevant one-loop triangle, box, and crossed box diagrams contributing to the NN T-matrix (or the momentum space amplitude). The finite parts of these diagrams have been evaluated analytically in section 3 of ref. [80] employing the usual nonrelativistic $\Delta \leftrightarrow \pi\mathrm{N}$ transition vertices and Δ-propagator (see eq. (4) in

ref. [80]). By closing the two open nucleon lines to either two rings or one ring one gets (in diagrammatic representation) the Hartree or Fock contribution to the energy density of nuclear matter. The Hartree contribution to the energy per particle evidently goes linear with the nucleon density $\rho = 2k_\mathrm{f}^3/3\pi^2$, namely $\bar{E}_2^{(\mathrm{H})}(k_\mathrm{f}) = -V_C(0)\,\rho/2$ with $V_C(0)$ the isoscalar central NN-amplitude at zero momentum transfer [80]. The Fock contribution on the other hand is obtained by integrating the spin- and isospin-contracted T-matrix (depending on the momentum transfer variable $|\mathbf{p}_1 - \mathbf{p}_2|$) over the product of two Fermi spheres $|\mathbf{p}_{1,2}| < k_\mathrm{f}$ of radius k_f. We separate regularization dependent short-range parts in the T-matrix (originating from the divergences of the loop diagrams) from the unique long-range terms with the help of a twice-subtracted dispersion relation. The resulting subtraction constants give rise to a contribution to the energy per particle of the form:

$$\bar{E}^{(\mathrm{NN})}(k_\mathrm{f}) = B_3 \frac{k_\mathrm{f}^3}{M_\mathrm{N}^2} + B_5 \frac{k_\mathrm{f}^5}{M_\mathrm{N}^4}\,, \tag{7.1}$$

where B_3 and B_5 are chosen for convenience as dimensionless. We interpret the parameters $B_{3,5}$ to subsume all unresolved short-distance NN-dynamics relevant for isospin-symmetric nuclear matter at low and moderate densities. The contributions of the 2π-exchange (two-body) Hartree diagrams are proportional to ρ and thus are also included in eq. (7.1) by means of the subtraction procedure. The long-range parts of the 2π-exchange (two-body) Fock diagrams can be expressed as:

$$\begin{aligned}\bar{E}_2^{(\mathrm{F})}(k_\mathrm{f}) = \frac{1}{8\pi^3}\int_{2m_\pi}^{\infty} \mathrm{d}\mu\, \mathrm{Im}(V_C + 3W_C + 2\mu^2 V_T + 6\mu^2 W_T)\Big\{ 3\mu k_\mathrm{f} - \frac{4k_\mathrm{f}^3}{3\mu} \\ + \frac{8k_\mathrm{f}^5}{5\mu^3} - \frac{\mu^3}{2k_\mathrm{f}} - 4\mu^2 \arctan\frac{2k_\mathrm{f}}{\mu} + \frac{\mu^3}{8k_\mathrm{f}^3}(12k_\mathrm{f}^2 + \mu^2)\ln\left(1 + \frac{4k_\mathrm{f}^2}{\mu^2}\right)\Big\}\,,\end{aligned} \tag{7.2}$$

where $\mathrm{Im}\,V_C$, $\mathrm{Im}\,W_C$, $\mathrm{Im}\,V_T$ and $\mathrm{Im}\,W_T$ are the spectral functions of the isoscalar and isovector central and tensor NN-amplitudes, respectively. Explicit expressions of these imaginary parts for the contributions of the triangle diagram with single Δ-excitation and the box diagrams with single and double Δ-excitation can be easily constructed from the analytical formulas given in section 3 of ref. [80]. The μ- and k_f-dependent weighting function in eq. (7.2) takes care that at low and moderate densities this spectral integral is dominated by low invariant ππ-masses $2m_\pi < \mu < 1\,\mathrm{GeV}$. The contributions to the energy per particle from irreducible 2π-exchange (with only nucleon intermediate states) can also be cast into the form eq. (7.2). The corresponding nonvanishing spectral functions [73] are given in eqs. (B.20) and (B.21). The dispersion integrals $\int_{2m_\pi}^{\infty}\mathrm{d}\mu\,\mathrm{Im}(\dots)$ in this and all following sections are understood to include the contributions from irreducible 2π-exchange (with only nucleon intermediate states).

Next, we come to the three-body terms which arise from Pauli blocking of intermediate nucleon states (i. e. from the $-2\pi\theta(k_\mathrm{f} - |\mathbf{p}|)$ terms of the in-medium nucleon propagators eq. (2.23)). The corresponding closed Hartree and Fock diagrams with single virtual Δ-excitation are shown in fig. 7.2. In the case of isospin-symmetric nuclear matter their isospin factors are 8, 0, and 8, in the order shown. For the three-loop Hartree diagram

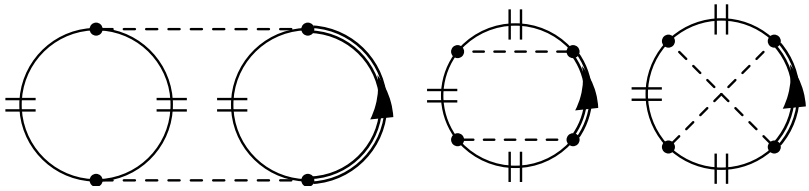

Figure 7.2: Hartree and Fock three-body diagrams related to 2π-exchange with single virtual Δ-isobar excitation. A single line with a double bar denotes the medium part of the in-medium nucleon propagator, eq. (2.23). Thus the shown diagrams represent interactions between three nucleons in the Fermi sea.

the occurring integral over the product of three Fermi spheres of radius k_f can be solved in closed form and the contribution to the energy per particle reads:

$$\bar{E}_3^{(\mathrm{H})}(k_\mathrm{f}) = \frac{g_\mathrm{A}^4 m_\pi^6}{\Delta(2\pi f_\pi)^4}\left[\frac{2}{3}u^6 + u^2 - 3u^4 + 5u^3 \arctan 2u - \frac{1}{4}(1+9u^2)\ln(1+4u^2)\right], \quad (7.3)$$

with the abbreviation $u = k_\mathrm{f}/m_\pi$ where $m_\pi = 135\,\mathrm{MeV}$ again stands for the (neutral) pion mass. The Delta propagator shows up in this expression merely via the (reciprocal) mass-splitting $\Delta = 293\,\mathrm{MeV}$. Additional corrections to the Delta propagator coming from differences of nucleon kinetic energies, etc. will make a contribution at least one order higher in the small-momentum expansion. In eq. (7.3) we have already inserted the empirically well-satisfied relation $g_{\pi\mathrm{N}\Delta} = 3g_{\pi\mathrm{N}}/\sqrt{2}$ for the πNΔ-coupling constant together with the Goldberger-Treiman relation $g_{\pi\mathrm{N}} = g_\mathrm{A} M_\mathrm{N}/f_\pi$ (see e. g. eq. (5) in ref. [80] for the $\Delta \to \mathrm{N}\pi$ decay width). As usual $f_\pi = 92.4\,\mathrm{MeV}$ denotes the weak pion decay constant and we choose the value $g_\mathrm{A} = 1.3$ in order to have a pion-nucleon coupling constant of $g_{\pi\mathrm{N}} = 13.2$ [33].

We note that eq. (7.3) includes a repulsive term quadratic in the nucleon density. This term is the only one which survives in the chiral limit $m_\pi = 0$. In that limit the momentum dependent πNΔ-interaction vertices get canceled by the pion propagators and thus one is effectively dealing with a zero-range three-nucleon contact interaction. It is important to notice that this equivalence holds only after taking the spin-traces but not at the level of the (spin and momentum dependent) 2π-exchange three-nucleon interaction. The contribution of the (right) three-body Fock diagram in fig. 7.2 to the energy per particle is given in eq. (B.24) in appendix B.2.1. The contributions to $\bar{E}(k_\mathrm{f})$ from the (relativistically improved) kinetic energy, from the 1π-exchange Fock diagram and from the iterated 1π-exchange Hartree and Fock diagrams have been written down in eqs. (B.11) to (B.16). The strongly attractive contribution from iterated 1π-exchange linear in the density and the cutoff Λ (see eq. (B.17)) is now of course not counted extra since B_3 in eq. (7.1) collects all such possible terms.

At this stage, let us look at some generic properties of the nuclear matter equation of state. Binding and saturation occurs in a wide range of the two adjustable parameters $B_{3,5}$. However, due to the repulsive ρ^2-term from the three-body Hartree diagram (see eq. (7.3)) the saturation curve rises much too steeply with increasing density. This causes

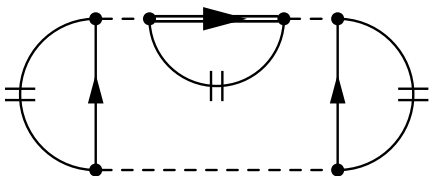

Figure 7.3: A 4-loop diagram which generates an attractive ρ^2-term similar to the NNN-contact term (7.4).

a too low saturation density ρ_0 and a too high nuclear matter compressibility, $K > 350\,\mathrm{MeV}$. We cure this problem in a minimal way by introducing an attractive three-body contact term,

$$\bar{E}^{(\mathrm{NNN})}(k_\mathrm{f}) = B_6 \frac{k_\mathrm{f}^6}{M_\mathrm{N}^5}\,. \tag{7.4}$$

The need for introducing such a three-body term into our calculation points to some short-distance physics whose dynamical origin lies outside the present framework of perturbative chiral pion-nucleon interactions. On the other hand, there are certain four-loop diagrams (such as the diagram in fig. 7.3 and the corresponding Fock diagram) which generate such attractive ρ^2-terms.

Adding all pieces we arrive at the full energy per particle $\bar{E}(k_\mathrm{f})$ at three-loop order. It involves three parameters, B_3 and B_5 of the two-body contact term eq. (7.1) and B_6 which controls the three-body contact term, eq. (7.4). With these three adjustable parameters it is in principle possible to fit the three quantities $\bar{E}_0$, ρ_0, and K exactly. On the other hand, one has to take into account that the parameter B_5 also influences the momentum dependence of the single-particle potential $U(p, k_\mathrm{f})$ (see next section). For example, while the values $B_3 = -8.25$, $B_5 = 10.5$, and $B_6 = -57$ yield excellent saturation properties, $\bar{E}_0 = -16\,\mathrm{MeV}$, $k_{\mathrm{f},0} = 262\,\mathrm{MeV}$, and $K = 270\,\mathrm{MeV}$, the resulting single-particle potential at $p = 0$ is too deep, $U(p = 0, k_{\mathrm{f},0} = 262\,\mathrm{MeV}) = -107\,\mathrm{MeV}$.

Both good saturation and good single-particle properties can be generated in the parameter range $B_3 \simeq -7.95 \ldots -8$, $B_5 \simeq -1 \ldots 1$, and $B_6 \simeq -29 \ldots -34$. Compared to $B_{3,5}$, the given values of B_6 controlling the three-body contact term appear to be relatively large. The resulting contribution to the energy per particle is however comparable to the contributions from the 3-loop 3-body diagrams shown in fig. 7.2: Using the value $\tilde{B}_6 = -g_\mathrm{A}^4 M_\mathrm{N}^5/[2\Delta(2\pi f_\pi)^4] = -31.3$, the three-body contact term eq. (7.4) exactly cancels the ρ^2-term in eq. (7.3) and an analogous attractive contribution from the three-body Fock diagram in eq. (B.24). For comparison, relativistic corrections (at sixth order in small momenta) to iterated 1π-exchange and irreducible 2π-exchange (see appendix B.1 in ref. [15]) generate an attractive ρ^2 term of approximately $-4.8 k_\mathrm{f}^6/M_\mathrm{N}^5$. On the other hand, the ρ^2 contribution to $\bar{E}(k_\mathrm{f})$ from the 4-loop diagram in fig. 7.3 is also quite large. The energy per particle from this diagram and the corresponding Pauli blocking diagram with four medium insertions (fig. B.1) has been evaluated in cut-off regularization in appendix B.2.3. For a cut-off momentum of $\Lambda \gtrsim 460\,\mathrm{MeV}$, the (cut-off dependent) ρ^2-term coming from these diagrams is equal to or larger than the NNN-contact term (7.4) with $B_6 = \tilde{B}_6 = -31.3$. Therefore, a value $B_6 \simeq -30$ is not unrealistic.

In the following, we set the three parameters to $B_3 = -7.99$, $B_5 = 0$, and $B_6 = \tilde{B}_6 = -31.3$. We consider this choice to be optimal in order to obtain at the same time good saturation properties and realistic single-particle properties (see next section). The full

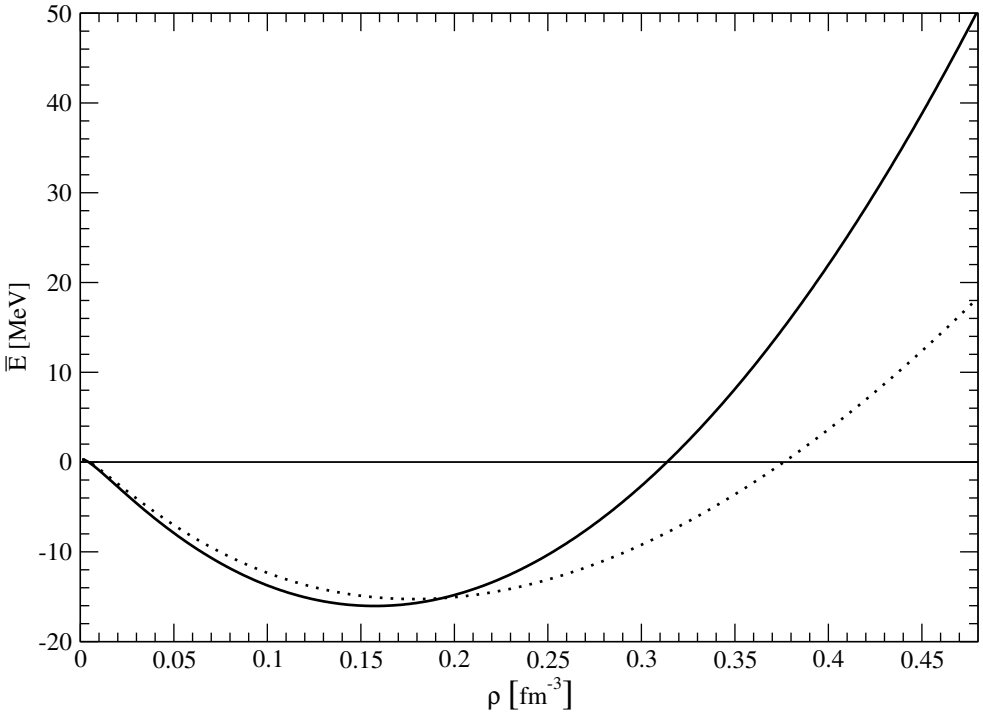

Figure 7.4: The energy per particle $\bar{E}(k_\mathrm{f})$ of isospin-symmetric nuclear matter as a function of the nucleon density $\rho = 2k_\mathrm{f}^3/3\pi^2$. The dashed line refers to the result of chapter 3, with only pions and nucleons as active degrees of freedom. The full line includes effects from 2π-exchange with virtual Δ-excitation. The short-range parameters are $B_3 = -7.99$, $B_5 = 0$, and $B_6 = -31.3$.

line in fig. 7.4 shows the energy per particle resulting from these parameter values. The predicted value of the saturation density is $\rho_0 = 0.157\,\mathrm{fm}^{-3}$, corresponding to a Fermi momentum $k_{\mathrm{f},0} = 261.6\,\mathrm{MeV} = 1.326\,\mathrm{fm}^{-1}$. This is very close to the semi-empirical value $\rho_0 = 0.158\,\mathrm{fm}^{-3}$ obtained by extrapolation from inelastic electron scattering off heavy nuclei [25]. The decomposition of the negative binding energy $\bar{E}_0 = -16.0\,\mathrm{MeV}$ into contributions of second, third, fourth, fifth, and sixth power in small momenta reads: $\bar{E}_0 = (21.9 - 145.5 + 107.8 + 13.6 - 13.8)\,\mathrm{MeV}$ with the typical balance between large third and fourth order terms (see section 3.2). Evidently, since $\bar{E}_0 = -16.0\,\mathrm{MeV}$ is a small number that needs to be fine-tuned in our calculation, there remains the question of the "convergence" of the small momentum expansion. The nuclear matter compressibility $K = k_{\mathrm{f},0}^2 \bar{E}''(k_{\mathrm{f},0})$ related to the curvature of the saturation curve at its minimum comes out as $K = 304\,\mathrm{MeV}$. This value is somewhat large but still acceptable. It exceeds e. g. the value $K = 272\,\mathrm{MeV}$ obtained in the relativistic mean-field model of ref. [82] by only 12%. The dashed line in fig. 7.4 shows for comparison the equation of state resulting from our previous chiral calculation from section 3.2 with no πNΔ-dynamics included. That calculation yielded a somewhat too high saturation density of $\rho_0 = 0.178\,\mathrm{fm}^{-3}$. The compressibility $K = 255\,\mathrm{MeV}$ had a better value, but the single-particle properties and the density of states at the Fermi surface were not satisfactory. The stronger rise of

the full curve in fig. 7.4 with density ρ is a consequence of including higher order terms in the (small-momentum) k_f-expansion. Of course, such behaviour at high density will be modified by further four-loop contributions to the energy density, in which genuine attractive three-body terms with intermediate Δ-hole excitations (such as fig. 7.3) play a prominent role.

7.2 Single-particle potential

7.2.1 Real part

In this section we discuss the real part $U(p, k_\mathrm{f})$ of the nucleon's single-particle potential. As outlined in section 3.4 the contributions to the (real) nuclear mean-field $U(p, k_\mathrm{f})$ can be classified as two-body and three-body potentials. The parameters $B_{3,5}$ and B_6 introduced in eqs. (7.1) and (7.4) reappear in contributions to the two- and three-body potentials, respectively. They have the form

$$U_2^{(\mathrm{NN})}(p, k_\mathrm{f}) = 2B_3 \frac{k_\mathrm{f}^3}{M_\mathrm{N}^2} + B_5 \frac{k_\mathrm{f}^3}{3M_\mathrm{N}^4}(3k_\mathrm{f}^2 + 5p^2)\,, \tag{7.5}$$

$$U_3^{(\mathrm{NNN})}(p, k_\mathrm{f}) = 3B_6 \frac{k_\mathrm{f}^6}{M_\mathrm{N}^5}\,. \tag{7.6}$$

Their density and momentum dependence (or lack thereof) is completely fixed by the Hugenholtz-van Hove theorem (3.15) and the sum rule,

$$\bar{E}(k_\mathrm{f}) = \frac{3}{k_\mathrm{f}^3} \int_0^{k_\mathrm{f}} \mathrm{d}p\, p^2 \left[T_\mathrm{kin}(p) + \frac{1}{2} U_2(p, k_\mathrm{f}) + \frac{1}{3} U_3(p, k_\mathrm{f}) \right], \tag{7.7}$$

which connects the single-particle potential to the energy per particle $\bar{E}(k_\mathrm{f})$ [31]. By splitting both sides of the sum rule (7.7) into contributions from the different diagrams it is possible to directly relate $\bar{E}^{(\mathrm{NN})}(k_\mathrm{f})$ and $\bar{E}^{(\mathrm{NNN})}(k_\mathrm{f})$ to the corresponding integrals over $U_2^{(\mathrm{NN})}(p, k_\mathrm{f})$ and $U_3^{(\mathrm{NNN})}(p, k_\mathrm{f})$, respectively.

Note that the three-body contact interaction (7.6) has no influence on the momentum dependence of the single-particle potential. The contributions of 2π-exchange with virtual Δ-excitations are given in equations (B.95) to (B.97) in the appendix. The real single-particle potential $U(p, k_\mathrm{f})$ is completed by adding to the terms eqs. (7.5,7.6) and (B.95-B.97) the contributions from 1π-exchange and iterated 1π-exchange written down in eqs. (B.87-B.91).

The slope of the real single-particle potential $U(p, k_\mathrm{f})$ at the Fermi surface $p = k_\mathrm{f}$ determines the effective nucleon mass (in the nomenclature of ref. [83], the product of "k-mass" and "E-mass" divided by the free nucleon mass $M_\mathrm{N} = 939\,\mathrm{MeV}$) via the relation:

$$M_\mathrm{N}^\star(k_\mathrm{f}) = M_\mathrm{N} \left[1 - \frac{k_\mathrm{f}^2}{2M_\mathrm{N}^2} + \frac{M_\mathrm{N}}{k_\mathrm{f}} \left. \frac{\partial U(p, k_\mathrm{f})}{\partial p} \right|_{p=k_\mathrm{f}} \right]^{-1}. \tag{7.8}$$

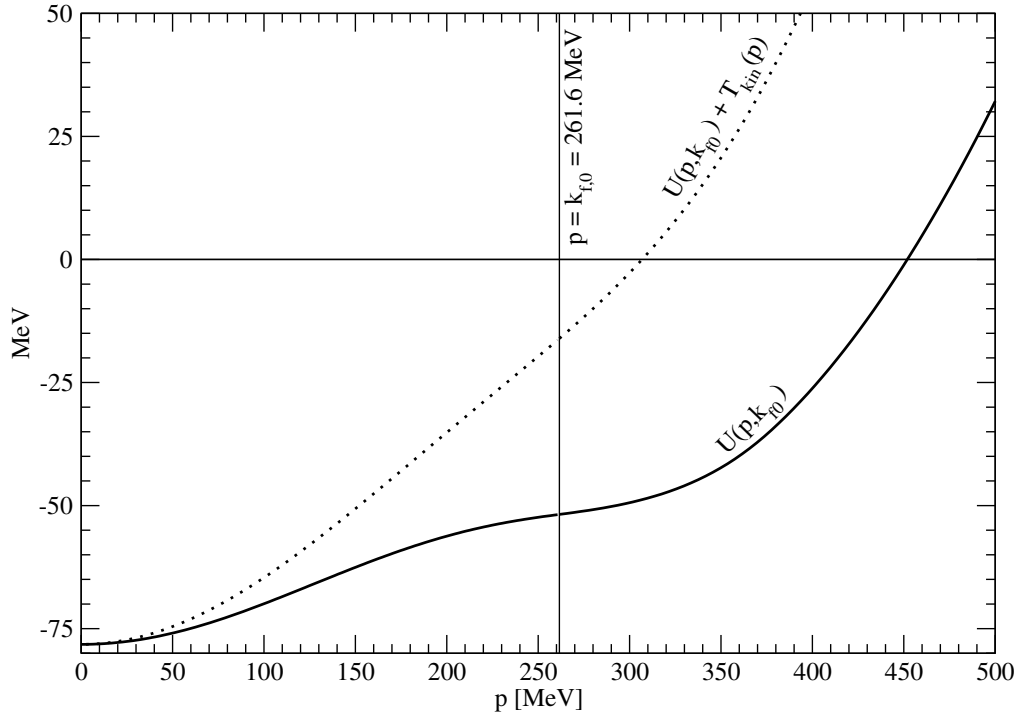

Figure 7.5: Full line: real part of the single-particle potential $U(p, k_{\rm f,0})$ at saturation density $k_{\rm f,0} = 261.6\,\mathrm{MeV}$ as a function of the nucleon momentum p. The dotted line includes in addition the relativistically improved kinetic energy $T_{\rm kin}(p) = p^2/2M_{\rm N} - p^4/8M_{\rm N}^3$.

The second term $-k_{\rm f}^2/2M_{\rm N}^2$ in the square brackets comes from the relativistic correction $-p^4/8M_{\rm N}^3$ to the kinetic energy.

The full line in fig. 7.5 shows the real part of the single-particle potential $U(p, k_{\rm f,0})$ at saturation density $k_{\rm f,0} = 261.6\,\mathrm{MeV}$ as a function of the nucleon momentum p. The dotted line includes in addition the relativistically improved kinetic energy $T_{\rm kin}(p) = p^2/2M_{\rm N} - p^4/8M_{\rm N}^3$. With the parameters $B_3 = -7.99$, $B_5 = 0$, and $B_6 = -31.3$ chosen in section 7.1 we find a potential depth of $U(0, k_{\rm f,0}) = -78.2\,\mathrm{MeV}$. This is very close to the result $U(0, k_{\rm f,0}) \simeq -80\,\mathrm{MeV}$ of the relativistic Dirac-Brueckner approach of ref. [38]. For comparison, the calculation of ref. [37] based on the Paris NN-interaction finds a somewhat shallower potential depth of $U(0, k_{\rm f,0}) \simeq -64\,\mathrm{MeV}$. One observes that with the chiral πNΔ-dynamics included, the real single-particle potential $U(p, k_{\rm f,0})$ grows monotonically with the nucleon momentum p. The downward bending above $p = 180\,\mathrm{MeV}$ displayed in fig. 3.4 is now eliminated. The slope at the Fermi surface $p = k_{\rm f,0}$ translates into an effective nucleon mass of $M_{\rm N}^\star(k_{\rm f,0}) = 0.88 M_{\rm N}$. This is now a realistic value compared to $M_{\rm N}^\star(k_{\rm f,0}) \simeq 3.5 M_{\rm N}$ obtained in section 3.4.1 without explicit Δ-isobars. Note also that the chiral approach of ref. [79] (see also chapter 6) has found the lower bound $M_{\rm N}^\star(k_{\rm f,0}) > 1.3 M_{\rm N}$.

The dotted curve in fig. 7.5 for the total single-particle energy $T_{\rm kin}(p) + U(p, k_{\rm f,0})$ hits the value $\bar{E}(k_{\rm f,0}) = \bar{E}_0 = -16\,\mathrm{MeV}$ at the Fermi surface $p = k_{\rm f,0}$, as required

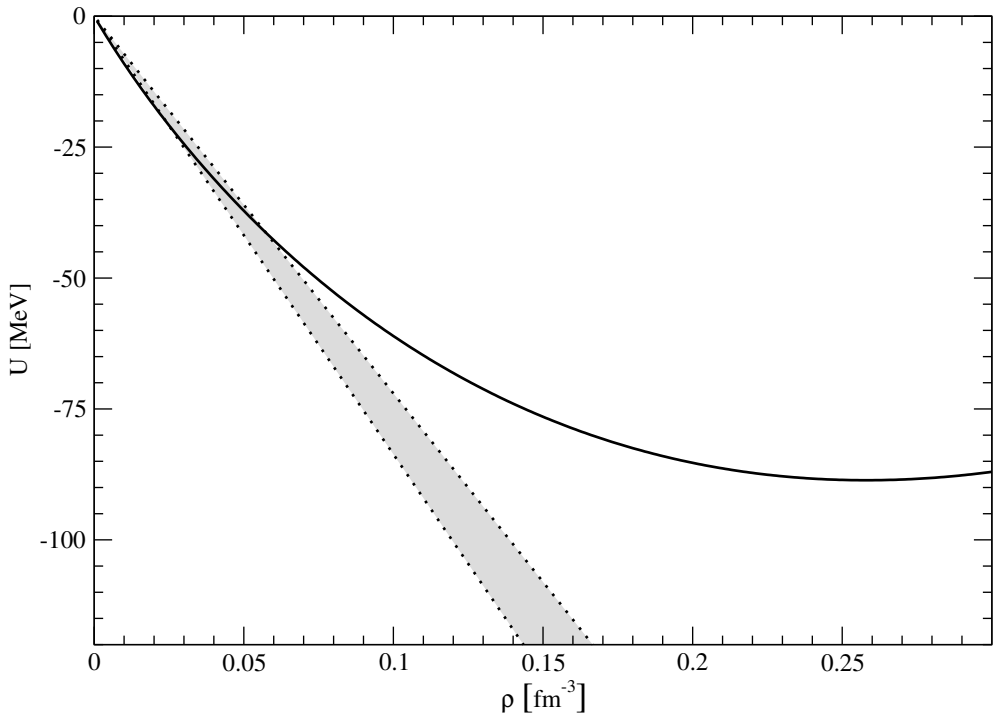

Figure 7.6: The full line shows the real part of the single-particle potential $U(0, k_\mathrm{f})$ at nucleon momentum $p = 0$ versus the density $\rho = 2k_\mathrm{f}^3/3\pi^2$. The band is obtained from the universal low-momentum NN-potential $V_{\mathrm{low}\,k}$ in linear density approximation.

by the Hugenholtz-van Hove theorem eq. (3.15). This important theorem holds strictly in our (perturbative) calculation, whereas (nonperturbative) Brueckner-Hartree-Fock approaches using ladder approximations often fail to respect it [84]. The smooth rise of $U(p, k_{\mathrm{f},0})$ as it crosses the Fermi surface and proceeds up to $p \simeq 400\,\mathrm{MeV}$ is compatible with other calculations [37,38]. Beyond this momentum scale one presumably exceeds the limits of validity of the present chiral perturbation theory calculation of nuclear matter.

The full line in fig. 7.6 shows the potential depth $U(0, k_\mathrm{f})$ for a nucleon at the bottom of the Fermi sea as a function of the nucleon density $\rho = 2k_\mathrm{f}^3/3\pi^2$. The band spanned by the dotted lines stems from the universal low-momentum NN-potential $V_{\mathrm{low}\,k}$ [19]. This $V_{\mathrm{low}\,k}$ is found by decimating model dependent details of various short-distance NN-interactions, using renormalization group methods. In linear density approximation the single-particle potential depth generated by $V_{\mathrm{low}\,k}(p, p')$ simply reads:

$$U(0, k_\mathrm{f}) = \frac{3\pi\rho}{2M_\mathrm{N}} \left[V_{\mathrm{low}\,k}^{(^1S_0)}(0,0) + V_{\mathrm{low}\,k}^{(^3S_1)}(0,0) \right], \tag{7.9}$$

with $V_{\mathrm{low}\,k}^{(^1S_0)}(0,0) \simeq -1.9\,\mathrm{fm}$ and $V_{\mathrm{low}\,k}^{(^3S_1)}(0,0) \simeq -(2.2 \pm 0.3)\,\mathrm{fm}$ [19, 85, 86], the two S-wave potentials at zero momentum. It is interesting to observe that both potential depths agree fairly well at low densities, $\rho \leq 0.07\,\mathrm{fm}^{-3}$. This agreement is by no means trivial since $V_{\mathrm{low}\,k}$ is constructed to reproduce accurately the low-energy NN-scattering

data (phase-shifts and mixing angles) when iterated in a two-body Lippmann-Schwinger equation, whereas our adjustment of the parameters B_i is made at saturation density, $\rho_0 = 0.16\,\mathrm{fm}^{-3}$. It is evident from fig. 7.6 that a linear extrapolation does not work from zero density up to nuclear matter saturation density. Strong curvature effects set in already at Fermi momenta around $k_\mathrm{f} \simeq m_\pi$ once pion dynamics is treated explicitly.[1] We note also that an "improved" determination of the potential depth $U(0, k_\mathrm{f})$ from $V_{\mathrm{low}\,k}$, taking into account its momentum dependence in the repulsive Fock contribution, leads to concave curves which bend below the straight dotted lines in fig. 7.6. In the case $V_{\mathrm{low}\,k}^{(^3S_1)}(0,0) = -1.9\,\mathrm{fm}$ the potential depth $U(0, k_{\mathrm{f},0})$ at saturation density would increase to $-132.6\,\mathrm{MeV}$ (compared to $-113.4\,\mathrm{MeV}$ in linear density approximation). The present observations concerning the potential depth $U(0, k_\mathrm{f})$ may indicate why the calculations of ref. [87] based on $V_{\mathrm{low}\,k}$ did not find saturation of nuclear matter. It seems that the Brueckner ladder does not generate all relevant medium modifications which set in already at rather low densities $k_\mathrm{f} \simeq m_\pi$ (if the pion dynamics is treated explicitly).

7.2.2 Imaginary part

For completeness, we reevaluate the imaginary part $W(p, k_\mathrm{f})$ of the single-particle potential. To the three-loop order we are working here it is still given completely by iterated 1π-exchange with no contribution from the $\pi\mathrm{N}\Delta$-dynamics or the contact interactions. The only difference from the result in section 3.4.2 is the changed Fermi momentum.

Figure 7.7 shows the imaginary part of the single-particle potential $W(p, k_{\mathrm{f},0})$ at the new equilibrium Fermi momentum $k_{\mathrm{f},0} = 261.6\,\mathrm{MeV}$ as a function of the nucleon momentum p. The quantity $\pm 2W(p, k_\mathrm{f})$ determines the width of a hole-state or a particle-state of momentum $p < k_\mathrm{f}$ or $p > k_\mathrm{f}$, respectively. The finite life time of such states originates from redistributing energy into additional particle-hole excitations. Our predicted value $W(0, k_{\mathrm{f},0}) = 24.0\,\mathrm{MeV}$ at $p = 0$ is slightly reduced compared to the value $W(0, k_\mathrm{f} = 272.7\,\mathrm{MeV}) = 29.7\,\mathrm{MeV}$ found in section 3.4.2. However, it still lies in between the results $W(0, k_{\mathrm{f},0}) \simeq 20\,\mathrm{MeV}$ of ref. [44] employing the Gogny D1 effective interaction and $W(0, k_{\mathrm{f},0}) \simeq 40\,\mathrm{MeV}$ of ref. [37] using the Paris NN-potential.

The rapid growth of $\Gamma_\mathrm{sp} = -2W(p, k_\mathrm{f})$ at large momenta is again an indication that the validity of our chiral perturbation theory calculation is limited to small momenta, $p \lesssim 400\,\mathrm{MeV}$.

7.3 Nuclear matter at finite temperature

We have seen that the inclusion of $\pi\mathrm{N}\Delta$-dynamics greatly improves the momentum dependence of the single particle potential near the Fermi surface. Now it is of further interest to see what this improved behavior implies for nuclear matter at finite temperature, $T \leq 30\,\mathrm{MeV}$, in particular with respect to the first-order liquid-gas phase transition.

[1] As example for the extreme inherent nonlinearities, consider the formula for the three-body potential $U_3^{(\mathrm{H})}(0, k_\mathrm{f})$ in eq. (B.96). Its mathematical Taylor-series expansion converges only for $k_\mathrm{f} < m_\pi/2$. This corresponds to tiny densities, $\rho < 0.003\,\mathrm{fm}^{-3}$.

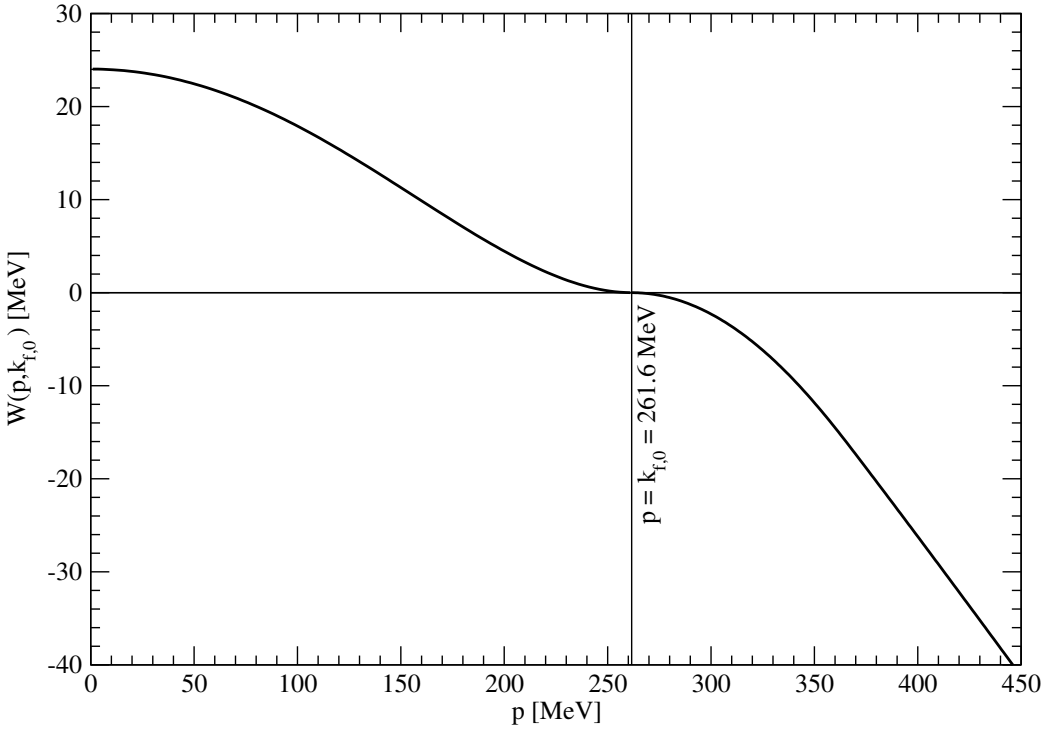

Figure 7.7: The imaginary part of the single-particle potential $W(p, k_{\mathrm{f},0})$ at saturation density ($k_{\mathrm{f},0} = 261.6\,\mathrm{MeV}$) as a function of the nucleon momentum p. The quadratic behavior around the Fermi surface $p = k_{\mathrm{f},0}$ with a sign change of the curvature is required by Luttinger's theorem [42].

The critical temperature $T_c = 25.5\,\mathrm{MeV}$ found in chapter 4 was considered too high in comparison with the accepted empirical range.

As described there, we express the free energy density $\rho\bar{F}(\rho, T)$ of isospin-symmetric nuclear matter as a sum of convolution integrals over interaction kernels $\mathcal{K}_j$ multiplied by powers of the density of nucleon states in momentum space. The kernel involving the subtraction constants $B_{3,5}$ reads

$$\mathcal{K}_2^{(\mathrm{NN})} = 24\pi^2 B_3 \frac{p_1 p_2}{M_{\mathrm{N}}^2} + 20\pi^2 B_5 \frac{p_1 p_2}{M_{\mathrm{N}}^4}(p_1^2 + p_2^2)\,, \tag{7.10}$$

while the additional three-body contact interaction generates the following kernel:

$$\mathcal{K}_3^{(\mathrm{NNN})} = 144\pi^4 B_6 \frac{p_1 p_2 p_3}{M_{\mathrm{N}}^5}\,. \tag{7.11}$$

Note that the B_3- and B_6-terms in eqs. (7.10) and (7.11) generate temperature independent contributions to the free energy per particle, $\bar{F}(\rho, T)^{(B_3)} = 3\pi^2 B_3 \rho / 2M_{\mathrm{N}}^2$ and $\bar{F}(\rho, T)^{(\mathrm{NNN})} = 9B_6\pi^4\rho^2/4M_{\mathrm{N}}^5$. The additional interaction kernels $\mathcal{K}_{2,3}$ arising from 2π-exchange with virtual Δ-excitation are given in eqs. (B.39) to (B.41) in the appendix. Temperature and density dependent Pauli blocking effects are incorporated in the three-body kernel $\mathcal{K}_3$. The remaining kernels building up the free nucleon gas part and the

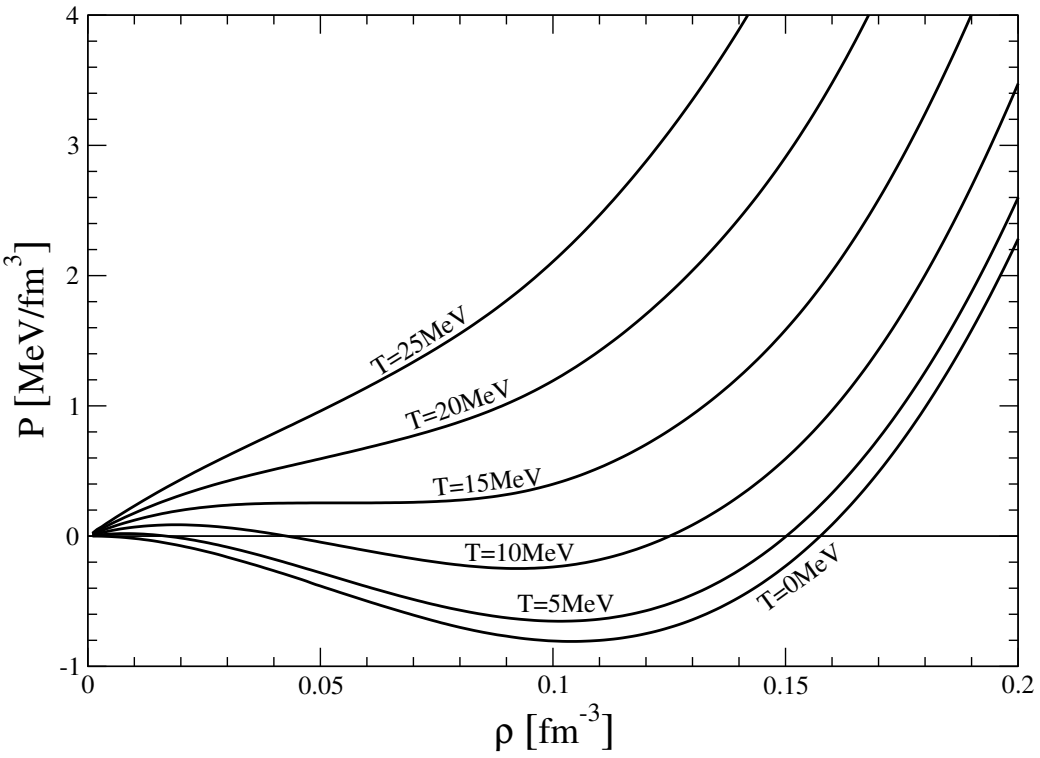

Figure 7.8: Pressure isotherms $P(\rho,T) = \rho^2 \partial \bar{F}(\rho,T)/\partial\rho$ of isospin-symmetric nuclear matter at finite temperature T. The coexistence region of the liquid and the gas phase ends at the critical point: $\rho_c \simeq 0.053\,\mathrm{fm}^{-3}$, $T_c \simeq 15\,\mathrm{MeV}$.

interaction contributions from 1π-exchange and iterated 1π-exchange have been written in eqs. (B.28-B.31), eqs. (B.33-B.34), and eq. (4.6). It is needless to say that the extension of our nuclear matter calculation to finite temperatures T does not introduce any new adjustable parameter.

Figure 7.8 shows the calculated pressure isotherms $P(\rho,T) = \rho^2 \partial \bar{F}(\rho,T)/\partial\rho$ of isospin-symmetric nuclear matter at six selected temperatures $T = 0,\ 5,\ 10,\ 15,\ 20,\ 25\,\mathrm{MeV}$. As before these curves display a first-order liquid-gas phase transition similar to that of the van der Waals gas. We find here a critical temperature of $T_c \simeq 15\,\mathrm{MeV}$ and a critical density of $\rho_c \simeq 0.053\,\mathrm{fm}^{-3} \simeq \rho_0/3$. This critical temperature is close to the value $T_c = (16.6 \pm 0.9)\,\mathrm{MeV}$ extracted in ref. [52] from an analysis of limiting temperatures in heavy ion collisions. In comparison, a critical temperature of $T_c = (20 \pm 3)\,\mathrm{MeV}$ has been deduced in ref. [88] from multi-fragmentation data in proton-on-gold collisions. Other nuclear matter calculations find a critical temperature typically around $T_c \simeq 18\,\mathrm{MeV}$ [27, 53, 54]. The reduction of T_c in comparison to $T_c \simeq 25.5\,\mathrm{MeV}$ obtained previously in chapter 4 results from the substantially improved momentum dependence of the real single-particle potential $U(p, k_{\mathrm{f},0})$ near the Fermi surface $p = k_{\mathrm{f},0}$ (see fig. 7.5). As a general rule the critical temperature T_c grows with the effective nucleon mass $M_{\mathrm{N}}^{\star}(k_{\mathrm{f},0})$ at the Fermi surface.

The single-particle properties and the density of states around the Fermi surface are decisive for the thermal excitations. They crucially influence the low temperature be-

havior of nuclear matter. The inclusion of the chiral πNΔ-dynamics leads to a realistic density of (thermally excitable) nucleon states at the Fermi surface, in contrast to an approach based on pions and nucleons only. This is an important observation.

7.4 Nuclear energy density functional

In section 5.1 we have calculated the nuclear energy density functional from 1π- and iterated 1π-exchange. Here we investigate the influence of πNΔ-dynamics on this energy density functional.

7.4.1 The strength functions

The contributions to the strength functions $F_{\tau,d}(k_\mathrm{f})$ generated by 2π-exchange with virtual Δ-excitation are given in appendix B.7.3. With the decomposition (5.8), these expressions determine the contributions to the strength functions $F_\nabla(k_\mathrm{f})$. The contributions from πNΔ-dynamics to the spin-orbit strength function $F_\mathrm{so}(k_\mathrm{f})$ have been calculated in ref. [89]. The relevant equations are quoted in eqs. (B.142) and (B.143).

The regularization dependent contributions are again encoded in subtraction constants:

$$F_\tau^{(\mathrm{NN})}(k_\mathrm{f}) = B_5 \frac{5k_\mathrm{f}^3}{3M_\mathrm{N}^4}\,, \qquad F_d^{(\mathrm{NN})}(k_\mathrm{f}) = \frac{B_d}{M_\mathrm{N}^4}\,, \qquad F_\mathrm{so}^{(\mathrm{NN})}(k_\mathrm{f}) = \frac{B_\mathrm{so}}{M_\mathrm{N}^4}\,, \tag{7.12}$$

where the new parameter $B_d = -M_\mathrm{N}^4 V_C''(0)/4$ relates to the two-body Hartree diagrams and the momentum transfer dependence of the isoscalar central NN-amplitude $V_C(q)$, while the new parameter $B_\mathrm{so} = -3M_\mathrm{N}^4[V_\mathrm{so}(0) + W_\mathrm{so}(0)]/4$ comes from two-body Hartree and Fock diagrams and the momentum transfer dependence of the isoscalar and isovector spin-orbit NN-amplitudes $V_\mathrm{so}(q)$ and $W_\mathrm{so}(q)$. The strength functions $F_{\tau,d,\mathrm{so}}(k_\mathrm{f})$ are completed by adding to the terms in eqs. (B.134-B.145) the contributions from 1π-exchange and iterated 1π-exchange as written in appendices B.7.1 and B.7.2. In order to be consistent with the calculation of the energy per particle $\bar{E}(k_\mathrm{f})$ and the single-particle potential $U(p, k_\mathrm{f})$ we include the relativistic $1/M_\mathrm{N}^2$-correction eq. (B.113) to the 1π-exchange contribution.

In the energy density functional (5.6), the expression multiplying the kinetic energy density $\tau(\mathbf{r})$ has the interpretation of a reciprocal density dependent effective nucleon mass:

$$\tilde{M}_\mathrm{N}^\star(\rho) = M_\mathrm{N}\left[1 - \frac{5k_\mathrm{f}^2}{28M_\mathrm{N}^2} + 2M_\mathrm{N}\,F_\tau(k_\mathrm{f})\right]^{-1}. \tag{7.13}$$

We note again that this effective nucleon mass $\tilde{M}_\mathrm{N}^\star(\rho)$ (entering the nuclear energy density functional) is conceptually different from the so-called "Landau"-mass $M_\mathrm{N}^\star(k_\mathrm{f})$ defined in eq. (7.8). Only if the real single-particle potential has a simple quadratic dependence on the nucleon momentum, $U(p, k_\mathrm{f}) = U_0(k_\mathrm{f}) + p^2 U_1(k_\mathrm{f})$, do these two variants of effective nucleon mass agree with each other (modulo very small differences related to the relativistic $k_\mathrm{f}^2/2M_\mathrm{N}^2$-correction).

In fig. 7.9 we show the ratio $\tilde{M}_\mathrm{N}^\star(\rho)/M_\mathrm{N}$ as a function of the nucleon density $\rho = 2k_\mathrm{f}^3/3\pi^2$. The dotted line corresponds to the result of section 5.1 based on 1π- and iterated

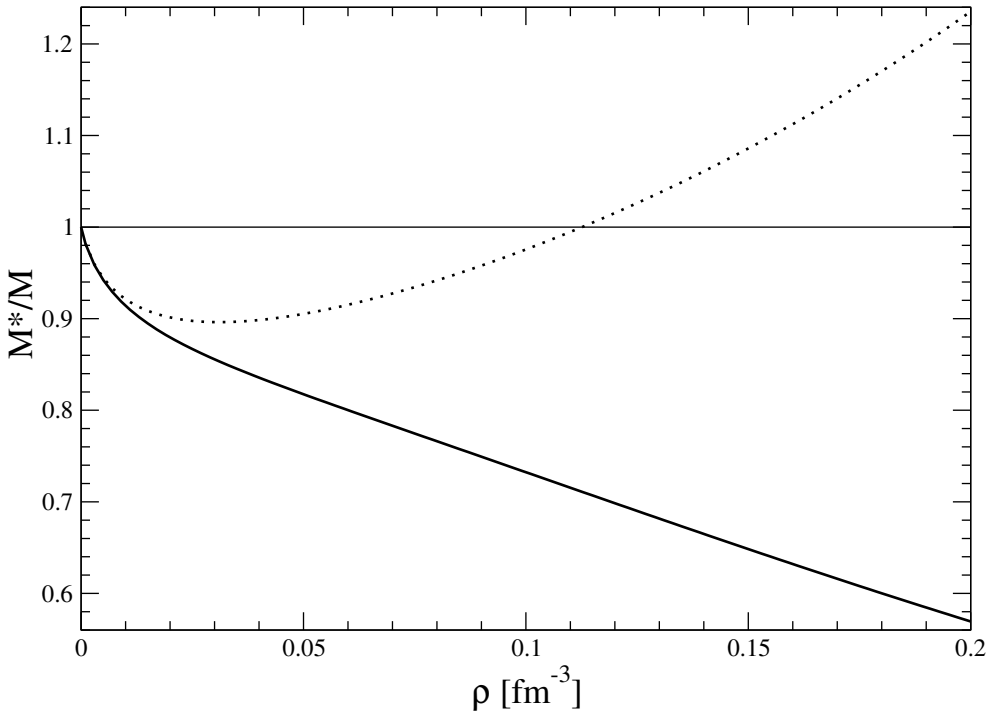

Figure 7.9: The effective nucleon mass $\tilde{M}_{\rm N}^{\star}(\rho)$ divided by the free nucleon mass $M_{\rm N}$ as a function of the nucleon density ρ. The dotted line shows the result of section 5.1 based on single and iterated pion exchange only. The full line includes in addition the effects from 2π-exchange with virtual Δ-excitation.

1π-exchange only. The full line includes in addition the effects from 2π-exchange with virtual Δ-excitation. It is clearly visible that the inclusion of the πNΔ-dynamics leads to a substantial improvement of the effective nucleon mass $\tilde{M}_{\rm N}^{\star}(\rho)$ as it now decreases monotonically with the density. This behavior is a direct reflection of the improved momentum dependence of the real single-particle potential $U(p, k_{\rm f})$ (see fig. 7.5). Our prediction for the effective nucleon mass at saturation density, $\tilde{M}_{\rm N}^{\star}(\rho_0) = 0.64 M_{\rm N}$, is comparable to the typical value $\tilde{M}_{\rm N}^{\star}(\rho_0) \simeq 0.7 M_{\rm N}$ found with phenomenological Skyrme forces [61, 64]. The full curve in fig. 7.9 again displays strong curvature effects at low densities $\rho < 0.05\,{\rm fm}^{-3}$. They originate from the explicit presence of the small mass scale $m_\pi = 135\,{\rm MeV}$ in our calculation.

Figure 7.10 shows the strength function $F_\nabla(k_{\rm f})$ attached to the $(\boldsymbol{\nabla}\rho)^2$-term in the nuclear energy density functional, versus the nucleon density $\rho = 2k_{\rm f}^3/3\pi^2$. The dotted line gives the result of section 5.1 based on 1π- and iterated 1π-exchange only and the full line includes in addition the effects from 2π-exchange with virtual Δ-excitations. The subtraction constant B_d (representing density independent short-range contributions) has been set to zero. In the region around saturation density $\rho_0 \simeq 0.16\,{\rm fm}^{-3}$ one observes a clear improvement. Now the full line meets the band spanned by the three phenomenological Skyrme forces SIII [61], Sly [64] and MSk [69]. However, the strong rise of $F_\nabla(k_{\rm f})$ towards low densities remains. As explained in section 5.1.3, this behavior reflects chiral singularities (of the form m_π^{-2} and m_π^{-1}) in the contributions from 1π-exchange and

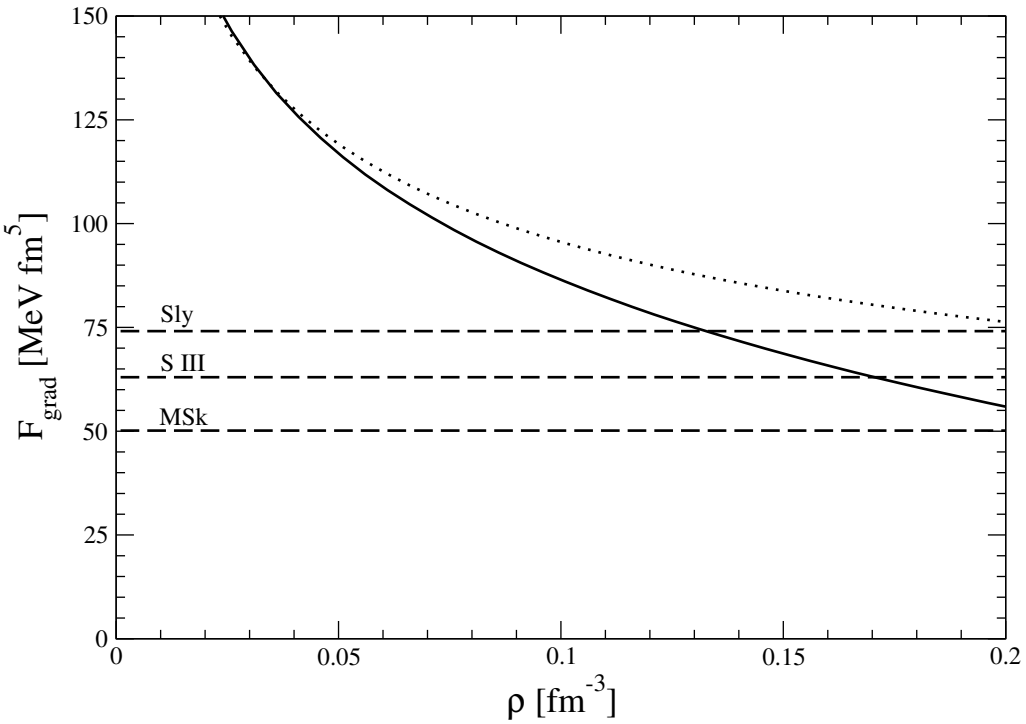

Figure 7.10: The strength function $F_\nabla(k_\mathrm{f})$ multiplying the $(\boldsymbol{\nabla}\rho)^2$-term in the nuclear energy density functional versus the nucleon density $\rho = 2k_\mathrm{f}^3/3\pi^2$. The dotted line shows the result of section 5.1 based on single and iterated pion exchange only. The full line includes in addition the effects from 2π-exchange with virtual Δ-excitation.

iterated 1π-exchange.

At lower densities $\rho \lesssim 0.5\rho_0$, the strength function $F_\nabla(k_\mathrm{f})$ and the equation of state $\bar{E}(k_\mathrm{f})$ are quite close to the results of section 5.1.3. The values of $F_\nabla(k_\mathrm{f})$ and $\bar{E}(k_\mathrm{f})$ in this density regime determine, via eq. (5.12), the surface energy a_s of semi-infinite nuclear matter. It is thus not surprising that the value $a_s = 24.2\,\mathrm{MeV}$, including the effects from 2π-exchange with virtual Δ-excitations, is only 1 MeV smaller than the value found in section 5.1.3 based solely on 1π-exchange. The number $a_s = 24.2\,\mathrm{MeV}$ still overestimates semi-empirical determinations of the surface energy, such as $a_s = 20.7\,\mathrm{MeV}$ of ref. [71] or $a_s = 18.2\,\mathrm{MeV}$ of ref. [70], by 17% or more.[2] Of course, considering the strong rise of the strength function $F_\nabla(k_\mathrm{f})$ at low densities, the same reservations regarding the reliability of the density-matrix expansion of Negele and Vautherin [60] at low densities apply as in section 5.1.3. Therefore, one should not trust the curves in fig. 7.10 below $\rho = 0.05\,\mathrm{fm}^{-3}$. Getting the right order of magnitude for $F_\nabla(k_\mathrm{f})$ in the density region $0.1\,\mathrm{fm}^{-3} < \rho < 0.2\,\mathrm{fm}^{-3}$ is already a highly satisfactory result.

In fig. 7.11 we show the strength function $F_\mathrm{so}(k_\mathrm{f})$ related to the $\boldsymbol{\nabla}\rho \cdot \mathbf{J}$-term in the energy density functional. The dotted line includes only the contributions from 1π- and

[2] One could reproduce the surface energy $a_s = 20.7\,\mathrm{MeV}$ of ref. [71] by adjusting the short-range parameter B_d in eq. (7.13) to the value $B_d = -75$. The full curve for $F_\nabla(k_\mathrm{f})$ in fig. 7.10 would then be shifted downward by $29\,\mathrm{MeV\,fm}^5$.

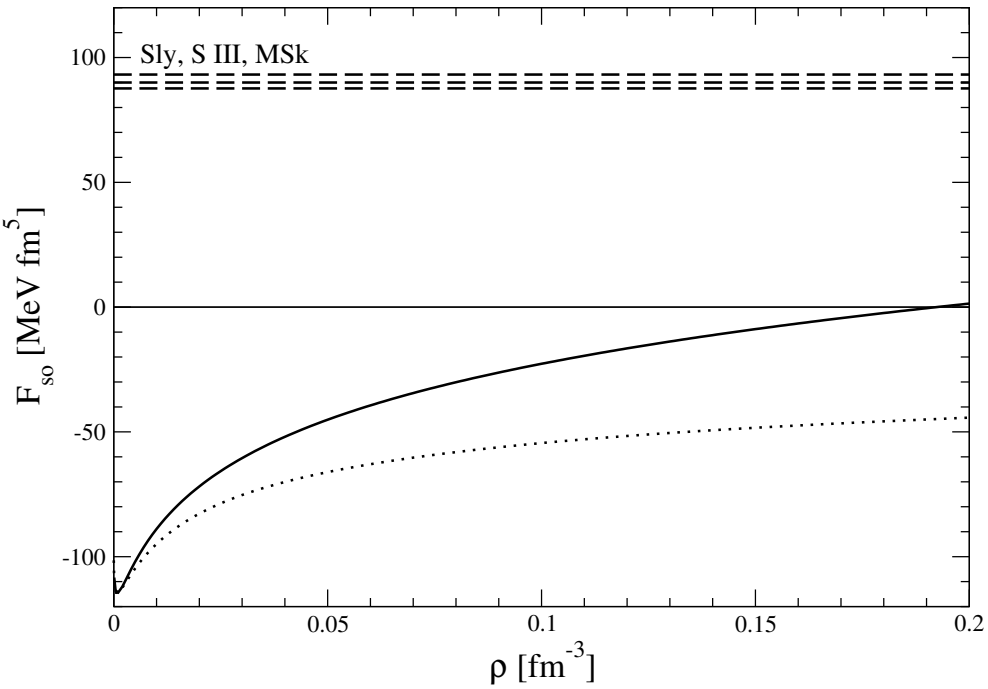

Figure 7.11: The strength function $F_{\rm so}(k_{\rm f})$ multiplying the $\boldsymbol{\nabla}\rho\cdot\mathbf{J}$-term in the nuclear energy density functional versus the nucleon density $\rho = 2k_{\rm f}^3/3\pi^2$. The dotted line shows the result of section 5.1 based on single and iterated pion exchange only. The full line includes in addition the effects from 2π-exchange.

iterated 1π-exchange. The full line also includes the contributions from 2π-exchange. The corresponding expressions involving Δ-excitations have been calculated in ref. [89] and are quoted in eqs. (B.142) and (B.143) while the contribution involving only nucleons in intermediate states is given in a suitably subtracted form in eq. (B.145) (see also [90]). Comparison of the full and dotted lines in fig. 7.11 shows that near saturation density, $\rho \simeq 0.16\,\mathrm{fm}^{-3}$, the contributions involving Δ-excitations nearly cancel the negative contributions from 1π- and iterated 1π-exchange. To get close to the empirical values from Skyrme calculations (the dashed lines in fig. 7.11), one still has to add a large positive term by adjusting the subtraction constant $B_{\rm so}$. This would account for the short range spin-orbit strength resulting from the strong scalar and vector background fields of the QCD ground state which is beyond chiral perturbation theory.

7.4.2 Example: Calculation of ^{40}Ca

The results for $F_\nabla(k_{\rm f})$ and $F_{\rm so}(k_{\rm f})$ shown in figs. 7.10 and 7.11 already indicate that the inclusion of πNΔ-dynamics will not change the results for ^{40}Ca significantly. Since $F_{\rm so}(k_{\rm f})$ still does not give a positive contribution, the conclusion that the spin-orbit force is mainly generated by the large scalar and vector mean fields of the nuclear ground state remains unchanged. Compared to section 5.1.4, a slightly smaller positive shift of $C_{\rm so} \simeq 108\,\mathrm{MeV\,fm}^5$ (corresponding to a value of $B_{\rm so} \simeq 280$ in eq. (7.12)) is required to

reproduce the correct 6 MeV spin-orbit splitting in the 1d orbital.

Compared to the results in section 5.1, the shift of $F_\nabla(k_\mathrm{f})$ towards the empirical region and the resulting slightly lower surface energy $a_s = 24.2\,\mathrm{MeV}$ entail somewhat improved values $E/A = -6.9\,\mathrm{MeV}$ for the binding energy and $r_\mathrm{C} = 3.53\,\mathrm{fm}$ for the charge radius. Adjusting $B_d = -23.5$ in eq. (7.12) (shifting $F_\nabla(k_\mathrm{f})$ downward by $C_\nabla = -9\,\mathrm{MeV\,fm}^5$) leads to the correct Coulomb radius $r_\mathrm{C} = 3.49\,\mathrm{fm}$. However, even in this case the binding energy $E/A = -7.3\,\mathrm{MeV}$ is still approximately 15% below the empirical value $E^\mathrm{exp}/A = -8.55\,\mathrm{MeV}$.

On the other hand, by using a constant strength function $F_\nabla(k_\mathrm{f}) = 72.7\,\mathrm{MeV\,fm}^5$ and minimally adjusting the nuclear matter saturation point to $k_{\mathrm{f},0} = 262.1\,\mathrm{MeV}$ and $\bar{E}_0 = -16.2\,\mathrm{MeV}$ (using $B_3 = -8.0$) leads to a reproduction of the experimental binding energy and Coulomb radius of ^{40}Ca with an error of only 1%. This shows again that the failure to describe ^{40}Ca is mainly due to the unrealistically strong rise of $F_\nabla(k_\mathrm{f})$ at low densities.

7.5 Equation of state of pure neutron matter

This section is devoted to the equation of state of pure neutron matter. In comparison with the calculation of isospin-symmetric nuclear matter in section 7.1, the only change is in the isospin factors of the 2π-exchange diagrams with virtual Δ-excitation. The short-range contribution reads

$$\bar{E}_\mathrm{n}^{(\mathrm{NN})}(k_\mathrm{n}) = B_{\mathrm{n},3}\frac{k_\mathrm{n}^3}{M_\mathrm{N}^2} + B_{\mathrm{n},5}\frac{k_\mathrm{n}^5}{M_\mathrm{N}^4}\,, \tag{7.14}$$

where $B_{\mathrm{n},3}$ and $B_{\mathrm{n},5}$ are two new subtraction constants. Note that the Pauli exclusion principle forbids a three-neutron contact interaction. The remaining contributions from 2π-exchange are given in eqs. (B.71-B.73) in the appendix. All three three-body diagrams in fig. 7.2 have now the same isospin factor 2/3 since only the $2\pi^0$-exchange is possible between neutrons. The additional contributions to $\bar{E}_\mathrm{n}(k_\mathrm{n})$ from the (relativistically improved) kinetic energy, from 1π-exchange and from iterated 1π-exchange have been written down in eqs. (B.62-B.67).

Figure 7.12 shows the energy per particle $\bar{E}_\mathrm{n}(k_\mathrm{n})$ of pure neutron matter as a function of the neutron density $\rho_\mathrm{n} = k_\mathrm{n}^3/3\pi^2$. The dashed (concave) curve gives the result based on chiral πN-dynamics only (see section 3.6). The full curve includes the chiral πNΔ-dynamics. The short-range parameters $B_{\mathrm{n},3}$ and $B_{\mathrm{n},5}$ (controlling the contribution of a nn-contact interaction to $\bar{E}_\mathrm{n}(k_\mathrm{n})$) have been adjusted to the values $B_{\mathrm{n},3} = -0.95$ and $B_{\mathrm{n},5} = -3.58$.[3] The dashed-dotted curve in fig. 7.12 is the result of the many-body calculation of the Urbana group [18], to be considered as representative of realistic neutron matter calculations. Moreover, the dotted curve gives one half of the kinetic energy of a free neutron gas, $\bar{E}_\mathrm{kin}(k_\mathrm{n})/2 = 3k_\mathrm{n}^2/20M_\mathrm{N}$. Results of recent quantum Monte-Carlo calculations in ref. [4] have demonstrated that the neutron matter equation of

[3] The short-range parameters $B_{\mathrm{n},3}$ and $B_{\mathrm{n},5}$ have been adjusted such that the asymmetry energy at saturation density takes on the value $\bar{A}(k_{\mathrm{f},0}) = 34\,\mathrm{MeV}$.

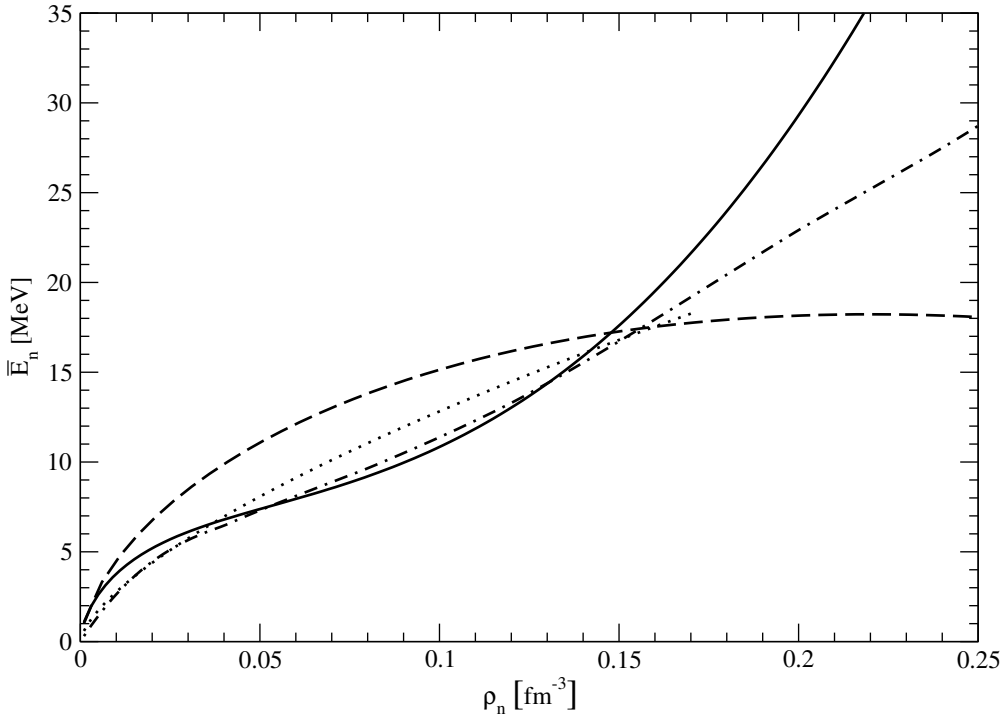

Figure 7.12: The energy per particle $\bar{E}_{\rm n}(k_{\rm n})$ of pure neutron matter as a function of the neutron density $\rho_{\rm n} = k_{\rm n}^3/3\pi^2$. The dashed curve gives the result of section 3.6. The full curve includes the πNΔ-dynamics and two adjusted short-range parameters $B_{\rm n,3} = -0.95$ and $B_{n,5} = -3.58$. The dashed-dotted curve stems from the sophisticated many-body calculation of the Urbana group [18]. The dotted curve gives one half of the kinetic energy $\bar{E}_{\rm n,kin}(k_{\rm n})/2 = 3k_{\rm n}^2/20M_{\rm N}$.

state at low neutron densities $\rho_{\rm n} < 0.05\,{\rm fm}^{-3}$ is well approximated by this simple form. One observes that up to $\rho_{\rm n} = 0.16\,{\rm fm}^{-3}$ our result for $\bar{E}_{\rm n}(k_{\rm n})$ is very close to that of the sophisticated many-body calculation [4, 18]. At higher densities we find a stiffer neutron matter equation of state. This behavior cannot be changed much by tuning the parameters $B_{\rm n,3}$ and $B_{\rm n,5}$. Again, one should not expect that our approach works at Fermi momenta larger than $k_{\rm n} \simeq 350\,{\rm MeV}$ corresponding to $\rho_{\rm n} = 0.19\,{\rm fm}^{-3}$. Note that the same Fermi momentum in symmetric nuclear matter corresponds to twice this density.

One of the most important results of the present calculation is that the unrealistic downward bending of $\bar{E}_{\rm n}(k_{\rm n})$ (as shown by the dashed curve in fig. 7.12) disappears after the inclusion of the chiral πNΔ-dynamics. This is a manifestation of improved isospin properties.

7.6 Asymmetry energy

As a further test of isospin properties we consider in this section the density dependent asymmetry energy $\bar{A}(k_{\rm f})$. As outlined in section 3.5, the asymmetry energy is generally

defined by the expansion of the energy per particle of isospin-asymmetric nuclear matter (described by different proton and neutron Fermi momenta $k_{\rm p,n} = k_{\rm f}(1 \mp \delta)^{1/3}$) around the symmetry line:

$$\bar{E}_{\rm as}(k_{\rm p}, k_{\rm n}) = \bar{E}(k_{\rm f}) + \delta^2\, \bar{A}(k_{\rm f}) + \mathcal{O}(\delta^4)\,. \tag{7.15}$$

Following the scheme in the previous sections we get the following contribution to the asymmetry energy $\bar{A}(k_{\rm f})$ involving the subtraction constants $B_{3,5}$:

$$\bar{A}^{(\rm NN)}(k_{\rm f}) = (2B_{\rm n,3} - B_3)\frac{k_{\rm f}^3}{M_{\rm N}^2} + (3B_{\rm n,5} - B_5)\frac{10k_{\rm f}^5}{9M_{\rm N}^4}\,. \tag{7.16}$$

Here we have taken care of the fact that there are only two independent (S-wave) NN-contact couplings which can produce terms linear in density. It is remarkable that also the other coefficient $10(3B_{\rm n,5} - B_5)/9$ in front of the $k_{\rm f}^5/M_{\rm N}^4$-term is completely fixed. This fact can be shown on the basis of the most general order-p^2 NN-contact interaction written down in eq. (2.2) of ref. [91]. Out of the seven low-energy constants $C_1, \ldots, C_7$ only two independent linear combinations, C_2 and $C_1 + 3C_3 + C_6$, come into play for homogeneous and spin-saturated nuclear matter.

The additional three-nucleon contact interaction $\sim B_6(\bar{N}N)^3$ has the interesting property that it contributes equally but with opposite sign to the energy per particle $\bar{E}(k_{\rm f})$ (see eq. (7.4)) and the asymmetry energy $\bar{A}(k_{\rm f})$:

$$\bar{A}^{(\rm NNN)}(k_{\rm f}) = -B_6\frac{k_{\rm f}^6}{M_{\rm N}^5}\,. \tag{7.17}$$

The asymmetry energy $\bar{A}(k_{\rm f})$ is completed (at 3-loop order) by adding to the new terms involving virtual Δ-excitations and the additional three-body contact interaction given in eqs. (7.16-7.17) and (B.57-B.59) the contributions from the (relativistically improved) kinetic energy, 1π-exchange and iterated 1π-exchange written down in eqs. (B.48-B.53) in the appendix.

In the calculation of the asymmetry energy we use consistently the previously fixed short-distance parameters $B_3 = -7.99$, $B_{\rm n,3} = -0.95$, $B_5 = 0$, $B_{\rm n,5} = -3.58$, and $B_6 = -31.3$. Figure 7.13 shows the asymmetry energy $\bar{A}(k_{\rm f})$ as a function of the nucleon density $\rho = 2k_{\rm f}^3/3\pi^2$. The dashed (concave) curve corresponds to the result based on chiral πN-dynamics only (see section 3.5). The full curve includes the chiral πNΔ-dynamics. The corresponding value of the asymmetry energy at saturation density $\rho_0 = 0.157\,{\rm fm}^{-3}$ is $\bar{A}(k_{\rm f,0}) = 34.0\,{\rm MeV}$. It decomposes as $\bar{A}(k_{\rm f,0}) = (12.1 + 119.3 - 109.9 - 1.3 + 13.8)\,{\rm MeV}$ into contributions of second, third, fourth, fifth, and sixth power of small momenta, again with a balance between large third and fourth order terms. The value $\bar{A}(k_{\rm f,0}) = 34.0\,{\rm MeV}$ is consistent with most of the existing empirical determinations of the asymmetry energy. For example, a recent microscopic estimate in a relativistic mean-field model (constrained by some specific properties of certain nuclei) gave the value $\bar{A}(k_{\rm f,0}) = (34 \pm 2)\,{\rm MeV}$ [92]. For comparison, other empirical values obtained from extensive fits of nuclide masses are $\bar{A}(k_{\rm f,0}) = 36.8\,{\rm MeV}$ [71] or $\bar{A}(k_{\rm f,0}) = 33.2\,{\rm MeV}$ [34]. The slope of the asymmetry energy at saturation density, $L = k_{\rm f,0}A'(k_{\rm f,0})$, is likewise an interesting quantity. As demonstrated in fig. 11 of ref. [93] the neutron skin thickness of ^{208}Pb is linearly correlated with the

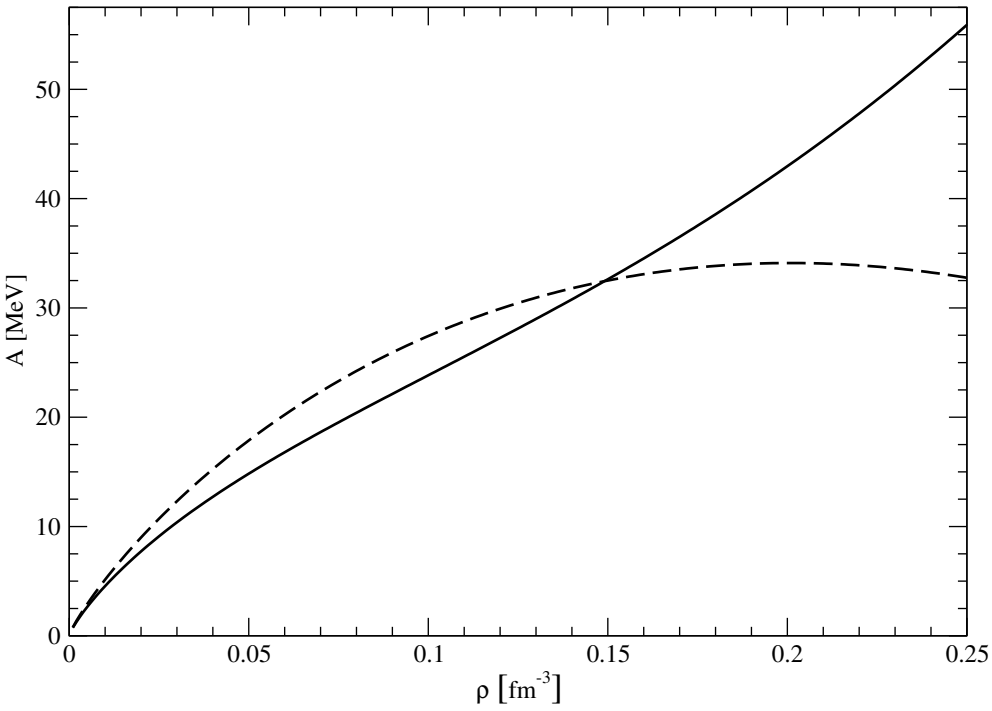

Figure 7.13: The asymmetry energy $\bar{A}(k_\mathrm{f})$ as a function of the nucleon density $\rho = 2k_\mathrm{f}^3/3\pi^2$. The dashed curve shows the result of section 3.5. The full curve includes the chiral πNΔ-dynamics.

slope parameter L. We extract from the full curve in fig. 7.13 the value $L = 90.8\,\mathrm{MeV}$. This prediction is not far from the values $L \simeq 100\,\mathrm{MeV}$ quoted in ref. [71] and $L = 119.2\,\mathrm{MeV}$ obtained from the "standard" relativistic force NL3 [94]. Furthermore, we extract from the curvature of our asymmetry energy $\bar{A}(k_\mathrm{f})$ at saturation density ρ_0 the positive asymmetry compressibility $K_\mathrm{as} = k_{\mathrm{f},0}^2 A''(k_{\mathrm{f},0}) - 2L = 160.5\,\mathrm{MeV}$.

Again, the most important feature visible in fig. 7.13 is that the inclusion of the chiral πNΔ-dynamics eliminates the (unrealistic) downward bending of the asymmetry $\bar{A}(k_\mathrm{f})$ at higher densities $\rho > 0.2\,\mathrm{fm}^{-3}$ (as displayed by the dashed curve in fig. 7.13). This is once more a manifestation of improved isospin properties.

Via a generalization of the Hugenholtz-van Hove theorem eq. (3.15) to isospin-asymmetric nuclear matter, one can relate the asymmetry energy $\bar{A}(k_\mathrm{f})$ to the isovector single-particle potential $U_I(p, k_\mathrm{f})$ at the Fermi surface ($p = k_\mathrm{f}$):

$$U_I(k_\mathrm{f}, k_\mathrm{f}) = 2\bar{A}(k_\mathrm{f}) - \frac{k_\mathrm{f}^2}{3M_\mathrm{N}} + \frac{k_\mathrm{f}^4}{6M_\mathrm{N}^3} - \frac{k_\mathrm{f}}{3}\,\frac{\partial U(p, k_\mathrm{f})}{\partial p}\bigg|_{p=k_\mathrm{f}} . \tag{7.18}$$

The isovector single-particle potential $U_I(p, k_\mathrm{f})$ is defined by the following decomposition of the (real) single-particle potential in isospin-asymmetric nuclear matter:

$$U(p, k_\mathrm{f}) - U_I(p, k_\mathrm{f})\,\tau_3\,\delta + \mathcal{O}(\delta^2)\,, \qquad \delta = \frac{\rho_\mathrm{n} - \rho_p}{\rho_\mathrm{n} + \rho_p}\,, \tag{7.19}$$

with $U(p, k_\mathrm{f})$ the isoscalar (real) single-particle potential discussed in section 7.2. The decomposition eq. (7.19) expresses the fact that any relative excess of neutrons over protons in the nuclear medium leads to a different "mean-field" for a proton and a neutron. $U_I(p, k_\mathrm{f})$ can also be calculated explicitly in our framework. The results are presented in ref. [95].

7.7 Chiral condensate

In this section we reinvestigate the influence of 1π- and 2π-exchange on the chiral condensate, now taking into account virtual Δ-excitations in intermediate states. As we have seen in section 3.7, the chiral condensate at finite density is determined by the dependence of the equation of state on the average quark mass $\bar{m}$. This quark mass dependence can be rewritten in terms of the pion mass:

$$\frac{\langle\bar{q}q\rangle_\rho}{\langle\bar{q}q\rangle_0} = 1 - \frac{\rho}{2m_\pi f_\pi^2}\left(\frac{2\sigma_{\pi\mathrm{N}}}{m_\pi} + \frac{\mathrm{d}\bar{E}(k_\mathrm{f})}{\mathrm{d}m_\pi}\right). \tag{7.20}$$

Apart from the explicit dependence on m_π, $\bar{E}(k_\mathrm{f})$ contains several quantities that have unknown m_π (or equivalently $\bar{m}$) dependence. Apart from M_N, g_A, and f_π already mentioned in section 3.7, the inclusion of Δ-excitations now leads to the appearance of the ΔN-mass splitting Δ and the ΔN-coupling (approximated as $3g_\mathrm{A}/\sqrt{2}$ in our calculations), which might also be modified when the pion mass changes. Because of these uncertainties, we again restrict ourselves to the explicit m_π dependencies in $\bar{E}(k_\mathrm{f})$.

The full line in fig. 7.14 shows the ρ dependence of the chiral condensate caused by 1π- and 2π-exchange taking into account both nucleon and virtual Δ(1232)-intermediate states. Comparison with the corresponding result incorporating only nucleon intermediate states (the dash-dotted line in fig. 7.14) shows that the contributions involving virtual Δ-excitations work against chiral restoration. However, even with this additional contribution, the long-range dynamics represented by chiral 1π- and 2π-exchange does not stabilize the chiral condensate. Therefore we expect that short-range dynamics encoded in the regularization dependent subtraction constants B_3 and B_5 will have a crucial influence on the behavior of the chiral condensate at finite density.

To improve the prediction of the chiral condensate, one would also have to take into account the implicit m_π dependence of g_A, M_N, etc. and calculate explicit expressions for the subtraction constants B_3 and B_5 in e. g. dimensional or cut-off regularization. However, these expressions would include not only the contributions from pion loops (with their specific m_π dependence) but also terms involving low energy constants encoding the contributions of contact interactions. These contact terms would then (just as the three-body term involving B_6) give rise to additional unknown m_π dependence. Therefore the best one could do within this given framework is calculate a band estimating a range for the behavior of the chiral condensate. Similar problems were encountered in a calculation of the deuteron binding energy in the chiral limit [96].

However, we can get an idea about the size of the missing corrections to the chiral condensate by looking at terms contributing to the subtraction constants B_3 and B_5.

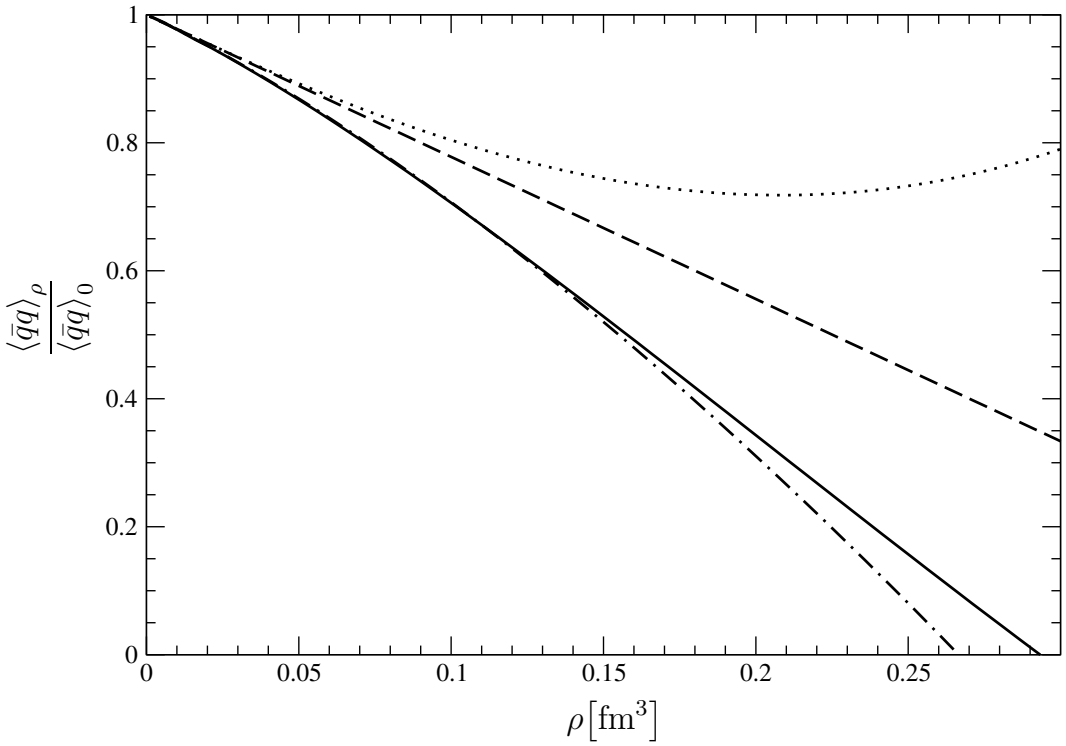

Figure 7.14: The chiral condensate at density ρ as given by the explicit m_π dependence of 1π- and 2π-exchange taking into account both virtual Δ and nucleon intermediate states (full line) and only nucleon intermediate states (dash-dotted line). These two curves do not include any contributions from short-range dynamics, while the dotted curve corresponds to the full line plus eq. (7.21). The dashed line shows the leading term from eq. (7.20) which involves $\sigma_{\pi\mathrm{N}}$.

Terms proportional to odd powers of m_π (i. e. fractional powers of the average quark mass $\bar{m}$) can only originate from pion loops since contact terms in the Lagrangian always involve integer powers of the quark mass. As a matter of fact, the contributions of the second and third diagram in fig. 7.1 give contributions to B_3 and B_5 proportional to m_π^3 and m_π^1 respectively:

$$B_3 = B_3^{(\mathrm{rest})} - \frac{15 g_\mathrm{A}^4 M_\mathrm{N}^2}{128\Delta f_\pi^4 \pi^3} m_\pi^3 \qquad B_5 = B_5^{(\mathrm{rest})} + \frac{11 g_\mathrm{A}^4 M_\mathrm{N}^4}{1280\Delta f_\pi^4 \pi^3} m_\pi \tag{7.21}$$

The m_π dependent terms shown in eq. (7.21) are equal for dimensional and cut-off regularization.[4] While the m_π term is quite small, the m_π^3 term gives a sizable contribution to the chiral condensate working against chiral restoration. The condensate including this effect is shown as the dotted line in fig. 7.14. Including more regularization and

[4]The explicit results for $B_{3,5}$ in cut-off regularization can be extracted from eqs. (B.12) to (B.18) of ref. [15].

scale dependent contributions from the pion loops to B_3 and B_5 results in a broad band around the dotted line in fig. 7.14.

Note that at saturation density ρ_0 the dotted line in in fig. 7.14 deviates from the leading linear term by only about 10%. The use of the leading linear approximation for the derivation of the scalar self energy from QCD sum rules in refs. [21, 22] is justified within such errors, modulo remaining short range pieces not covered by the present expansion.

As a conclusion we stress again that the long range contributions of 1π- and 2π-exchange alone do not allow a reliable estimate for the chiral condensate. The short range dynamics encoded in the subtraction constants B_3 and B_5 gives large corrections which probably work against chiral restoration.

7.8 Final remarks

We have seen that by including the effects from two-pion exchange with single and double virtual $\Delta(1232)$-isobar excitation, the description of several semi-empirical properties of nuclear matter can be greatly improved, however at the price of introducing an additional three-nucleon interaction involving the new parameter B_6. This three-body term accounts for short-range correlations in three-body terms outside of chiral perturbation theory and for higher order terms such as 4-loop contributions to the energy density. The momentum dependence of the real single-particle potential $U(p, k_\mathrm{f})$ is improved significantly by including the chiral πNΔ-dynamics. As a consequence the critical temperature of the liquid-gas phase transition gets lowered to the realistic value $T_c \simeq 15\,\mathrm{MeV}$. The isospin properties of nuclear matter are also substantially improved. The energy per particle $\bar{E}_\mathrm{n}(k_\mathrm{n})$ of pure neutron matter and the asymmetry energy $\bar{A}(k_\mathrm{f})$ now show a monotonic growth with density. In the density regime $\rho = 2\rho_\mathrm{n} < 0.2\,\mathrm{fm}^{-3}$ relevant for conventional nuclear physics, we find good agreement with sophisticated many-body calculations and (semi)-empirical values.

In passing we note that the inclusion of the chiral πNΔ-dynamics guarantees the spin-stability of nuclear matter [97]. These improvements can be traced back to repulsive two-body Fock terms as well as three-body terms with a very specific density and momentum dependence. Open questions concerning the role of yet higher orders in the small momentum expansion and its convergence remain and should be further explored.

Our calculation now accounts for the fact that there exist two hadronic scales, the pion mass $m_\pi = 135\,\mathrm{MeV}$ and the delta-nucleon mass splitting $\Delta = 293\,\mathrm{MeV}$, which are smaller than or comparable to the Fermi momentum $k_{\mathrm{f},0} \simeq 262\,\mathrm{MeV}$ of equilibrated nuclear matter. Propagation effects of quasi-particles associated with these "light" scales are resolvable. Therefore pions and Δ-isobars must be included as explicit degrees of freedom in the nuclear many-body problem. Controlled by a systematic expansion in small scales $(k_\mathrm{f}, m_\pi, \Delta)$, the dynamics of the interacting πNΔ-system is worked out up to three-loop order in the energy density. In this effective field theory approach the basic mechanism for nuclear binding and saturation are attractive 2π-exchange interactions of the van der Waals type on which Pauli blocking acts in the nuclear medium. Most

other phenomenological approaches ignore these "light" physical degrees of freedom and parameterize the relevant low-energy dynamics in terms of strongly coupled heavy scalar and vector bosons (σ, ω, ρ, δ, etc.). Their propagation takes place on length scales of 0.5 fm or less and can therefore not be resolved in the domain relevant to nuclear physics. We are instead guided by the observation that the nuclear many-body problem involves the separation of scales that is characteristic of low-energy QCD and its (chiral) symmetry breaking pattern.

Chapter 8

Conclusions and outlook

In this thesis we have established a connection of various (semi-)empirical nuclear matter observables to important aspects of low-energy QCD, using a calculational framework based on chiral perturbation theory. The key ingredient is the separation of low and high energy scales present in QCD. This separation becomes apparent in the hadron spectrum as a mass gap between the pion mass $m_\pi \simeq 0.14\,\mathrm{GeV}$ and other typical hadronic masses like the nucleon mass $M_\mathrm{N} \simeq 1\,\mathrm{GeV}$. At the densities of interest in nuclear physics, the relevant scale in nuclear matter, the Fermi momentum $k_\mathrm{f} \simeq 2m_\pi$, is roughly comparable in magnitude to the pion mass. This fact leads to the identification of the pion as an important dynamical degree of freedom that must be treated explicitly in nuclear matter calculations. On the other hand, the detailed dynamics represented by the exchange of heavier mesons, such as the ρ and the ω, is not resolved at the densities of interest and can be subsumed in a few nucleon-nucleon contact interaction terms.

In addition to the nucleons and the pions, the $\Delta(1232)$-isobar constitutes another important degree of freedom that should be treated explicitly. Since the relevant scale arising in its contributions, the delta-nucleon mass splitting $\Delta = 293\,\mathrm{MeV}$, is also comparable to the Fermi momentum in nuclear matter, propagation effects of the $\Delta(1232)$ can be resolved at the densities of interest. The $\Delta(1232)$-resonance has been included as a dynamical degree of freedom in the extended version of our calculational scheme presented in chapter 7.

We have seen that a nuclear equation of state with realistic saturation properties can already be generated by the simplest version of our framework, including only the contributions of chiral one- and iterated one-pion exchange up to order $\mathcal{O}(k_\mathrm{f}^4)$ and parameterizing all unresolved short-range dynamics with a simple momentum cut-off. This finding is quite remarkable in two respects. Firstly, it is possible to reproduce three (semi-)empirical quantities, namely the energy per particle $\bar{E}_0 \simeq -16\,\mathrm{MeV}$, the saturation density ρ_0, and the compression modulus K, by fine-tuning only a single adjustable parameter. Secondly, since the saturation energy $\bar{E}_0$ arises by a cancellation of individually large terms, even comparatively small contributions are important on the scale of $\bar{E}_0$ as we have demonstrated by omitting various parts of the pion exchange T-matrix. It is therefore quite surprising how well the equation of state is reproduced by this simple scheme. On the other hand, it is not important for the bulk saturation properties whether the $\Delta(1232)$-isobar is treated explicitly as a dynamical degree of freedom or implicitly via the effective low-energy constants c_i of the chiral pion-nucleon effective Lagrangian

(see ref. [17]), thus counting the corresponding contributions as fifth or sixth order in small momenta respectively. Nuclear saturation is already achieved by the lower order terms up to $\mathcal{O}(k_\mathrm{f}^4)$. In our framework, an adjustable term linear in ρ accounts for all short-distance and nonperturbative dynamics, including possible strong Lorentz scalar and vector fields which tend to cancel each other in nuclear properties with the exception of the spin-orbit splitting.

Besides the saturation point we have also investigated several other interesting properties of nuclear matter. Among these are the single particle potential and the asymmetry energy of nuclear matter and the equation of state of pure neutron matter. We have seen that results for these quantities produced by a simple scheme not including the $\Delta(1232)$-degree of freedom and subsuming all short-range dynamics in a single adjustable cut-off parameter are only partially satisfactory. For example, while the asymmetry energy $\bar{A}(\rho_0)$ at the saturation point is well reproduced and neutron matter is predicted to be unbound, the curves for both the asymmetry energy and the neutron matter equation of state show a downward bending behavior at higher densities that is presumably not realistic. Furthermore, while the real part of the single particle potential has the correct depth at $p = 0$, its momentum dependence is too strong resulting in an incorrect density of states near the Fermi surface which in turn leads to a too high critical temperature for the liquid-gas phase transition in nuclear matter.

These deficiencies are fixed by the extended framework introduced in chapter 7 which includes the $\Delta(1232)$-isobar explicitly and employs two parameters per isospin channel for the unresolved short-range physics. The expansion is carried out up to three-loop order and up to fifth order in small scales (m_π, k_f, Δ). In this scheme, the asymmetry energy energy and the neutron matter equation of state are monotonically rising. The momentum dependence of the single particle potential is significantly improved. As a consequence the liquid-gas phase transition of nuclear matter has now a realistic critical temperature $T_c \simeq 15\,\mathrm{MeV}$.

The calculation of inhomogeneous nuclear matter and finite nuclei described in chapter 5.1 using the energy density functional from πN-dynamics alone has not been quite as successful. Chiral πN-dynamics alone turns out not to be able to provide the strong spin-orbit force known from nuclear phenomenology. In the standard Skyrme interactions, this feature is simply fixed by hand. A more satisfactory way is treating chiral pion exchange as fluctuations on top of the large scalar and vector mean-fields of the QCD ground state in the presence of a nuclear medium [21,22]. While these background fields mostly cancel each other in the energy per particle they produce a large spin-orbit force in a natural way.

The problems caused by the strong density dependence of our energy density functional, leading to incorrect binding energies for finite nuclei, need to be further addressed. The reason for this is not yet understood and it remains to be seen whether this is an inherent problem of the density-matrix expansion [72] or whether it is related to our perturbative framework. Perturbation theory may work in a certain range of Fermi momenta, but fails at very low densities where the in-medium NN-amplitude must turn into the (unitary) free T-matrix which cannot be handled perturbatively in central partial waves.

While these questions require further studies, our framework is successful at describing most (semi-)empirical properties of nuclear matter such as the equations of state of isospin symmetric nuclear matter and of pure neutron matter, the asymmetry energy, the single particle potential, and the liquid-gas phase transition. We can therefore conclude that a connection from nuclear physics to low-energy QCD in the spirit of effective field theory is indeed possible. For this purpose it is important to incorporate the fact that there are two hadronic scales, the pion mass and the delta-nucleon mass splitting that are smaller than or comparable to the Fermi momentum of nuclear matter in equilibrium. Therefore pions and Δ-isobars have to be included as explicit degrees of freedom in the nuclear many-body problem. In our effective field theory approach nuclear binding and saturation are primarily caused by attractive 2π-exchange interactions of the van der Waals type on which Pauli blocking acts in the nuclear medium. The main guiding principle is the separation of scales that is characteristic for low-energy QCD and its (chiral) symmetry breaking pattern.

While we have investigated many features of the nuclear many-body problem, further work still remains to be done. An obvious task is to look into the problems we had with calculating finite nuclei based on the density-matrix expansion. It will also be interesting to see whether the spin-orbit strength of nonrelativistic origin arising in this approach will help understanding the much reduced spin-orbit splitting in Λ-hypernuclei.

Another area of interest is the already quite successful point-coupling model of refs. [21, 22] that treats chiral pionic fluctuations on top of the strong background fields arising from the QCD ground state. This model is being updated towards our extended framework that includes $\Delta(1232)$-isobars explicitly. In this context, one should also verify that the equivalence of the short-range interactions iterated to all orders in a Dirac-Brueckner calculation to the effective NN-contact interactions in our approach still holds when including the $\Delta(1232)$.

Of course another possible goal is to see whether our positive results persist when the expansion in small momenta is carried out one order further, i. e. up to $\mathcal{O}(k_\mathrm{f}^6)$. While the relativistic corrections arising from three-loop diagrams seem to be rather small [15], the very large number and complexity of four-loop diagrams make this enterprise very difficult indeed. Before venturing this way, one should remember that a perturbative expansion in quantum field theories generally results in an asymptotic series that converges towards the real result only up to some optimal order. Such questions could also arise for in-medium chiral effective field theory, in a window of Fermi momenta for which the expansion parameter $k_\mathrm{f}/4\pi f_\pi$ is still small compared to one.

Finally, we want to mention the possibility to extend our calculations to spin-polarized nuclear matter [97]. A comparison with Fermi liquid theory would then allow to calculate the Landau-Migdal parameters g_0 and g_0' which are important for many spin dependent properties of nuclei [98]. The Fermi liquid parameter g_0' has been accurately determined from Gamow-Teller resonances [99] and could provide a further quantitative test for our calculational framework.

Appendix A

Outline of the Skyrme-Hartree-Fock method

A.1 The Hartree-Fock method

The notion that nucleons in a nucleus move independently in an average potential created by all of the nucleons can be justified by the success of the phenomenological shell model (see section 2.1). This assumption leads to the problem of how to extract such a single-particle potential out of the sum of two-body interactions. This can be done by a variational principle using Slater determinants as trial wave functions. In the following, we will give an outline of this method (see e. g. ref. [65] for a more complete introduction and proofs of all the statements).

The variational equation,

$$\delta E[\Psi] = 0\,, \tag{A.1}$$

with

$$E[\Psi] = \frac{\langle\Psi|H|\Psi\rangle}{\langle\Psi|\Psi\rangle}\,, \tag{A.2}$$

is equivalent to the exact Schrödinger equation

$$H|\Psi\rangle = E|\Psi\rangle\,. \tag{A.3}$$

Variational methods become approximate as soon as $|\Psi\rangle$ is restricted to a set of mathematically simple trial wave functions, as is usually the case. If the true function is not in this set, the variation no longer yields the exact eigenfunction. However, variational methods are especially well suited for finding the ground state of a system, since the true ground state energy E_0 is a lower bound for the energy of any trial wave function $|\Psi\rangle$,

$$E[\Psi] \geq E_0\,. \tag{A.4}$$

In principle, it is also possible to calculate higher exited states by imposing the additional condition that the wave function of the next exited state is orthogonal to the (previously calculated) wave functions of the ground state and all lower exited states. Obviously, this approach can get quite complicated for higher excitations.

For a Fermion system, the simplest trial wave function is a Slater determinant

$$|\mathrm{HF}\rangle = |\Phi(1\dots A)\rangle = \prod_{i=1}^{A} a_i^\dagger |0\rangle\,, \tag{A.5}$$

in which the Fermion operators $a_k^\dagger, a_k$ correspond to the single-particle wave functions ϕ_k. This wave function $\Phi(1\dots A)$ is the eigenfunction of an average single-particle potential

$$H^{\mathrm{HF}} = \sum_{i=1}^{A} h(i)\,, \tag{A.6}$$

where the single-particle wave functions ϕ_k are in turn eigenfunctions of the single particle Hamiltonians:

$$h(i)\phi_k(i) = \epsilon_k \phi_k(i), \qquad i = \{\mathbf{r}_i, s_i, t_i\}\,. \tag{A.7}$$

If the Hamiltonian contains the kinetic energy and a two-body interaction, it can be written as

$$H = \sum_{l_1,l_2} t_{l_1 l_2} a_{l_1}^\dagger a_{l_2} + \frac{1}{4} \sum_{l_1,l_2,l_3,l_4} \bar{v}_{l_1 l_2 l_3 l_4} a_{l_1}^\dagger a_{l_2}^\dagger a_{l_4} a_{l_3}\,, \tag{A.8}$$

with the antisymmetrized matrix elements

$$\bar{v}_{l_1 l_2 l_3 l_4} = v_{l_1 l_2 l_3 l_4} - v_{l_1 l_2 l_4 l_3}\,. \tag{A.9}$$

Carrying out the variation (A.1) while making sure that one stays within the set of Slater determinants leads to

$$h_{kk'} = t_{kk'} + \sum_{i=1}^{A} \bar{v}_{kik'i} = \epsilon_k \delta_{kk'}\,. \tag{A.10}$$

In general, one does not know the wave functions ϕ_k beforehand and uses some arbitrary, complete and orthogonal set of single-particle wave functions $\{\chi_l\}$. The ϕ_k can then be expanded in this basis,

$$\phi_k = \sum_l D_{lk}\, \chi_l\,, \tag{A.11}$$

with D unitary, i. e. $D^\dagger D = D D^\dagger = 1$. With the transformation D, one converts eq. (A.10) into the Hartree-Fock equations

$$\sum_{l'} h_{ll'} D_{l'k} = \sum_{l'} \left(t_{ll'} + \sum_{i=1}^{A} \sum_{pp'} \bar{v}_{lp'l'p} D_{pi} D^*_{p'i} \right) D_{l'k} = \epsilon_k D_{lk}\,. \tag{A.12}$$

These represent a Hermitian eigenvalue problem. The coefficients D_{lk} found by its solution determine the single-particle wave functions ϕ_k. The problem is nonlinear because the matrix h depends on the wave functions ϕ_k and thus on the density ρ. Eq. (A.6) can now be written as:

$$H^{\mathrm{HF}} = \sum_{kk'} h_{kk'} a_k^\dagger a_{k'} = \sum_{kk'} \left(t_{kk'} + \sum_{j=1}^{A} \bar{v}_{kjk'j} \right) a_k^\dagger a_{k'} = \sum_k \epsilon_k a_k^\dagger a_k\,. \tag{A.13}$$

The Slater determinant $|\mathrm{HF}\rangle$, where the lowest A levels are occupied, corresponds to an energy E which is stationary against small variations of the wave functions. This energy can be expressed as

$$E_0^{\mathrm{HF}} = \sum_{i=1}^{A} \epsilon_i - \frac{1}{2} \sum_{i,j=1}^{A} \bar{v}_{ijij} \,. \tag{A.14}$$

Note that this is not the sum of the single-particle energies.

A.2 The Skyrme force

Of the many phenomenological interactions that have been used in Hartree-Fock calculations, the Skyrme force has been particularly popular because of its analytical simplicity and its ability to reproduce nuclear properties over the whole periodic table. It is a zero-range, density and momentum dependent force of the form

$$\begin{aligned} V_{\mathrm{Skrme}} = & t_0(1 + x_0 P_\sigma)\delta(\mathbf{r}_1 - \mathbf{r}_2) + \frac{1}{2} t_1 (1 + x_1 P_\sigma)\left[\mathbf{p}_{12}^2 \delta(\mathbf{r}_1 - \mathbf{r}_2) + \delta(\mathbf{r}_1 - \mathbf{r}_2)\mathbf{p}_{12}^2\right] \\ & + t_2(1 + x_2 P_\sigma)\mathbf{p}_{12} \cdot \delta(\mathbf{r}_1 - \mathbf{r}_2)\mathbf{p}_{12} + \frac{1}{6} t_3 (1 + x_3 P_\sigma)\rho^\alpha(\mathbf{R})\delta(\mathbf{r}_1 - \mathbf{r}_2) \\ & + \mathrm{i} W_0 \mathbf{p}_{12} \cdot \delta(\mathbf{r}_1 - \mathbf{r}_2)(\boldsymbol{\sigma}_1 + \boldsymbol{\sigma}_2) \times \mathbf{p}_{12} \,, \end{aligned} \tag{A.15}$$

with the relative momentum operator $\mathbf{p}_{12} = (\boldsymbol{\nabla}_1 - \boldsymbol{\nabla}_2)/2\mathrm{i}$, the spin exchange operator $P_\sigma = \frac{1}{2}(1 + \boldsymbol{\sigma}_1 \boldsymbol{\sigma}_2)$, and $\mathbf{R} = \frac{1}{2}(\mathbf{r}_1 + \mathbf{r}_2)$. For $x_3 = \alpha = 1$, the density dependent term proportional to t_3 is equivalent to a zero-range three-body force:

$$V_3 = t_3 \, \delta(\mathbf{r}_1 - \mathbf{r}_2) \, \delta(\mathbf{r}_2 - \mathbf{r}_3) \,. \tag{A.16}$$

However, this equivalence is only valid in even-even nuclei with time-reversal symmetry. For simplicity, we consider only $N = Z$ nuclei with time-reversal invariance, neglect the Coulomb field, and set $x_1 = x_2 = 0$ in the following.

When using density dependent interactions, one has to modify the scheme described in section A.1 by calculating the energy first and only afterwards vary with respect to the density [65]. Because of the δ-function character of the Skyrme force, it is possible to express the expectation value of the energy E in terms of three local quantities, the nucleon density,

$$\rho(\mathbf{r}) = \sum_{i,s,t} |\phi_i(\mathbf{r}, s, t)|^2 \,, \tag{A.17}$$

the kinetic energy density,

$$\tau(\mathbf{r}) = \sum_{i,s,t} |\boldsymbol{\nabla} \phi_i(\mathbf{r}, s, t)|^2 \,, \tag{A.18}$$

and the spin orbit densities,

$$\mathbf{J}(\mathbf{r}) = (-\mathrm{i}) \sum_{i,s,s',t} \phi_i^*(\mathbf{r}, s, t)[\boldsymbol{\nabla} \phi_i(\mathbf{r}, s', t) \times \boldsymbol{\sigma}_{ss'}] \,. \tag{A.19}$$

The sums are taken over all occupied single-particle states. One gets

$$E = \int \mathrm{d}^3 r \, \mathcal{E}(\mathbf{r}) \,, \tag{A.20}$$

with

$$\begin{aligned} \mathcal{E}_{\mathrm{Skyrme}}(\mathbf{r}) = {} & \frac{1}{2M_{\mathrm{N}}}\tau + \frac{3}{8}t_0\rho^2 + \frac{1}{16}t_3\rho^{\alpha+2} + \frac{1}{16}(3t_1+5t_2)\rho\tau \\ & + \frac{1}{64}(9t_1-5t_2)(\boldsymbol{\nabla}\rho)^2 + \frac{3}{4}W_0\,\mathbf{J}\cdot\boldsymbol{\nabla}\rho + \frac{1}{32}(t_1-t_2)\mathbf{J}^2 \end{aligned} \tag{A.21}$$

In general, it is difficult to express τ and $\mathbf{J}$ in terms of ρ. However, it is possible to rewrite the variation of the energy as

$$\delta E = \int \mathrm{d}^3 r [B(\mathbf{r})\delta\tau(\mathbf{r}) + U(\mathbf{r})\delta\rho(\mathbf{r}) + \mathbf{W}(\mathbf{r})\delta\mathbf{J}(\mathbf{r})] \,, \tag{A.22}$$

with the local potentials

$$B(\mathbf{r}) = \frac{\delta\mathcal{E}}{\delta\tau(\mathbf{r})} \,, \qquad U(\mathbf{r}) = \frac{\delta\mathcal{E}}{\delta\rho(\mathbf{r})} \,, \qquad \mathbf{W}(\mathbf{r}) = \frac{\delta\mathcal{E}}{\delta\mathbf{J}(\mathbf{r})} \,. \tag{A.23}$$

$B(\mathbf{r}) = 1/2M^{\star}_{\mathrm{N}}(\mathbf{r})$ is proportional to the inverse effective mass. After inserting the variations of $\delta\tau$, $\delta\rho$, and $\delta\mathbf{J}$ with respect to ϕ_i into eq. (A.22), one gets the Hartree-Fock equations in coordinate space:

$$\left\{ -\boldsymbol{\nabla}B(\mathbf{r})\boldsymbol{\nabla} + U(\mathbf{r}) + \mathbf{W}(\mathbf{r})\frac{1}{\mathrm{i}}(\boldsymbol{\nabla}\times\boldsymbol{\sigma}) \right\}\phi_i(\mathbf{r}) = \epsilon_i\phi_i(\mathbf{r}) \,. \tag{A.24}$$

It is also possible to directly parameterize the energy density functional (A.21) without reference to an effective two-body force. The form of the energy functional is then obtained as local density approximation to the nuclear T-matrix [7,60]. We have adapted this procedure to calculate the energy density functional from chiral pion nucleon dynamics in section 5.1.

Appendix B

Analytical expressions for some results

In this appendix we present explicit results that are too bulky to be presented in the main text. For easy reference, we also include some of the results of refs. [14, 15, 31, 90].

B.1 Abbreviations

Here we collect abbreviations and auxiliary functions used often throughout this appendix.

$$u = \frac{k_{\rm f}}{m_\pi} \qquad \text{for symmetric nuclear matter} \tag{B.1}$$

$$u = \frac{k_{\rm n}}{m_\pi} \qquad \text{for pure neutron matter} \tag{B.2}$$

$$H = \ln \frac{u + xy}{u - xy} \tag{B.3}$$

$$s = xy + \sqrt{u^2 - x^2 + x^2 y^2} \tag{B.4}$$

$$t = xz + \sqrt{u^2 - x^2 + x^2 z^2} \tag{B.5}$$

$$\sigma = \xi y + \sqrt{u^2 - \xi^2 + \xi^2 y^2} \tag{B.6}$$

$$\sigma_x = \xi y + \sqrt{u^2 - x^2 + \xi^2 y^2} \tag{B.7}$$

$$R = \sqrt{(1 + x^2 - \xi^2)^2 + 4\xi^2(1 - y^2)} \tag{B.8}$$

$$y_{\rm min} = \sqrt{1 - u^2/x^2} \tag{B.9}$$

$$G(x) = u(1 + u^2 + x^2) - \frac{1}{4x}\big[1 + (u + x)^2\big]\big[1 + (u - x)^2\big] \ln \frac{1 + (u + x)^2}{1 + (u - x)^2} \tag{B.10}$$

B.2 Energy per particle of symmetric nuclear matter

B.2.1 Zero temperature

Here, we repeat for the reader's convenience the results of ref. [14] for the energy per nucleon of symmetric nuclear matter.

Kinetic energy

including the first relativistic correction:

$$\bar{E}_{\rm kin}(k_{\rm f}) = \frac{3k_{\rm f}^2}{10M_{\rm N}} - \frac{3k_{\rm f}^4}{56M_{\rm N}^3}\,. \tag{B.11}$$

One-pion exchange

Fock diagram:

$$\bar{E}_2^{(1\pi)} = \frac{3g_{\rm A}^2 m_\pi^3}{(4\pi f_\pi)^2}\Bigg\{\frac{u^3}{3} + \frac{1}{8u} - \frac{3u}{4} + \arctan 2u - \left(\frac{3}{8u} + \frac{1}{32u^3}\right)\ln(1+4u^2) + \frac{m_\pi^2}{40M_{\rm N}^2}\left[\frac{40}{3}u^3 - 8u^5 + 9u + \frac{1}{2u} - (12u^2+5)\arctan 2u - \frac{1}{8u^3}\ln(1+4u^2)\right]\Bigg\}. \tag{B.12}$$

When truncating at $\mathcal{O}(k_{\rm f}^4)$, the second line in eq. (B.12) has to be omitted. The one-pion exchange Hartree diagram vanishes for a spin-saturated system.

Iterated one-pion exchange

$\bar{E}_{2,3}^{(\rm H,F)}$ give the contributions of the Hartree and Fock diagrams with two and three medium insertions, respectively. The terms coming from linear divergences specific to cut-off regularization are collected in eq. (B.17).

$$\bar{E}_2^{(\rm H)} = \frac{3g_{\rm A}^4 M_{\rm N} m_\pi^4}{5(8\pi)^3 f_\pi^4}\left\{\frac{9}{2u} - 59u + (60+32u^2)\arctan 2u - \left(\frac{9}{8u^3} + \frac{35}{2u}\right)\ln(1+4u^2)\right\} \tag{B.13}$$

$$\bar{E}_2^{(\rm F)} = \frac{g_{\rm A}^4 M_{\rm N} m_\pi^4}{(4\pi)^3 f_\pi^4}\left\{\frac{u^3}{2} + \int_0^u {\rm d}x \frac{3x(u-x)^2(2u+x)}{2u^3(1+2x^2)}\times \Big[(1+8x^2+8x^4)\arctan x - (1+4x^2)\arctan 2x\Big]\right\} \tag{B.14}$$

$$\bar{E}_3^{(\rm H)} = \frac{9g_{\rm A}^4 M_{\rm N} m_\pi^4}{(4\pi f_\pi)^4 u^3}\int_0^u {\rm d}x\, x^2 \int_{-1}^1 {\rm d}y \Big[2uxy + (u^2 - x^2y^2)H\Big]\times \left[\frac{2s^2+s^4}{1+s^2} - 2\ln(1+s^2)\right] \tag{B.15}$$

$$\bar{E}_3^{(\rm F)} = \frac{9g_{\rm A}^4 M_{\rm N} m_\pi^4}{(4\pi f_\pi)^4 u^3}\int_0^u {\rm d}x \Bigg\{\frac{G^2(x)}{8} + \frac{x^2}{4}\int_{-1}^1 {\rm d}y \int_{-1}^1 {\rm d}z \frac{yz\,\theta(y^2+z^2-1)}{|yz|\sqrt{y^2+z^2-1}}\times$$

$$\left[s^2-\ln(1+s^2)\right]\left[\ln(1+t^2)-t^2\right]\Bigg\} \quad \text{(B.16)}$$

The Hartree and Fock diagram contribute to eq. (B.17) with a ratio of 4:1.

$$\bar{E}_\Lambda(k_\mathrm{f}) = \frac{-10 g_\mathrm{A}^4 M_\mathrm{N}}{(4\pi f_\pi)^4} k_\mathrm{f}^3 \Lambda \quad \text{(B.17)}$$

Irreducible two-pion exchange in cut-off regularization

$$\begin{aligned}
\bar{E}^{(2\pi)} = \frac{m_\pi^5}{(4\pi f_\pi)^4}\Bigg\{ & \left[\frac{3}{32u^3}(43g_\mathrm{A}^4+6g_\mathrm{A}^2-1)+\frac{3}{4u}(23g_\mathrm{A}^4+2g_\mathrm{A}^2-1)\right]\times \\
& \ln^2(u+\sqrt{1+u^2})+\left[\frac{u^4}{5}(11g_\mathrm{A}^4-10g_\mathrm{A}^2-1)+\frac{u^2}{10}(59g_\mathrm{A}^4-50g_\mathrm{A}^2-9)+\right. \\
& \left.\frac{1}{40}(883g_\mathrm{A}^4-90g_\mathrm{A}^2-73)+\frac{3}{16u^2}(1-6g_\mathrm{A}^2-43g_\mathrm{A}^4)\right]\sqrt{1+u^2}\,\ln\left(u+\sqrt{1+u^2}\right)+ \\
& \frac{3}{32u}(43g_\mathrm{A}^4+6g_\mathrm{A}^2-1)+\frac{u}{160}(397+210g_\mathrm{A}^2-5647g_\mathrm{A}^4)+\frac{u^3}{5}(4+5g_\mathrm{A}^2+31g_\mathrm{A}^4)+ \\
& \frac{u^5}{600}(119+710g_\mathrm{A}^2-349g_\mathrm{A}^4)+\left[u^3(15g_\mathrm{A}^4-6g_\mathrm{A}^2-1)+\right. \\
& \left.\left.\frac{u^5}{5}(11g_\mathrm{A}^4-10g_\mathrm{A}^2-1)\right]\ln\frac{m_\pi}{2\Lambda}\right\}+\frac{(3g_\mathrm{A}^2+1)(g_\mathrm{A}^2-1)}{(4\pi f_\pi)^4}k_\mathrm{f}^3\Lambda^2 \quad \text{(B.18)}
\end{aligned}$$

Regularization with dispersion integral

Here, we give the results for 2π-exchange (involving nucleons and Deltas in intermediate states) in an dispersion integral representation. The long-range parts of the 2π-exchange (two-body) Fock diagrams are:

$$\begin{aligned}
\bar{E}_2^{(\mathrm{F})}(k_\mathrm{f}) = \frac{1}{8\pi^3}\int_{2m_\pi}^\infty \mathrm{d}\mu\,\mathrm{Im}(V_C+3W_C+2\mu^2V_T+6\mu^2W_T)\Bigg\{3\mu k_\mathrm{f}-\frac{4k_\mathrm{f}^3}{3\mu} \\
+\frac{8k_\mathrm{f}^5}{5\mu^3}-\frac{\mu^3}{2k_\mathrm{f}}-4\mu^2\arctan\frac{2k_\mathrm{f}}{\mu}+\frac{\mu^3}{8k_\mathrm{f}^3}(12k_\mathrm{f}^2+\mu^2)\ln\left(1+\frac{4k_\mathrm{f}^2}{\mu^2}\right)\Bigg\}. \quad \text{(B.19)}
\end{aligned}$$

$\mathrm{Im}\,V_C$, $\mathrm{Im}\,W_C$, $\mathrm{Im}\,V_T$ and $\mathrm{Im}\,W_T$ are the spectral functions of the isoscalar and isovector central and tensor NN-amplitudes, respectively. Explicit expressions of these imaginary parts for the contributions of the triangle diagram with single Δ-excitation and the box diagrams with single and double Δ-excitation can be easily constructed from the analytical formulas given in section 3 of ref. [80]. The corresponding nonvanishing spectral functions for irreducible two-pion exchange (with only nucleon intermediate states) read [73]:

$$\mathrm{Im}\,W_C(i\mu)=\frac{\sqrt{\mu^2-4m_\pi^2}}{3\pi\mu(4f_\pi)^4}\left[4m_\pi^2(1+4g_\mathrm{A}^2-5g_\mathrm{A}^4)+\mu^2(23g_\mathrm{A}^4-10g_\mathrm{A}^2-1)+\frac{48g_\mathrm{A}^4m_\pi^4}{\mu^2-4m_\pi^2}\right], \quad \text{(B.20)}$$

$$\mathrm{Im}\, V_T(i\mu) = -\frac{6g_\mathrm{A}^4\sqrt{\mu^2-4m_\pi^2}}{\pi\mu(4f_\pi)^4}\,. \tag{B.21}$$

The double subtraction of the dispersion integral (B.19) leads to the following contact contribution with the two subtraction constants B_3 and B_5:

$$\bar{E}^{(\mathrm{NN})}(k_\mathrm{f}) = B_3\frac{k_\mathrm{f}^3}{M_\mathrm{N}^2} + B_5\frac{k_\mathrm{f}^5}{M_\mathrm{N}^4}\,, \tag{B.22}$$

The Hartree diagram with three medium insertions gives:

$$\bar{E}_3^{(\mathrm{H})}(k_\mathrm{f}) = \frac{g_\mathrm{A}^4 m_\pi^6}{\Delta(2\pi f_\pi)^4}\left[\frac{2}{3}u^6 + u^2 - 3u^4 + 5u^3\arctan 2u - \frac{1}{4}(1+9u^2)\ln(1+4u^2)\right]. \tag{B.23}$$

The Fock diagram with three medium insertions gives:

$$\bar{E}_3^{(\mathrm{F})}(k_\mathrm{f}) = -\frac{3g_\mathrm{A}^4 m_\pi^6 u^{-3}}{4\Delta(4\pi f_\pi)^4}\int_0^u \mathrm{d}x\Big[2G_S^2(x,u) + G_T^2(x,u)\Big]\,, \tag{B.24}$$

where we have introduced the two auxiliary functions:

$$G_S(x,u) = \frac{4ux}{3}(2u^2-3) + 4x\Big[\arctan(u+x) + \arctan(u-x)\Big] + (x^2-u^2-1)\ln\frac{1+(u+x)^2}{1+(u-x)^2}\,, \tag{B.25}$$

$$G_T(x,u) = \frac{ux}{6}(8u^2+3x^2) - \frac{u}{2x}(1+u^2)^2 + \frac{1}{8}\left[\frac{(1+u^2)^3}{x^2} - x^4 + (1-3u^2)(1+u^2-x^2)\right]\ln\frac{1+(u+x)^2}{1+(u-x)^2}\,. \tag{B.26}$$

Additional three-body contact interaction

$$\bar{E}^{(\mathrm{NNN})}(k_\mathrm{f}) = B_6\frac{k_\mathrm{f}^6}{M_\mathrm{N}^5}\,. \tag{B.27}$$

B.2.2 Finite temperature kernels

In this section, we present the kernels which determine via eq. (4.1) the non-anomalous contributions to the free energy per particle $\bar{F}(\rho,T)$ at finite temperature. The one-body kernel $\mathcal{K}_1$ reads:

$$\mathcal{K}_1 = \tilde{\mu} - \frac{p_1^2}{3M_\mathrm{N}} - \frac{p_1^4}{8M_\mathrm{N}^3} \tag{B.28}$$

One-pion exchange

1π-exchange Fock diagram including the relativistic $1/M_{\rm N}^2$-correction:

$$\mathcal{K}_2^{(1\pi)} = \frac{3g_{\rm A}^2}{16f_\pi^2}\Bigg\{8p_1p_2 - 2m_\pi^2\ln\frac{m_\pi^2+(p_1+p_2)^2}{m_\pi^2+(p_1-p_2)^2} + \frac{1}{M_{\rm N}^2}\Bigg[-4p_1p_2(p_1^2+p_2^2) + m_\pi^2(p_1^2+p_2^2)\ln\frac{m_\pi^2+(p_1+p_2)^2}{m_\pi^2+(p_1-p_2)^2} - \frac{2m_\pi^2p_1p_2(p_1^2-p_2^2)^2}{[m_\pi^2+(p_1+p_2)^2][m_\pi^2+(p_1-p_2)^2]}\Bigg]\Bigg\} \quad \text{(B.29)}$$

Iterated one-pion exchange

Iterated 1π-exchange Hartree graph (second diagram in fig. 3.1) two-body term:

$$\mathcal{K}_2^{(\rm H)} = \frac{3g_{\rm A}^4M_{\rm N}m_\pi^2}{8\pi f_\pi^4}\Bigg\{(p_1+p_2)\arctan\frac{p_1+p_2}{m_\pi} + (p_2-p_1)\arctan\frac{p_1-p_2}{m_\pi} - \frac{5}{8}m_\pi\ln\frac{m_\pi^2+(p_1+p_2)^2}{m_\pi^2+(p_1-p_2)^2}\Bigg\}. \quad \text{(B.30)}$$

Iterated 1π-exchange Fock graph (third diagram in fig. 3.1) two-body term:

$$\mathcal{K}_2^{(\rm F)} = \frac{3g_{\rm A}^4M_{\rm N}m_\pi}{32\pi f_\pi^4}\Bigg\{2p_1p_2 + m_\pi^2\int_{|p_1-p_2|/2m_\pi}^{(p_1+p_2)/2m_\pi}\frac{{\rm d}x}{1+2x^2}\times\Big[(1+8x^2+8x^4)\arctan x - (1+4x^2)\arctan 2x\Big]\Bigg\} \quad \text{(B.31)}$$

In the two previous expression we have omitted the contribution of a linear divergence proportional to the momentum cut-off Λ. These are given by

$$\mathcal{K}_2^{(\Lambda)} = -\frac{15g_{\rm A}^4M_{\rm N}}{16\pi^2f_\pi^4}\Lambda\,p_1p_2\,, \quad \text{(B.32)}$$

with the Hartree and Fock diagrams contributing in the ratio 4 : 1. Note that the kernel $\mathcal{K}_2^{(\Lambda)}$ in eq. (B.32) (and the term proportional to Λ^2 in eq. (B.36)) leads to a temperature independent contribution to free energy per particle $\bar{F}(\rho,T)\sim\rho$. Therefore it is fully equivalent to a momentum independent NN-contact interaction.

Next, we come to the three-body kernel $\mathcal{K}_3$ which incorporates the temperature and density dependent Pauli blocking effects in intermediate NN-states. The iterated 1π-exchange Hartree graph contributes to the three-body kernel $\mathcal{K}_3$ in the form:

$$\mathcal{K}_3^{(\rm H)} = \frac{3g_{\rm A}^4M_{\rm N}}{4f_\pi^4}\int_{|p_1-p_2|}^{p_1+p_2}{\rm d}q\,\frac{q^4}{(m_\pi^2+q^2)^2}\ln\frac{|p_1^2-p_2^2+q^2+2p_3q|}{|p_1^2-p_2^2+q^2-2p_3q|}\,, \quad \text{(B.33)}$$

and from the iterated 1π-exchange Fock graph one finds,

$$\mathcal{K}_3^{(\mathrm{F})} = \frac{3g_\mathrm{A}^4 M_\mathrm{N}}{16 f_\pi^4}\Bigg\{ \frac{1}{8p_3^3}\left[4p_1p_3 + (p_3^2 - p_1^2 - m_\pi^2)\ln\frac{m_\pi^2 + (p_1+p_3)^2}{m_\pi^2 + (p_1-p_3)^2}\right]\times \left[4p_2p_3 + (p_3^2 - p_2^2 - m_\pi^2)\ln\frac{m_\pi^2 + (p_2+p_3)^2}{m_\pi^2 + (p_2-p_3)^2}\right] + \int_{|p_2-p_3|}^{p_2+p_3}\mathrm{d}q\,\frac{q^2}{m_\pi^2+q^2}\left[\ln\frac{|p_1+h|}{|p_1-h|} + \frac{m_\pi^2}{R_h}\ln\frac{|p_1R_h + (p_1^2 - p_3^2 - m_\pi^2)h|}{|p_1R_h + (p_3^2 + m_\pi^2 - p_1^2)h|}\right]\Bigg\}, \quad \text{(B.34)}$$

with the abbreviations

$$R_h = \sqrt{(m_\pi^2 + p_1^2 - p_3^2)^2 + 4m_\pi^2(p_3^2 - h^2)}\,, \qquad h = \frac{1}{2q}(p_2^2 - p_3^2 - q^2)\,. \quad \text{(B.35)}$$

Irreducible two-pion exchange in cut-off regularization

The irreducible two-pion exchange Fock diagrams (see fig. 3.2) with only nucleons in intermediate states yield

$$\mathcal{K}_2^{(2\pi)} = \frac{m_\pi^4}{128\pi^2 f_\pi^4}\left\{ I\left(\frac{p_1+p_2}{2m_\pi}\right) - I\left(\frac{|p_1-p_2|}{2m_\pi}\right)\right\} + \frac{(9g_\mathrm{A}^2+3)(g_\mathrm{A}^2-1)}{32\pi^2 f_\pi^4}\Lambda^2\, p_1p_2\,, \quad \text{(B.36)}$$

with the function

$$I(x) = 3(11g_\mathrm{A}^4 - 2g_\mathrm{A}^2 - 1)\ln^2(x+\sqrt{1+x^2}) + 2(g_\mathrm{A}^2-1)\Big[g_\mathrm{A}^2(31+22x^2) + 5 + 2x^2\Big]\, x\sqrt{1+x^2}\ln(x+\sqrt{1+x^2}) + (7 - 2g_\mathrm{A}^2 + 91g_\mathrm{A}^4)x^2 + (3 + 14g_\mathrm{A}^2 - g_\mathrm{A}^4)x^4 + \Big[12(15g_\mathrm{A}^4 - 6g_\mathrm{A}^2 - 1)x^2 + 4(11g_\mathrm{A}^4 - 10g_\mathrm{A}^2 - 1)x^4\Big]\ln\frac{m_\pi}{2\Lambda}\,, \quad \text{(B.37)}$$

obtained from solving the pion-loop integrals.

Note that all integrands in representations of $\mathcal{K}_{2,3}$ are odd functions of their respective integration variable and therefore one could even drop the absolute magnitude on the lower integration limits. We also remind that (non-anomalous) terms involving the product of four Fermi-Dirac distributions are effectively absent in second order perturbation theory [57]. Because of the antisymmetry of the accompanying energy denominator under the exchange of two pairs of momenta these terms integrate to zero.

The anomalous contribution involving πN-dynamics is given in eq. (4.6).

Two-pion exchange involving virtual Delta excitations

The two-body kernels read:

$$\mathcal{K}_2^{(\mathrm{NN})} = 24\pi^2 B_3 \frac{p_1p_2}{M_\mathrm{N}^2} + 20\pi^2 B_5 \frac{p_1p_2}{M_\mathrm{N}^4}(p_1^2 + p_2^2)\,, \quad \text{(B.38)}$$

$$\mathcal{K}_2^{(\mathrm{F})} = \frac{1}{\pi}\int_{2m_\pi}^{\infty} \mathrm{d}\mu\, \mathrm{Im}(V_C + 3W_C + 2\mu^2 V_T + 6\mu^2 W_T)\times \left\{\mu \ln\frac{\mu^2+(p_1+p_2)^2}{\mu^2+(p_1-p_2)^2} - \frac{4p_1p_2}{\mu} + \frac{4p_1p_2}{\mu^3}(p_1^2+p_2^2)\right\}. \quad \text{(B.39)}$$

The contributions of the Hartree and Fock diagrams in fig. 7.2 to the three-body kernel read:

$$\mathcal{K}_3^{(\mathrm{H})} = \frac{3g_\mathrm{A}^4 p_3}{\Delta f_\pi^4}\left\{2p_1p_2 + \frac{2m_\pi^4 p_1p_2}{[m_\pi^2+(p_1+p_2)^2][m_\pi^2+(p_1-p_2)^2]} - m_\pi^2 \ln\frac{m_\pi^2+(p_1+p_2)^2}{m_\pi^2+(p_1-p_2)^2}\right\}, \quad \text{(B.40)}$$

$$\mathcal{K}_3^{(\mathrm{F})} = -\frac{g_\mathrm{A}^4}{4\Delta f_\pi^4 p_3}\Big[2X(p_1)X(p_2) + Y(p_1)Y(p_2)\Big], \quad \text{(B.41)}$$

$$X(p_1) = 2p_1p_3 - \frac{m_\pi^2}{2}\ln\frac{m_\pi^2+(p_1+p_3)^2}{m_\pi^2+(p_1-p_3)^2}, \quad \text{(B.42)}$$

$$Y(p_1) = \frac{p_1}{4p_3}(5p_3^2 - 3m_\pi^2 - 3p_1^2) + \frac{3(p_1^2-p_3^2+m_\pi^2)^2 + 4m_\pi^2 p_3^2}{16p_3^2}\ln\frac{m_\pi^2+(p_1+p_3)^2}{m_\pi^2+(p_1-p_3)^2}. \quad \text{(B.43)}$$

Additional three-body contact interaction

$$\mathcal{K}_3^{(\mathrm{NNN})} = 144\pi^4 B_6 \frac{p_1p_2p_3}{M_\mathrm{N}^5}. \quad \text{(B.44)}$$

B.2.3 Selected higher order diagrams

Let us consider diagrams of the type of fig. 7.3 and fig. B.1, where a pion couples to a Delta-hole pair. The energy per particle generated by such diagrams can be calculated by considering iterated 1π-exchange diagrams and replacing one pion propagator according to fig. B.2. The additional factors introduced by this replacement can be implemented by a combination of derivatives with respect to the pion mass. In the case of the two

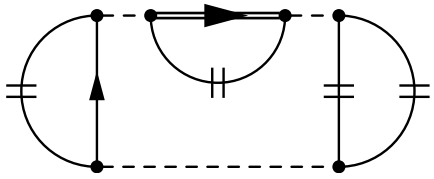

Figure B.1: A 4-loop diagram which can be easily calculated from results from iterated 1π-exchange by replacing the pion propagator.

Figure B.2: Replacement which generates fig. B.1 from iterated 1π-exchange (see fig. 3.1).

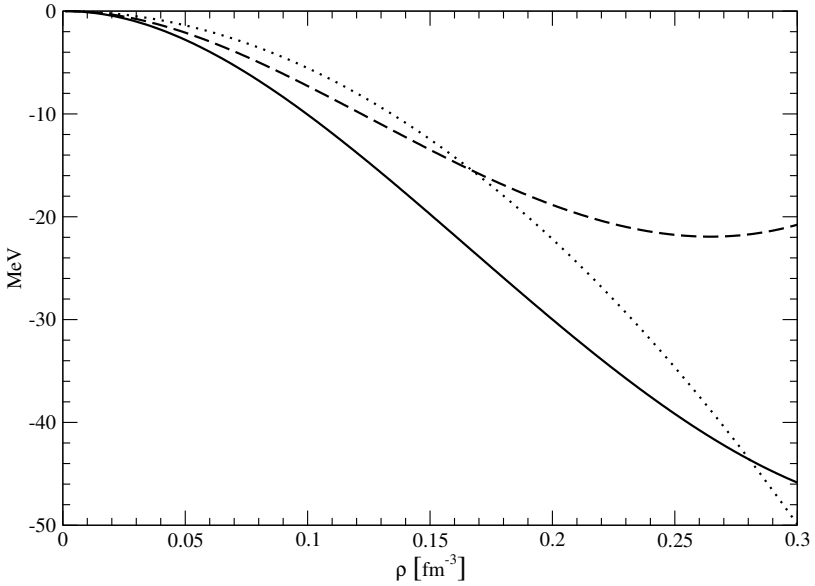

Figure B.3: Comparison of the contribution $\bar{E}^{(4H)}(\rho, \Lambda)$ from the 4-loop Hartree diagrams figs. 7.3 and B.1 for $\Lambda = 440\,\mathrm{MeV}$ (dashed line) and $\Lambda = 460\,\mathrm{MeV}$ (full line) with the three-body contact interaction eq. (7.4) using $B_6 = -31.3$ (dotted line).

Hartree diagrams of fig. 7.3 and fig. B.1 this procedure results in:

$$\bar{E}^{(4H)}(k_f, \Lambda) = \frac{4 g_A^2 \rho}{\Delta f_\pi^2} \left(\bar{E}^{(it.1\pi,H)}(k_f, \Lambda) + \frac{m_\pi}{4} \frac{\partial}{\partial m_\pi} \bar{E}^{(it.1\pi,H)}(k_f, \Lambda) \right), \tag{B.45}$$

where

$$\bar{E}^{(it.1\pi,H)}(k_f, \Lambda) = \bar{E}_2^{(H)}(k_f) + \bar{E}_3^{(H)}(k_f) + \frac{4}{5} \bar{E}_\Lambda(k_f, \Lambda) \tag{B.46}$$

is the result (using cut-off regularization) from the (3-loop) iterated 1π-exchange Hartree diagram (see eqs. (B.13), (B.15), and (B.17)). A possible numerical approximation to eq. (B.45) is:

$$\bar{E}^{(4H)}(k_f, \Lambda) \simeq \big(2.742 u^6 - 0.4424 u^7 + 0.1865 u^8\big)\mathrm{MeV} - \frac{\Lambda u^6}{153.3}, \tag{B.47}$$

with $u = k_f/m_\pi$. With a cut-off $\Lambda \simeq 460\,\mathrm{MeV}$, the ρ^2-term in the approximation eq. (B.47) is equal in magnitude to the three-body contact term $\bar{E}^{(NNN)}(k_f)$ with a strength parameter $B_6 = -31.3$. The complete contribution $\bar{E}^{(4H)}(\rho, \Lambda = 460\,\mathrm{MeV})$ is shown as the full line in fig. B.3. For comparison, $\bar{E}^{(NNN)}(\rho)$ is drawn as dotted line in this figure. The dashed curve in fig. B.3 shows $\bar{E}^{(4H)}(\rho, \Lambda = 440\,\mathrm{MeV})$. Obviously, there is a strong cut-off dependence in $\bar{E}^{(it.1\pi,H)}(k_f, \Lambda)$.

B.3 Asymmetry energy

The abbreviations s, t, H, and $G(x)$ are given in section B.1. The kinetic energy contribution reads:

$$\bar{A}_{\rm kin}(k_{\rm f}) = \frac{k_{\rm f}^2}{6M_{\rm N}} - \frac{k_{\rm f}^4}{12M_{\rm N}^3}\,. \tag{B.48}$$

1π-exchange yields:

$$\bar{A}^{(1\pi,{\rm F})}(k_{\rm f}) = \frac{g_{\rm A}^2 m_\pi^3}{(4\pi f_\pi)^2}\Bigg\{ \left(\frac{u}{3}+\frac{1}{8u}\right)\ln(1+4u^2) - \frac{u}{2} - \frac{u^3}{3} + \frac{m_\pi^2}{M_{\rm N}^2}\left[u^3 - \frac{u^2}{2}\arctan 2u - \frac{u^3}{3}\ln(1+4u^2)\right]\Bigg\}. \tag{B.49}$$

The contributions from the iterated 1π-exchange Hartree and Fock diagrams with j medium insertions are given by $\bar{A}_j^{({\rm H,F})}(k_{\rm f})$ respectively. The corresponding cut-off dependent pieces have been collected in eq. (B.55).

$$\bar{A}_2^{({\rm H})}(k_{\rm f}) = \frac{g_{\rm A}^4 M_{\rm N} m_\pi^4}{(8\pi)^3 f_\pi^4}\Bigg\{ \left(\frac{25}{3}u+\frac{7}{6u}\right)\ln(1+4u^2) - \frac{14}{3}u - 16u^2\arctan 2u\Bigg\}, \tag{B.50}$$

$$\bar{A}_2^{({\rm F})}(k_{\rm f}) = \frac{g_{\rm A}^4 M_{\rm N} m_\pi^4}{(4\pi)^3 f_\pi^4}\Bigg\{ -\frac{5}{6}u^3 + \int_0^u {\rm d}x \frac{3x^2-4u^2}{6u(1+2x^2)}\Big[(1+8x^2+8x^4)\arctan x - (1+4x^2)\arctan 2x\Big]\Bigg\}, \tag{B.51}$$

$$\bar{A}_3^{({\rm H})}(k_{\rm f}) = \frac{g_{\rm A}^4 M_{\rm N} m_\pi^4}{(4\pi f_\pi)^4 u^3}\int_0^u {\rm d}x\, x^2 \int_{-1}^1 {\rm d}y \Bigg\{ \left[\frac{uxy\,(26u^2-30x^2y^2)}{3\,(u^2-x^2y^2)} + \left(3u^2-5x^2y^2\right)H\right]\times \left[\frac{2s^2+s^4}{1+s^2} - 2\ln(1+s^2)\right] - \frac{4u^2 H\, s^6}{3(1+s^2)^2} + \Big[2uxy + \left(u^2-x^2y^2\right)H\Big]\times \Big[(5+s^2)\left(3s^2-8ss'+8s'^2\right) + 8s(1+s^2)\left(s''-5s'+3s\right)\Big]\frac{s^4}{3(1+s^2)^3}\Bigg\}. \tag{B.52}$$

Here, s' and s'' denote the partial derivatives

$$s' = u\frac{\partial s}{\partial u} \quad \text{and} \quad s'' = u^2\frac{\partial^2 s}{\partial u^2}\,.$$

$$\bar{A}_3^{({\rm F})}(k_{\rm f}) = \frac{g_{\rm A}^4 M_{\rm N} m_\pi^4}{(4\pi f_\pi)^4 u^3}\int_0^u {\rm d}x \Bigg\{ \frac{G(x)}{24}(3G_{20}-2G_{11}+3G_{02}-8G_{01}-3G(x)) + \frac{G_{10}+G_{01}}{24}(3G_{10}-5G_{01}) + \frac{x^2}{6}\int_{-1}^1 {\rm d}y \int_{-1}^1 {\rm d}z \frac{yz\,\theta(y^2+z^2-1)}{|yz|\sqrt{y^2+z^2-1}}\times$$

$$\left[\frac{2s^3t^4(8s'-3s)}{(1+s^2)(1+t^2)}+\Big[(3+s^2)(8ss'-3s^2-8s'^2)+ 4s(1+s^2)(6s'-3s-2s'')\Big]\frac{s^2[t^2-\ln(1+t^2)]}{(1+s^2)^2}\right\}. \quad \text{(B.53)}$$

The partial derivatives of $G(x)$ are written in the following way:

$$G_{ij}=x^iu^j\frac{\partial^{i+j}G(x)}{\partial x^i\partial u^j}\,,\quad 1\le i+j\le 2\,.$$

Cut-off regularization

The Hartree and Fock diagrams of irreducible 2π-exchange with only nucleons in intermediate states give the following contribution (in cut-off regularization):

$$\begin{aligned}\bar{A}^{(2\pi)}(k_\mathrm{f})=\frac{m_\pi^5}{(4\pi f_\pi)^4}\Bigg\{&\left[\frac{1}{12u}\left(1-2g_\mathrm{A}^2-23g_\mathrm{A}^4\right)+\frac{u}{3}\left(1+2g_\mathrm{A}^2-7g_\mathrm{A}^4\right)\right]\times\\ &\ln^2(u+\sqrt{1+u^2})+\left[\frac{1}{6}\left(23g_\mathrm{A}^4+2g_\mathrm{A}^2-1\right)+u^2\left(\frac{1}{3}+2g_\mathrm{A}^2-5g_\mathrm{A}^4\right)-\frac{16}{3}g_\mathrm{A}^4u^4\right]\times\\ &\sqrt{1+u^2}\ln(u+\sqrt{1+u^2})+\frac{u}{12}\left(1-2g_\mathrm{A}^2-23g_\mathrm{A}^4\right)+u^3\left(\frac{1}{4}+\frac{11}{2}g_\mathrm{A}^2-\frac{245}{12}g_\mathrm{A}^4\right)-\\ &\frac{u^5}{27}\left(1+10g_\mathrm{A}^2+g_\mathrm{A}^4\right)+u^3\left[\frac{5}{3}+10g_\mathrm{A}^2-25g_\mathrm{A}^4-\frac{16}{3}g_\mathrm{A}^4u^2\right]\ln\frac{m_\pi}{2\Lambda}\Bigg\}. \quad \text{(B.54)}\end{aligned}$$

The polynomial divergences from iterated 1π- and irreducible 2π-exchange give rise to the following cut-off dependent terms:

$$\bar{A}_2^{(\Lambda)}(k_\mathrm{f})=\frac{k_\mathrm{f}^3}{3(4\pi f_\pi)^4}\left[26g_\mathrm{A}^4M_\mathrm{N}\Lambda+5(3g_\mathrm{A}^2+1)(1-g_\mathrm{A}^2)\Lambda^2\right]. \quad \text{(B.55)}$$

Two-pion exchange in dispersion integral representation

On the other hand, using the dispersion integral representation of chapter 7 and including the full πNΔ-dynamics, we get the following contributions from irreducible 2π-exchange:

$$\bar{A}^{(\mathrm{NN})}(k_\mathrm{f})=(2B_{\mathrm{n},3}-B_3)\frac{k_\mathrm{f}^3}{M_\mathrm{N}^2}+(3B_{\mathrm{n},5}-B_5)\frac{10k_\mathrm{f}^5}{9M_\mathrm{N}^4}\,, \quad \text{(B.56)}$$

$$\begin{aligned}\bar{A}_2^{(2\pi,\mathrm{F})}(k_\mathrm{f})=\frac{1}{12\pi^3}\int_{2m_\pi}^\infty\mathrm{d}\mu\Bigg\{&\mathrm{Im}(V_C+2\mu^2V_T)\times\\ &\left[\mu k_\mathrm{f}-\frac{2k_\mathrm{f}^3}{\mu}+\frac{16k_\mathrm{f}^5}{3\mu^3}-\frac{\mu^3}{4k_\mathrm{f}}\ln\left(1+\frac{4k_\mathrm{f}^2}{\mu^2}\right)\right]+\end{aligned}$$

$$\mathrm{Im}(W_C + 2\mu^2 W_T)\left[3\mu k_\mathrm{f} + \frac{2k_\mathrm{f}^3}{\mu} - \frac{\mu}{4k_\mathrm{f}}(8k_\mathrm{f}^2 + 3\mu^2)\ln\left(1 + \frac{4k_\mathrm{f}^2}{\mu^2}\right)\right]\Bigg\}, \quad \text{(B.57)}$$

$$\bar{A}_3^{(2\pi,\mathrm{H})}(k_\mathrm{f}) = \frac{g_\mathrm{A}^4 m_\pi^6 u^2}{9\Delta(2\pi f_\pi)^4}\left[\left(\frac{9}{4} + 4u^2\right)\ln(1+4u^2) - 2u^4 - 8u^2 - \frac{u^2}{1+4u^2}\right], \quad \text{(B.58)}$$

$$\begin{aligned}\bar{A}_3^{(2\pi,\mathrm{F})}(k_\mathrm{f}) = \frac{g_\mathrm{A}^4 m_\pi^6 u^{-3}}{36\Delta(4\pi f_\pi)^4}\int_0^u \mathrm{d}x\Big\{&4G_{S01}G_{S10} - 2G_{S01}^2 - 6G_{S10}^2 + \\ &2G_S(3G_S + 8G_{S01} - 3G_{S02} + 2G_{S11} - 3G_{S20}) + 2G_{T01}G_{T10} - \\ &7G_{T01}^2 - 3G_{T10}^2 + G_T(3G_T + 8G_{T01} - 3G_{T02} + 2G_{T11} - 3G_{T20})\Big\}. \quad \text{(B.59)}\end{aligned}$$

The auxiliary functions $G_{S,T}(x,u)$ have been defined in eqs. (B.25,B.26) and we have introduced a double-index notation for their partial derivatives:

$$G_{Ijk}(x,u) = x^j u^k \frac{\partial^{j+k} G_I(x,u)}{\partial x^j \partial u^k}, \qquad I = S,T, \quad 1 \le j+k \le 2. \quad \text{(B.60)}$$

For notational simplicity we have omitted the arguments x and u in the integrand of eq. (B.59).

Additional three-body contact interaction

$$\bar{A}^{(\mathrm{NNN})}(k_\mathrm{f}) = -B_6 \frac{k_\mathrm{f}^6}{M_\mathrm{N}^5}. \quad \text{(B.61)}$$

B.4 Equation of state of pure neutron matter

In this section, the meaning of u changes to $u = k_\mathrm{n}/m_\pi$. The kinetic energy contribution to the neutron matter equation of state reads:

$$\bar{E}_{\mathrm{n},k}(k_\mathrm{n}) = \frac{3k_\mathrm{n}^2}{10M_\mathrm{N}} - \frac{3k_\mathrm{n}^4}{56M_\mathrm{N}^3}. \quad \text{(B.62)}$$

1π-exchange yields:

$$\begin{aligned}\bar{E}_\mathrm{n}^{(1\pi)}(k_\mathrm{n}) = \frac{g_\mathrm{A}^2 m_\pi^3}{(4\pi f_\pi)^2}\Bigg\{&\frac{u^3}{3} + \frac{1}{8u} - \frac{3u}{4} + \arctan 2u - \left(\frac{3}{8u} + \frac{1}{32u^3}\right)\ln(1+4u^2) + \\ &\frac{m_\pi^2}{40M_\mathrm{N}^2}\left[\frac{40}{3}u^3 - 8u^5 + 9u + \frac{1}{2u} - (12u^2+5)\arctan 2u - \frac{1}{8u^3}\ln(1+4u^2)\right]\Bigg\}. \quad \text{(B.63)}\end{aligned}$$

The contributions from the iterated 1π-exchange Hartree and Fock diagrams with j medium insertions are given by $\bar{E}_{\mathrm{n},j}^{(\mathrm{H,F})}(k_\mathrm{n})$ respectively. The corresponding cut-off dependent pieces have been collected in eq. (B.69).

$$\bar{E}^{(\mathrm{H})}_{\mathrm{n},2}(k_\mathrm{n}) = \frac{g_\mathrm{A}^4 M_\mathrm{N} m_\pi^4}{10(8\pi)^3 f_\pi^4}\bigg\{\frac{9}{2u} - 59u + (60+32u^2)\arctan 2u - \left(\frac{9}{8u^3}+\frac{35}{2u}\right)\ln(1+4u^2)\bigg\}, \quad \text{(B.64)}$$

$$\bar{E}^{(\mathrm{F})}_{\mathrm{n},2}(k_\mathrm{n}) = \frac{g_\mathrm{A}^4 M_\mathrm{N} m_\pi^4}{(4\pi)^3 f_\pi^4}\bigg\{-\frac{u^3}{6} + \int_0^u \mathrm{d}x \frac{x(u-x)^2(2u+x)}{2u^3(1+2x^2)}\Big[(1+4x^2)\arctan 2x - \big(1+8x^2+8x^4\big)\arctan x\Big]\bigg\}, \quad \text{(B.65)}$$

$$\bar{E}^{(\mathrm{H})}_{\mathrm{n},3}(k_\mathrm{n}) = \frac{3g_\mathrm{A}^4 M_\mathrm{N} m_\pi^4}{(4\pi f_\pi)^4 u^3}\int_0^u \mathrm{d}x\, x^2 \int_{-1}^1 \mathrm{d}y \Big[2uxy + \big(u^2 - x^2y^2\big)\,H\Big]\times \left[\frac{2s^2+s^4}{2(1+s^2)} - \ln(1+s^2)\right], \quad \text{(B.66)}$$

$$\bar{E}^{(\mathrm{F})}_{\mathrm{n},3}(k_\mathrm{n}) = \frac{3g_\mathrm{A}^4 M_\mathrm{N} m_\pi^4}{(4\pi f_\pi)^4 u^3}\int_0^u \mathrm{d}x \bigg\{-\frac{G^2(x)}{8} + \frac{x^2}{4}\int_{-1}^1 \mathrm{d}y \int_{-1}^1 \mathrm{d}z \frac{yz\,\theta(y^2+z^2-1)}{|yz|\sqrt{y^2+z^2-1}}\times \Big[s^2 - \ln(1+s^2)\Big]\Big[t^2 - \ln(1+t^2)\Big]\bigg\}. \quad \text{(B.67)}$$

Cut-off regularization

The Hartree and Fock diagrams of irreducible 2π-exchange with only nucleons in intermediate states give the following contribution (in cut-off regularization):

$$\begin{aligned}\bar{E}^{(2\pi)}_{\mathrm{n}}(k_\mathrm{n}) = \frac{m_\pi^5}{(4\pi f_\pi)^4}\bigg\{&\frac{1}{32u}\left(83g_\mathrm{A}^4 + 6g_\mathrm{A}^2 - 1\right) + \frac{u}{480}\left(397 + 210g_\mathrm{A}^2 - 11159g_\mathrm{A}^4\right) + \\ &\left[\frac{1}{32u^3}\left(83g_\mathrm{A}^4 + 6g_\mathrm{A}^2 - 1\right) + \frac{1}{4u}\left(47g_\mathrm{A}^4 + 2g_\mathrm{A}^2 - 1\right)\right]\ln^2(u+\sqrt{1+u^2}) + \\ &\left[\frac{u^2}{30}\left(3g_\mathrm{A}^4 - 50g_\mathrm{A}^2 - 9\right) - \frac{u^4}{15}\left(13g_\mathrm{A}^4 + 10g_\mathrm{A}^2 + 1\right) + \frac{1}{120}\left(1691g_\mathrm{A}^4 - 90g_\mathrm{A}^2 - 73\right) + \right. \\ &\left.\frac{1}{16u^2}\left(1 - 6g_\mathrm{A}^2 - 83g_\mathrm{A}^4\right)\right]\sqrt{1+u^2}\ln(u+\sqrt{1+u^2}) + \\ &\frac{u^5}{1800}\left(119 + 710g_\mathrm{A}^2 + 107g_\mathrm{A}^4\right) + \frac{u^3}{15}\left(9 + 55g_\mathrm{A}^2 - 108g_\mathrm{A}^4\right) + \\ &\left[u^3\left(\frac{1}{3} + 2g_\mathrm{A}^2 - 5g_\mathrm{A}^4\right) - \frac{u^5}{15}\left(13g_\mathrm{A}^4 + 10g_\mathrm{A}^2 + 1\right)\right]\ln\frac{m_\pi}{2\Lambda}\bigg\}. \quad \text{(B.68)}\end{aligned}$$

The polynomial divergences from iterated 1π- and irreducible 2π-exchange give rise to the following cut-off dependent terms:

$$\bar{E}^{(\Lambda)}_{\mathrm{n},2}(k_\mathrm{n}) = -\frac{k_\mathrm{n}^3}{3(4\pi f_\pi)^4}\Big[2g_\mathrm{A}^4 M_\mathrm{N}\Lambda + (3g_\mathrm{A}^2+1)(g_\mathrm{A}^2-1)\Lambda^2\Big]\,. \tag{B.69}$$

Two-pion exchange in dispersion integral representation

On the other hand, using the dispersion integral representation of chapter 7 and including the full πNΔ-dynamics, we get the following contributions from irreducible 2π-exchange:

$$\bar{E}^{(\mathrm{NN})}_{\mathrm{n}}(k_\mathrm{n}) = B_{\mathrm{n},3}\frac{k_\mathrm{n}^3}{M_\mathrm{N}^2} + B_{\mathrm{n},5}\frac{k_\mathrm{n}^5}{M_\mathrm{N}^4}\,, \tag{B.70}$$

$$\begin{aligned}\bar{E}^{(2\pi,\mathrm{F})}_{\mathrm{n},2}(k_\mathrm{n}) = \frac{1}{8\pi^3}\int_{2m_\pi}^{\infty}\mathrm{d}\mu\,\mathrm{Im}(V_C+W_C+2\mu^2V_T+2\mu^2W_T)\Big\{3\mu k_\mathrm{n} - \frac{4k_\mathrm{n}^3}{3\mu} + \\ \frac{8k_\mathrm{n}^5}{5\mu^3} - \frac{\mu^3}{2k_\mathrm{n}} - 4\mu^2\arctan\frac{2k_\mathrm{n}}{\mu} + \frac{\mu^3}{8k_\mathrm{n}^3}(12k_\mathrm{n}^2+\mu^2)\ln\left(1+\frac{4k_\mathrm{n}^2}{\mu^2}\right)\Big\}\,.\end{aligned} \tag{B.71}$$

Here, the relative weights of isoscalar ($V_{C,T}$) and isovector ($W_{C,T}$) NN-amplitudes have changed by a factor 3 in comparison to eq. (7.2). The diagrams with three medium insertions yield:

$$\bar{E}^{(2\pi,\mathrm{H})}_{\mathrm{n},3}(k_\mathrm{n}) = \frac{g_\mathrm{A}^4 m_\pi^6}{6\Delta(2\pi f_\pi)^4}\left[\frac{2}{3}u^6+u^2-3u^4+5u^3\arctan 2u - \frac{1}{4}(1+9u^2)\ln(1+4u^2)\right]\,, \tag{B.72}$$

$$\bar{E}^{(2\pi,\mathrm{F})}_{\mathrm{n},3}(k_\mathrm{n}) = -\frac{g_\mathrm{A}^4 m_\pi^6 u^{-3}}{4\Delta(4\pi f_\pi)^4}\int_0^u \mathrm{d}x\Big[G_S^2(x,u)+2G_T^2(x,u)\Big]\,, \tag{B.73}$$

with $G_{S,T}(x,u)$ defined in eqs. (B.25,B.26).

B.5 Toy model

Here we present the results for the toy model of section 3.3 and ref. [59]. For $T=0$ the contributions to the energy per particle $\bar{E}$ are:

$$\bar{E}_2^{(1,F)}(k_\mathrm{f}) = \frac{9C\gamma}{4\pi^2}\left[\frac{1}{8u} - \frac{3u}{4} + \arctan 2u - \left(\frac{3}{8u}+\frac{1}{32u^3}\right)\ln\left(1+4u^2\right)\right]\,, \tag{B.74}$$

$$\bar{E}_2^{(2,\mathrm{H})}(k_\mathrm{f}) = \frac{9C^2M_\mathrm{N}}{8\pi^2}\left[\frac{1}{8u} - \frac{3u}{4} + \arctan 2u - \left(\frac{3}{8u}+\frac{1}{32u^3}\right)\ln\left(1+4u^2\right)\right]\,, \tag{B.75}$$

$$\bar{E}_2^{(2,\mathrm{F})}(k_\mathrm{f}) = \frac{9C^2M_\mathrm{N}}{(2\pi u)^3}\int_0^u \mathrm{d}x\frac{x(u-x)^2(2u+x)}{1+2x^2}[\arctan 2x - \arctan x]\,, \tag{B.76}$$

$$\bar{E}_3^{(2,\mathrm{H})}(k_\mathrm{f}) = \frac{9C^2M_\mathrm{N}}{(2\pi)^4}\Big\{1+2u\arctan 2u - \left(\frac{3}{2}+\frac{1}{4u^2}\right)\ln\left(1+4u^2\right)+$$

$$\frac{3}{2u^3}\int_0^u \mathrm{d}x\big(u^2-x^2\big)\ln\frac{u+x}{u-x}\Bigg[\ln\big(1+4x^2\big)-\ln\frac{1+(u+x)^2}{1+(u-x)^2}+ 2x\big(\arctan(u+x)+\arctan(u-x)-\arctan(2x)\big)\Bigg]\Bigg\}, \tag{B.77}$$

$$\bar{E}_3^{(2,\mathrm{F})}(k_\mathrm{f}) = -\frac{27C^2M_\mathrm{N}}{64\pi^4u^3}\int_0^u \mathrm{d}x\,x^2\int_{-1}^1\mathrm{d}y\int_{-1}^1\mathrm{d}z\frac{yz\theta(y^2+z^2-1)}{|yz|\sqrt{y^2+z^2-1}}\times \ln\big(1+s^2\big)\ln\big(1+t^2\big)\,. \tag{B.78}$$

$\bar{E}_j^{(i,\mathrm{H})}$ and $\bar{E}_j^{(i,\mathrm{F})}$ denote the contribution of the ith order Hartree and Fock diagrams with j medium insertions, respectively.

The kernels for $T\neq 0$ are:

$$K_2^{(1,\mathrm{F})} = -\frac{9}{2}C\ln\frac{\lambda^2+(p_1+p_2)^2}{\lambda^2+(p_1-p_2)^2}\,, \tag{B.79}$$

$$K_2^{(2,\mathrm{H})} = -\frac{9C^2M_\mathrm{N}}{4\pi\lambda}\ln\frac{\lambda^2+(p_1+p_2)^2}{\lambda^2+(p_1-p_2)^2}\,, \tag{B.80}$$

$$K_2^{(2,\mathrm{F})} = \frac{9C^2M_\mathrm{N}}{2\pi\lambda}\int_{|p_1-p_2|/2\lambda}^{(p_1-p_2)/2\lambda}\mathrm{d}x\frac{\arctan 2x-\arctan x}{1+2x^2}\,, \tag{B.81}$$

$$K_3^{(2,\mathrm{H})} = 36C^2M_\mathrm{N}\int_{|p_1-p_2|}^{p_1+p_2}\frac{\mathrm{d}q}{(\lambda^2+q^2)^2}\ln\frac{|p_1^2-p_2^2+q^2+2p_3q|}{|p_1^2-p_2^2+q^2-2p_3q|}\,, \tag{B.82}$$

$$K_3^{(2,\mathrm{F})} = -9C^2M_\mathrm{N}\int_{|p_2-p_3|}^{p_2+p_3}\frac{\mathrm{d}q}{(\lambda^2+q^2)R_\lambda}\ln\frac{|p_1R_\lambda+(p_1^2-p_3^2-\lambda^2)h|}{|p_1R_\lambda-(p_1^2-p_3^2-\lambda^2)h|}\,, \tag{B.83}$$

with

$$R_\lambda=\sqrt{(\lambda^2+p_1^2-p_3^2)^2+4\lambda(p_3^2-h^2)}\,,\qquad h=\frac{1}{2q}(p_2^2-p_3^2-q^2)\,. \tag{B.84}$$

The anomalous contribution is:

$$\bar{A}=-\frac{\big[\Omega'_{1\pi}(\rho,T)\big]^2}{2\rho\Omega''_0(\rho,T)}+\frac{81C^2}{8T\rho}\int_0^\infty\mathrm{d}p_1\int_0^\infty\mathrm{d}p_2\int_0^\infty\mathrm{d}p_3\,d(p_1)d(p_2)\times \big[2\pi^2d(p_2)p_2\big]d(p_3)\frac{1}{p_2^2}\ln\frac{\lambda^2+(p_1+p_2)^2}{\lambda^2+(p_1-p_2)^2}\ln\frac{\lambda^2+(p_3+p_2)^2}{\lambda^2+(p_3-p_2)^2}\,, \tag{B.85}$$

with

$$\Omega'_{1\pi}(\rho,T)=-18CM_\mathrm{N}\int_0^\infty\mathrm{d}p_1\int_0^\infty\mathrm{d}p_2\,d(p_1)\frac{d(p_2)}{p_2}\times \left[\frac{p_1+p_2}{\lambda^2+(p_1+p_2)^2}+\frac{p_1-p_2}{\lambda^2+(p_1-p_2)^2}\right]. \tag{B.86}$$

B.6 Single-particle potential

As usual, we use $u = k_\mathrm{f}/m_\pi$ and $x = p/m_\pi$. $U_j^{(\mathrm{H})}$ and $U_j^{(\mathrm{F})}$ are the contributions of the iterated 1π-exchange Hartree and Fock diagrams with j medium insertions, respectively. The abbreviations s, t, σ, R, and y_min are given in sec. B.1.

B.6.1 Real part below the Fermi surface

One-pion exchange

$$U_2^{(1\pi,\mathrm{F})}(p,k_\mathrm{f}) = \frac{3g_\mathrm{A}^2 m_\pi^3}{(4\pi f_\pi)^2}\Bigg\{\frac{2u^3}{3} - u + \arctan(u+x) + \arctan(u-x) + \frac{x^2-u^2-1}{4x}\ln\frac{1+(u+x)^2}{1+(u-x)^2} + \frac{m_\pi^2}{16M_\mathrm{N}^2}\Bigg[4u\left(1-\frac{u^2}{3}-\frac{4u^4}{5}+3x^2-\frac{4}{3}u^2x^2\right) - \big(2+8x^2\big)\Big[\arctan(u+x) + \arctan(u-x)\Big] + \frac{1}{x}\big(u^2-x^2\big)\big(u^2+3x^2\big)\ln\frac{1+(u+x)^2}{1+(u-x)^2}\Bigg]\Bigg\} \quad \text{(B.87)}$$

Iterated one-pion exchange

The contributions of the linear divergence which are proportional to the momentum cut-off Λ are given in eq. (B.93).

$$U_2^{(\mathrm{H})}(p,k_\mathrm{f}) = \frac{g_\mathrm{A}^4 M_\mathrm{N} m_\pi^4}{(4\pi)^3 f_\pi^4}\Bigg\{\left(\frac{9}{2}+3u^2+\frac{2u^3}{x}-x^2\right)\arctan(u+x) + \left(\frac{9}{2}+3u^2-\frac{2u^3}{x}-x^2\right)\arctan(u-x) - \frac{11u}{2} + \frac{1}{8x}\big(15x^2-15u^2-7\big)\ln\frac{1+(u+x)^2}{1+(u-x)^2}\Bigg\} \quad \text{(B.88)}$$

$$U_2^{(\mathrm{F})}(p,k_\mathrm{f}) = \frac{g_\mathrm{A}^4 M_\mathrm{N} m_\pi^4}{(4\pi)^3 f_\pi^4}\Bigg\{u^3 + \left[\int_0^{(u-x)/2}\mathrm{d}\xi\, 2\xi + \int_{(u-x)/2}^{(u+x)/2}\mathrm{d}\xi\frac{1}{4x}\left(u^2-(2\xi-x)^2\right)\right]\times \frac{3}{1+2\xi^2}\Big[\big(1+8\xi^2+8\xi^4\big)\arctan\xi - \big(1+4\xi^2\big)\arctan 2\xi\Big]\Bigg\} \quad \text{(B.89)}$$

$$U_3^{(\mathrm{H})}(p,k_\mathrm{f}) = \frac{6g_\mathrm{A}^4 M_\mathrm{N} m_\pi^4}{(4\pi f_\pi)^4}\int_{-1}^{1}\mathrm{d}y\Bigg\{\left[2uxy + \big(u^2-x^2y^2\big)\ln\frac{u+xy}{u-xy}\right]\left[\frac{2s^2+s^4}{2(1+s^2)} - \ln(1+s^2)\right]$$

$$+\int_{-xy}^{s-xy}\mathrm{d}\xi\left[2u\xi+(u^2-\xi^2)\ln\frac{u+\xi}{u-\xi}\right]\frac{(xy+\xi)^5}{[1+(xy+\xi)^2]^2}+ \int_0^u\mathrm{d}\xi\,\frac{\xi^2}{x}\ln\frac{|x+\xi y|}{|x-\xi y|}\left[\frac{2\sigma^2+\sigma^4}{1+\sigma^2}-2\ln(1+\sigma^2)\right]\Bigg\} \quad \text{(B.90)}$$

$$U_3^{(\mathrm{F})}(p,k_\mathrm{f})=\frac{3g_\mathrm{A}^4M_\mathrm{N}m_\pi^4}{(4\pi f_\pi)^4}\Bigg\{\frac{G^2(x)}{8x^2}+\int_0^u\mathrm{d}\xi\,G(\xi)\left[1+\frac{\xi^2-x^2-1}{4x\xi}\ln\frac{1+(x+\xi)^2}{1+(x-\xi)^2}\right]+ \int_{-1}^1\mathrm{d}y\left[\int_{-1}^1\mathrm{d}z\frac{yz\,\theta(y^2+z^2-1)}{4|yz|\sqrt{y^2+z^2-1}}\Big[s^2-\ln(1+s^2)\Big]\Big[\ln(1+t^2)-t^2\Big]+ \int_0^u\mathrm{d}\xi\,\frac{\xi^2}{x}\Big[\ln(1+\sigma^2)-\sigma^2\Big]\Bigg(\ln\frac{|x+\xi y|}{|x-\xi y|}+ \frac{1}{R}\ln\frac{[xR+(x^2-\xi^2-1)y\xi]^2}{[1+(x+\xi)^2][1+(x-\xi)^2)]|x^2-\xi^2y^2|}\Bigg)\Bigg]\Bigg\} \quad \text{(B.91)}$$

Irreducible two-pion exchange in cut-off regularization

This expression does not include the effects from πNΔ-dynamics.

$$U^{(2\pi)}(p,k_\mathrm{f})=\frac{m_\pi^5}{(4\pi f_\pi)^4}\left[\int_0^{(u-x)/2}\mathrm{d}\xi\,8\xi+\int_{(u-x)/2}^{(u+x)/2}\mathrm{d}\xi\,\frac{1}{x}\big(u^2-(2\xi-x)^2\big)\right]\Bigg\{\frac{4}{\sqrt{1+\xi^2}}\times \ln\Big(\xi+\sqrt{1+\xi^2}\Big)\Big[g_\mathrm{A}^4(11\xi^4+16\xi^2+8)-2g_\mathrm{A}^2(5\xi^4+7\xi^2+2)-(1+\xi^2)^2\Big]+ (1-14g_\mathrm{A}^2+61g_\mathrm{A}^4)\xi+2(1+2g_\mathrm{A}^2+5g_\mathrm{A}^4)\xi^3+ \Big[6(15g_\mathrm{A}^4-6g_\mathrm{A}^2-1)\xi+4(11g_\mathrm{A}^4-10g_\mathrm{A}^2-1)\xi^3\Big]\ln\frac{m_\pi}{2\Lambda}\Bigg\}. \quad \text{(B.92)}$$

The contributions of the polynomial divergence which are proportional to Λ^2 are given in eq. (B.93).

Polynomial divergences from cut-off regularization

$$U_2^{(\Lambda)}(p,k_\mathrm{f})=\frac{2k_\mathrm{f}^3}{(4\pi f_\pi)^4}\Big[-10g_\mathrm{A}^4M_\mathrm{N}\,\Lambda+(3g_\mathrm{A}^2+1)(g_\mathrm{A}^2-1)\,\Lambda^2\Big]. \quad \text{(B.93)}$$

Dispersion integral form of irreducible two-pion exchange

The subtraction constants $B_{3,5}$ subsuming unresolved short distance dynamics give the following contribution:

$$U_2^{(\mathrm{NN})}(p,k_\mathrm{f})=2B_3\frac{k_\mathrm{f}^3}{M_\mathrm{N}^2}+B_5\frac{k_\mathrm{f}^3}{3M_\mathrm{N}^4}(3k_\mathrm{f}^2+5p^2). \quad \text{(B.94)}$$

The contribution of the Fock diagrams of 2π-exchange (both with and without virtual Δ-excitations) to the two-body potential can be written as a (subtracted) dispersion integral:

$$U_2^{(\mathrm{F})}(p,k_\mathrm{f}) = \frac{1}{2\pi^3}\int_{2m_\pi}^{\infty}\mathrm{d}\mu\,\mathrm{Im}(V_C+3W_C+2\mu^2V_T+6\mu^2W_T)\times \\ \left\{\mu k_\mathrm{f}+\frac{2k_\mathrm{f}^3}{15\mu^3}(3k_\mathrm{f}^2+5p^2)-\frac{2k_\mathrm{f}^3}{3\mu}-\mu^2\arctan\frac{k_\mathrm{f}+p}{\mu}- \right. \\ \left. \mu^2\arctan\frac{k_\mathrm{f}-p}{\mu}+\frac{\mu}{4p}(\mu^2+k_\mathrm{f}^2-p^2)\ln\frac{\mu^2+(k_\mathrm{f}+p)^2}{\mu^2+(k_\mathrm{f}-p)^2}\right\}. \quad \text{(B.95)}$$

By opening a nucleon line in the three-body diagrams of fig. 7.2 one gets (per diagram) three different contributions to the three-body potential. In the case of the (left) Hartree diagram they read altogether:

$$U_3^{(\mathrm{H})}(p,k_\mathrm{f}) = \frac{g_\mathrm{A}^4m_\pi^6}{\Delta(2\pi f_\pi)^4}\left\{2u^6+u^2-7u^4-\frac{1}{4}(1+9u^2)\ln(1+4u^2)+5u^3\Big[\arctan 2u+ \right. \\ \left. \arctan(u+x)+\arctan(u-x)\Big]+\frac{u^3}{2x}(2x^2-2u^2-3)\ln\frac{1+(u+x)^2}{1+(u-x)^2}\right\}. \quad \text{(B.96)}$$

On the other hand the (right) Fock diagram in fig. 7.2 generates a total contribution to the three-body potential of the form:

$$U_3^{(\mathrm{F})}(p,k_\mathrm{f}) = -\frac{g_\mathrm{A}^4m_\pi^6x^{-2}}{4\Delta(4\pi f_\pi)^4}\left\{2G_S^2(x,u)+G_T^2(x,u)+ \right. \\ \left. \int_0^u\mathrm{d}\xi\left[4G_S(\xi,u)\frac{\partial G_S(\xi,x)}{\partial x}+2G_T(\xi,u)\frac{\partial G_T(\xi,x)}{\partial x}\right]\right\}, \quad \text{(B.97)}$$

with $G_{S,T}(x,u)$ defined in eqs. (B.25,B.26).

Additional three-body contact interaction

The additional three-body contact interaction generates the following (momentum independent) contribution:

$$U_3^{(\mathrm{NNN})}(k_\mathrm{f}) = 3B_6\frac{k_\mathrm{f}^6}{M_\mathrm{N}^5}\,. \quad \text{(B.98)}$$

B.6.2 Real part above the Fermi surface

Eqs. (B.87,B.88,B.93-B.98) remain unchanged. Eq. (B.89) is modified to:

$$U_2^{(\mathrm{F})}(p,k_\mathrm{f}) = \frac{g_\mathrm{A}^4M_\mathrm{N}m_\pi^4}{(4\pi)^3f_\pi^4}\left\{u^3+\frac{3}{4x}\int_{(x-u)/2}^{(u+x)/2}\mathrm{d}\xi\,\frac{u^2-(2\xi-x)^2}{1+2\xi^2}\times \right. \\ \left. \Big[(1+8\xi^2+8\xi^4)\arctan\xi-(1+4\xi^2)\arctan 2\xi\Big]\right\}. \quad \text{(B.99)}$$

Eq. (B.90) gets modified to:

$$U_3^{(\mathrm{H})}(p,k_\mathrm{f}) = \frac{6g_\mathrm{A}^4 M_\mathrm{N} m_\pi^4}{(4\pi f_\pi)^4}\Bigg\{ \int_{y_\mathrm{min}}^1 \mathrm{d}y \Bigg\{ \Bigg[2uxy + (u^2 - x^2y^2)\ln\frac{u+xy}{|u-xy|}\Bigg]\times \\ \mathcal{A}_y\Bigg[\frac{2s^2+s^4}{2(1+s^2)} - \ln(1+s^2)\Bigg] + \\ \int_{xy-s}^{s-xy}\mathrm{d}\xi\,\Bigg[2u\xi + (u^2-\xi^2)\ln\frac{u+\xi}{u-\xi}\Bigg]\,\frac{(xy+\xi)^5}{[1+(xy+\xi)^2]^2}\Bigg\} + \\ \int_{-1}^1 \mathrm{d}y \int_0^u \mathrm{d}\xi\,\frac{\xi^2}{x}\,\Bigg[\frac{2\sigma^2+\sigma^4}{1+\sigma^2} - 2\ln(1+\sigma^2)\Bigg]\ln\frac{x+\xi y}{x-\xi y}\Bigg\}. \quad \text{(B.100)}$$

Eq. (B.91) gets modified to:

$$U_3^{(\mathrm{F})}(p,k_\mathrm{f}) = \frac{3g_\mathrm{A}^4 M_\mathrm{N} m_\pi^4}{(4\pi f_\pi)^4}\Bigg\{ \frac{G^2(x)}{8x^2} + \int_0^u \mathrm{d}\xi\, G(\xi)\Bigg[1 + \frac{\xi^2-x^2-1}{4x\xi}\ln\frac{1+(x+\xi)^2}{1+(x-\xi)^2}\Bigg] + \\ \int_{y_\mathrm{min}}^1 \mathrm{d}y \int_{y_\mathrm{min}}^1 \mathrm{d}z \frac{\theta(y^2+z^2-1)}{4\sqrt{y^2+z^2-1}}\,\mathcal{A}_y\Big[s^2 - \ln(1+s^2)\Big]\mathcal{A}_z\Big[\ln(1+t^2) - t^2\Big] + \\ \int_{-1}^1 \mathrm{d}y \int_0^u \mathrm{d}\xi\,\frac{\xi^2}{x}\Big[\ln(1+\sigma^2) - \sigma^2\Big]\Bigg(\ln\frac{x+\xi y}{x-\xi y} + \\ \frac{1}{R}\ln\frac{xR + (x^2-\xi^2-1)y\xi}{xR + (1-x^2+\xi^2)y\xi}\Bigg)\Bigg\}, \quad \text{(B.101)}$$

where we have introduced the antisymmetrization prescription $\mathcal{A}_y[f(y)] = f(y) - f(-y)$. The auxiliary functions $G(x)$ and R are given in section B.1. Eq. (B.92) gets modified to:

$$U^{(2\pi)}(p,k_\mathrm{f}) = \frac{m_\pi^5}{(4\pi f_\pi)^4}\int_{(x-u)/2}^{(u+x)/2}\mathrm{d}\xi\,\frac{1}{x}\big(u^2-(2\xi-x)^2\big)\Bigg\{\frac{4}{\sqrt{1+\xi^2}}\ln\Big(\xi+\sqrt{1+\xi^2}\Big)\times \\ \Big[g_\mathrm{A}^4(11\xi^4+16\xi^2+8) - 2g_\mathrm{A}^2(5\xi^4+7\xi^2+2) - (1+\xi^2)^2\Big] + \\ (1-14g_\mathrm{A}^2+61g_\mathrm{A}^4)\xi + 2(1+2g_\mathrm{A}^2+5g_\mathrm{A}^4)\xi^3 + \\ \Big[6(15g_\mathrm{A}^4-6g_\mathrm{A}^2-1)\xi + 4(11g_\mathrm{A}^4-10g_\mathrm{A}^2-1)\xi^3\Big]\ln\frac{m_\pi}{2\Lambda}\Bigg\}. \quad \text{(B.102)}$$

B.6.3 Imaginary part below the Fermi surface

$W_j^{(\mathrm{H})}$ and $W_j^{(\mathrm{F})}$ are the contributions from the iterated 1π-exchange Hartree and Fock diagrams with j medium insertions respectively.

$$W_2^{(\mathrm{H})}(p,k_\mathrm{f}) = \frac{\pi g_\mathrm{A}^4 M_\mathrm{N} m_\pi^4}{(4\pi f_\pi)^4}\Bigg\{ \left(9+6u^2+\frac{4u^3}{x}-2x^2\right)\ln\left[1+(u+x)^2\right]-3u^4+ x^2\left(\frac{x^2}{5}-2u^2+\frac{50}{3}\right)+\left(9+6u^2-\frac{4u^3}{x}-2x^2\right)\ln\left[1+(u-x)^2\right]- 34u^2-14+\frac{1}{x}\left(7+15u^2-15x^2\right)\Big[\arctan(u+x)-\arctan(u-x)\Big]\Bigg\} \quad \text{(B.103)}$$

$$W_2^{(\mathrm{F})}(p,k_\mathrm{f}) = \frac{3\pi g_\mathrm{A}^4 M_\mathrm{N} m_\pi^4}{(4\pi f_\pi)^4}\Bigg\{ \frac{u^4}{4}+\frac{u^2x^2}{6}-\frac{x^4}{60}- \left[\int_0^{(u-x)/2}\mathrm{d}\xi\,4\xi+\int_{(u-x)/2}^{(u+x)/2}\mathrm{d}\xi\frac{1}{2x}\left(u^2-(2\xi-x)^2\right)\right]\frac{1+4\xi^2}{1+2\xi^2}\ln(1+4\xi^2)\Bigg\} \quad \text{(B.104)}$$

$$W_3^{(\mathrm{H})}(p,k_\mathrm{f}) = \frac{g_\mathrm{A}^4 M_\mathrm{N} m_\pi^4}{(8\pi)^3 f_\pi^4}\Bigg\{35+151u^2+25u^4-\frac{197x^2}{3}-2u^2x^2-7x^4+18\ln(1+4x^2)+ \left(\frac{21}{2x}-30x\right)\arctan 2x+\Big[\arctan(u+x)-\arctan(u-x)\Big]\times \frac{1}{2x}\Big[(x^2-u^2)^3+9(4u^2+15)(x^2-u^2)-56\Big]+ 4\Big(3x^2-9-\frac{2u^3}{x}-9u^2\Big)\ln[1+(u+x)^2]+ 4\Big(3x^2-9+\frac{2u^3}{x}-9u^2\Big)\ln[1+(u-x)^2]\Bigg\} \quad \text{(B.105)}$$

$$W_3^{(\mathrm{F})}(p,k_\mathrm{f}) = \frac{3g_\mathrm{A}^4 M_\mathrm{N} m_\pi^4}{(4\pi f_\pi)^4}\int_{-1}^{1}\mathrm{d}y\Bigg\{\int_{-1}^{1}\mathrm{d}z\frac{\theta(1-y^2-z^2)}{4\sqrt{1-y^2-z^2}}\Big[s^2-\ln(1+s^2)\Big]\times \Big[\ln(1+t^2)-t^2\Big]+\int_0^u\mathrm{d}\xi\,\frac{\pi\xi^2}{x}\,\theta(x-\xi|y|)\Big[\ln(1+\sigma^2)-\sigma^2\Big]\left(1-\frac{1}{R}\right)\Bigg\} \quad \text{(B.106)}$$

$$W_4^{(\mathrm{H})}(p,k_\mathrm{f}) = \frac{g_\mathrm{A}^4 M_\mathrm{N} m_\pi^4}{(8\pi)^3 f_\pi^4}\Bigg\{\frac{63x^4}{5}-13u^4-7-2u^2(49+3x^2)+\frac{142x^2}{3}-36\ln(1+4x^2)+ \left(60x-\frac{21}{x}\right)\arctan 2x+\Big[\arctan(u+x)-\arctan(u-x)\Big]\times \frac{1}{2x}\Big[(u^2-x^2)^3-9x^4-18u^2x^2+27u^4-135x^2+75u^2+49\Big]+ 4(9+6u^2-2x^2)\ln\Big([1+(u+x)^2][1+(u-x)^2]\Big)\Bigg\} \quad \text{(B.107)}$$

$$W_4^{(\mathrm{F})}(p,k_\mathrm{f}) = \frac{3\pi g_\mathrm{A}^4 M_\mathrm{N} m_\pi^4}{(4\pi f_\pi)^4} \int_{-1}^{1}\mathrm{d}y \int_0^u \mathrm{d}\xi\, \frac{\xi^2}{x}\left(1-\frac{1}{R}\right)\Big\{\theta(x-\xi|y|)\,\theta(\xi-x)\times \Big[\sigma^2-\ln(1+\sigma^2)\Big] + \theta(x-\xi)\Big[\sigma_x^2-\ln(1+\sigma_x^2)\Big]\Big\} \quad \text{(B.108)}$$

B.6.4 Imaginary part above the Fermi surface

Hartree diagrams of iterated one-pion exchange

$$W^{(\mathrm{H})}(p,k_\mathrm{f}) = \frac{\pi g_\mathrm{A}^4 M_\mathrm{N} m_\pi^4}{(4\pi f_\pi)^4}\Bigg\{\left(9+6u^2+\frac{4u^3}{x}-2x^2\right)\ln[1+(u+x)^2] + 4ux(2-u^2) + \left(\frac{4u^3}{x}+2x^2-9-6u^2\right)\ln[1+(x-u)^2] + \frac{1}{x}\Bigg[\frac{12u^5}{5}-\frac{21u}{2}-8u^3\ln(1+4u^2) + (7+15u^2-15x^2)[\arctan(u+x)-\arctan(x-u)] - \left(15u^2+\frac{7}{4}\right)\arctan 2u\Bigg] + 3\theta\big(\sqrt{2}u-x\big)\int_{y_\mathrm{min}}^{u/x}\mathrm{d}y(x^2y^2-u^2)\mathcal{A}_y\left[\frac{2s^2+s^4}{1+s^2}-2\ln(1+s^2)\right] + \int_{y_\mathrm{min}}^{1}\mathrm{d}y\,\mathcal{A}_y\Bigg[\frac{3s^4x^2(y^2-1)}{1+s^2}-\frac{9s^4}{2}+10xy(3\arctan s-3s+s^3) + (9+6u^2-6x^2y^2)[s^2-\ln(1+s^2)]\Bigg]\Bigg\}. \quad \text{(B.109)}$$

Note that there is a term in eq. (B.109) which vanishes identically above $p=\sqrt{2}k_\mathrm{f}$. A geometrical explanation for this nonsmooth behavior is that an orthogonal pair of vectors connecting the origin with two points inside a sphere ceases to exist if the center of the sphere is displaced too far from the origin (namely by more than $\sqrt{2}$ times the sphere radius). The orthogonality of the (momentum difference) vectors is imposed here by the nonrelativistic on-mass-shell condition for a nucleon.

Fock diagrams of iterated one-pion exchange

$$W^{(\mathrm{F})}(p,k_\mathrm{f}) = \frac{\pi g_\mathrm{A}^4 M_\mathrm{N} m_\pi^4}{(4\pi f_\pi)^4}\Bigg\{u^3x+\frac{u^5}{5x}+\frac{3}{2x}\int_{(x-u)/2}^{(x+u)/2}\mathrm{d}\xi\Big[(2\xi-x)^2-u^2\Big]\frac{1+4\xi^2}{1+2\xi^2}\times \ln(1+4\xi^2) + \frac{3}{4\pi}\theta\big(\sqrt{2}u-x\big)\int_{y_\mathrm{min}}^{1}\mathrm{d}y\int_{y_\mathrm{min}}^{1}\mathrm{d}z\,\frac{\theta(1-y^2-z^2)}{\sqrt{1-y^2-z^2}}\,\mathcal{A}_y\Big[s^2-\ln(1+s^2)\Big]\times \mathcal{A}_z\Big[t^2-\ln(1+t^2)\Big] + \frac{3}{x}\int_{-1}^{1}\mathrm{d}y\int_0^u\mathrm{d}\xi\,\xi^2\Big[\ln(1+\sigma^2)-\sigma^2\Big]\left(1-\frac{1}{R}\right)\Bigg\} \quad \text{(B.110)}$$

B.7 Energy density functional

B.7.1 One-pion exchange

The Hartree diagram vanishes. The nonvanishing contributions for the Fock diagram with two medium insertions read up to $\mathcal{O}(k_{\rm f}^4)$ (as used in chapter 5):

$$F_\tau^{(1\pi)}(k_{\rm f}) = \frac{35 g_{\rm A}^2 m_\pi}{(16\pi f_\pi)^2 u^5}\left\{\frac{4}{3}u^4 + 24u^2 - 1 - 20u\arctan 2u + \left(\frac{9}{2} - 6u^2 + \frac{1}{4u^2}\right)\ln(1+4u^2)\right\}, \quad \text{(B.111)}$$

$$F_J^{(1\pi)}(k_{\rm f}) = \frac{g_{\rm A}^2}{(8 m_\pi f_\pi)^2}\left\{\frac{10+24u^2}{(1+4u^2)^2} + \frac{1}{2u^2}\ln(1+4u^2)\right\}. \quad \text{(B.112)}$$

The expression for $F_\tau^{1\pi}(k_{\rm f})$ in eq. (B.111) follows simply from inserting the static 1π-exchange single particle potential (eq. (B.87) in the limit $M_{\rm N} \to \infty$) into the "master formula" (5.7). The vanishing of $F_d^{1\pi}(k_{\rm f})$ has the following reason. The momentum transfer $\pm\mathbf{q}$ at the upper and lower medium insertion does not flow into the exchanged virtual pion line (because of momentum conservation at each interaction vertex). Therefore there is no factor of $\mathbf{q}^2$ which could produce via Fourier transformations a $(\boldsymbol{\nabla}\rho)^2$-factor. The spin-orbit strength $F_{\rm so}^{1\pi}(k_{\rm f})$ vanishes as a result of the spin-trace: $\mathrm{Tr}[\boldsymbol{\sigma}\cdot(\mathbf{p}_1-\mathbf{p}_2)\;\boldsymbol{\sigma}\cdot(\mathbf{p}_{1,2}\times\mathbf{J})\;\boldsymbol{\sigma}\cdot(\mathbf{p}_1-\mathbf{p}_2)] = 0$.

When doing the expansion up to order $\mathcal{O}(k_{\rm f}^5)$ (as in chapter 7), one has to include the additional relativistic $1/M_{\rm N}^2$-correction:

$$F_\tau^{(1\pi,{\rm rel})}(k_{\rm f}) = \frac{g_{\rm A}^2 m_\pi^3 u^{-5}}{(32\pi f_\pi M_{\rm N})^2}\left\{\frac{280}{3}u^6 - \frac{15}{2} + 2u(525 - 700u^2 - 96u^4)\arctan 2u - 64u^8 + 744u^4 - 1777u^2 + \left(1050u^2 - 77 + \frac{15}{8u^2}\right)\ln(1+4u^2)\right\}. \quad \text{(B.113)}$$

B.7.2 Iterated one-pion exchange

Hartree diagram with two medium insertions

We find the following closed form expressions:

$$F_\tau^{({\rm H},2)}(k_{\rm f}) = \frac{g_{\rm A}^4 M_{\rm N} m_\pi^2}{(8\pi)^3 (u f_\pi)^4}\left\{\frac{151}{3}u^3 - (350+16u^4)\arctan 2u + 444u - \frac{55}{4u} + \left(\frac{55}{16u^3} + \frac{567}{8u} - \frac{245}{2}u\right)\ln(1+4u^2)\right\}, \quad \text{(B.114)}$$

$$F_d^{({\rm H},2)}(k_{\rm f}) = \frac{g_{\rm A}^4 M_{\rm N}}{\pi m_\pi (4 f_\pi)^4}\left\{\frac{4}{u}\arctan 2u - \frac{23}{16u^2}\ln(1+4u^2) - \frac{3+20u^2}{12(1+4u^2)^2}\right\}, \quad \text{(B.115)}$$

$$F_{\rm so}^{(\rm H,2)}(k_{\rm f}) = \frac{g_{\rm A}^4 M_{\rm N}}{\pi m_\pi (4f_\pi)^4}\left\{\frac{4}{1+4u^2} - \frac{3}{2u^2}\ln(1+4u^2)\right\}. \tag{B.116}$$

Again, $F_\tau^{(\rm H,2)}(k_{\rm f})$ in eq. (B.114) stems from inserting the two-body potential $U_2^{(\rm H)}(p,k_{\rm f})$ from eq. (B.88) into the "master formula" (5.7). Note that any p-independent contribution, in particular the cut-off dependent term eq. (B.93), drops out. The vanishing of $F_J^{(\rm H,2)}(k_{\rm f})$ results from the spin-trace over a nucleon ring being equal to zero (as demonstrated in the previous section). Let us briefly explain the mechanism which generates the strength function $F_d^{(\rm H,2)}(k_{\rm f})$. The exchanged pion-pair transfers the momentum $\mathbf{q}$ between the left and the right nucleon ring. This momentum $\mathbf{q}$ enters both the pseudovector πN-interaction vertices and the pion propagators. After expanding the inner loop integral to order $\mathbf{q}^2$ the Fourier transformation in eq. (5.5) converts this factor $\mathbf{q}^2$ into a factor $(\boldsymbol{\nabla} k_{\rm f})^2$. The rest is a solvable integral over the product of two Fermi surfaces. The spin-orbit strength $F_{\rm so}^{(\rm H,2)}(k_{\rm f})$ arises from the spin-trace: $\mathrm{Tr}[\boldsymbol{\sigma}\cdot(\mathbf{l}+\mathbf{q}/2)\,\boldsymbol{\sigma}\cdot(\mathbf{l}-\mathbf{q}/2)\,\boldsymbol{\sigma}\cdot(\mathbf{p}_{1,2}\times\mathbf{J})] = 2\mathrm{i}\,(\mathbf{q}\times\mathbf{l})\cdot(\mathbf{p}_{1,2}\times\mathbf{J})$ where $\mathbf{q}$ gets again converted to $\boldsymbol{\nabla}k_{\rm f}$ by Fourier transformation. The remainder is a solvable integral over delta-functions and derivatives thereof.

Fock diagram with two medium insertions

We find the following contributions from the last diagram in fig. 3.1 with two medium insertions at non-neighboring nucleon propagators:

$$F_\tau^{(\rm F,2)}(k_{\rm f}) = \frac{35 g_{\rm A}^4 M_{\rm N} m_\pi^2}{(4\pi)^3 f_\pi^4 u^7}\int_0^u {\rm d}x \frac{x^2(u-x)^2}{2(1+2x^2)}(2x^2+4ux-3u^2)\times \left[(1+8x^2+8x^4)\arctan x - (1+4x^2)\arctan 2x\right], \tag{B.117}$$

$$F_d^{(\rm F,2)}(k_{\rm f}) = \frac{g_{\rm A}^4 M_{\rm N}}{\pi m_\pi (8f_\pi)^4}\left\{\frac{4}{u}(\arctan u - 2\arctan 2u) + \frac{1}{u^2}\ln\frac{(1+2u^2)(1+4u^2)}{(1+u^2)^2} + \frac{4}{1+2u^2} + \frac{2}{u^2}\int_0^u {\rm d}x \frac{3+18x^2+16x^4}{(1+2x^2)^3}\Big[\arctan 2x - \arctan x\Big]\right\}, \tag{B.118}$$

$$F_{\rm so}^{(\rm F,2)}(k_{\rm f}) = \frac{g_{\rm A}^4 M_{\rm N}}{\pi m_\pi (4f_\pi)^4}\left\{\frac{1}{4u^2}\ln\frac{1+4u^2}{1+u^2} + \frac{3+4u^2}{2u(1+2u^2)}\arctan u - \frac{\arctan 2u}{2u(1+2u^2)} + \frac{1}{2u^2}\int_0^u {\rm d}x \frac{\arctan x - \arctan 2x}{1+2x^2}\right\}, \tag{B.119}$$

$$F_J^{(\rm F,2)}(k_{\rm f}) = \frac{g_{\rm A}^4 M_{\rm N}}{\pi m_\pi (8f_\pi)^4}\left\{\frac{2\arctan 2u}{u(1+2u^2)} - \frac{2(5+8u^2)}{u(1+2u^2)}\arctan u - \frac{1}{1+u^2} - \frac{1}{u^2}\ln\frac{1+4u^2}{1+u^2} + \frac{2}{u^2}\int_0^u {\rm d}x \frac{\arctan 2x - \arctan x}{1+2x^2}\right\}. \tag{B.120}$$

The basic mechanisms which lead to these results are the same as explained before. Concerning kinematics and spin-algebra the iterated 1π-exchange Fock diagram is somewhat more involved than the Hartree diagram. Even though all occurring inner d^3l-loop integrals can be solved in closed form there remain some nonelementary integrals from the integration over the product of two Fermi spheres of radius k_f.

Hartree diagram with three medium insertions

In this case one has to evaluate nine-dimensional principal value integrals over the product of three Fermi spheres of radius k_f. Using the techniques explained in the appendix we find the following contributions to the strength functions:

$$F_\tau^{(\mathrm{H},3)}(k_\mathrm{f}) = \frac{175 g_\mathrm{A}^4 M_\mathrm{N} m_\pi^2}{(4\pi f_\pi)^4 u^7} \int_0^u \mathrm{d}x\, x^2 \int_{-1}^1 \mathrm{d}y \Bigg\{ u^3 xy \left[\ln(1+s^2) - \frac{2s^2+s^4}{2(1+s^2)} \right] + \left[2uxy + (u^2 - x^2y^2)H \right] \left[\frac{3}{4} \left(3 + \frac{13}{5}u^2 - 4x^2 - x^2y^2 \right) \ln(1+s^2) + \left(4x^2 + x^2y^2 - \frac{13}{5}u^2 - 2 \right) \frac{3(2s^2+s^4)}{8(1+s^2)} + \frac{3}{8}s^2(s^2-2) + sxy(6-s^2) + \frac{3sxy}{2(1+s^2)} - \frac{15}{2}xy \arctan s \right] \Bigg\}, \quad \text{(B.121)}$$

$$F_d^{(\mathrm{H},3)}(k_\mathrm{f}) = \frac{g_\mathrm{A}^4 M_\mathrm{N} u^{-4}}{\pi^2 m_\pi (4f_\pi)^4} \int_0^u \mathrm{d}x\, x^2 \int_{-1}^1 \mathrm{d}y \times \left\{ H \left[\frac{s^2}{4(1+s^2)^4} (7s^6 + 38s^4 + 63s^2 + 24) - 6\ln(1+s^2) \right] + \frac{uxy}{u^2 - x^2y^2} \left[\frac{s^2}{6(1+s^2)^3} (23s^4 + 51s^2 + 24) - 4\ln(1+s^2) \right] \right\}, \quad \text{(B.122)}$$

$$F_\mathrm{so}^{(\mathrm{H},3)}(k_\mathrm{f}) = \frac{2 g_\mathrm{A}^4 M_\mathrm{N} u^{-6}}{\pi^2 m_\pi (4f_\pi)^4} \int_0^u \mathrm{d}x\, x^2 \int_{-1}^1 \mathrm{d}y \Bigg\{ \frac{2us^4[2x^2y^2(s-s') - u^2 s]}{(1+s^2)^2(u^2 - x^2y^2)} + \left[\frac{u(3u^2 - 5x^2y^2)}{u^2 - x^2y^2} - 4xyH \right] \left[3\arctan s - \frac{3s + 2s^3}{1+s^2} \right] + \frac{Hs^4}{(1+s^2)^3} \Big[(5+s^2)s'^2 - 2xys'(7+3s^2) + sxy(11+7s^2) + (s+s^3)(s''-s') \Big] \Bigg\}. \quad \text{(B.123)}$$

Here we have used the partial derivatives $s' = u\partial s/\partial u$ and $s'' = u^2\partial^2 s/\partial u^2$.

$$F_J^{(\mathrm{H},3)}(k_\mathrm{f}) = \frac{g_\mathrm{A}^4 M_\mathrm{N}}{\pi^2 m_\pi (4f_\pi)^4} \left\{ \frac{96u^6 + 24u^4 - 12u^2 - 1}{u(1+4u^2)^3} + \frac{1+2u^2}{4u^3} \ln(1+4u^2) + \right.$$

$$\int_0^1 \mathrm{d}y\, \frac{8u^3y^2}{(1+4u^2y^2)^4}\Big[(30+32u^2)y^2-5+(16u^4-24u^2-35)y^4- 56u^2y^6-48u^4y^8\Big]\ln\frac{1+y}{1-y}\Big\}. \quad \text{(B.124)}$$

The last contribution $F_J^{(\mathrm{H},3)}(k_\mathrm{f})$ in eq. (B.124) is obtained when both insertions proportional to $\boldsymbol{\sigma}\cdot(\mathbf{p}_{1,2}\times\mathbf{J})$ (producing, after integration, the overall $\mathbf{J}^2$-factor) are under a single spin-trace. For the other two possible combinations the spin-traces are equal to zero.

Fock diagram with three medium insertions

The evaluation of this diagram is most tedious . It is advisable to split the contributions to the four strength functions $F_\tau^{(\mathrm{F},3)}(k_\mathrm{f})$, $F_d^{(\mathrm{F},3)}(k_\mathrm{f})$, $F_\mathrm{so}^{(\mathrm{F},3)}(k_\mathrm{f})$ and $F_J^{(\mathrm{F},3)}(k_\mathrm{f})$ into "factorizable" and "nonfactorizable" parts. These two pieces are distinguished by whether the nucleon propagator in the denominator can be canceled or not by terms from the product of πN-interaction vertices in the numerator. We find the following "factorizable" contributions:

$$F_\tau^{(\mathrm{F,3f})}(k_\mathrm{f}) = \frac{35g_\mathrm{A}^4M_\mathrm{N}m_\pi^2}{2(8\pi f_\pi)^4u^7}\int_0^u \mathrm{d}x\,\Big[u(1+u^2+x^2)-[1+(u+x)^2][1+(u-x)^2]L\Big]\times \Big\{5u(5x^4+19x^2-2)-u^3\Big(\frac{26}{3}x^2+17\Big)-7u^5- 80x^2\Big[\arctan(u+x)+\arctan(u-x)\Big]+\Big[(1+u^2)^2(10+7u^2)+ 3x^2(25+8u^2-13u^4)+3x^4(19u^2-40)-25x^6\Big]L\Big\}, \quad \text{(B.125)}$$

with the auxiliary function:

$$L=\frac{1}{4x}\ln\frac{1+(u+x)^2}{1+(u-x)^2}, \quad \text{(B.126)}$$

$$F_d^{(\mathrm{F,3f})}(k_\mathrm{f}) = \frac{g_\mathrm{A}^4M_\mathrm{N}u^{-2}}{\pi^2m_\pi(8f_\pi)^4}\Big\{\frac{1+6u^2}{4u^3}\ln^2(1+4u^2)+\frac{6u(1+8u^2)}{1+4u^2}- \frac{19u^2}{1+u^2}\arctan 2u-\frac{5+52u^2+104u^4}{2u(1+u^2)(1+4u^2)}\ln(1+4u^2)+ 8\int_0^u \mathrm{d}x\Big\{\Big[1+u^2+3(1+u^2)^2x^{-2}\Big]L^2+3u^2x^{-2}+ \Big[(4u-x)[1+(u+x)^2]^{-1}+(4u+x)[1+(u-x)^2]^{-1}-4u- 6(u+u^3)x^{-2}-2x[1+(u+x)^2]^{-2}+2x[1+(u-x)^2]^{-2}\Big]L\Big\}\Big\}, \quad \text{(B.127)}$$

$$F_{\rm so}^{(\rm F,3f)}(k_{\rm f}) = \frac{g_{\rm A}^4 M_{\rm N} u^{-3}}{\pi^2 m_\pi (4f_\pi)^4}\Bigg\{\frac{1+2u^2}{32u^2}\ln^2(1+4u^2) - \frac{3u^4\ln(1+4u^2)}{(1+u^2)(1+4u^2)} + \frac{u^2(3+20u^2)}{2(1+4u^2)} - \frac{u(1+11u^2+16u^4)}{(1+u^2)(1+4u^2)}\arctan 2u + \int_0^u {\rm d}x\,\Bigg\{\Big[3(1+u^2)^2x^{-2} - 4x^2 - 1 - u^2\Big]uL^2 + \Big[(1+5u^2+5ux)[1+(u+x)^2]^{-1} + (1+5u^2-5ux)[1+(u-x)^2]^{-1} - 6(u^2+u^4)x^{-2} - 2\Big]L + 3u^3x^{-2}\Bigg\}\Bigg\}, \quad \text{(B.128)}$$

$$F_{J}^{(\rm F,3f)}(k_{\rm f}) = \frac{g_{\rm A}^4 M_{\rm N} u^{-3}}{\pi^2 m_\pi (8f_\pi)^4}\Bigg\{\frac{3+12u^2+8u^4}{4u^4}\ln^2(1+4u^2) - \frac{7+8u^2+8u^4}{u^2(1+u^2)}\ln(1+4u^2) + \frac{2(5-2u^2)(2+3u^2)}{u(1+u^2)}\arctan 2u + \frac{8(8u^6-158u^4-73u^2-9)}{3(1+4u^2)^2} + 8\int_0^u {\rm d}x\,\Bigg\{\Big[3(1+u^2)^2x^{-2} + 3x^2 - 2 - 2u^2\Big]uL^2 + 3u^3x^{-2} + 2\Big[2 + u^2 - 3x^{-2}(u^2+u^4) + (u^2-ux-1)[1+(u+x)^2]^{-1} + (u^2+ux-1)[1+(u-x)^2]^{-1}\Big]L\Bigg\}\Bigg\}. \quad \text{(B.129)}$$

The "nonfactorizable" contributions (stemming from nine-dimensional principal value integrals over the product of three Fermi spheres of radius $k_{\rm f}$) read on the other hand:

$$F_{\tau}^{(\rm F,3n)}(k_{\rm f}) = \frac{35 g_{\rm A}^4 M_{\rm N} m_\pi^2}{(8\pi f_\pi)^4 u^7}\int_0^u {\rm d}x\,x^2\int_{-1}^1 {\rm d}y\int_{-1}^1 {\rm d}z\frac{yz\,\theta(y^2+z^2-1)}{|yz|\sqrt{y^2+z^2-1}}\times \Big[t^2 - \ln(1+t^2)\Big]\Big\{(45x^2-27u^2-30)\ln(1+s^2) + 120xy\arctan s + 2sxy(17u^2-30-35x^2+20x^2y^2)\Big\}, \quad \text{(B.130)}$$

$$F_{d}^{(\rm F,3n)}(k_{\rm f}) = \frac{g_{\rm A}^4 M_{\rm N} u^{-6}}{\pi^2 m_\pi (8f_\pi)^4}\int_0^u {\rm d}x\,x^2\int_{-1}^1 {\rm d}y\int_{-1}^1 {\rm d}z\frac{yz\,\theta(y^2+z^2-1)}{|yz|\sqrt{y^2+z^2-1}}\Bigg\{\frac{2s^2}{(1+s^2)^2}\times \Big[2\ln(1+t^2) - \frac{t^2(3+t^2)}{(1+t^2)^2}\Big]\Big[(6s+4s^3)s' - (3+s^2)s'^2 - (s+s^3)s''\Big] + \frac{4s^3s't^2(2t^4+5t^2-1)}{(1+s^2)(1+t^2)^3}\Bigg\}, \quad \text{(B.131)}$$

$$F_{\rm so}^{(\rm F,3n)}(k_{\rm f}) = \frac{g_{\rm A}^4 M_{\rm N}}{\pi^2 m_\pi (4f_\pi)^4}\int_{-1}^{1}{\rm d}y\int_{-1}^{1}{\rm d}z\frac{yz\,\theta(y^2+z^2-1)}{|yz|\sqrt{y^2+z^2-1}}\Big\{16y^2z\,\theta(y)\theta(z)\times \Big[\frac{1+2u^2y^2}{(1+4u^2y^2)^2}\Big(\arctan 2uz - 2uz\Big) + \frac{u^3z(1-2z^2)}{(1+4u^2y^2)(1+4u^2z^2)}\Big] + \int_0^u {\rm d}x\,\frac{u^{-8}x^2st^2t'}{2(1+s^2)^2(1+t^2)}\Big[(s+s^3)(s'-s'')(st+sxz-txy) + s'^2(2txy-(3s+s^3)(t+xz))\Big]\Big\}, \quad \text{(B.132)}$$

$$F_{J}^{(\rm F,3n)}(k_{\rm f}) = \frac{g_{\rm A}^4 M_{\rm N}}{\pi^2 m_\pi (4f_\pi)^4}\int_{-1}^{1}{\rm d}y\int_{-1}^{1}{\rm d}z\frac{yz\,\theta(y^2+z^2-1)}{|yz|\sqrt{y^2+z^2-1}}\Big\{y^2\,\theta(y)\theta(z)\times \Big[\Big[\ln(1+4u^2z^2)-4u^2z^2\Big]\frac{9+4u^2(5+2y^2)+16u^4(y^2+y^4)}{u(1+4u^2y^2)^3} + \frac{16u^3(3+4u^2y^2)z^2(1-2z^2)}{(1+4u^2y^2)^2(1+4u^2z^2)}\Big] + \int_0^u {\rm d}x\,\frac{x^4s^2t^2(1-y^2-z^2)}{4u^{10}(1+s^2)^2(1+t^2)^2}\Big[(s+s^3)(s''-s')+(3+s^2)s'^2\Big]\times \Big[(t+t^3)(t''-t')+(3+t^2)t'^2\Big]\Big\}, \quad \text{(B.133)}$$

with the partial derivatives $t' = u\partial t/\partial u$ and $t'' = u^2\partial^2 t/\partial u^2$. For the numerical evaluation of the ${\rm d}y\,{\rm d}z$-double integrals in eqs. (B.130-B.133) it is advantageous to first antisymmetrize the integrands both in y and z and then to substitute $z = \sqrt{y^2\alpha^2+1-y^2}$. This way the integration region becomes equal to the unit-square $0 < y, \alpha < 1$.

B.7.3 Two-pion exchange

Here we list the contributions of 2π-exchange with virtual Δ-excitation to the strength functions $F_{\tau,d}(k_{\rm f})$.

Contact terms:

$$F_\tau^{(\rm NN)}(k_{\rm f}) = B_5\frac{5k_{\rm f}^3}{3M_{\rm N}^4}, \qquad F_d^{(\rm NN)}(k_{\rm f}) = \frac{B_d}{M_{\rm N}^4}. \quad \text{(B.134)}$$

Two-body Fock diagrams contribute only to $F_\tau(k_{\rm f})$ via a (subtracted) dispersion integral:

$$F_\tau^{(2\pi\rm F,2)}(k_{\rm f}) = \frac{35}{24\pi^3k_{\rm f}^4}\int_{2m_\pi}^{\infty}{\rm d}\mu\,{\rm Im}(V_C+3W_C+2\mu^2V_T+6\mu^2W_T)\times \Big\{\frac{8k_{\rm f}^7}{35\mu^3} - \frac{\mu k_{\rm f}^3}{3} - 6\mu^3k_{\rm f} + \frac{\mu^5}{4k_{\rm f}} + 5\mu^4\arctan\frac{2k_{\rm f}}{\mu} + \frac{\mu^3}{16k_{\rm f}^3}(24k_{\rm f}^4-18k_{\rm f}^2\mu^2-\mu^4)\ln\Big(1+\frac{4k_{\rm f}^2}{\mu^2}\Big)\Big\}. \quad \text{(B.135)}$$

The evaluation of the (left) three-body Hartree diagram in fig. 7.2 leads to the results:

$$F_\tau^{(\Delta\mathrm{H},3)}(k_\mathrm{f}) = \frac{35 g_\mathrm{A}^4 m_\pi^4}{\Delta(2\pi f_\pi)^4}\left\{\frac{13}{4} - \frac{5}{24u^2} + \frac{u^2}{9} - \frac{35}{12u}\arctan 2u + \left(\frac{5}{96u^4} + \frac{3}{4u^2} - \frac{3}{4}\right)\ln(1+4u^2)\right\}, \quad \text{(B.136)}$$

$$F_d^{(\Delta\mathrm{H},3)}(k_\mathrm{f}) = \frac{g_\mathrm{A}^4 m_\pi}{128\pi^2\Delta f_\pi^4}\left\{23\arctan 2u - \frac{7}{u}\ln(1+4u^2) - 16u - \frac{2u(3+16u^2)}{3(1+4u^2)^2}\right\}. \quad \text{(B.137)}$$

Somewhat more involved is the evaluation of the (right) Fock diagram in fig. 7.2 for which we find:

$$F_\tau^{(\Delta\mathrm{F},3)}(k_\mathrm{f}) = \frac{35 g_\mathrm{A}^4 m_\pi^4}{\Delta(8\pi f_\pi)^4 u^7}\int_0^u \mathrm{d}x\Big[2G_S(x,u)\widetilde{G}_S(x,u) + G_T(x,u)\widetilde{G}_T(x,u)\Big], \quad \text{(B.138)}$$

$$\widetilde{G}_S(x,u) = \frac{4ux}{3}(6u^4 - 22u^2 - 45 + 30x^2 - 10u^2x^2) + 4x(10 + 9u^2 - 15x^2)\Big[\arctan(u+x) + \arctan(u-x)\Big] + (35x^2 + 14u^2x^2 - 10x^4 - 5 - 9u^2 - 4u^4)\ln\frac{1+(u+x)^2}{1+(u-x)^2}, \quad \text{(B.139)}$$

$$\widetilde{G}_T(x,u) = \frac{ux}{12}(69u^4 + 70u^2 - 15) - \frac{ux^3}{12}(45 + 31u^2) - \frac{15ux^5}{4} - \frac{u}{4x}(1+u^2)^2(5+3u^2) + \frac{[1+(u+x)^2][1+(u-x)^2]}{16x^2}\times (5 + 8u^2 + 3u^4 - 18u^2x^2 + 15x^4)\ln\frac{1+(u+x)^2}{1+(u-x)^2}, \quad \text{(B.140)}$$

$$F_d^{(\Delta\mathrm{F},3)}(k_\mathrm{f}) = \frac{g_\mathrm{A}^4 m_\pi}{\pi^2\Delta(8f_\pi)^4}\left\{-\frac{3+12u^2+26u^4+40u^6}{u^5(1+4u^2)}\ln(1+4u^2) + \frac{3}{8u^7}(1+2u^2+8u^4)\ln^2(1+4u^2) + \frac{2(3+6u^2+16u^4)}{u^3(1+4u^2)}\right\}, \quad \text{(B.141)}$$

with $G_{S,T}(x,u)$ defined in eqs. (B.25,B.26).

The contributions to the spin-orbit strength function $F_\mathrm{so}(k_\mathrm{f})$ caused by virtual Δ-excitations have been calculated in ref. [89]. The two relevant equations are

$$F_\mathrm{so}^{(\Delta\mathrm{H})}(k_\mathrm{f}) = \frac{g_\mathrm{A}^4 m_\pi}{8\pi^2\Delta f_\pi^4}\left[\frac{u+2u^3}{1+4u^2} - \frac{1}{4u}\ln\left(1+4u^2\right)\right] \quad \text{(B.142)}$$

and

$$F_\mathrm{so}^{(\Delta\mathrm{F})}(k_\mathrm{f}) = \frac{g_\mathrm{A}^4 m_\pi}{\pi^2\Delta(16f_\pi)^4 u^3}\left[8u^2 - 12 + \left(\frac{3}{u^2} + 4\right)\ln\left(1+4u^2\right)\right]^2. \quad \text{(B.143)}$$

In addition to that, there is the contact term,

$$F_{\rm so}^{(\rm NN)}(k_{\rm f}) = \frac{B_{\rm so}}{M_{\rm N}^4}\,. \tag{B.144}$$

The contribution to $F_{\rm so}(k_{\rm f})$ by the irreducible 2π-exchange with only nucleons in intermediate states is given in cut-off regularization in eq. (5.14). After subtracting the value at $\rho = 0$ to remove all regularization dependent parts, one gets [90]:

$$F_{\rm so}^{(2\pi)}(k_{\rm f}) = \frac{g_{\rm A}^2}{\pi M_{\rm N}(4f_\pi)^4}\left\{\frac{m_\pi^3}{6k_{\rm f}^2}(4-3g_{\rm A}^2)\ln\frac{k_{\rm f}^2+m_\pi^2}{m_\pi^2} + \frac{m_\pi}{6}(20-9g_{\rm A}^2) + \right.$$
$$\left. \frac{2}{3k_{\rm f}}\Big[3m_\pi^2(g_{\rm A}^2-2) - 4k_{\rm f}^2\Big]\arctan\frac{k_{\rm f}}{m_\pi}\right\}. \tag{B.145}$$

B.7.4 Master integrals

In this appendix we collect the set of master integrals one encounters in the diagrammatic evaluation of the energy density functional $\mathcal{E}[\rho,\tau,\mathbf{J}]$. Contributions to the strength functions $F_{\tau,d,J}(k_{\rm f})$ from diagrams with two medium insertions are of the generic form:

$$\int\limits_{|\mathbf{p}_{1,2}|\le k_{\rm f}} \frac{{\rm d}^3p_1{\rm d}^3p_2}{(2\pi)^6}\,(5\mathbf{p}_1^2 - 3k_{\rm f}^2) f(|\mathbf{p}_1-\mathbf{p}_2|) =$$
$$\frac{2k_{\rm f}^8}{3\pi^4}\int_0^1 {\rm d}x\, x^3(1-x)^2(2x^2+4x-3) f(2xk_{\rm f})\,, \tag{B.146}$$

$$\boldsymbol{\nabla}_1\cdot\boldsymbol{\nabla}_2 \int\limits_{|\mathbf{p}_j|\le k_{\rm f}(\mathbf{r}_j)} \frac{{\rm d}^3p_1{\rm d}^3p_2}{(2\pi)^6}\, f(|\mathbf{p}_1-\mathbf{p}_2|)\Big|_{\mathbf{r}_j=\mathbf{r}} = (\boldsymbol{\nabla}\rho)^2\int_0^1 {\rm d}x\,\frac{x}{8} f(2xk_{\rm f})\,, \tag{B.147}$$

$$\int \frac{{\rm d}^3p_1{\rm d}^3p_2}{(2\pi)^6}\, f(|\mathbf{p}_1-\mathbf{p}_2|)\,\mathbf{p}_1\cdot\mathbf{p}_2 \prod_{j=1}^2[\delta(k_{\rm f}-|\mathbf{p}_j|) - k_{\rm f}\delta'(k_{\rm f}-|\mathbf{p}_j|)] =$$
$$\frac{k_{\rm f}^6}{8\pi^4}\Big[f(0) - f(2k_{\rm f}) - 2k_{\rm f}f'(2k_{\rm f})\Big]\,, \tag{B.148}$$

$$\int \frac{{\rm d}^3p_1{\rm d}^3p_2}{(2\pi)^6}\,\frac{f(|\mathbf{p}_1-\mathbf{p}_2|)}{|\mathbf{p}_1-\mathbf{p}_2|^2}\prod_{j=1}^2 \mathbf{p}_j\cdot(\mathbf{p}_1-\mathbf{p}_2)\,[\delta(k_{\rm f}-|\mathbf{p}_j|) - k_{\rm f}\delta'(k_{\rm f}-|\mathbf{p}_j|)] =$$
$$\frac{k_{\rm f}^6}{8\pi^4}\left[-3f(2k_{\rm f}) - 2k_{\rm f}f'(2k_{\rm f}) - 2\int_0^1 {\rm d}x\, x^{-1} f(2xk_{\rm f})\right], \qquad f(0) = 0\,. \tag{B.149}$$

These reduction formulas can be derived with the help of a power series ansatz, $f(q) = \sum_{\nu=0}^\infty f_\nu q^{2\nu}$, which covers all practically relevant cases. The Hartree diagram with three medium insertions leads to nine-dimensional principal value integrals of the form:

$$\fint_{|\mathbf{p}_j|\leq k_j} \frac{\mathrm{d}^3p_1\mathrm{d}^3p_2\mathrm{d}^3p_3}{(2\pi)^3}\,\frac{f(|\mathbf{p}_1-\mathbf{p}_2|)}{(\mathbf{p}_1-\mathbf{p}_2)\cdot(\mathbf{p}_1-\mathbf{p}_3)} = \int_0^{k_1}\mathrm{d}p\,p^2\int_{-1}^{1}\mathrm{d}y\left[2k_3py+(k_3^2-p^2y^2)\ln\frac{k_3+py}{k_3-py}\right]\int_0^{q_\mathrm{max}}\mathrm{d}q\,q\,f(q)\,, \quad \text{(B.150)}$$

with $q_\mathrm{max}=py+\sqrt{k_2^2-p^2+p^2y^2}$ under the subsidiary condition $k_1\leq k_{2,3}$. In order to achieve this reduction one eliminates $\mathbf{p}_2$ in favor of $\mathbf{q}=\mathbf{p}_1-\mathbf{p}_2$ whose integration domain is a shifted Fermi sphere $|\mathbf{q}-\mathbf{p}_1|\leq k_2$. By taking appropriate (multiple) derivatives $\partial/\partial k_j$ one can also handle δ- and δ'-type weighting functions in this principal value integral. For analogous contributions from the Fock diagram with three medium insertions one performs this shift of integration variable for $\mathbf{p}_2$ and $\mathbf{p}_3$ simultaneously, and one employs the identity:

$$\frac{1}{2\pi}\fint_0^{2\pi}\frac{\mathrm{d}\phi}{yz+\sqrt{(1-y^2)(1-z^2)}\cos\phi} = \frac{yz\,\theta(y^2+z^2-1)}{|yz|\sqrt{y^2+z^2-1}}\,. \quad \text{(B.151)}$$

The denominator on the left hand side arises through the application of the cosine law of spherical geometry.

B.7.5 Fits to the strength functions

The fits in eqs. (B.152–B.155) reproduce the curves shown in figs. 5.2–5.5 respectively.

$$\tilde{M}_\mathrm{N}^\star(\rho)/M_\mathrm{N}|_{fit} = 1-3.054\,\mathrm{fm}^2\cdot\rho^{2/3}+6.345\,\mathrm{fm}^3\cdot\rho \quad \text{(B.152)}$$

$$F_\nabla(k_\mathrm{f})|_{fit} = 45.43\,\mathrm{MeV\,fm}^4\cdot\rho^{-1/3}-0.229\,\mathrm{MeV\,fm}^2\cdot\rho^{-1} \quad \text{(B.153)}$$

$$F_\mathrm{so}(k_\mathrm{f})|_{fit} = 1.898\,\mathrm{MeV\,fm}^3\cdot\rho^{-2/3}-29.37\,\mathrm{MeV\,fm}^4\cdot\rho^{-1/3} \quad \text{(B.154)}$$

$$F_J(k_\mathrm{f})|_{fit} = 12.80\,\mathrm{MeV\,fm}^{7/2}\cdot\rho^{-1/2}+7.041\,\mathrm{MeV\,fm}^4\cdot\rho^{-1/3} \quad \text{(B.155)}$$

In this context we mention also the fitted form of the nuclear matter equation of state truncated at $\mathcal{O}(k_\mathrm{f}^4)$ [41] underlying the calculation of chapter 5 (and ref. [66]):

$$\bar{E}(k_\mathrm{f})|_{fit} = 111.63\,\mathrm{MeV\,fm}^2\cdot\rho^{2/3}-752.82\ \mathrm{MeV\,fm}^3\cdot\rho+832.74\,\mathrm{MeV\,fm}^4\cdot\rho^{4/3}\,. \quad \text{(B.156)}$$

The results including full $\pi\mathrm{N}\Delta$-dynamics shown in figs. 7.9–7.11 can be approximated by the fits given in eqs. (B.157–B.159) respectively:

$$\tilde{M}_\mathrm{N}^\star(\rho)/M_\mathrm{N}|_{fit} = \left(2.66046\,\mathrm{fm}^2\rho^{2/3}-3.38432\,\mathrm{fm}^3\rho+13.1732\,\mathrm{fm}^6\rho^2\right)^{-1} \quad \text{(B.157)}$$

$$\begin{aligned} F_\nabla(k_\mathrm{f})|_{fit} = &-2.00791\,\mathrm{MeV\,fm}^3\rho^{-2/3}+42.1051\,\mathrm{MeV\,fm}^4\rho^{-1/3} \\ &+64.7979\,\mathrm{MeV\,fm}^5-128.492\,\mathrm{MeV\,fm}^6\rho^{1/3} \end{aligned} \quad \text{(B.158)}$$

$$\begin{aligned} F_\mathrm{so}(k_\mathrm{f})|_{fit} = &-273.048\,\mathrm{MeV\,fm}^5-0.212279\,\mathrm{MeV\,fm}^3\rho^{-2/3} \\ &+10.5076\,\mathrm{MeV\,fm}^2\rho^{-1/3}+837.849\,\mathrm{MeV\,fm}^6\rho^{1/3} \\ &-985.005\,\mathrm{MeV\,fm}^7\rho^{2/3}+520.285\,\mathrm{MeV\,fm}^8\rho \end{aligned} \quad \text{(B.159)}$$

List of figures

Bibliography

[1] R. Brockmann, R. Machleidt, *Phys. Rev.* **C42** (1990) 1965; and references therein.

[2] R. B. Wiringa, *Rev. Mod. Phys.* **65** (1993) 231; and references therein.

[3] S. C. Pieper, V. R. Pandharipande, R. B. Wiringa, J. Carlson, *Phys. Rev.* **C64** (2001) 014001; and references therein.

[4] J. Carlson, J. Morales, V. R. Pandharipande, D. G. Ravenhall, *Phys. Rev.* **C68** (2003) 025802.

[5] S. Fantoni, A. Sarsa, K. E. Schmidt, *Phys. Rev. Lett.* **87** (2001) 181101.

[6] E. Caurier, G. Martinez-Pinedo, F. Nowacki, A. Poves, A. P. Zuker, "The Shell Model as Unified View of Nuclear Structure", arXiv:nucl-th/0402046; and references therein.

[7] M. Bender, P.-H. Heenen, P.-G. Reinhard, *Rev. Mod. Phys.* **75** (2003) 121; and references therein.

[8] T. H. R. Skyrme, *Nucl. Phys.* **9** (1959) 615.

[9] B. D. Serot, J. D. Walecka, *Adv. Nucl. Phys.* **16** (1986) 1; and references therein.

[10] B. D. Serot, J. D. Walecka, *Int. J. Mod. Phys.* **E6** (1997) 515; and references therein.

[11] P. Ring, *Prog. Part. Nucl. Phys.* **37** (1996) 193;
P. Ring, *Lecture Notes in Physics* **581**, Eds. J.M. Arias, M. Lozana, Springer, Berlin Heidelberg 2001, page 195; and references therein.

[12] G. A. Lalazissis, P. Ring, D. Vretenar (Eds.), "Extended Density Functionals in Nuclear Structure Physics", Lect. Notes Phys. **641**, Springer, Berlin Heidelberg 2004.

[13] M. Lutz, B. Friman, C. Appel, *Phys. Lett.* **B474** (2000) 7.

[14] N. Kaiser, S. Fritsch, W. Weise, *Nucl. Phys.* **A697** (2002) 255.

[15] S. Fritsch, "Chirale Dynamik und Kernmaterie", *Diplomarbeit*, TU München, September 2001.

[16] S. Weinberg, *Physica* **A96** (1979) 327;
J. Gasser, H. Leutwyler, *Ann. Phys. (N. Y.)* **158** (1984) 142;
J. Gasser, H. Leutwyler, *Nucl. Phys.* **B250** (1985) 465.

[17] V. Bernard, N. Kaiser, U.–G. Meißner, *Int. J. Mod. Phys.* **E4** (1995) 193.

[18] A. Akmal, V. R. Pandharipande, D. G. Ravenhall, *Phys. Rev.* **C58** (1998) 1804.

[19] S. K. Bogner, T. T. S. Kuo, A. Schwenk, *Phys. Rep.* **386** (2003) 1; and references therein.

[20] D. R. Entem, R. Machleidt, *Phys. Rev.* **C68** (2003) 041001.

[21] P. Finelli, N. Kaiser, D. Vretenar, W. Weise, *Eur. Phys. J.* **A17** (2003) 573.

[22] P. Finelli, N. Kaiser, D. Vretenar, W. Weise, *Nucl. Phys.* **A735** (2004) 449.

[23] A. deShalit, H. Feshbach, "Theoretical Nuclear Physics, Vol. 1 — Nuclear Structure", John Wiley & Sons, New York 1974.

[24] D. N. Basu, P. R. Chowdhury, "Evaluations of energy coefficients of Bethe-Weizsacker mass formula", arXiv:nucl-th/0408013.

[25] Ingo Sick, private communication;
see also Day et al., *Phys. Rev.* **C40** (1989) 1011.

[26] D. Durand, E. Suraud, B. Tamain, "Nuclear Dynamics in the Nucleonic Regime", Institute of Physics Publishing, Bristol Philadelphia 2001;
see also J.-P. Blaizot, *Nucl. Phys.* **A649** (1999) 61c.

[27] B. Friedman, V. R. Pandharipande, *Nucl. Phys.* **A361** (1981) 502.

[28] M. Baldo (Ed.), "Nuclear Methods and the Nuclear Equation of State", Int. Rev. Nucl. Phys. **8** (1999), World Scientific, Singapore

[29] H. Hellmann, "Einführung in die Chantenchemie", Deuticke Verlag, Leipzig 1937;
R. P. Feynman, *Phys. Rev.* **56** (1939) 340.

[30] T. D. Cohen, R. J. Furnstahl, D. K. Griegel, *Phys. Rev. Lett.* **67** (1991) 961.

[31] N. Kaiser, S. Fritsch, W. Weise, *Nucl. Phys.* **A700** (2002) 343.

[32] S. Fritsch, N. Kaiser, W. Weise, *Phys. Lett.* **B545** (2002) 73.

[33] M. M. Pavan, R. A. Arndt,I. I. Strakovsky, *Physica Scripta* **T87** (2000) 65.

[34] P. A. Seeger, W. M. Howard, *Nucl. Phys.* **A238** (1975) 491.

[35] G. E. Brown, "Unified Theory of Nuclear Models and Forces", 3rd ed., North-Holland Publishing, Amsterdam London 1971, chapters X and XI.

[36] N. Kaiser, *Nucl. Phys.* **A709** (2002) 251.

[37] P. Grange, J. P. Cugnon, A. Lejeune, *Nucl. Phys.* **A473** (1987) 365.

[38] G. Q. Li, R. Machleidt, R. Brockmann, *Phys. Rev.* **C45** (1992) 2782.

[39] A. Bohr, B. R. Mottelson, "Nuclear Structure, Vol.I", Benjamin, New York 1969, chapter 2.4.

[40] N. M. Hugenholtz, L. Van Hove, *Physica* **24** (1958) 363.

[41] S. Fritsch, N. Kaiser, *Eur. Phys. J.* **A17** (2003) 11.

[42] J. M. Luttinger, *Phys. Rev.* **121** (1961) 942.

[43] V. M. Galitskii, *Sov. Phys. JEPT* **7** (1958) 104.

[44] R. W. Hasse, P. Schuck, *Nucl. Phys.* **A445** (1985) 205.

[45] W. Zuo, I. Bombaci, U. Lombardo, *Phys. Rev.* **C60** (1999) 024605.

[46] P. Danielewicz, R. Lacey, W. G. Lynch, *Science* **298** (2002) 1592.

[47] J. V. Steele, "Effective field theory power counting at finite density", arXiv:nucl-th/0010066.

[48] J. Gasser, H. Leutwyler, M. Sainio, *Phys. Lett.* **B253** (1991) 252.

[49] W. Weise, "Quarks, Hadrons and Dense Nuclear Matter", Les Houches, Session LXVI (1996) 423, Elsevier Science.

[50] R. Brockmann, W. Weise, *Phys. Lett.* **B367** (1996) 40.

[51] L. B. Csernai, J. I. Kapusta, *Phys. Reports* **131** (1986) 223; and references therein.

[52] J. B. Natowitz et al., *Phys. Rev. Lett.* **89** (2002) 212701.

[53] J. I. Kapusta, "Finite-temperature Field Theory", Cambridge University Press, Cambridge 1989, chapt. 10.

[54] G. Sauer, H. Chandra, U. Mosel, *Nucl. Phys.* **A264** (1976) 221.

[55] A. Lejeune, P. Grange, M. Martzolff, J. Cugnon, *Nucl. Phys.* **A453** (1986) 189.

[56] W. Kohn, J. M. Luttinger, *Phys. Rev.* **118** (1960) 41;
J.M. Luttinger, J.C. Ward, *Phys. Rev.* **118** (1960) 1417.

[57] D. J. Thouless, "The Quantum Mechanics of Many-Body-Systems", Academic Press, New York London 1961, chapter 7.3.

[58] A. L. Fetter, J. D. Walecka, "Quantum Theory of Many-Particle Systems", McGraw-Hill, New York 1971.

[59] A. Beraudo, A. De Pace, M. Martini, A. Molinari, *Annals Phys.* **311** (2004) 81.

[60] J. W. Negele, D. Vautherin, *Phys. Rev.* **C5** (1972) 1472.

[61] M. Beiner, H. Flocard, N. Van Giai, P. Quentin, *Nucl. Phys.* **A238** (1975) 29.

[62] H. Krivine, J. Treiner, O. Bohigas, *Nucl. Phys.* **A336** (1980) 155.

[63] J. Bartel, P. Quentin, M. Brack, C. Guet, H.-B. Håkansson, *Nucl. Phys.* **A386** (1982) 79.

[64] E. Chabanat, P. Bonche, P. Haensel, J. Meyer, R. Schaeffer, *Nucl. Phys.* **A627** (1997) 710; **A635** (1998) 231; and references therein.

[65] P. Ring, P. Schuck, "The Nuclar Many-Body Problem", Springer, Berlin Heidelberg 1980.

[66] N. Kaiser, S. Fritsch, W. Weise, *Nucl. Phys.* **A724** (2003) 47.

[67] N. Kaiser, *Phys. Rev.* **C68** (2003) 014323.

[68] C. Titin-Schnaider, P. Quentin, *Phys. Lett.* **B49** (1974) 397.

[69] J. M. Pearson, S. Goriely, M. Samyn, *Eur. Phys. J.* **A15** (2002) 13;
F. Tondour, S. Goriely, J. M. Pearson, M. Onsi, *Phys. Rev.* **C62** (2000) 024308.

[70] M. Brack, C. Guet, H.-B. Håkansson, *Physics Reports* **123** (1985) 275.

[71] J. P. Blaizot, *Phys. Rep.* **64** (1980) 171.

[72] J. Dobaczewski, work in progress and private communications.

[73] N. Kaiser, R. Brockmann, W. Weise, *Nucl. Phys.* **A625** (1997) 758.

[74] N. Kaiser, *Nucl. Phys.* **A720** (2003) 157.

[75] V. Bernard, N. Kaiser, J. Kambor, Ulf-G. Meißner, *Nucl. Phys.* **B388** (1992) 315; and references therein.

[76] P.-G. Reinhard, "The Skyrme-Hartree-Fock Model of the Nuclear Ground State" in K. Langanke, J. A. Maruhn, S. E. Koonin (Eds.), "Computational Nuclear Physics 1: Nuclear Structure", Springer, Berlin Heidelberg 1991.

[77] P. E. Hodgson, "Growth Points in Nuclear Physics, Vol. 3", Pergamon Press, Oxford 1981, chapter 2.

[78] T. Gross-Boelting, C. Fuchs, A. Faessler, *Nucl. Phys.* **A648**, (1999) 105.

[79] S. Fritsch, N. Kaiser, *Eur. Phys. J.* **A21** (2004) 117.

[80] N. Kaiser, S. Gerstendörfer, W. Weise, *Nucl. Phys.* **A637** (1998) 395.

[81] M. Ericson, A. Figureau, *J. Phys.* **G7** (1981) 1197.

[82] D. Vretenar, G. A. Lalazissis, R. Behnsch, W. Pöschl, P. Ring, *Nucl. Phys.* **A621** (1997) 853.

[83] C. Mahaux, R. Sartor, *Adv. Nucl. Phys.* **22** (1991) 1; and references therein.

[84] P. Bozek, P. Czerski, *Eur. Phys. J.* **A11** (2001) 271; and references therein.

[85] A. Schwenk, G. E. Brown, B. Friman, *Nucl. Phys.* **A703** (2002) 745.

[86] H. Feldmeier, T. Neff, R. Roth, J. Schnack, *Nucl. Phys.* **A632** (1998) 61.

[87] J. Kuckei, F. Montani, H. Müther, A. Sedrakian, *Nucl. Phys.* **A723** (2003) 32.

[88] V. A. Karnaukhov et al., *Phys. Rev.* **C67** (2003) 011601(R).

[89] N. Kaiser, *Phys. Rev.* **C68** (2003) 054001.

[90] N. Kaiser, *Phys. Rev.* **C70** (2004) 034307.

[91] E. Epelbaum, W. Glöckle, Ulf-G. Meißner, *Nucl. Phys.* **A671** (2000) 295.

[92] D. Vretenar, T. Niksic, P. Ring, *Phys. Rev.* **C68** (2003) 024310.

[93] R. J. Furnstahl, *Nucl. Phys.* **A706** (2002) 85.

[94] T. Niksic, D. Vretenar, P. Finelli, P. Ring, *Phys. Rev.* **C66** (2002) 024306.

[95] S. Fritsch, N. Kaiser, W. Weise, "Chiral approach to nuclear matter: Role of two-pion exchange with virtual Delta-isobar excitation", subm. to *Nucl. Phys.* **A**, arXiv:nucl-th/0406038.

[96] E. Epelbaum, U. G. Meissner, W. Gloeckle, *Nucl. Phys.* **A714** (2003) 535.

[97] N. Kaiser, "Spin-asymmetry energy of nuclear matter", subm. to *Phys. Rev.* **C**, arXiv:nucl-th/0410021.

[98] A. B. Migdal, "Theory of finite Fermi Systems and Applications to Atomic Nuclei", Interscience, New York 1967.

[99] T. Suzuki, H. Sakai, *Phys. Lett.* **B455** (1999) 25.

Acknowledgments

There are many people who have, directly or indirectly, contributed to the success of this work. I would like to thank all of them, especially...

- Prof. Dr. Wolfram Weise, for his support and interest, for many insightful and motivating discussions, and for making my stay at the ECT* in Trento possible.
- Norbert Kaiser, for the incredible amount of work he put into our project and for all the advice he gave me.
- all people who made my stay in Trento such a nice experience. Special thanks go to Rachel and Donatella, who took care of all the organizational details, and to Ewan and Cesar, for the lively after-work program.
- Prof. Dr. Peter Ring and Milena Serra, for providing various Skyrme-Hartree-Fock codes.
- Markus Bleuel, Roland Kuhn, and Michael Thaler, who made Garching appear not quite that isolated.
- Jörn Kersten, Thorsten Renk, and Roland Schneider, for many nice evenings with games or movies.
- all members of T39, for the nice working climate.